Thèse n° 7619

Structural performance and mechanical properties investigation of spent nuclear fuel rods under static and dynamic bending loads

Présentée le 12 juillet 2021

Faculté des sciences de base
Laboratoire de physique des réacteurs et de comportement des systèmes
Programme doctoral en énergie

pour l'obtention du grade de Docteur ès Sciences

par

Efstathios VLASSOPOULOS

Acceptée sur proposition du jury

Prof. D. Dujic, président du jury
Prof. A. Pautz, Dr S. Caruso, directeurs de thèse
Dr V. V. Rondinella, rapporteur
Dr J. Bertsch, rapporteur
Prof. H.-M. Prasser, rapporteur

École
polytechnique
fédérale
de Lausanne

2021

To my loving family,
Pantelis, Foteini, Giorgos and Alexandros

Acknowledgements

This work was financially supported by the Association of Swiss Electricity Companies (VSE), from the European Commission through the Gentle Project and traineeship scheme, as well as from Nagra. First and foremost, I would like to thank Prof. Dr. Andreas Pautz for trusting my abilities and giving me the opportunity to conduct this study. My sincere gratitudes go to my supervisors Dr. Stefano Caruso and Dr. Vincenzo Rondinella. Thank you for offering me the best conditions possible to conduct this work, for your continuous support and for the spark you inspired me to develop both professionally and personally. In addition, I would like to thank Prof. Dr. Horst-Michael Prasser and Dr. Johannes Bertsch for accepting to participate in my jury committee. Thank you for your time and feedback on my work and for the interesting discussions.

In the last 5 years, I found myself between two organizations in Switzerland and Germany. My PhD journey began at the facilities of JRC-Karlsruhe and continued in Nagra. As a result, this study was a collective effort and could not have been realized without the contribution of many.

Above all, I owe my sincere gratitudes to Dimitris Papaioannou and Ramil Nasyrow. No words can describe my appreciation to both of you. This work would not have been the same without your contribution. However, I most importantly thank you for your friendship and support. You were my family in Germany, who welcomed me from the very beginning and supported me every single day since.

A big thank to all colleagues from JRC-Karlsruhe that actively supported and contributed to this work. At first, I would like to acknowledge Dr. Joseph Somers, who welcomed me in his group at the hot-cell facilities. A huge thank goes to the amazing team at the hot-cells, Ralf, Gianni, Lorenzo, Gegé, Ernesto, Laurent and Matthias, who actively supported my work and helped me with various activities. Thanks to Klaus for the wonderful technical support he gave me. Special thanks are conveyed to Dr. Paul Van Uffelen and Dr. Thierry Wiss for their scientific advices and fruitful discussions.

My heartfelt acknowledgements are due to many colleagues in Nagra for supporting me and making my life easier during these years. I highly appreciate all the support from Ben, Susanne, Tim, Irina, Valentyn, Madalina, Caroline, Stefan and Nicolas. Special thanks to all the students that worked with me and contributed to this project, Michele, Olympios and Valeria.

The years I spent in Karlsruhe offered me the possibility to meet many people, make new friends and share unforgettable moments. Special thanks go to Petros, Myrto, Alex, Depie, Thomas, Eugenia for all the amazing trips, nice evenings and long nights, basketball games and food/wine "tastings"... Also, many thanks to Miguel, Björn, Elli and Matilda! I would also like to thank my "Swiss" fiends for their support and for the memories we shared, Nikitas, Ahmed, Alessandro, Rosa, Miguel, Mauricio, Zhexi and Benoit! Special gratitude to Dionisis, Vera and Alkis for their friendship and support in the good and bad times.

Also, I have the need to thank the first people that inspired me and gave me the desire to study and love nuclear engineering. For this reason, a huge thank to my Physics teacher Aris Antonopoulos, as well to Prof. M.J. Anagnostakis and Prof. N. Petropoulos.

Finally, the last acknowledgment goes to the most important person, Aleka. Thank you for all the patience, support and love you gave me during the last years. You made this trip easier and happier. Cheers to the better times ahead with more dancing and less trains ;-)

Abstract

Currently, most Spent Nuclear Fuel (SNF) is kept safely in storage either at on-site facilities or at centralized interim storage sites. Moreover, many countries face delays in implementing their waste management programmes for SNF and high-level waste disposal. As storage pools approach their capacity, an increasing demand for interim dry-storage solutions is foreseen in the near future and, is associated with emerging regulatory issues. Storage prolongation in interim facilities for time periods far beyond than what originally envisaged, requires license renewal of the facility, as well as of transport and storage casks. At the same time, the safety of SNF operation activities (transportation and handling) at surface encapsulation facilities must be ensured.

In order to evaluate the SNF response under normal or accident scenarios, in different stages of the back-end of the nuclear fuel cycle, it is essential to assess the mechanical properties of fuel rods, as well as their evolution during and after irradiation. Several previous studies have identified mechanisms that could affect such properties during dry-storage. However, data generated from experiments with irradiated SNF are extremely rare. This PhD complements previous studies by generating new data for the structural performance of SNF, in areas where technical gaps have been identified. In particular, the mechanical properties of SNF as function of burnup have been investigated both experimentally and numerically, under quasi-static and dynamic bending loads.

The experimental activities were conducted at the hot-cell facilities of JRC-Karlsruhe and include three-point bending and gravitational impact tests performed at room temperature on pressurized samples from commercially used PWR UO2 rods. Their dynamic response was studied by successfully applying a new Image Analysis methodology developed in this work. Preliminary tests were conducted on surrogate rodlets consisting of fresh and hydrogenated Zircaloy-4 cladding tubes filled with alumina pellets. The results showed that the sample's ductility decreases with increasing hydrogen concentration in the cladding.

Five SNF rods, with a wide range of burnup, were selected for the tests on irradiated fuel. High burnup samples showed higher toughness due to irradiation damage on the cladding, and less ductile behavior. Overall, strain rate had marginal influence on ductility for high-burnup samples, whereas for low burnup ones, ductility decreased significantly with strain rate. The flexural mechanical properties of the claddings as function of burnup were derived from the 3-point bending tests using the Euler-Bernoulli beam theory for beam elements with hollow-circular profile. A series of post-test examinations concerning the rod failure processes showed that fuel release in case of rod fracture is very limited, amounting to less than the mass of one pellet.

Finite Element Analysis was performed in order to simulate the experiments and the rods' bending behavior under the examined load conditions. An extensive sensitivity analysis was performed to minimize modeling uncertainties and the final model was calibrated against experimental data from the 3-point bending tests. Good agreement was observed between numerically predicted and experimentally derived mechanical properties, and the model can be used to simulate the mechanical behavior of SNF rods under different loading configurations.

Keywords: spent nuclear fuel, mechanical properties, structural performance, finite element analysis, spent fuel integrity

Zusammenfassung

Derzeit wird der größte Teil des Abgebrannten Kernbrennstoffs (Spent Nuclear Fuel SNF) entweder in Anlagen vor Ort oder in zentralen Zwischenlagern sicher gelagert. Außerdem gibt es in vielen Ländern Verzögerungen bei der Umsetzung ihrer Abfallentsorgungsprogramme. Da sich die Abklingbecken ihrer Kapazität annähern, ist in absehbare Zeit ein steigender Bedarf für trockene Zwischenlagerung zu erwarten, der mit neuen regulatorischen Angelegenheiten verbunden ist. Die Verlängerung der Zwischenlagerung erfordert Lizenzerneuerung sowohl für die Anlage als auch für die Transport- und Lagerbehälter. Gleichzeit, soll die Sicherheit der SNF-Betriebsaktivitäten (Transport und Behandlung) in Kapselungsanlagen gewährleistet werden.

Um das Verhalten von SNF unter normalen oder unter Unfallbedingungen an verschiedenen Phasen des Endes der Brennstoffkette zu bestimmen, ist es wesentlich, ihre mechanischen Eigenschaften zu ermitteln. Frühere Studien haben Mechanismen identifiziert, die solche Eigenschaften während der trockenen Zwischenlagerung beeinflussen könnten. Daten aus Experimenten mit bestrahltem SNF sind jedoch sehr spärlich. Diese Doktorarbeit ist mit der Generierung neuer Daten zum mechanischen Verhalten von SNF ein wichtiger Beitrag zu diesem Thema. Insbesondere wurden die mechanischen Eigenschaften von SNF als Funktion ihres Abbrandes, sowohl experimentell als auch numerisch, unter quasistatischer und dynamischer Biegebeanspruchung untersucht.

Die experimentellen Untersuchungen wurden in den Heissen Zellen des JRC-Karlsruhe durchgeführt und umfassen 3-Punkt-Biegeversuche und Schlagtests, an DWR UO2 Brennstabproben bei Raumtemperatur. Um das Verhalten der Proben unter dynamischen Belastungen zu erfassen wurde eine Bildanalyse-Methode unter Verwendung einer Hochgeschwindigkeitskamera entwickelt. Vorläufige Untersuchungen wurden an Surrogat-Stabproben durchgeführt, die aus frischen und hydrierten Zircaloy-4-Hüllrohren, gefüllt mit Aluminiumoxid-Pellets, bestanden. Die Ergebnisse zeigten, dass die Duktilität der Proben mit zunehmender Wasserstoffkonzentration im Hüllrohr abnimmt. Für die Hauptuntersuchungen wurden fünf Brennstabproben mit einem breiten Spektrum an Abbrand ausgewählt. Proben mit hohem

Abbrand zeigten höhere Zähigkeit und ein weniger duktiles Verhalten. Insgesamt hatte die Dehnungsrate einen marginalen Einfluss auf die Duktilität bei Proben mit hohem Abbrand. Die Duktilität bei Proben mit niedrigem Abbrand nahm signifikant mit der Dehnungsrate ab. Die biegemechanischen Eigenschaften des Hüllrohrs als Funktion des Abbrandes wurden aus den 3-Punkt-Biegeversuchen unter Anwendung der Euler-Bernoulli-Balkentheorie für Balkenelemente mit hohlkreisförmigem Profil abgeleitet. Nachuntersuchungen zu den Stabversagensprozessen zeigten, dass die Brennstofffreisetzung im Fall eines Stabbruchs geringfügig ist (niedriger als die Masse eines Pellets)

Finite Elemente Analyse basierend auf statischen Strukturmodellen wurde verwendet, um das Brennstabverhalten unter den untersuchten Lastbedingungen zu simulieren. Eine umfangreiche Sensitivitätsanalyse wurde durchgeführt und das endgültige Model wurde gegen Daten aus den 3-Punkt-Biegeversuchen kalibriert. Eine gute Übereinstimmung zwischen numerischen Vorhersagen und experimentell abgeleiteten Eigenschaften wurde beobachtet.

Schlüsselwörter: abgebrannter Kernbrennstoff, mechanische Eigenschaften, strukturelle Leistung, Finite-Elemente-Analyse, Integrität des abgebrannten Brennstoffs

Table of contents

List of figures **xiii**

List of tables **xxvii**

Glossary **xxix**

Acronyms **xxxi**

1 Introduction **1**

1.1 Swiss spent nuclear fuel management 1

1.2 Basic mechanisms affecting structural behaviour of Spent Nuclear Fuel (SNF) 4

1.2.1 State-of-the-art 9

1.3 Thesis motivation 15

1.4 Thesis Outline 16

2 Description of experimental setup and methods **19**

2.1 Experimental framework 19

2.2 Three-point bending device 22

2.2.1 Primary steps in the development of the bending device 23

2.2.2 Conceptual and functionality control of the bending device 25

2.2.3 Final geometrical characteristics 36

2.2.4 Instrumentation and data acquisition 38

2.2.5 Experimental method - Simple beam theory 43

2.3 Impact or dynamic three-point bending test 49

2.3.1 Early version of the impact tower 49

2.3.2 Upgrade and development of a new impact device 53

2.3.3 Revising the concept of the impact tests 56

2.3.4 High speed camera monitoring and image analysis 61

2.4 Summary 71

3 Experimental investigations on surrogate samples 75

3.1 Surrogate samples properties 75

3.2 Sample preparation 78

3.3 Three-point bending tests 79

3.3.1 Use of fresh Zircaloy-4 (Zry-4) cladding tubes 81

3.3.2 Use of hydrogenated Zry-4 cladding tubes 84

3.3.3 Experimental results 87

3.3.4 Flexural properties of surrogate rods 93

3.3.5 Fracture behavior and crack initiation 95

3.3.6 Post-test examinations 98

3.4 Impact tests 99

3.4.1 Use of fresh and hydrogenated Zry-4 samples 100

3.4.2 Post-test examinations 102

3.5 Summary 103

4 Experimental investigation on irradiated samples 105

4.1 Spent nuclear fuel samples 105

4.1.1 Post irradiation examinations 107

4.2 Sample selection and preparation 108

4.3 Three-point bending tests 110

- 4.3.1 Experimental results . . . 111
- 4.4 Impact tests . . . 115
  - 4.4.1 First test on old impact setup . . . 116
  - 4.4.2 Impact test campaign using the new setup . . . 118
  - 4.4.3 Results from Image Analysis . . . 120
- 4.5 Static flexural properties of irradiated PWR rods . . . 124
- 4.6 Post-test examinations . . . 128
  - 4.6.1 Fracture behavior . . . 128
  - 4.6.2 Fuel mass release . . . 130
  - 4.6.3 Hydrogen concentration at fracture . . . 135
  - 4.6.4 Hydride morphology . . . 137
- 4.7 Summary . . . 140

5 Numerical investigation of SNF rodlet performance under flexural loads 143

- 5.1 Introduction . . . 144
- 5.2 Finite Element Analysis (FEA) of bending setup . . . 145
- 5.3 Development of fuel rod Finite Element Model (FEM) under bending loads 147
  - 5.3.1 Material parameters . . . 147
  - 5.3.2 Sensitivity analysis on various parameters of FEM . . . 153
  - 5.3.3 Symmetry and pellet positioning . . . 154
  - 5.3.4 Cladding modeling approach . . . 158
  - 5.3.5 End-pellet boundary condition . . . 160
  - 5.3.6 Rod internal pressure . . . 162
  - 5.3.7 Contact formulation . . . 163
  - 5.3.8 Mesh independence . . . 165
  - 5.3.9 Weak springs . . . 166
  - 5.3.10 Conclusions and construction of final FEM version . . . 167
- 5.4 FEM calibration based on experimental results . . . 170

5.4.1 Optimization process 172
5.4.1.1 Derivation of cladding's effective mechanical properties . 174
5.5 Summary 176

6 Conclusions and outlook 179
6.1 Summary and main conclusions 179
6.2 Future work recommendation 183

References 187

Appendix A Flexural stress-strain results of surrogate samples 199

Appendix B Uncertainty analysis of flexural properties in three-point bending test 203

Appendix C Effect of sample pressurization on its dynamic response 207
C.1 Impact Mock-up Tower 207
C.2 Experimental Campaign 210

Appendix D Hydrogen measurement analysis 215
D.1 Calibration methodology 217
D.2 Bias estimation 218
D.3 Methodology selection and application 219

Appendix E Finite element modeling details 225

List of figures

1.1 Waste streams in the Swiss management concept [1]. 2

1.2 Simplified illustration of Spent Fuel Assembly (SFA) unloading/loading in the Nagra encapsulation facility. Transport and Storage Cask (TSC) docking station (left), final disposal canister docking station (right). 3

1.3 Schematic representation of a Light Water Reactor (LWR) fuel rod [2] . . . 4

1.4 Schematic representation of Pellet-Cladding Mechanical Interaction (PCMI) [2] 5

1.5 Peak oxide layer thickness as function of burnup for Zircaloy-4 and Zr1%Nb (M5) [3]. 6

1.6 Schematic diagram of hoop stress condition on cladding tubes during a) in-reactor operation and b) interim dry storage [4] 7

1.7 a) BISON prediction of temperature and hoop stress in the cladding throughout fuel cycle [5] and b) generic terminal solid solubilities of hydrogen in α-Zr-alloys for dissolution (TSSd) and precipitation (TSSp) as a function of the temperature [6] 7

1.8 a) Circumferential and b) radial hydrides [3]. 8

1.9 Calculated hoop stress corresponding to temperature of cladding during dry storage for Pressurized Water Reactor (PWR) type fuel and threshold stress for hydride reorientation [7] 9

1.10 9 m drop test on fresh a) PWR and b) Boiling Water Reactor (BWR) assembly, and c) bending test of fresh PWR fuel rod sample[8]. 10

1.11 Fuel rod failure modes [9] 12

1.12 Two dimensional modelling of the fuel assembly; Left: mesh of the assembly in the (x,z) plane; Right: schemes for the equivalent behaviour of the beams representing the guide thimbles and rods [10]. 14

1.13 Estimation of maximum potential rod deflection [11]. 14

2.1 Flowchart illustration of the experimental campaign overview. 21

2.2 Schematic presentation of the loading process during the 3-point bending test [12]. Bending loads are applied by the former on the testing sample which is left laying (lays horizontally) on two cylindrical supports. 23

2.3 Overview of the initial device, where the axis rotation is driven manually via a torque wrench. 24

2.4 Load and displacement as measured during a three-point bending test with the use of torque wrench to manually drive the loading axis. 25

2.5 Overview of the second device version, where a step-motor is used to apply constant torque to the axis. A specimen is shown at the maximum possible bending angle (use of longer former). 26

2.6 2D schematic drawing of the three-point bending test device, highlighting its main configurations and geometric characteristics. 27

2.7 Cross section view of the three-point bending test device at the sample's symmetry vertical symmetry plane, illustrating the working principle of the moving loading axis. 28

2.8 Three-point bending test on a Zry-4 cladding tube filled with alumina pellets. The applied load is plotted against time; oscillation and sudden load drops are observed in the plastic regime. 29

2.9 Technical drawing of the supports initially used in the three-point bending test device. The parts were simply supported, and not fixed to the metallic frame, allowing their rotation. 29

2.10 Types of stress oscillation characteristics for the Portevin–Le Chatelier (PLC) effect [13, 14]. Type A is relevant to our ambient temperature testing conditions. 30

2.11 Closer examination of the oscillations which occurred in different regions of the experimental test. The oscillations differ in both, magnitude and shape, but they develop periodically with the same frequency. 31

2.12 a) Discrete Fourier Transformation (DFT) analysis on the first derivate of the load curve, revealing the predominant frequency on the load signal; b) slope of the load curve derived at three different locations (elastic, strain hardening and necking). 33

2.13 Two different types of supports used to test their contribution to the development of the load oscillations in the plastic regime during bending: (a) rigid support (no rotation allowed); (b) rolling support (rotation allowed). 34

2.14 Comparison of two different support systems for the assessment of the load instabilities in the plastic region during bending test. 35

2.15 First version of bending former made of hard copper. 36

2.16 Technical drawing of the final version of the rolling supports used for the three-point bending tests. 37

2.17 Technical drawing of the final version of the former used for the three-point bending tests. 37

2.18 Overview of a typical three-point bending test configuration illustrating sensors' positioning. 39

2.19 Force application direction (a) and mounting system (b) of the used load cell sensor. 40

2.20 The sample's deflection is measured indirectly, by following the displacement of the bottom metallic plate where the sensor is located. 40

2.21 Use of end-plugs to pressurize and seal (right) the rodlets and to measure the internal pressure (left). 41

2.22 Schematic representation of the test-rig and data acquisition process for the three-point bending test. 42

2.23 LabVIEW program used to control the test process of the three-point bending test and acquire high-frequency data from the sensors. 42

2.24 Beam subjected to pure bending before and after the bending moment has been applied. 44

2.25 Shear and moment diagrams for simply supported beam with central point load. 45

2.26 Bending stress distribution (compressive σ_c or tensile σ_T) for a) hollow-circular and b) circular cross-sections. 46

2.27 Typical flexural stress–strain behavior to fracture for fresh Zry-4 cladding tube. 48

2.28 Schematic representation of the first version of the impact tower used in [15–17]. 50

2.29 First version of the impact tower operated at the hot-cell facilities of JRC-Karlsruhe. The optical parallaxes effect gives the impression, that the guiding tube was broken and tilted, but in reality it was straight and perfectly perpendicular to the specimen axis. 51

2.30 Photograms from the high-speed camera video illustrating the impact fracture of a 74 GWd/tHM PWR fuel rodlet, using the first version of the impact tower [15–17]. 52

2.31 Overview (CAD model) of the impact device used for the present campaigns. 54

2.32 Cross section view (CAD model) of the closed chamber, illustrating the working principle of the new impact tower. 55

2.33 Selected frame from a high-speed camera video illustrating the closed chamber geometry and the testing principle. The hammer impacts onto an unirradiated untreated zircaloy cladding tube containing dummy alumina pellets. . 55

2.34 Cross section view of the impact test device at the symmetry planes, illustrating the test working principle and main dimensions. 57

2.35 Cross section view (CAD model) of the modified chamber, highlighting the new rounded supports and side walls. 59

2.36 Technical drawing of the new rounded support, highlighting its main dimensions. 59

2.37 Cross-section view of the new chamber, at the symmetry plane of the sample, illustrating the main dimensions of the new loading configuration. 60

2.38 2D drawing and main dimensions illustration of the revised impact tower. . 61

2.39 Representative selected frames of the image sequence during an impact test. 62

2.40 Perspective projection of pin-hole camera model without distortion [18]. . 64

2.41 Comparison of non-distorted image against images of common type of radial distortions. 66

2.42 Sectional side view of the geometrical configuration of the impacting chamber showing a cross-section on the symmetry plane. The effect of the impactor's prospective projection is shown by highlighting axes, along which the object with known dimensions moves (in red and black). 67

2.43 Technical drawing of the impactor including basic dimensions. 67

2.44 Basic principles on which the image analysis methodology was built. The loading point velocity is calculated by tracking an object drawn at the front view of the impactor. In addition, points A and B are considered to have same directional velocities. 68

2.45 Spatial calibration process of frames acquired from the high-speed camera. (a) Linear fit of measured section lengths in different axial positions. (b) Transformation of pixel sizes, along the symmetry and in different axial positions, to "real-world" dimensions (mm). 69

2.46 Object tracking procedure, from the raw data to the final result, obtained with the use of Image-PRO. 70

2.47 (a) Application of spatial calibration upon object tracking results and (b) normalized Image Analysis (IA) results highlighting the impact of the spatial calibration. 71

2.48 Typical result of the application of the IA methodology, describing the impactor's loading point velocity per frame. 72

3.1 Technical drawing illustrating main dimensions of the surrogate rodlets used in the analogue studies. 76

3.2 Influence of hydrogenation process on Zr hydride orientation; a) 550°C, $t_{hydrogenation}$= 60 s, hydrogen 330 wppm: circumferential orientation of hydrides, b) 750°C, $t_{hydrogenation}$= 30 s, $t_{annealing}$ =600 s, hydrogen 330 wppm: random hydride orientation. 78

3.3 Not to scale schematic representation of a surrogate rodlet. 79

3.4 Pressurized hydrogenated Zry-4 cladding tube used of the three-point bending experiments. 80

3.5 Setup for three-point bending tests on surrogate rodlets under cold conditions. 81

3.6 Load-displacement curves for fresh Zry-4 cladding tubes with (black) and without (red) alumina pellets. 82

3.7 a) photograph showing the fresh cladding tube, alumina pellet, sponge filler and end-plug used for the sample preparation, b) rod deflection before fracture shaped based on pellets' positioning and c) cladding fracture under tension (bottom area) at the pellet-cladding interface closest to the loading axis. 83

3.8 Three-point bending experiments on pressurized hydrogenated Zry-4 cladding tube. 84

3.9 Hydrogen axial distribution in the pressurized hydrogenated Zry-4 cladding tube used for the three-point bending experiments. The position markers on the cladding allow determining the local hydrogen content at the point of fracture. 85

3.10 Analogue bending tests; a) Bending test of non-hydrogenated sample. The rod shows very high ductility; b) Bending test of sample with intermediate Zr hydride content; c) Importance of the presence of pellets during the test. The sample breaks always at the pellet-pellet interface; d) Bending test in high Zr hydride content (> 700 ppm) sample. The rod shows brittle behavior (low deflection at fracture) when compared to the other rods. 88

3.11 Load-displacement curves of surrogate samples from group 1 and 2, including Zry-4 cladding tubes hydrogenated at 550°C with the use of a) big and b) small alumina pellets. 89

3.12 Load-displacement curves of surrogate samples including big pellets and Zry-4 cladding tubes hydrogenated at a) 650°C and b) 750°C. 90

3.13 Displacement to fracture of surrogate samples as a function of hydrogen concentration. Black, blue and green dots correspond to samples having experienced hydrogenation temperatures of 550°C, 650°C and 750°C, respectively. The red dots correspond to samples including pellets of smaller diameter. The displacement to fracture becomes independent of hydrogen content above 650 ppm. 91

3.14 a) Bending angle to fracture as a function of hydrogen concentration for surrogate samples under three-point bending test; b) linear fit of bending angle to fracture of the reference samples (group 1 on table 3.4) with hydrogen content between 100 ppm and 650 ppm. 93

3.15 Sample internal pressure drop after fracture vs. time. 95

3.16 Flexural modulus of hydrogenated and fresh Zry-4 cladding tubes. 96

3.17 Cladding failure initiation and crack propagation in surrogate samples. . . . 97

3.18 Typical observations of cladding failure and pellet release of hydrogenated samples after three-point bending tests. The tensile and shear failure modes are seen in a), whereas the cracked pellets and mass release are shown in b) and c). 97

3.19 Extensive pellet release upon cladding's brittle failure for sample with extremely high hydrogen content (2500 ppm). 98

3.20 Metallographic images illustrating the hydride orientation in Zry-4 cladding samples with $\sim$ 350 ppm hydrogen content, hydrogenated at different temperatures; circumferential orientation prevails at 550°C, while randomly oriented hydrides formed at 650°C and 750°C. 99

3.21 Impact test on pressurized non-hydrogenated Zry-4 sample filled with alumina pellets. Sample breaks under the loading point, but not at the fixed ends illustrating high ductile behavior. 101

3.22 Impact test on a pressurized hydrogenated Zry-4 cladding tube filled with small alumina pellets. High speed camera photograms illustrate the additional cracking at the sample holders under the impacting hammer, as well as the extensive pellet release due to open gap. 101

3.23 a) Scanning Electron Microscopy (SEM) analysis of dispersed aluminium oxide particulates on a carbon filter and b) colour mapping of the alumina particulates dispersed on the carbon filter by Energy-dispersive X-ray Spectroscopy (EDX) analysis. 102

3.24 Back-scattered Electron (BSE) micrograph of fine particulates and aerosol deposited on the filter coupled to the aspiration device connected to the impact testing chamber after fracture of the surrogate sample. 103

4.1 Nominal dimensions for cladding and pellets of the SNF rods used in the current study. 107

4.2 Gamma scanning and profilometry measurements on a Kernkraftwerk Gösgen-Däniken (KKG) spent fuel rod. Segment number 6, highlighted in orange, was used from each rod to perform the mechanical tests. 109

4.3 Three-point bending device installed in hot-cell at JRC-Karlsruhe. 110

4.4 Bending response of the irradiated sample KKG A07 as recorded by the camera inside the hot-cell. 111

4.5 Load-displacement curves from bending tests on SNF rodlets and fresh Zry-4 samples. 112

4.6 a) Bending angle and load to fracture as a function of burnup under three-point bending test; b) linear fit of bending angle to fracture as function of bunup for the KKG samples with Zry-4. 113

4.7 Segment pressure drop after fracture as function of time. 115

4.8 Side view of the impact test device installed at the hot-cell. 116

4.9 Representative photograms illustrating the dynamic response under impact of a pressurized PWR Uranium Dioxide (UO2) rodlet irradiated to a burnup of 67 GWd/tHM at Kernkraftwerk Grohnde (KWG). 117

4.10 Representative photograms illustrating the dynamic response under impact of pressurized PWR UO2 rodlets. 119

4.11 Qualitative indication of KKG samples' ductility as function of burnup from direct comparison of their deformation to fracture. 120

4.12 Hammer's velocity as derived from IA for the impact test on samples a) KKG A11, b) KKG D08, c) KKG A07, d) KKG D02 and e) A16-5. 122

4.13 Comparison of samples' ductility in bending and impact test as function of their a) displacement and b) bending angle to fracture. 123

4.14 Work of absorbed energy until fracture of the SNF rodlets subjected to three-point bending and impact. 124

4.15 Flexural stress-strain curves for beam elements with a) hollow-circular and b) circular cross-sections derived from three-point bending tests on pressurized SNF rodlets. 125

4.16 a) Flexural modulus of elasticity and b) yield strength and 0.2% offset yield strength derived from three-point bending results for beam elements with hollow-circular cross-section. 127

4.17 Failure profiles of SNF rodlets subjected to three-point bending test. 129

4.18 Failure profiles of SNF rodlets subjected to impact test. 129

4.19 Fuel mass release per fracture of SNF rod samples under impact and bending tests. 131

4.20 Fractional size distribution of the heavy particles collected at the bottom of the testing chamber after impact tests. 132

4.21 SEM micrographs showing fine fuel particles filtered through a) & b) 8 µm, and c) & d) 3 µm mesh filters coupled with the aspiration device connected to the impact testing chamber after the impact test on samples a) & b)KWG A16-5, and c) & d) KKG A07. 133

4.22 SEM micrographs of particles collected from a swipe of the lower inner walls of the testing chamber after impact test on fuel KWG A16-5. 134

4.23 Classification of fuel particles based on their Equivalent Circle Diameter (ECD) from SEM photographs resulting from impact test on sample KKG A07.135

4.24 Fractional size distribution of particles deposited on a) 8 µm vacuum filter after impact on sample KWG A16-5 and on carbon filters after impact on samples b) KKG A11, c)KKG A07and d) KKG D02. 136

4.25 SNF rodlet cutting for sample preparation to perform cladding hydrogen concentration measurements. 136

4.26 Hydrogen concentration at cladding fracture region as measured with the hot-gas extraction method. 137

4.27 a) Hydrogen content as function of burnup and b) bending angle to fracture as function of hydrogen content of the Zry-4 KKG samples. 138

4.28 Microscopic examination of metallography samples from the tested SNF rodlets. Left: macrographs of the full cross section; right: micrographs showing the hydride distribution and orientation. The angular positions of the micrographs are indicated at the bottom of each image. 139

5.1 a) Mesh of an FEM of the three-point bending device and b) boundary conditions considered for investigating the stiffness behavior of the device. . 146

5.2 Total deformation at maximum applied load of 5 kN. 146

5.3 3D implicit FEM simulating the bending behavior of a fuel rodlet under three-point bending test. 148

5.4 a) Cast iron plasticity model assigned to pellets; Pellet material model comparison between cast-iron and BISO for different b) Young's modulus, c) plastic modulus and d) yield stress values. 149

5.5 Voce non-linear isotropic hardening model used in cladding. 151

5.6 Results of the sensitivity studies performed on the Voce parameters of the 3D reference model. The effect of different a) yield stress, b) R_{inf}, c) R_0 and d) b values on the laod-displacement curve of the simulation is presented. The red dots represent response of the reference FEM. 152

5.7 Load-displacement curve of the reference 3D static structural model calibrated against three-point bending test experiment on surrogate sample "H1960_Z4". 154

5.8 Representative results from reference FEM at max displacement. 155

5.9 Equivalent (Von Mises) stress at maximum displacement of a) half symmetry model with bonded pellet at one end (left) to constrain the pellets and b) half symmetry model with bonded pellet at one end. 156

5.10 Load-displacement curves of FEMs with different modeling approaches. . . 157

5.11 Penetration at pellet-to-pellet interface (PPI) of half symmetry model with bonded pellet at one end (left). 158

5.12 Load-displacement curves of FEMs with different cladding modeling approaches. 159

5.13 Equivalent plastic strain at cladding with a) one and b) 3 mesh elements through its thickness. 160

5.14 Load-displacement curves of FEMs with different modeling approaches on the end-pellet boundary condition. 161

5.15 Sensitivity study on the end-pellet boundary condition with the use of spring; a) maximum load and cladding stress (Von Misses) difference and b) maximum pellet stress (Von Mises) and pellet contact pressure at maximum displacement for different spring stiffness factors. 162

5.16 Sensitivity study on the bending response of the model with regard to the internal pressure; a) resulting load-displacement curves and b) maximum load and pellet/cladding stress (Von Misses) differences for various internal pressure values. 163

5.17 Load-displacement curves of FEMs with different modeling approaches for the contact formulation. 164

5.18 Friction coefficients sensitivity studies performed on the reference 3D model; resulting load-displacement curves for the a) pellet to pellet friction coefficient study and b) pellet to cladding friction coefficient study. 165

5.19 Mesh independence study of the FEM; a) load-displacement curves for different mesh densities and elements and b) load at maximum displacement for different mesh densities of the 3D reference model. 166

5.20 a) load-displacement curves for different weak springs options and b) load at maximum displacement for different values of the weak spring stiffness factor. 167

5.21 a) cladding failure at point of highest plastic strain, b) permanent bending of cladding after long plastic deformation under the loading points and c) areas of highest stress development at the pellets. 169

5.22 a) Spider plot and b) parallel coordinates plot showing the value selection for the generated FEMs through LHR sampling. 171

5.23 a) Force-displacement curves of the generated design points obtained from sampling the variables' range with optiSLang and b) Metamodel of Optimal Prognosis (MOP) showing the result deviation or error of each simulation (red points) from the experimental results. The error is plotted as function of the most important parameters of the FEM being the cladding yield stress and the Voce exponential coefficient. 172

5.24 Example from $CoP(X_i)$ resulting from the Metamodel of Optimal Prognosis (MoP) generation. 174

5.25 Load-displacement results of all the 3D model OptiSlang fittings for the a) 18.3 GWd/tHM (KKG-A11), b) 46.9 GWd/tHM (KKG-D08) and c) 58.6 GWd/tHM (KKG-A07) models compared to the corresponding experimental data. The best-fit is highlighted in red, whereas the experimental data curve is presented in black. The grey lines are the OptiSlang generated FEM simulations. 175

5.26 Comparison of the a) Young's modulus and b) yield strength between the experimentally and numerically derived mechanical properties of the cladding. 177

6.1 Conceptual design of a new impact test setup aiming to extend the data acquisition capabilities and facilitate the test procedure within the hot-cells. 184

A.1 Flexural stress-strain curves for beam elements with circular cross-section derived from three-point bending tests on surrogate samples including Zry-4 cladding tubes hydrogenated at a) 550°C , b) 650°C, c) 750°C and d) with the use of smaller alumina pellets. 200

A.2 Flexural stress-strain curves for beam elements with hollow-circular cross-section derived from three-point bending tests on surrogate samples including Zry-4 cladding tubes hydrogenated at a) 550°C , b) 650°C, c) 750°C and d) with the use of smaller alumina pellets. 201

B.1 Standard deviation of load measurements. 206

B.2 Standard deviation of displacement measurements. 206

C.1 Impact mock-up test rig placed in cold laboratory, replicating the impact tower installed in the hot-cell, with extended acquisition capabilities. 208

C.2 2D drawing of the load application at the impact and bending devices. . . . 209

C.3 Set-up of new acquisition capabilities on the impact mock-up test rig. . . . 209

C.4 Stainless Steel (SST) sample prepared for the IA impact validation campaign with the use of the mock-up impact tower. 211

C.5 Piezoelectric load cell response to impact loads on SST rodlet. 212

C.6 Load-cell reaction force in impact loading for different recording frequencies.212

C.7 Dynamic response of the SST sample with and without the use of end-plugs; a) raw and b) smoothed data of the recorded loads against time 213

C.8 table:IAval 213

D.1 Asymmetric Least Squares Smoothing (ALSS) baseline determination for all measurements on certified material with different hydrogen content. . . . 216

D.2 Linear regression model used to fit all certified material measurements. . . . 217

D.3 Linear regression model used to fit measurements of a) 62 ppm, b) 107 ppm and c) 192 ppm standard samples, respectively. 218

D.4 Uncertainty associated with the observation of a measurand χ, adapted from [19, 20] 219

D.5 Uncertainty associated with the measurement of certified materials of different hydrogen content with the use of different calibration curves. 221

D.6 Hydrogen range of validity for the application of the three calibration curves. 222

List of tables

2.1 Main dimensions and description of symbols used for the three-point bending test. 38

2.2 Main dimensions and description of symbols used for the impact test. . . . 62

3.1 Geometric dimensions of the surrogate samples consisting of pellets and cladding used in analogue studies. 76

3.2 Mechanical properties of cladding and pellet samples used in analogue studies. 77

3.3 Testing conditions for the three-point bending tests on surrogate rodlets. . . 80

3.4 Characteristics of hydrogenated surrogate samples used for bending tests. . 86

3.5 Summary of experimental results on surrogate rods. 92

3.6 Flexural modulus of elasticity and toughness of surrogate samples assuming circular and hollow-circular cross-section. 94

4.1 Characteristics of spent fuel rods used in this study. 106

4.2 Rod internal pressure of SNF rods, measured with puncture tests at room temperature. 109

4.3 Experimental results of three-point bending tests on irradiated PWR rodlets. 112

4.4 Impact test results until sample crack initiation for the KKG fuel rodlets. . . 121

4.5 Impact test results until sample rupture for the KKG fuel rodlets. 123

4.6 Flexural mechanical properties of beam elements with hollow-circular cross-sections derived from the three-point bending results. 126

4.7 Flexural mechanical properties of beam elements with circular cross-sections derived from the three-point bending results. 126

4.8 Fuel mass release per fracture resulting from three-point bending and impact tests on SNF rodlets. 130
4.9 Fit parameters of second order polynomial Eq.4.2 estimating fuel mass release per fracture in bending and impact. 131
4.10 Geometrical dimensions irradiated of cladding. 140

5.1 Summery of representative results at maximum sample deflection from different modeling approaches. 157
5.2 Representative results at maximum sample deflection from different cladding modeling approaches. 159
5.3 Representative results at maximum sample deflection from different modeling approaches on the end-pellet boundary condition. 161
5.4 Representative results at max sample deflection from different modeling approaches on contact formulations. 164
5.5 Representative results at max sample deflection from different mesh densities and options of the FEM. 166
5.6 Cladding properties and associated Coefficient of Prognosis (CoP) values as calculated in optiSLang. 176

B.1 List of sources of uncertainties in all measuring quantities 205

C.1 Test parameters for the IA validation campaign. 210
C.2 Test parameters for the IA validation campaign. 211

D.1 Overview of measurements performed on certified materials for the calibration process. 215
D.2 Method and parameters used for the baseline determination of the peak signal with the use of the OriginPro software. 216
D.3 Linear regression model parameters as derived for the different methods. . . 218
D.4 Derivation of hydrogen content of the certified standard materials (62 ppm) using different calibration curves. 220

D.5 Derivation of hydrogen content of the certified standard materials (107 ppm) using different calibration curves. 220

D.6 Derivation of hydrogen content of the certified standard materials (192 ppm) using different calibration curves. 221

D.7 Bias uncertainty based on different calibration methods for a range of hydrogen content samples. 221

D.8 Ranges of applicability of calibration curves given fitting parameters and experimental bias. 223

Acronyms

ALSS Asymmetric Least Squares Smoothing

BEVA SF/HLW encapsulation plant

BSE Back-scattered Electron

BWR Boiling Water Reactor

CoP Coefficient of Prognosis

CtT compression-to-tension

DFT Discrete Fourier Transformation

DGR Deep Geological Repository

DIC Digital Image Correlation

DoF Degrees of Freedom

ECD Equivalent Circle Diameter

EDX Energy-dispersive X-ray Spectroscopy

FEA Finite Element Analysis

FEM Finite Element Model

FIB Focused Ion Beam

HLW High Level Waste

HR Hydride Reorientation

IA Image Analysis

JRC Joint Research Centre

KKG Kernkraftwerk Gösgen-Däniken

KWG Kernkraftwerk Grohnde

LWR Light Water Reactor

MoP Metamodel of Optimal Prognosis

MOX Mixed Oxide

NPP Nuclear Power Plant

PCMI Pellet-Cladding Mechanical Interaction

PIE Post-Irradiation Examination

PLC Portevin–Le Chatelier

PPI pellet-to-pellet interface

PWR Pressurized Water Reactor

RCT Ring Compression Test

RD&D Research, Development and Demonstration

RIP Rod Internal Pressure

SED Strain Energy Density

SEM Scanning Electron Microscopy

SFA Spent Fuel Assembly

SNF Spent Nuclear Fuel

SST Stainless Steel

TSC Transport and Storage Cask

UO2	Uranium Dioxide
Zry-4	Zircaloy-4

Chapter 1

Introduction

1.1 Swiss spent nuclear fuel management

Radioactive Waste Production in Switzerland originates primarily from the four commercial Nuclear Power Plants (NPPs) with five nuclear reactors in total. In the frame of the waste management concept – approved by the Swiss Federal Council and Parliament – radioactive waste produced in Switzerland will undergo deep geological disposal domestically. NPP operators are responsible for fuel cycle management under the 2003 Nuclear Energy Act and 2004 Nuclear Energy Ordinance and operate with a "polluter-pays" policy [21, 22]. For this purpose, in 1972 the Swiss waste producers have established a cooperative called Nagra - the Swiss National Cooperative for the Disposal of Radioactive Waste - with the mandate to develop and implement the waste disposal solution. Nagra has proposed that a Deep Geological Repository (DGR) is the only method for managing radioactive waste that meets the strict requirements related to long-term safety [23].

Two types of disposal sites have been chosen and are currently further investigated; one for the low and intermediate level waste and one for the long lived and High Level Waste (HLW) [24, 25]. HLW consists of Spent Fuel Assemblies (SFAs), and vitrified waste arising from the reprocessing of the spent nuclear fuel. A 10-year moratorium on the export of spent fuel for reprocessing was started in July 2006 and a permanent ban has been then accepted by the Swiss people in a popular vote in May 2017. Before the start of the moratorium, about 1139 t of SNF had been shipped from the NPPs to La Hague, France and Sellafield, United Kingdom for reprocessing, since the utilities were free to choose between reprocessing and direct disposal of the spent fuel [26]. The largest contribution to the HLW DGR concerning the sheer volume and total radiological inventory will come from SFAs being discharged from the NPPs over their total life span [27]. All utilities plan to operate for a minimum of 50 years, with the exception of Mühleberg BWR that ceased operation at the end of 2019 (after 47 years of operation), resulting to more than 10,000 SFAs.

Fig. 1.1 illustrates the waste flow streams of the Swiss management concept. The upper part of the figure highlights the process for the disposal of the SFAs. In more detail, SFAs are stored in wet storage pools at the NPPs sites for a minimum of five years. Having decayed sufficiently to lower their thermal power the SFAs are loaded in to dual purpose Transport and Storage Casks (TSCs) for transport to dry interim storage facilities. Gösgen NPP (KKG) has also an external wet-storage facility that was commissioned in 2008 and has a storage capacity of 1056 spent fuel assemblies. The TSCs are stored either at the centralized Interim Storage Facility (ZWILAG) or at a separate interim radioactive waste storage facility in Beznau NPP (ZWIBEZ). SFAs will undergo interim storage for several decades approximately until 2060 (at least), when according to the current timetable the repository for HLW is expected to become operational [26].

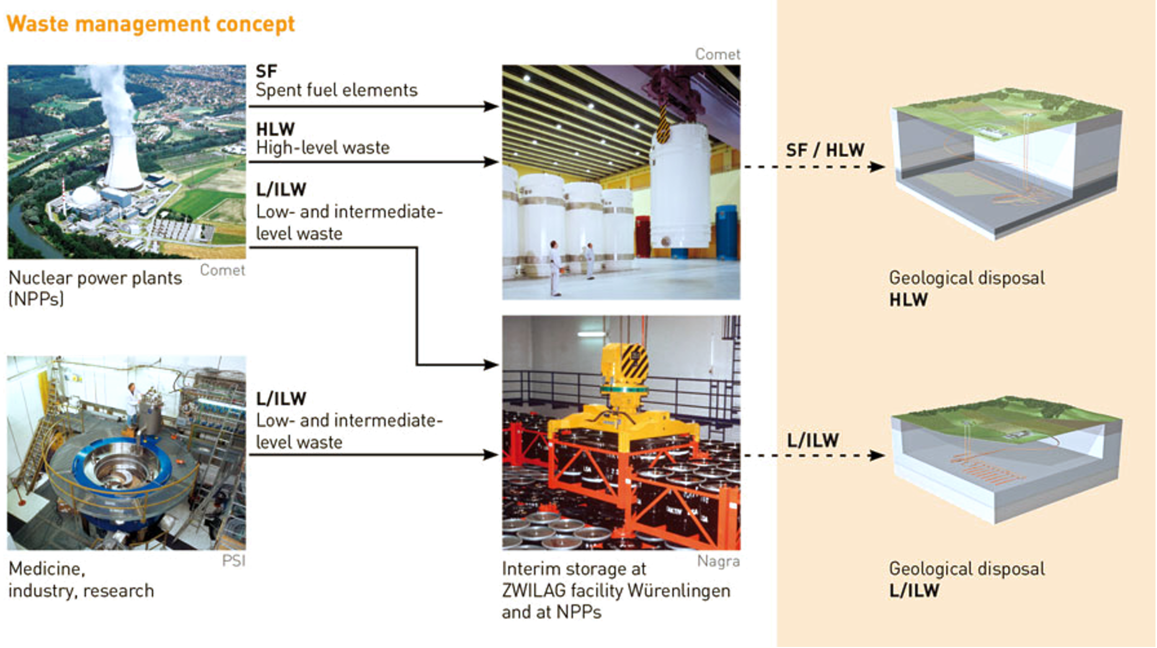
Waste management concept
SF
Spent fuel elements
HLW
High-level waste
L/ILW
Low- and intermediate-level waste
Nuclear power plants (NPPs)
Comet
Comet
L/ILW
Low- and intermediate-level waste
Medicine, industry, research
PSI
Interim storage at ZWILAG facility Würenlingen and at NPPs
Nagra
SF / HLW
Geological disposal
HLW
L/ILW
Geological disposal
L/ILW

Fig. 1.1 Waste streams in the Swiss management concept [1].

The final disposal of SFAs in an underground repository requires an above ground facility to encapsulate all waste packages into canisters suitable for emplacement in the repository, ensuring their long-term safety and confinement. An SF/HLW encapsulation plant (“Brennelementverpackungsanlage” hereafter referred as BEVA) is thus required for the operation of the repository, where the SNF can be controlled and handled. The TSCs will be transferred to SF/HLW encapsulation plant (BEVA) via rail, which will be able to accommodate a given number of casks. After transport, the casks will be handled and loaded in big hot-cell facilities with the use of cranes. Fig. 1.2 gives a simplified illustration of the foreseen operations within these hot-cells. Both the TSC and the final disposal canisters are mounted in the hot-cell with open lids. The SFAs are removed from the TSC with the help of a crane and are moved into the canisters. The sequence of the SFA loading and TSC selection takes into account residual power and characteristics of the SFAs, and aims to minimize the total number of canisters and consequently the size of the repository [28]. The loaded canisters are sealed and then transferred underground for their final disposal. Each canister will be placed on a bentonite plinth in the disposal tunnel and the entire tunnel will be backfilled with bentonite granulate. Together with the overlying clay formations, the host rock forms the geological barrier.

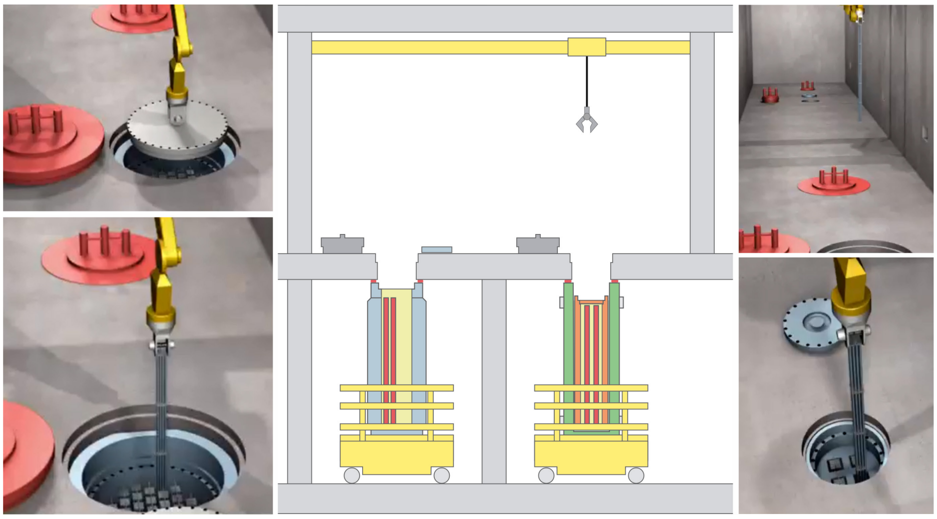

Fig. 1.2 Simplified illustration of SFA unloading/loading in the Nagra encapsulation facility. TSC docking station (left), final disposal canister docking station (right).

In recent years, regulatory issues associated to dry storage, transportation and handling of SNF have been arising. Possible the main reason is related to the inevitable need of prolonging the storage of SNF in interim facilities for time periods far beyond what was originally envisaged, which would require the license renewal of both the TSCs and of the storage facilities [29]. Another reason is related to the planning and licensing processes of the surface encapsulation facilities, where the safety of all SNF operation activities (transportation and handling) will have to be ensured under normal and accident conditions. The properties of SNF rods change significantly during their operation life in the reactor core. Further changes occur after their discharge mainly due to the heating-cooling processes and possible ageing associated with the cumulative effects of radioactive decay induced damage in the fuel [30].

In any case, the ageing mechanisms that could potentially affect the mechanical performance of the SNF after prolonged dry storage conditions have to be better understood and their effect on the structural integrity of the rods should be demonstrated. Towards this goal, in the recent years many research projects have been initiated aiming to provide a better understanding on the evolution of the SNF mechanical properties after irradiation and upon extended dry storage conditions [31–37].

1.2 Basic mechanisms affecting structural behaviour of SNF

A schematic drawing of a LWR fuel rod is given in Fig. 1.3 [2]. The rod consists of a cylindrical hollow metallic tube (cladding) in which the stack of the nuclear fuel pellets is loaded. The size of the rods differs between the various reactor types; being approximately 4 m in length and 9-11 mm or 12-14 mm in diameter for PWRs and BWRs, respectively. In all cases, the cladding is made of zirconium alloys (zircaloy) and the fuel does not cover the full length of the rod. At the top of the rod a free volume (plenum) is kept to accommodate the fission gas release and a spring is placed at this position to keep the fuel pellets in place. The top and bottom plenum are separated from the fuel stack by alumina pellets (insulators). The rods are pressurized with helium to approximately 20-25 bar in PWRs and 3 bar in BWRs, which partly compensates the effect of the external coolant pressure and prevents the clad from collapsing during the initial stages of irradiation.

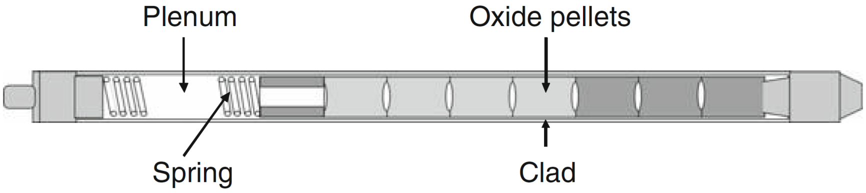

Fig. 1.3 Schematic representation of a LWR fuel rod [2]

During irradiation, the shape of the pellets changes to a so-called hourglass shape due to the high radial temperature gradient and differential thermal swelling, as shown in Fig. 1.4. Even at low linear heat generation rates the internal thermal stresses in the cylindrical fresh pellet exceed the fracture stress of UO2 leading to pellet cracking. Upon that, the pellets deform under the effect of the temperature field, tend to bow outwards and later also swell during irradiation (gaseous fission products, lattice damage, etc.). In addition, the cladding tends to creep towards the pellets (during the first part of the irradiation) under the action of the pressure difference between the primary water circuit and the initial internal fill gas pressure. Moreover, the cladding undergoes thermal expansion; however, the expansion rate of zircaloy is less than of UO2 causing a gradual closure of the original gap between pellets and cladding. Considering all phenomena, the closure of the gap corresponds to the onset of the PCMI, and it is affected by a number of design and fabrication parameters. Once PCMI has started, both the pellet geometry and the material properties of the interacting components influence the maximum stresses and strains as well as their evolution [2].

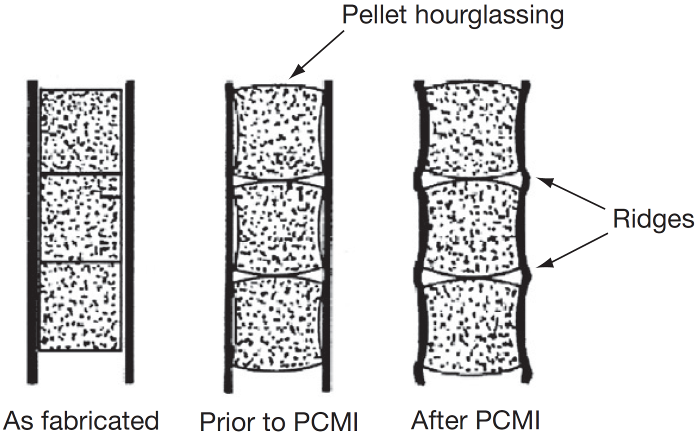

Fig. 1.4 Schematic representation of PCMI [2]

Another very important mechanism that limits the in-reactor design life of the SNF rod is the cladding degradation due to waterside corrosion, where hydrogen ingresses into the cladding and causes cladding embrittlement. Corrosion of zirconium alloys in an aqueous environment is principally related to the oxidation of the zirconium by the oxygen in the coolant, dissolved or produced by radiolysis of water. A small amount of oxygen can be dissolved in the metal, but once the thermodynamic solubility limit is exceeded, zirconium oxide is formed on the metal [3]. The oxidation and hydrogen uptake of Zircaloy is determined by many factors, i.e. the chemical and physical state of the material: composition, metallurgical condition, and surface condition. These conditions are usually specific to the material and related to the fabrication process. Fig. 1.5 shows the different behavior of Zircaloy-4 and Zr1%Nb (M5) in terms of the peak oxide layer thickness: it significantly increases with burnup for the former, whereas it only shows a moderate increase for the latter [3].

Apart from reducing the actual thickness of the zircaloy cladding, the oxide layer formation would not severely affect the cladding behavior, unless a fraction of the hydrogen diffuses through the oxide layer into the metal. The solubility limit of hydrogen is very low in zirconium alloys, and once it is exceeded the hydrogen precipitates as a zirconium hydride

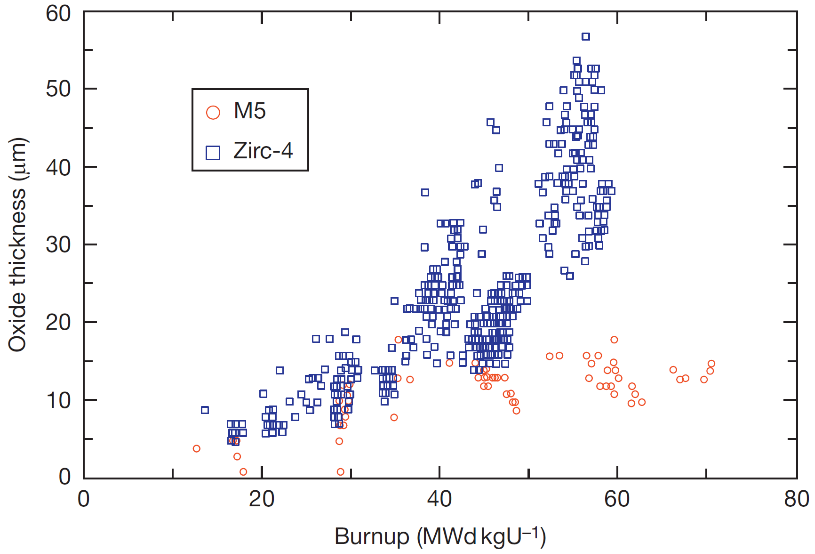

Fig. 1.5 Peak oxide layer thickness as function of burnup for Zircaloy-4 and Zr1%Nb (M5) [3].

phase. This could cause hydrogen embrittlement, lowering of fracture toughness, delayed hydride cracking (DHC) and acceleration of corrosion and of irradiation growth. The most important mechanism is the hydrogen embrittlement, which greatly affects the mechanical resistance of the cladding by reducing its ductility. The hydrogen embrittlement depends on the volume fraction of the hydrides, on their orientation in the cladding and on their degree of agglomeration [38, 3]. Therefore, it is of paramount importance to understand its underlying mechanisms.

The process of the hydride formation and orientation is also strongly dependent on the temperature conditions and hoop stresses in the cladding. After irradiation and during storage these conditions can significantly change and potentially lead to hydride formation and/or re-orientation. Hoop stresses are developed in the cladding due to PCMI and pressure difference between the Rod Internal Pressure (RIP) and atmospheric storage conditions, as shown in Fig.1.6 [4].

After cooling in the spent fuel pool, the SNF is dried in the TSC in a vacuum environment for 24 hours. During this time, the temperature rises because the decay heat must be dissipated by radiation in absence of a heat-exchanging medium. The temperature and hoop stress evolution during the fuel cycle of a PWR rod are shown in Fig. 1.7a, as calculated with the BISON code [5]. The temperature and hoop stresses during drying are close to 400 °C and about 70 MPa, respectively. Solubility of hydrogen is important because hydrides can only precipitate after the solubility limit is exceeded. The dissolution terminal solid

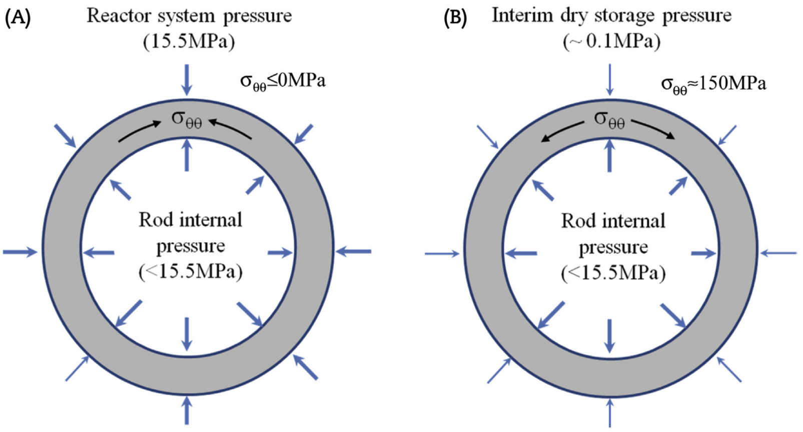
(A)
Reactor system pressure
(15.5MPa)
$\sigma_{\theta\theta}\leq 0$MPa
$\sigma_{\theta\theta}$
Rod internal
pressure
(<15.5MPa)
(B)
Interim dry storage pressure
(~0.1MPa)
$\sigma_{\theta\theta}\approx 150$MPa
$\sigma_{\theta\theta}$
Rod internal
pressure
(<15.5MPa)

Fig. 1.6 Schematic diagram of hoop stress condition on cladding tubes during a) in-reactor operation and b) interim dry storage [4]

solubility (TSSd) and the precipitation terminal solid solubility (TSSp) describe the solubility of hydrogen and precipitation of zirconium hydrides in Zr-alloys, respectively. Fig 1.7b gives a generic plot of TSSd and TSSp and the progress followed by a specimen during heating and successive cooling [6].

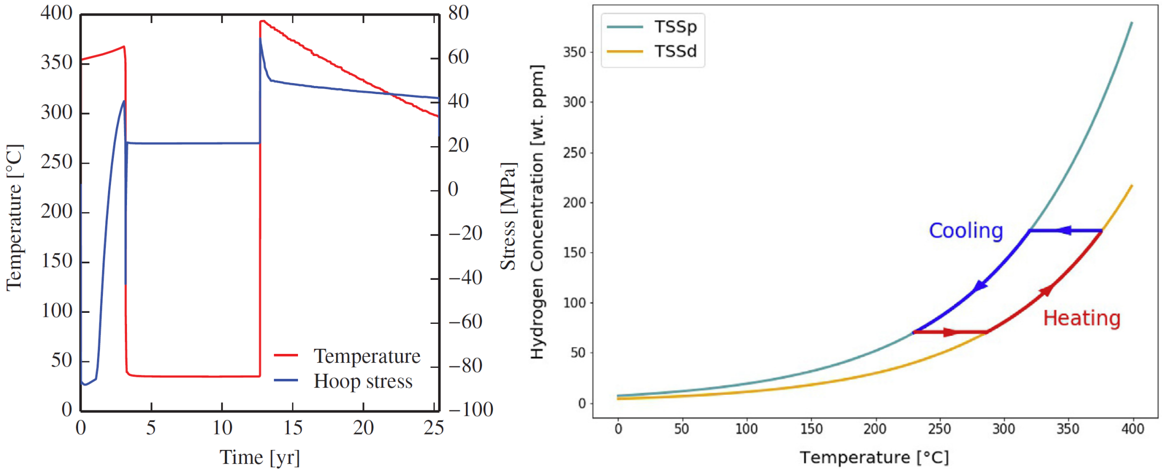

(a) (b)

Fig. 1.7 a) BISON prediction of temperature and hoop stress in the cladding throughout fuel cycle [5] and b) generic terminal solid solubilities of hydrogen in α-Zr-alloys for dissolution (TSSd) and precipitation (TSSp) as a function of the temperature [6]

The hydrides, if formed, can be circumferential or radial, as shown in Fig. 1.8. The hydride orientation is relative to the stress orientation [39] and the cladding embrittlement is influenced by the orientation of hydrides relative to the stress. Hydrides that are oriented normal to the tensile load enhance embrittlement by providing an easy path for the growth of cracks through the cladding [40]. Radial hydrides are of greater concern, as they are oriented perpendicular to the hoop stresses that arise during reactor operation of storage conditions [3]. Therefore, they can be detrimental to the mechanical properties of the cladding. In these conditions, the hydrides can dissolve into the matrix as the temperature rises and precipitate upon cooling in the radial direction, in a phenomenon called hydride re-orientation [41].

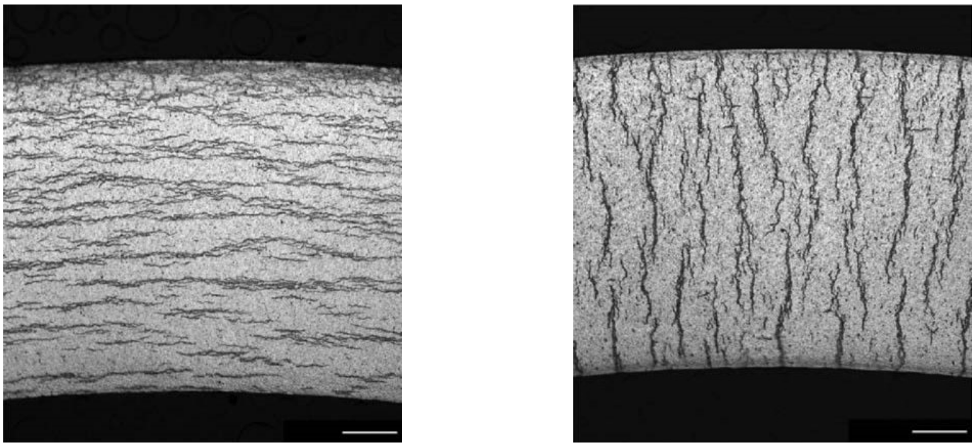
(a) (b)

Fig. 1.8 a) Circumferential and b) radial hydrides [3].

Fig. 1.9 shows the hoop stress range and hydride re-orientation (HR) threshold stress for a 17×17 Westinghouse (WH) PWR fuel type as function of temperature [42, 7]. In other words, this plot provides the conditions where Hydride Reorientation (HR) could occur. The dashed lines correspond to the hoop stresses for the indicated burnup at each temperature. The hoop stress over the threshold line for HR (highlighted in red) indicates that HR can occur. The maximum allowable cladding temperature during the drying process is 400 °C, according to the United States Nuclear Regulatory Commission (US-NRC) that has also be followed/applied in other countries as well [43]. Based on this graph, HR is not probable for low and intermediate burnup fuels. However, in high and very high burnup fuel (above 45 GWd/tHM) HR could become relevant under certain conditions.

In Switzerland, SNF comes from a wide range of LWR fuel types (UO2 and Mixed Oxide (MOX)) produced by several fuel vendors; factors such as cladding materials, initial enrichment and operational histories vary. In addition, much of the spent fuel is characterized by a relatively high burnup at discharge (60–70 GWd/tHM). Therefore, the characterization of the mechanical properties of the SNF is a challenging task, which has to be addressed in order to evaluate its response in different stages and conditions of the back-end fuel cycle.

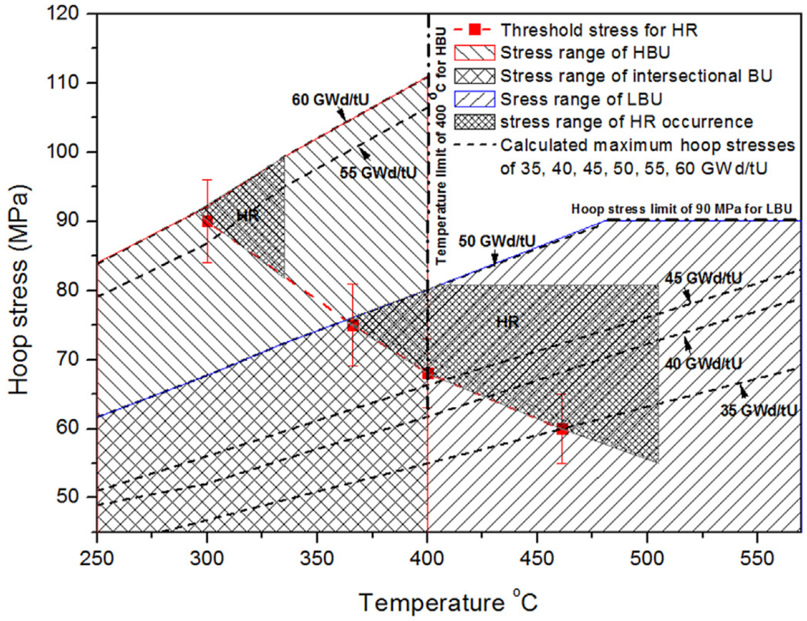

Fig. 1.9 Calculated hoop stress corresponding to temperature of cladding during dry storage for PWR type fuel and threshold stress for hydride reorientation [7]

1.2.1 State-of-the-art

Extensive research studies have been performed to investigate phenomena that affect the mechanical state of nuclear fuel and cladding (e.g. PCMI, oxidation, hydrogen update, HR, creep, irradiation damage, etc.) during and after irradiation. Often, experimental approaches are limited to the use of surrogate materials and seldom data exist on real irradiated fuel rods. In addition, numerical studies with fuel-performance codes can examine the thermo-mechanical properties of the fuel and cladding during irradiation; however, their applicability and validation for “out-of-core” conditions are limited. Usually, these investigations study fundamentally the various phenomena aiming to provide a better understanding of the relevant mechanisms that govern their behavior.

More investigations are needed to macroscopically examine the mechanical properties of SNF rods and their evolution during storage and prior to their disposal. The need for such investigations is mainly associated to the licensing requirements related to the extension of the SNF dry storage periods in TSCs and to the need for SNF integrity evaluation after transport and/or handling operations related to final disposal. Experimental activities using SNF rods in dry storage conditions are rather limited. The primary reason is the inherent difficulty of working with highly activated materials in addition to the associated cost of such experiments. Moreover, it is difficult to study ageing processes that may be relevant over many decades on relatively young spent fuel rods. The need to generate experimental data, especially for the high-burnup and MOX cases, has been highlighted in order to contribute to the validation and further development of analytical and numerical models [44, 31]. This section attempts to provide a review on the studies attempted to examine the mechanical response of SNF rods by integrating both experimental and numerical approaches.

One of the first integrated programmes addressing SNF integrity after dry storage was developed by Areva TN and International Nuclear Services in the early 2000s. The Fuel Integrity Project (FIP) studied the impact response of both irradiated and unirradiated fuel with the main objective being the development of a methodology to evaluate the nature and extent of damage to SNF assemblies during TSC drop accidents [45]. The experimental work included an extensive testing programme on both fresh and irradiated fuel rodlets in order to obtain information on the SNF rod properties (as a fuel/cladding composite material) and to assess some uncertainties (e.g. pellet/cladding friction coefficients) relative to specific loading configurations of the SNF rods (i.e. static and dynamic bending, buckling). Representative illustrations from the different experimental activities performed are shown in Fig. 1.10.

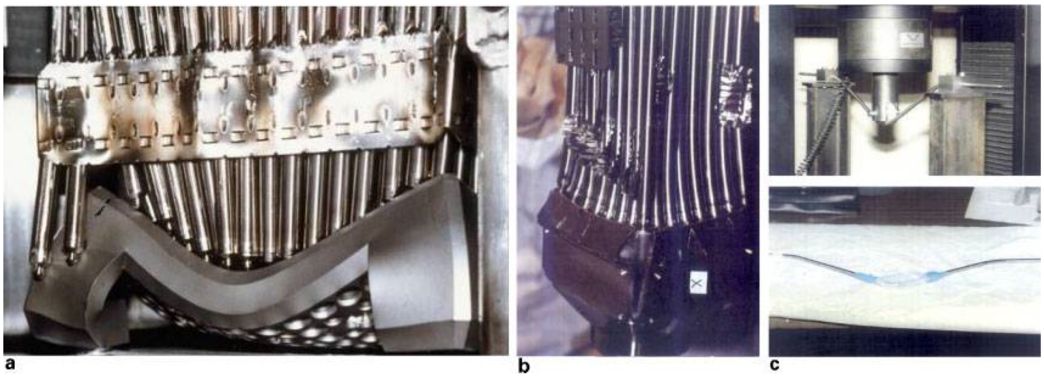

Fig. 1.10 9 m drop test on fresh a) PWR and b) BWR assembly, and c) bending test of fresh PWR fuel rod sample[8].

The main results of the experimental campaign are summarised in [45, 8], where the data obtained are used to develop analytical calculations for the rod behaviour in the elastic domain of the cladding and numerical models for FEA of the rod behaviour in the cladding plastic domain. The FEMs were validated against 3-point bending tests on SNF rods and lateral compression tests on claddings [46, 47]. The data collected during the experimental campaign led to the observation and the understanding of the main phenomena that lead to fuel rod and fuel assembly damage and failure and, in turn, allowed the determination of the maximum allowable loads that a fuel rod in a transport accident scenario can withstand.

This knowledge, on the other hand, allowed the construction of a conservative methodology that either directly (from the test results) or indirectly (by means of FEA) can predict the status a of fuel rod or assembly and the extent of damage in a given accident scenario. The FIP methodology was built upon these results, and it distinguishes cases depending on the type of load (direction), the type of fuel assembly and the irradiation state (fresh or used) of the rod [8, 48]. This methodology is a series of flow charts, which through step-by-step guidelines allows the analysis of the fuel rod mechanical behaviour in all possible accident scenarios arising from transportation. The major results of this project concerned the uncertainties in the modelling of the fuel rods, the determination of the irradiated cladding properties related to burnup and assumptions on the fuel-mass-release analysis.

Another methodology has been proposed by Structural Integrity Associates, Inc. (former ANATECH) that considers the high-burnup effects mostly associated with the hydrogen concentration and hydride orientation in the cladding [49]. A major assumption of this method is the consideration of a static analysis, rather than dynamic, which conservatively bounds the dynamic analysis results. FEMs have been developed, whose essential feature is the damage formulation, which describes the interactions of the cladding response to specific failure modes, as shown in Fig. 1.11 [9]. Therefore, no a posteriori application of failure criteria is needed in comparison to the FIP methodology. The cladding-failure criteria have been derived from limited experimental data on burst tests of empty claddings [50, 51], with no reference tests used for the FEM validation. Although this method provides a step towards a quantitative analysis of the SNF rod failures for transport accidents, its application is rather complicated and experimental validation using real SNF rods is still needed.

In order to address some of the aforementioned data gaps, it was necessary to develop experimental campaigns to macroscopically and fundamentally study the mechanical response and failure processes of the fuel/cladding composite system under static and dynamic loads. Joint Research Centre (JRC)–Karlsruhe and Oak Ridge National Laboratory (ORNL) were among the first to independently develop such integrated campaigns and make their findings public. JRC–Karlsruhe initiated an extensive experimental campaign to characterise the dynamic response of surrogate and LWR SNF rodlets using gravitational impact tests. In collaboration with GNS (Germany) and Areva, the first results of the impact tests were published in [15, 16, 52]. These studies focused on the characterisation of the fuel mass release and revealed remarkable similarities among all samples used, corresponding to 2 g of fuel release per fracture, and no indication indicating preferential fragmentation and release associated with high-burnup rim structure in the size classification of the released particulates.

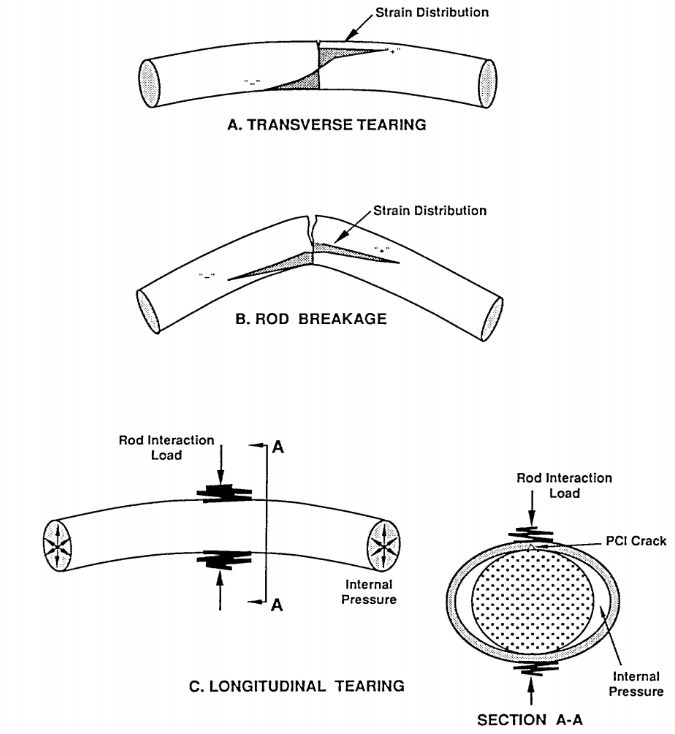
Strain Distribution
"-"
"+"
A. TRANSVERSE TEARING
Strain Distribution
"-"
"+"
B. ROD BREAKAGE
Rod Interaction Load
A
A
Internal Pressure
C. LONGITUDINAL TEARING
Rod Interaction Load
PCI Crack
Internal Pressure
SECTION A-A

Fig. 1.11 Fuel rod failure modes [9]

Another major campaign was established by the U.S. Department of Energy - Office of Nuclear Energy (DOE-NE). The Used Fuel Disposition Campaign (UFDC) [53] aims to conduct Research, Development and Demonstration (RD&D) activities related to storage, transport and disposal of SNF and high-level waste. Within this framework, ORNL has developed an SNF-vibration testing procedure to quantify the integrity of the SNF during transport [54, 55]. Experimental activities include static and dynamic SNF testing under simulated transport conditions using a cyclic integrated reversible-bending fatigue tester (CIRFT). The studies provided a detailed understanding of the mechanical interactions between pellets and cladding, and of the effect of loading rate and loading mode on the fatigue damage evolution of high-burnup SNF under transport conditions [55]. Major findings have shown the importance of the SNF system interface bonding in the vibration performance, the contribution of the fuel to the SNF system stiffness and the SNF failure initiation at the pellet-cladding interface region.

FEA was used to investigate the relative importance of the pellet-pellet and pellet-cladding interfacial bonding efficiency with regard to the SNF dynamic system performance, which showed a significant reduction of the SNF system flexural rigidity in case of de-bonding [56, 57]. The intensity of the contact interaction as well as the impact loading between spacer grids and SNF rods has also been investigated using FEA. A first approach towards SNF assembly modelling was made by simulating a sub-assembly model to investigate the SNF system's dynamic stability under normal transport conditions [58].

Complementary numerical studies within the UFDC framework, conducted as part of a collaborative effort between different U.S. national laboratories, include FEA at the rod scale [59] and at the SFA level [60]. In these studies, the importance of the uncertainties in the SNF material properties and in the non-linear geometric behaviour of the model has been highlighted. For this reason, it was considered necessary to develop the equivalent beam properties of the detailed SNF system. In this respect, the aims of the detailed modelling are to establish reasonable lower/upper bounds and best-estimate material properties. The transport-damage prediction in a worst-case scenario during normal conditions of transport (NCT) was found to be approximately 18%.

For the estimation of the SNF assembly behaviour during handling operations, the French Alternative Energies and Atomic Energy Commission (CEA) (with the support of EDF) has conducted three-point bending tests on six-cycle fuel rod segments complemented by FEA [10]. An equivalent constitutive equation for the SNF rod system has been derived, taking into account the experimental force-displacement curve and maximum failure strain/curvature. The relative contribution of the pellets and cladding to the rod global behaviour has been estimated. The results were used to model a two-dimensional SFA with beam elements in CAST3M, as shown in Fig. 1.12. Bending calculations were performed and failure criteria were derived by comparing the calculated bending angles to the experimental ones at failure.

To evaluate the mechanical integrity of high-burnup SNF assemblies under accident transport conditions, the Federal Institute for Materials Research and Testing in Germany (BAM) has developed an analytical methodology [11, 61]. The rods are considered as continuous beams, supported at the positions of the grids, and are excited dynamically through the supports (and not by directly applied external loading), as shown in Fig. 1.13. The beams are modelled with only elastic material behaviour. This assumption seems to be justified by the drastic decrease in cladding ductility in high-burnup rods. In addition, radial hydrides are not considered to affect the failure mode under bending loadings. Considering certain boundary conditions, an analytical derivation of the effective static load and the beam's global displacement is possible. To estimate the fuel mass release, the critical deflection of the cladding is compared against the limiting beam deflection, and a bounding release per rod-breakage has been considered. This study clearly highlights the importance of the experimental verification of the approach as well as the importance of the accessibility of data generated by experimental testing of SNF rods.

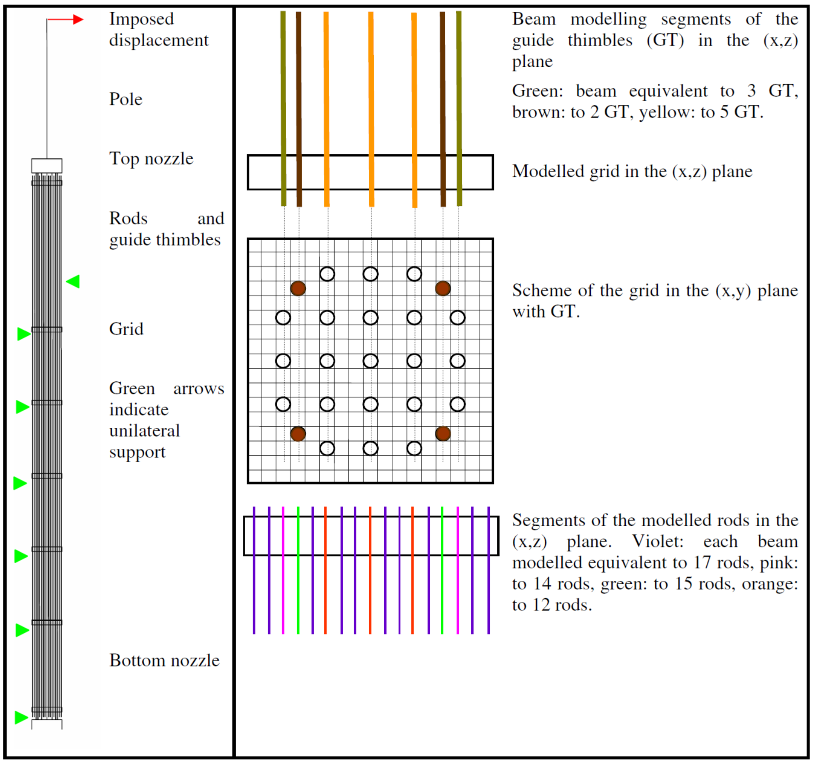
Imposed displacement
Pole
Top nozzle
Rods and guide thimbles
Grid
Green arrows indicate unilateral support
Bottom nozzle
Beam modelling segments of the guide thimbles (GT) in the (x,z) plane
Green: beam equivalent to 3 GT, brown: to 2 GT, yellow: to 5 GT.
Modelled grid in the (x,z) plane
Scheme of the grid in the (x,y) plane with GT.
Segments of the modelled rods in the (x,z) plane. Violet: each beam modelled equivalent to 17 rods, pink: to 14 rods, green: to 15 rods, orange: to 12 rods.

Fig. 1.12 Two dimensional modelling of the fuel assembly; Left: mesh of the assembly in the (x,z) plane; Right: schemes for the equivalent behaviour of the beams representing the guide thimbles and rods [10].

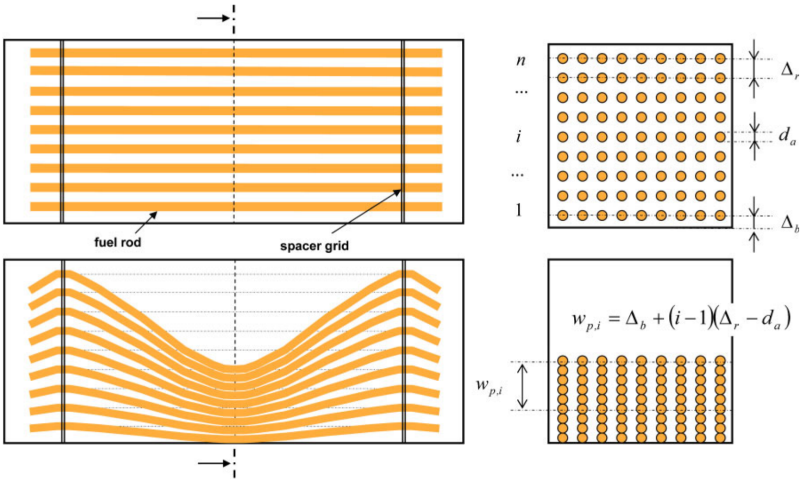
fuel rod
spacer grid
n
...
i
...
1
Δ_r
d_a
Δ_b
$w_{p,i} = \Delta_b + (i-1)(\Delta_r - d_a)$
$w_{p,i}$

Fig. 1.13 Estimation of maximum potential rod deflection [11].

Another extensive integrated campaign aimed at evaluating the dynamic response of SNF rods has been carried out in a collaborative effort by several Japanese institutions, as was already reported in the SPAR III programme [62]. The experimental activities include basic mechanical tests on claddings and dynamic impact tests on fuel rods [63–65]. Axial and lateral loading of fuel rods were used to study the rod failure loads, strains, and the fuel mass release. The fuel material release from BWR SNF rods was equivalent to approximately two or three pellets under axial and lateral impact testing, respectively. For the PWR cases, the fuel mass release was bounded to 1.4 g. FEA was used to study the SNF rod buckling behaviour [66] as well as the dynamic response of fuel rods under side drop loading [65].

1.3 Thesis motivation

In a decision of August 2013, the Swiss Federal Council concluded that Nagra must submit an RD&D plan together with the Waste Management Programme. This RD&D plan for the disposal of radioactive waste in Switzerland was published in December 2016 [67]. In addition, according to the Swiss Federal Nuclear Safety Inspectorate (ENSI) Nagra has to ensure the safety of the SNF handling and encapsulation operations in BEVA and investigate fuel element ageing mechanisms during dry storage [68].

This PhD study constitutes the initiation and the main activity of various Nagra's RD&D investigations on the broad topic of "SNF performance in dry storage conditions related to interim storage, transport and encapsulation operations". The main objective is to examine the response of the SNF under mechanical solicitations and to assess the consequences of a fuel rods failure with the intention of providing valuable input data for the optimisation of the SNF and TSC management actions required for their safe handling and disposal [24].

To this purpose, Nagra joined forces with JRC-Karlsruhe and the Swiss Federal Institute of Technology in Lausanne (EPFL), in order to conduct an experimental campaign with the use of commercial spent fuel rod samples. This experimental campaign follows previous studies [15, 16, 52] and aims to extend and deepen the macroscopic characterization of the mechanical behavior of the SNF rods in a more systematic way.

In particular, this study investigates, experimentally and numerically, the mechanical response of irradiated nuclear fuel rods to mechanical solicitations. The experimental activities are performed in JRC-Karlsruhe and include a set of mechanical tests on surrogate and irradiated SNF rod segments. FEA is used to simulate the rod's behaviour and the experimental results are used to calibrate the models. The examination of various numerical parameters towards the FEM optimization, the calibration of the FEM against the experimental results and the determination of the mechanical properties of the SNF are the main objectives of the numerical studies [24].

As discussed in section 1.2.1, there is only a limited amount of experimental data available in literature characterizing the mechanical behavior of SNF. In addition, these data are restricted to specific types of fuels and loading conditions. This study complements and extends previous experimental investigations by generating new data concerning areas where technical gaps have been identified. Particularly, it examines the response of PWR SNF rods under a wide range of burnup, from very low to extremely high, covering the spectrum of conditions that can be encountered in practice. The examined loading conditions on SNF rods represent bending applications, as this type of load is mostly encountered in handling operations of SFAs. In terms of experimental analysis, an innovative IA methodology was developed to examine the dynamic response of SNF under impact bending loads. In this way, the dependence of flexural mechanical properties from strain rate was determined, which is very important in order to distinguish and analyse scenarios including either static (storage or handling) or dynamic loads (transportation, handling).

Moreover, the fracture behavior of SNF rods was studied and the subsequent fuel mass release and its dependence on SNF burnup and strain rate were determined. In case of accident scenarios analysis, and especially for criticality calculations, this information is valuable for reducing uncertainties and making best-estimate assumptions. Finally, the development and calibration of the FEM were performed against the experimental data; this constitutes a relevant achievement, since there are only a handful of studies combining experimental and numerical investigations. After an extensive sensitivity analysis on various modelling parameters, the generated FEM can be used to examine the mechanical response of SNF in conditions and configurations which extend beyond those tested in this experimental study. As a result, the need for large-scale experimental investigations that are costly and time-consuming can be reduced.

1.4 Thesis Outline

This thesis summarizes the experimental and numerical investigations conducted in the framework of this study, as well as the related findings. The thesis is structured in the following way.

Chapter 2 presents the experimental setup and methods that were used in order to examine the flexural properties of surrogate and SNF rod segments under different imposed strain rates. For this purpose, two devices have been developed and installed at the hot-cell facilities of Joint Research Centre (JRC)-Karlsruhe, which are able to conduct two sorts of mechanical tests, namely three-point bending and gravitational impact tests. The development process of both devices, the instrumentation, the measuring techniques and the data processing methods are thoroughly discussed. Particular focus is given on a newly developed IA methodology for processing data from impact tests.

Chapter 3 deals with the experimental characterisation of surrogate samples. This was the first experimental campaign in this study and aimed at investigating and comparing mechanical properties of fresh versus hydrogenated Zry-4 claddings. Results from three-point bending and impact tests on the surrogate samples are presented here and are also used for the derivation of flexural stress-strain curves for the examined samples.

The experimental campaign that involved all the mechanical tests on irradiated PWR UO2 samples is presented in Chapter 4. The main purpose of these tests was to investigate the flexural mechanical properties of the composite cladding/fuel rod samples and to examine the fuel mass release in case of cladding integrity loss. Sample preparation for the mechanical tests as well as test conduction are thoroughly described in this chapter together with the respective test results. Post-test examinations and findings concerning the fracture behaviour of the examined rods are also presented in this chapter.

Finally, Chapter 5 focuses on the numerical investigations that were performed in order to model and predict the bending behaviour and the mechanical properties of the examined SNF rods. The development of the employed FEMs with the use of ANSYS Mechanical is described in this chapter along with an extensive sensitivity analysis to evaluate the relative importance of different model parameters. Moreover, the chapter presents the calibration procedure that was applied in order to define model parameters with the use of experimental results from the three-point bending. Finally, the resulting predictions concerning effective mechanical properties of the rods are compared with experimental values.

Concluding remarks and research recommendations are provided in Chapter 6.

Chapter 2

Description of experimental setup and methods

Abstract *This chapter presents the experimental set-up employed to investigate the mechanical stability/properties of surrogate and SNF rod segments. Two devices have been developed, thoroughly checked and installed at the hot-cell facilities of JRC-Karlsruhe to conduct two sorts of mechanical tests, namely three-point bending and gravitational impact tests. Both types of tests aim to examine the flexural properties of the composite fuel/cladding system in different strain rates. The following paragraphs describe the development process of both devices, the instrumentation, the measuring techniques and data analysis methods applied. A new methodology based on Image Analysis (IA) principles has been established for the analysis of the impact tests.*

2.1 Experimental framework

Prior to the current study, a number of impact loading tests on LWR SNF rodlets (mainly PWR and one BWR) have been performed at the hot-cell facilities of the JRC-Karlsruhe, in the frame of the collaboration with AREVA [15–17]. The main objectives of those studies were the characterization of the fuel mass release in case of rod fracture and the assessment of the potential consequences associated with such release and dispersion. Those tests were a first approach towards a macroscopic investigation of the SNF response under impact loads. Aspects related to the consequences of a rod fracture were determined; however, detailed study of the rod's impact resistance based on the data acquisition capabilities of the impact-load test apparatus employed at that time was not possible. Therefore, a new experimental equipment had to be developed in order to extend and deepen the macroscopic characterization and study the mechanical behavior of the SNF rods in a more systematic way.

To this purpose, this PhD project expands the prior knowledge by studying the mechanical integrity of SNF rods under various mechanical loading conditions, simulating normal and/or accidental conditions during predisposal activities. The experimental campaign was conducted at the hot-cell facilities of the JRC-Karlsruhe. Two new devices for mechanical testing on fueled and pressurized SNF rod segments have been developed for three-point bending and gravitational impact tests. The main objectives of this program are the determination of rod response to external loads, the study of the rod failure progress and the characterization of fuel release in case of rod fracture. Additionally, the effects associated with the presence of hydride phases in the cladding is assessed with a series of post-tests examinations investigating and associating the Zr hydride content and morphology to the rod's response.

An overview of the experimental campaign is given in Fig. 2.1. The campaign consisted of two phases, namely: (a) the development and optimization of the mechanical testing devices and procedures with non-active, "cold" specimens - the so called analogue studies or cold tests - prior to (b) their installation and application to carry out experiments on irradiated spent fuel rod segments in the hot-cells.

The analogue studies are of great importance to develop and optimize the mechanical devices, as well as to study the mechanical behavior of hydrogenated zircaloy (mainly Zry-4) under bending stresses. The highly inhomogeneous material properties distribution and geometrical configuration of the SNF hampers implementing a direct cause-effect investigation and analysis of individual phenomena (i.e. PCMI, Zr hydride orientation and/or concentration, etc.). On the contrary, the "cold-test" campaign was conducted with homogenous certified materials (refer to section 3.1), thus most geometrical and heterogeneity-related uncertainties are excluded. This facilitates a deeper understanding of the physics and the phenomena involved, which drive the mechanical response of the rodlets during the tests. The outcomes of the cold tests were used for the further development and optimization of the devices. Furthermore, results obtained by these tests served as preliminary evaluation of cladding properties for the final campaign on commercial SNF. Finally, due to the well-controlled

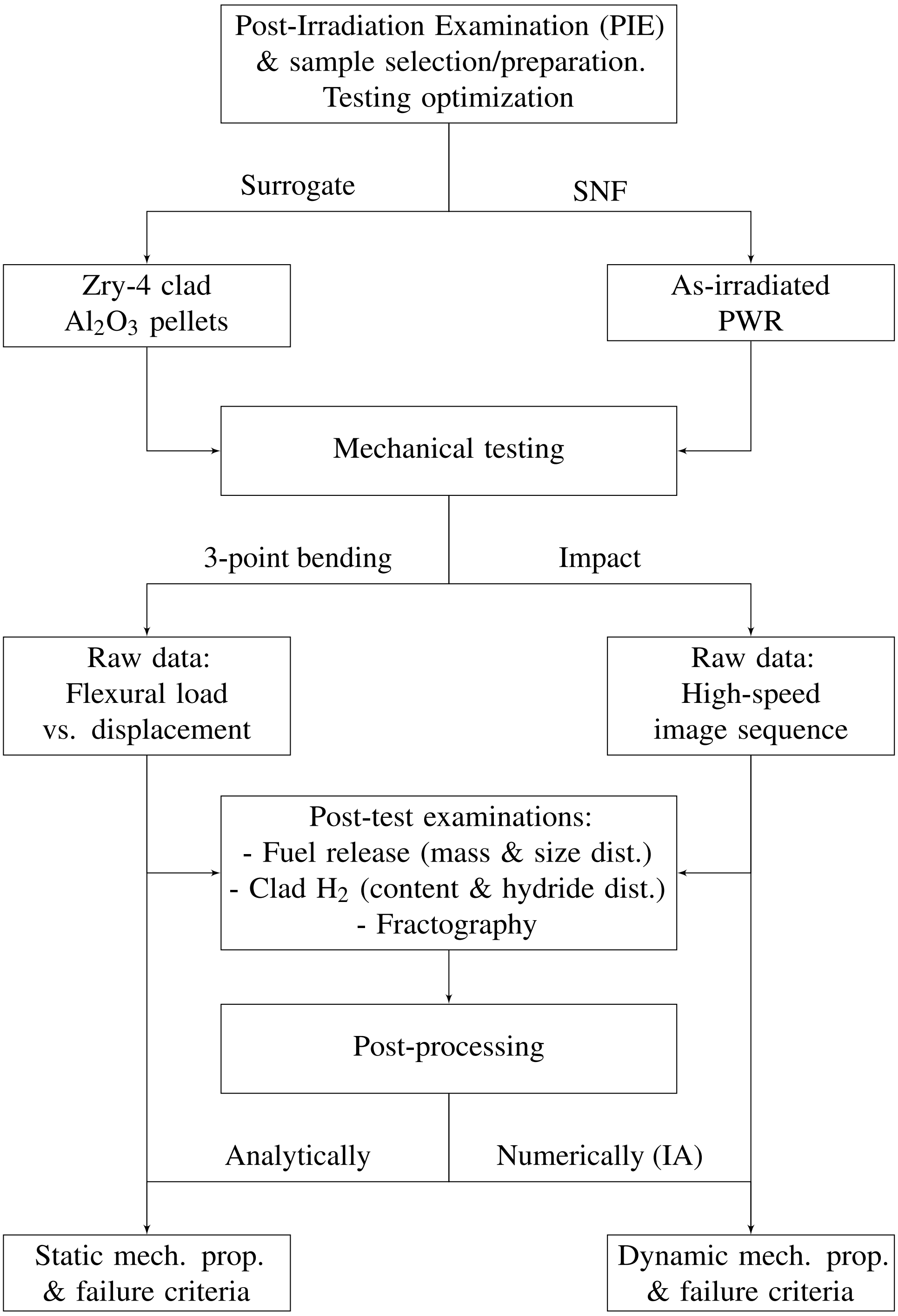
Post-Irradiation Examination (PIE)
& sample selection/preparation.
Testing optimization
Surrogate
SNF
Zry-4 clad
Al_2O_3 pellets
As-irradiated
PWR
Mechanical testing
3-point bending
Impact
Raw data:
Flexural load
vs. displacement
Raw data:
High-speed
image sequence
Post-test examinations:
- Fuel release (mass & size dist.)
- Clad H_2 (content & hydride dist.)
- Fractography
Post-processing
Analytically
Numerically (IA)
Static mech. prop.
& failure criteria
Dynamic mech. prop.
& failure criteria

Fig. 2.1 Flowchart illustration of the experimental campaign overview.

testing environment the cold tests were used for the development and validation of FEMs simulating rods under bending stresses.

Following the analogue studies, both devices were installed in a hot-cell to conduct experiments with commercial LWR SNF rod segments. Analysis of different sets of PIE data was used to select and prepare the segments for the mechanical testing (refer to section 4.1.1). The objective of the“hot-test” campaign was to select, analyze and combine information from the mechanical tests and post-test examinations in order to characterize the mechanical response of the composite fuel/cladding system. The goal was to derive empirical formulas to describe the flexural properties of the rods as a function of their properties (i.e. burnup, H_2 concentration and/or orientation, etc.). Post-test examinations were performed to investigate the cladding properties and fracture and to assess the fuel mass release (refer to section 4.6).

The analysis and post-processing of the experimental results from the two mechanical tests differ since the testing apparatuses do not share the same acquisition capabilities. Static mechanical properties and failure criteria were derived analytically from the three-point bending test results, whereas an image analysis (IA) methodology (refer to section 2.3.4) was developed to characterize the mechanical response of the SNF rods during the impact tests.

2.2 Three-point bending device

The experimental campaign was designed to provide information covering a broad range of SNF rod management activities prior to final disposal (i.e. storage, transportation and handling). Accordingly, the three-point bending test was considered most appropriate to characterize the mechanical behavior of the SNF. The flexural or bending test has long been a predominant technique to measure the uniaxial tensile strength of brittle and composite materials [69]. Due to the particularity of the SNF rod as material, the three-point bending test is the simplest way to subject a specimen to tension, compression and shear simultaneously [70], which are types of loads that SNF experiences during the different stages of the spent fuel management. Direct tension tests are less commonly used due to the large test piece size, the high costs of specimen utilization and testing, and the difficulties of gripping without misalignments [71, 72]. The three-point bending studies the correlation between applied load and elongation of the materials. Therefore, it is widely used also to measure their ductility.

In the bending test the rodlet sample is exposed to plastic deformation by applying perpendicular stresses to the sample axis, until a (pre-)defined bending angle “α” is reached. The test sequence is schematically presented in Fig. 2.2 [12]. The testing device basically consists of two supports and a former of cylindrical shape and sufficient hardness. The sample lays horizontally on top of the supports, while is loaded (forced) by the former. The bending stops either when the sample breaks or when the maximum bending angle"α" has been achieved.

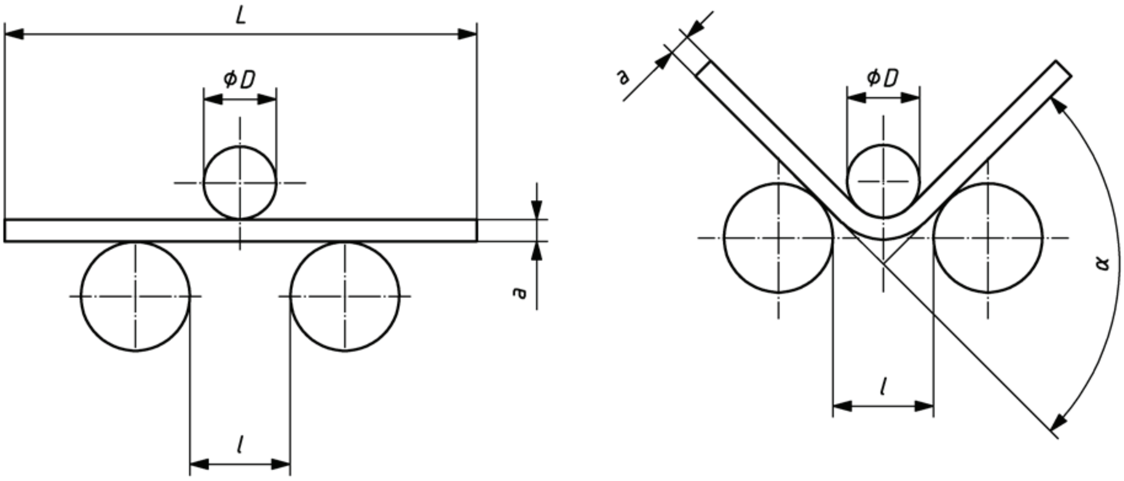

Fig. 2.2 Schematic presentation of the loading process during the 3-point bending test [12]. Bending loads are applied by the former on the testing sample which is left laying (lays horizontally) on two cylindrical supports.

2.2.1 Primary steps in the development of the bending device

The development of the three-point bending test device had started in the JRC-Karlsruhe shortly before the official start of the current research activities. A first version of the device had been built; during the present research programme, several alteration/improvements were applied prior to its final use, as described in the following paragraphs.

A considerable amount of time has been devoted to the development and optimization of the testing apparatus for the experimental campaign. During the first year of the program the device underwent a series of improvements aiming at establishing a robust test sequence, by minimizing the introduced errors and uncertainties, expanding the acquisition capabilities and facilitating the handling and operation of the device (especially in view of the remote handling via telemanipulators in hot cell).

An overview of the very first version of the device is given in Fig. 2.3. Its main characteristic was that the vertical displacement of the former was obtained by manually operating a screw system in which axis rotation was achieved via a torque wrench. Former and supports were made of bronze, a relatively soft material. Deflectors with two different lengths were used; with the longer the maximum bending angle could be achieved, since the axis displacement is limited by the length of the four metallic columns used to keep the loading axis in place.

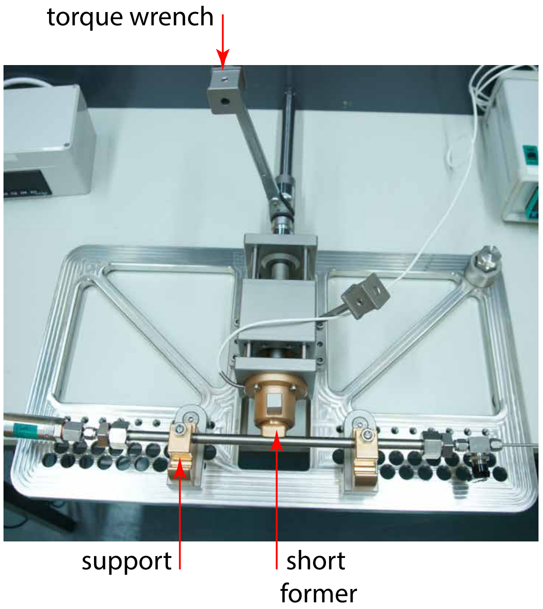

Fig. 2.3 Overview of the initial device, where the axis rotation is driven manually via a torque wrench.

The most significant restriction of this device was the inconsistent rate of torque provided to the axis, due to the manual transmission. This caused uneven axis rotation, hence axial movements, which resulted in irregular strain rates applied to the specimen. This effect is illustrated in Fig. 2.4, where the raw data of the applied load and axis displacement for a test on a Zry-4 sample driven by manual torque application are given. The axis displacement curve is not smooth, but has a discrete step-line format, where each step indicates one manual movement of the torque wrench. The data are plotted against time; a very small pause between consecutive movements can be noticed. In addition, the slope of this line gives the rate of the axis displacement. It can be noticed that the strain rate (or axis velocity) is not constant.

Despite the inconsistencies, the load curve shows clearly the elastic and elasto-plastic regions of the sample's behavior during the test. However, the load curve develops in a step-wise approach, following the rate of the axis displacement. The steps are more noticeable here since the material shows a relaxation behavior during the small pauses between the torque wrench movements. With this configuration, the identification of characteristic material

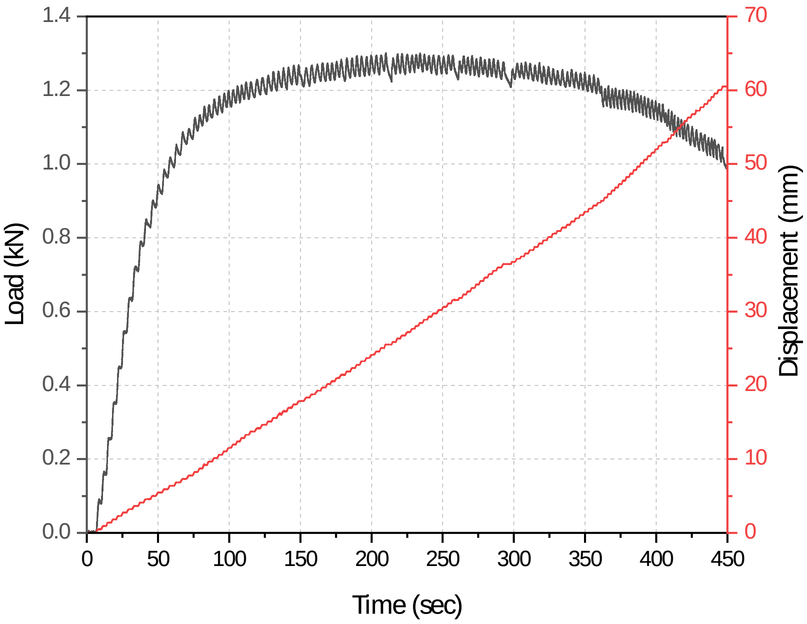

Fig. 2.4 Load and displacement as measured during a three-point bending test with the use of torque wrench to manually drive the loading axis.

properties, i.e. yield strength, modulus of elasticity, maximum strength, etc., would be a challenging task.

2.2.2 Conceptual and functionality control of the bending device

To overcome the inconsistencies imposed by the manual loading via axis rotation, the torque wrench was replaced by a step-motor, as shown in Fig. 2.5. Fig. 2.6 illustrates the evolutionary improvement of the new bending setup. A 2-phase step-motor “SECM299-E4.5 (AE)” by EC-Motion GmbH was used with a stepping angle of 1.8° [73]. The step-motor can be directly controlled by digital signals and rotate at constant angles according to a pulse signal. Therefore, the axis rotation could be stabilized to provide constant displacement rate. The displacement rate could be varied by altering the pulse frequency. A gearhead was used to amplify the maximum torque that the stepper motor can supply to generate a load at any desired speed. The gearhead is essential to cope with materials of high stiffness, such as SNF rodlets, which are difficult to bend and require higher loads. The step-motor can be operated within its safety range (torque and speed) to avoid any loss of the motor’s synchronism.

The basic schematic design of the device is given in Fig. 2.6. The device incorporates the concept of the modular design by accommodating the use of different former types and supports and by having the flexibility to adjust the sample’s effective length. The concept of

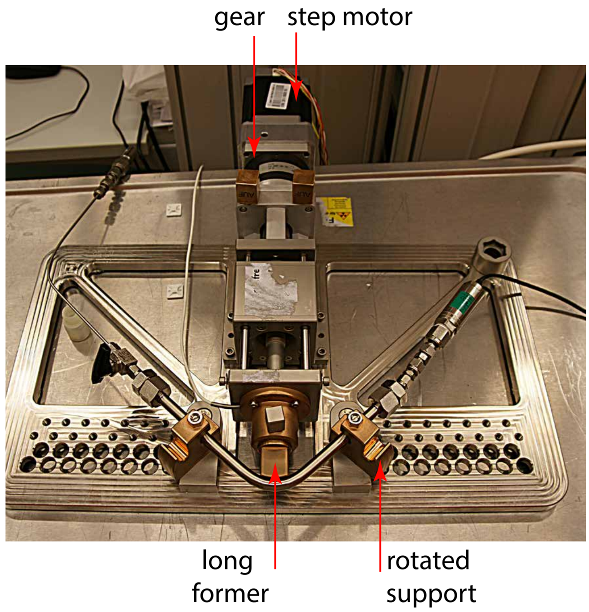

Fig. 2.5 Overview of the second device version, where a step-motor is used to apply constant torque to the axis. A specimen is shown at the maximum possible bending angle (use of longer former).

the testing apparatus was to use a mechanism that can drive a loading axis (no.3) with an attached former (no.6) perpendicular to the sample orientation (no.7). To establish loading conditions along the same direction a thread mechanism was used (no.4). The axis receives a torque and its rotational movement is translated into vertical displacement by the thread. The maximum displacement of the axis is limited by the length of its machined part (internal thread). The device is consisted of a metallic frame, stable enough to “absorb” the high stresses generated during the test. The goal was to create a robust device with no loose parts that might move during measurement and affect the recorded loads, leading thus to wrong-results . The distance between the supports (no.8) corresponds to the effective length of the sample under study and varies from a minimum distance of 140 mm up to max. 480 mm, with steps of 10 mm. The variable support distance allows testing of samples with different lengths. The geometrical configuration of the device follows the prerequisites of a standard bending test, as specified in the ISO 7438 standard [12].

Another illustration of the working principle is given in Fig. 2.7. The device has been sectioned at the vertical symmetry plane of the specimen, as seen from the side view at the left of the figure. A full section view is given in A-A, where the parts are highlighted and a zoomed view (circle B inclusion) is given at the right of the figure. The part highlighted

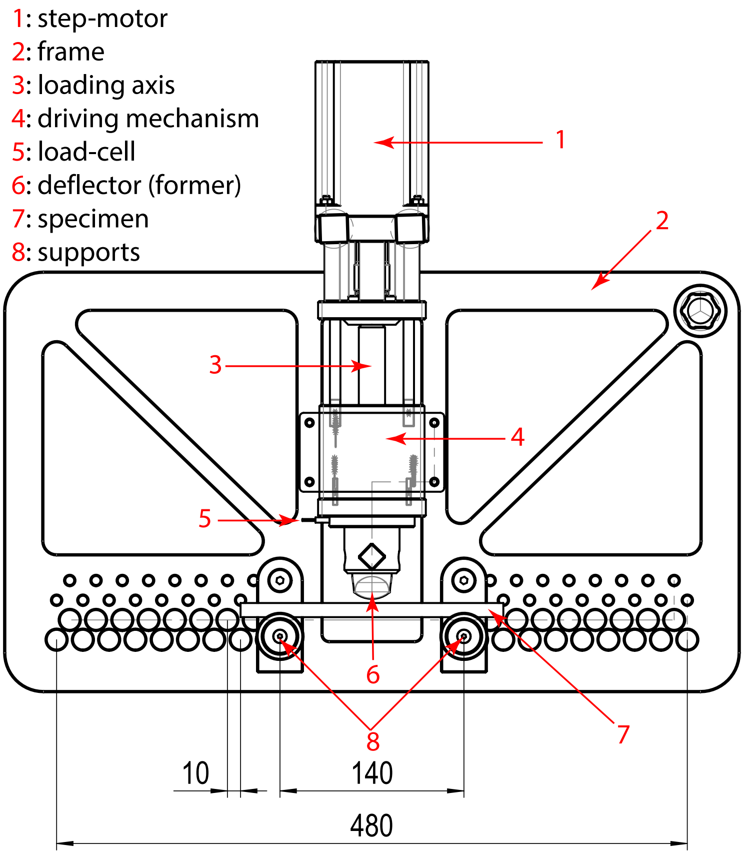

Fig. 2.6 2D drawing of the three-point bending test device, highlight its main configurations and geometric characteristics.

in light yellow is fixed to the metallic frame of the device by four diagonal screws. Its top part has been machined in a way to receive the axis external thread and translate its circular motion to vertical displacement. The part highlighted in dark yellow is used to hold the load-cell and the former in place. It is fixed to a metallic plate from the top, where ball-bearings are used to allow the free rotation around the axis. The load-cell sensor used to record the applied loads on the former is highlighted in red. The deflector is fixed to the dark yellow part with a cylindrical through bolt.

To examine the functionality of the device, a bending test of a Zry-4 cladding tube filled with Al_2O_3 pellets was performed. The axis displacement rate was set to $12.5\,\mu m\,s^{-1}$. The result in the form of applied load against time is given in Fig. 2.8. The use of the step-motor has significantly diminished the step-line format of the load curve, observed in Fig. 2.4. Therefore, the distinction between the elastic and the plastic regimes became clearer. The sample showed a very ductile behavior by preserving the cladding integrity up to the

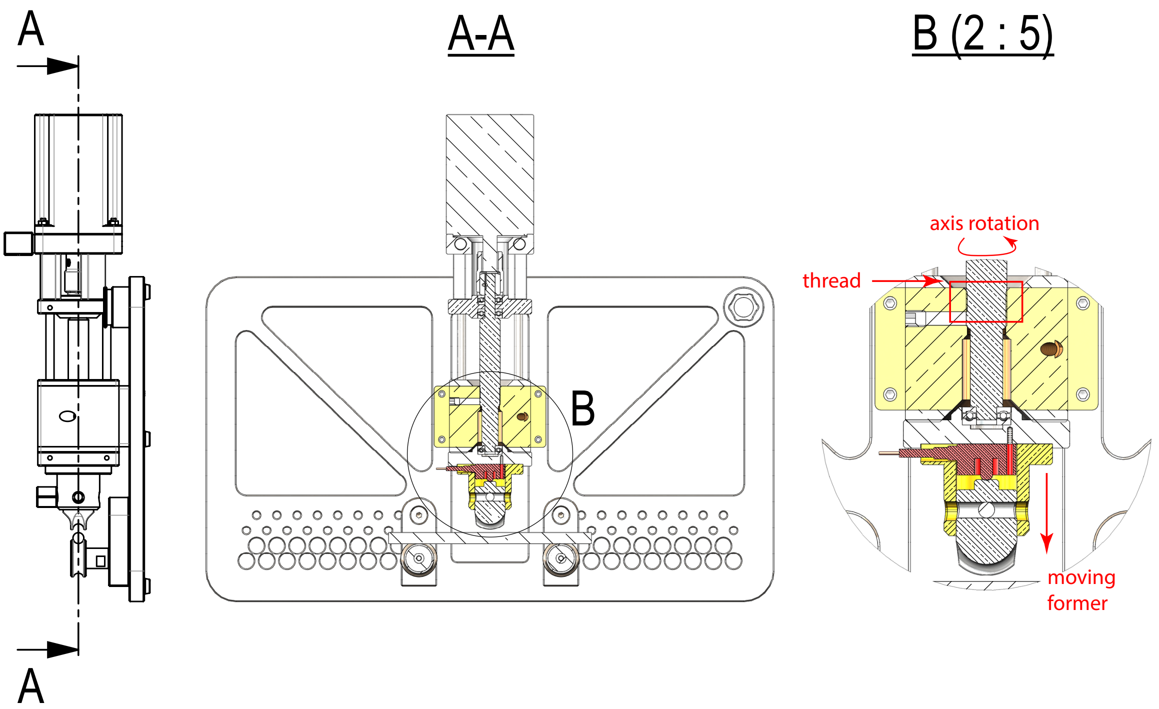

Fig. 2.7 Cross section view of the three-point bending test device at the sample's symmetry vertical symmetry plane, illustrating the working principle of the moving loading axis.

maximum achievable bending angle. A photograph of the sample's final deflection is shown in Fig. 2.8.

There are two main interfering effects observed in the load curve. The first is the sudden load drop, which appeared twice during the test. In these regions, indicated with the blue arrows, the load drops abruptly by approximately 40 N. This is an undesirable effect which creates "discontinuities" and introduces artefacts complicating data interpretation. This effect is due by the supports, which were not rigidly fixed to the device's metallic frame, but they were simply supported. Therefore, rotation was allowed around their fixation point as shown by the technical drawing in Fig.2.9. Accordingly, the sample deflection can be accommodated, up to a certain point, by the rotation of the support, giving no relative movement between those parts. In other words, during bending the sample simply lays on the support while the support rotates. The first sudden load drop occurred when the supports reached the "maximum" rotation angle (defined by the device geometrical characteristics) and any further deflection was accommodated by sliding of the sample on the support. This increases the effective sample length, which alters slightly the testing conditions. With increased effective length, the sample exhibits some relaxation, since the system becomes less stiff. Similar load drops are observed in Fig. 2.4, as well.

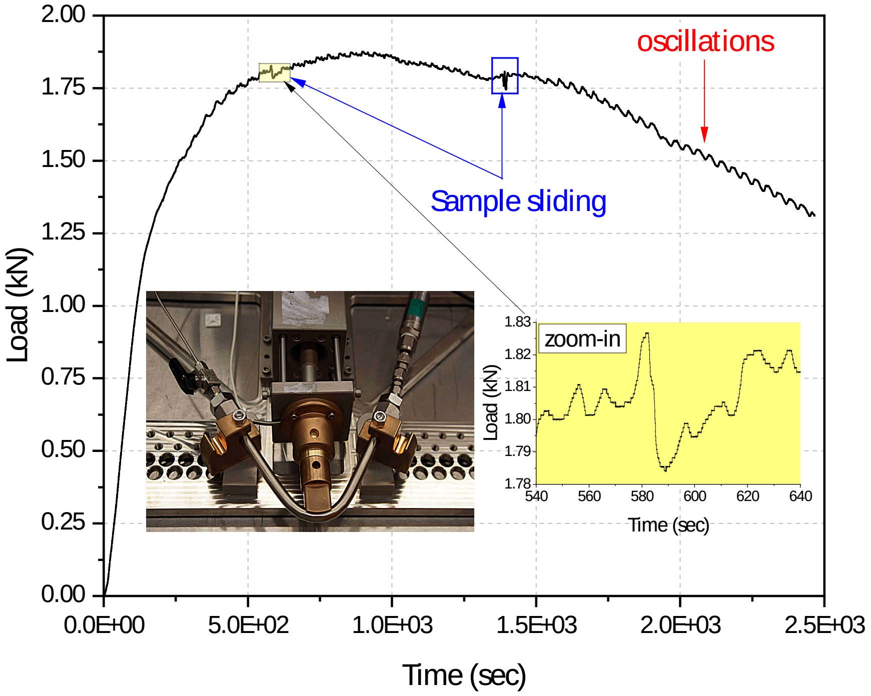

Fig. 2.8 Three-point bending test on a Zry-4 cladding tube filled with alumina pellets. The applied load is plotted against time; oscillation and sudden load drops are observed in the plastic regime.

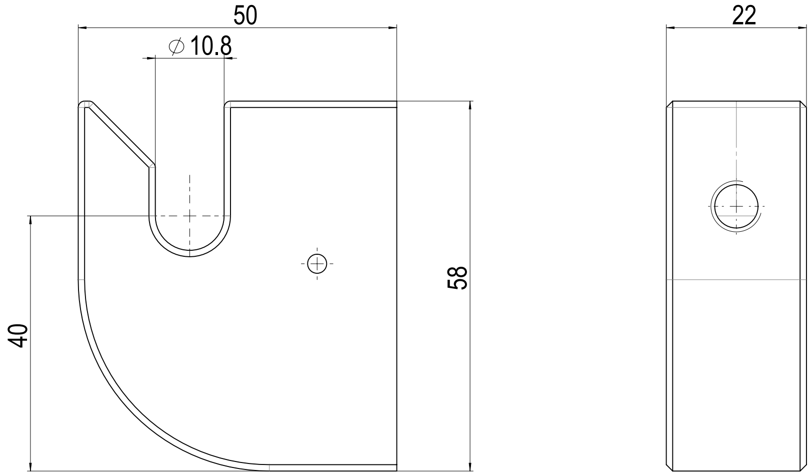

Fig. 2.9 Technical drawing of the supports initially used in the three-point bending test device. The parts were simply supported, and not fixed to the metallic frame, allowing their rotation.

The second effect is the load oscillations observed during sample's plastic deformation. There was no clear explanation for the origin of this effect, therefore further investigations were required. Similar observations had been reported for lateral bending tests on SNF by

Dallongeville et al. [46]. The oscillations were attributed to the PLC effect and the results of these tests, i.e. the load-displacement curves, were smoothed. The PLC effect appears in metal alloys during plastic deformation. The effect has been first researched by Portevin and Le Chatelier [74] who focused their attention on the force instability during tension. Processes responsible for the appearance of the PLC effect are not yet fully explained and differing views concerning the physical basis of this phenomenon are reported. Characteristic stress oscillations seen on the work-hardening curve in the range of plastic flow, differ from each other in both shape and size, which, among others, depend on temperature and strain rate ($\dot{\varepsilon}$) [75]. The character of those oscillations has been investigated [13, 14] and it has been classified into three categories, as shown in Fig. 2.10. Type A has been observed at low temperature tensile tests. Its characteristic is the load growth followed by a sudden decrease, which occurs periodically. Types B and C occur at elevated temperatures, therefore there are not relevant to our testing conditions.

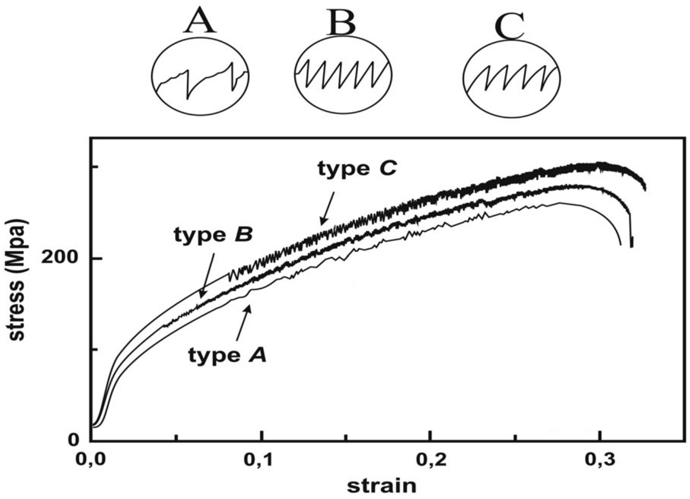

Fig. 2.10 Types of stress oscillation characteristics for the PLC effect [13, 14]. Type A is relevant to our ambient temperature testing conditions.

The periodicity of the oscillations has also been observed in our experiments. Specific investigations and analysis were needed to fully understand this heterogeneous range of plastic deformation. Fig. 2.11, shows higher resolution examination of the shape of the oscillations observed in our experiment. Two different regions have been highlighted to illustrate two phenomena. The first region is located in the strain hardening region of the curve, while the second is at the necking of that curve.

A clear difference on the shape and magnitude of the oscillations within these regions can be observed. Therefore, they cannot be of the same PLC type and as only Type A occurs in lower temperature ranges, this effect is not relevant.

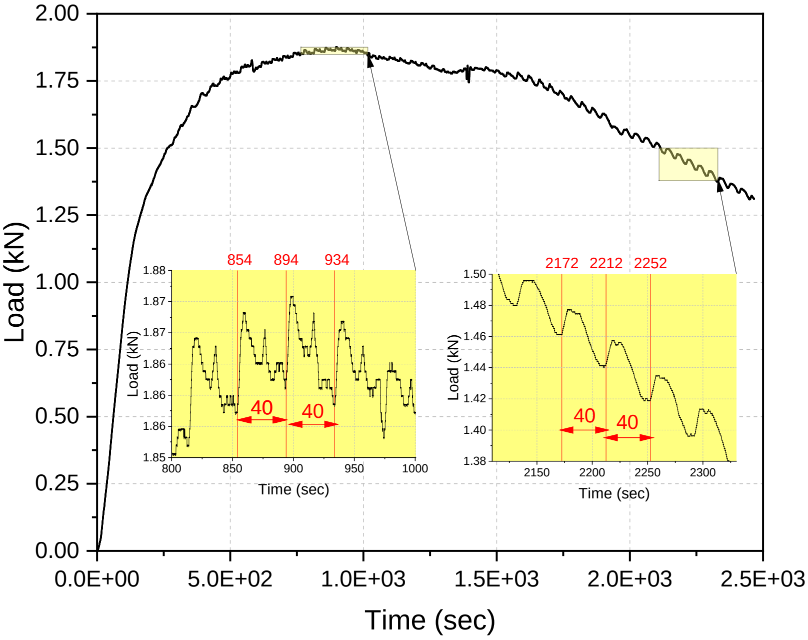

Fig. 2.11 Closer examination of the oscillations which occurred in different regions of the experimental test. The oscillations differ in both, magnitude and shape, but they develop periodically with the same frequency.

The second observation has to do with the periodicity of those oscillations, where in both regions they develop with the same frequency. This effect was studied by analyzing the first derivative of the load curve and by applying a DFT (using the OriginLab Pro 2019 [76]), which converts the signal in the time domain into its counterpart in the frequency domain. The results are given in Fig. 2.12a, where the amplitude of the derived frequencies within the whole load range are shown. The predominant frequency occurs at $f \approx 0.025$ Hz. This result coincides with the observed periodicity of $T \approx 40$ s in Fig. 2.11, which is equal to the step-motor frequency. The loading axis completes a full turn every 40 s, therefore these oscillations could be linked to the step-motor integral function of the experimental apparatus. Taking this into account, it is only reasonable to assume that this frequency appears and affects the load signal during the whole test and not only in the plastic deformation region, where the oscillations are observed.

Fig. 2.12b helps towards a better understanding on this phenomenon, where the slope of the load curve is given at three different points representing the elastic regime (θ_{el}), the strain hardening regime (θ_{pl_1}) and the necking regime (θ_{pl_2}). The oscillations become visible only when the relative change of the load rate is lower than the amplitude of the step-motor's frequency ($A_{f_{motor}}$). This condition is given in Eq. (2.1). The amplitude of the predominant frequency after the DFT application is found approximately equal to $A_{f_{motor}} \approx 0.83\,\mathrm{N\,s^{-1}}$.

The load rate in the elastic region, $\theta_{el} \approx 9.88\ \mathrm{N\,s^{-1}}$, is more than one order of magnitude higher than the amplitude of this frequency. Consequently, the step-motor effect cannot be visible, whereas in the plastic regime the load rate decreases significantly, and the oscillations are observed. The relationship between the amplitude of the step-motor frequency and the slope of the load curve in the elastic and plastic regimes is given in the Eq. (2.2).

$$\theta = \frac{\mathrm{d}f}{\mathrm{d}t} > A_{f_{motor}} \tag{2.1}$$

and

$$\theta_{pl} < A_{f_{motor}} < \theta_{pl} \tag{2.2}$$

Although the oscillations are linked to the step-motor frequency, the primary cause of the stress fluctuation is still unclear. There are four possible mechanisms that could be linked to this cause and generate this effect:

- step-motor irregular movement;
- mechanical “relaxation” of the bending device when elevated stresses are applied;
- mechanical asymmetry of the axis rotation mechanism;
- misalignment of the load-cell sensor.

In case that the step-motor operates in an irregular way, the first and the third point can be linked. If the motor has periods of slightly higher or lower pulse rate generation then the axis movement will be inconsistent generating different strain rates during the bending test. This discontinuity in the axis movement could possibly cause the load oscillations, however the periodicity does not fit with this reasoning. In addition, there are no other sources mentioning any related issues to the step-motor’s functionality.

The third point can also be valid in case of a mechanical issue on the axis rotation mechanism (see Fig. 2.7). Other mechanical misalignment could possibly justify the second argument, which is related to an integral device behavior causing mechanical “relaxation” periods of the device during the tests. To investigate further the relevance of those arguments, a displacement sensor was used to extend the acquisition capabilities of the bending test. Up to that point, the axis displacement was derived from the pulses of the step-motor (electronically) and not by any other means of measurement. Two new experiments were

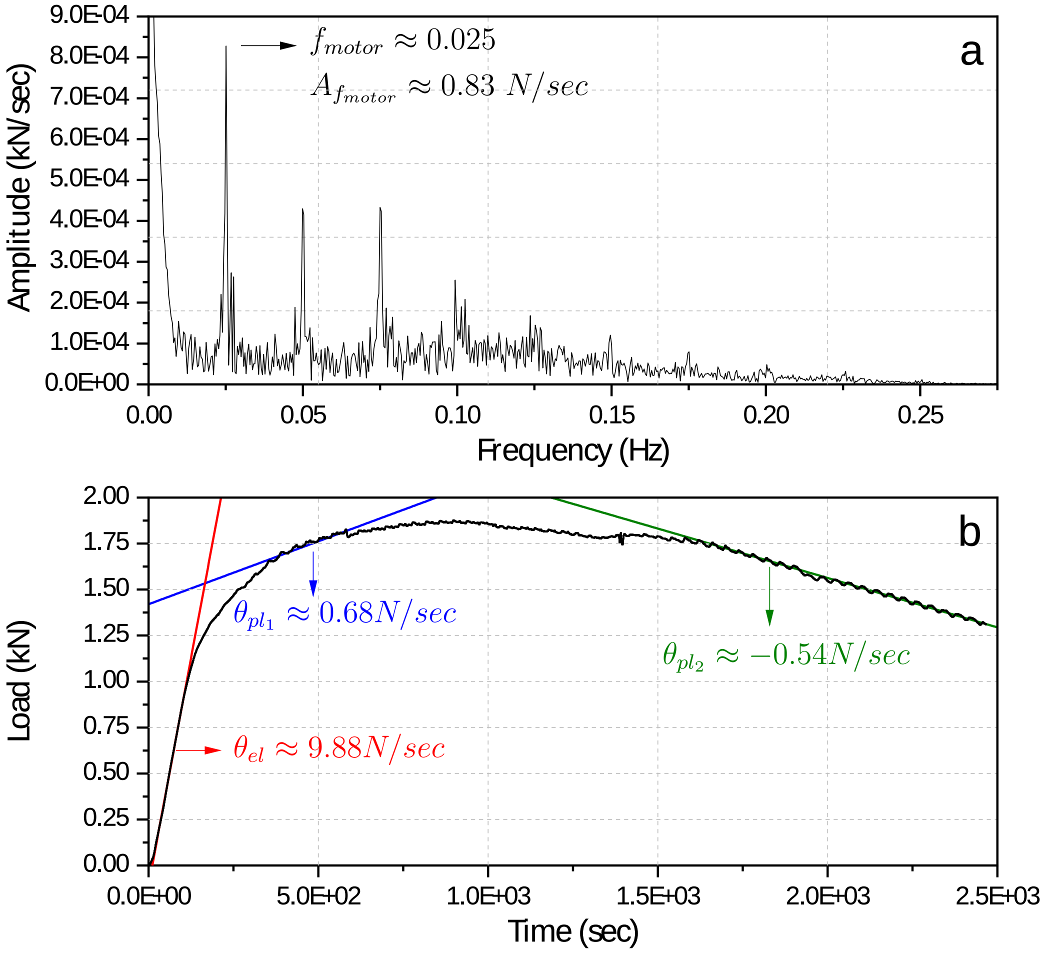

Fig. 2.12 a) DFT analysis on the first derivate of the load curve, revealing the predominant frequency on the load signal; b) slope of the load curve derived at three different locations (elastic, strain hardening and necking).

performed with identical conditions, but having the displacement sensor with different orientations. At first, the sensor was placed along the axis to measure accurately its vertical movement. Then, it was placed perpendicularly to the axis to measure any possible lateral oscillation during its movement. The results showed a slight non-constant but periodic behavior in both experiments. The magnitude of those oscillations was however very small. The periodicity of the oscillation coincides with one turn of the axis showing a direct link with the movement of the step-motor. Different speeds of the step motor were tested in order to prove this result. In every experiment, it was observed that the oscillation varied dependently and correspondingly to the rpm of the step-motor.

After measuring carefully the old axis, it was proven that there was a slight asymmetry, and this could also be a possible reason for its lateral displacement. At that point, it was decided to construct a new axis to exclude any possible mechanical relaxation of the whole device. In parallel to the construction of the old axis, new bearings (used to transfer the movement from the radial direction – axially) were introduced able to withstand loads up to 5 kN.

Finally, the contribution of the supports to the development of the load oscillations was investigated. The geometrical characteristics of the first pair of supporting units used are provided in Fig. 2.9. The sudden drops observed in the load curve were attributed to their mode of operation (see Fig. 2.8), which allowed their rotation thus causing abrupt changes to the effective sample length during bending. For this reason, a new pair of supports was constructed and tested, as shown in Fig. 2.13a. The supports are now fixed to the metallic frame of the device, therefore their rotation is not permitted. They have cylindrical shape with a machined part to the desired support radius.

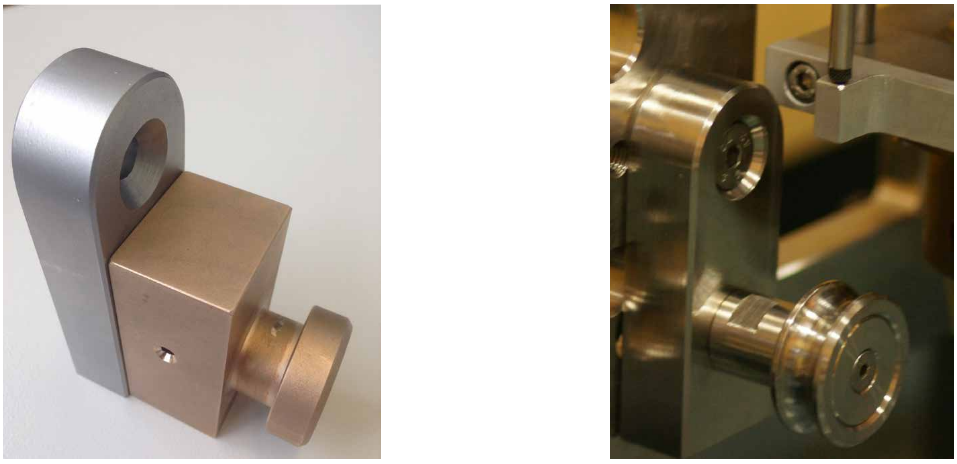

(a) Cylindrical supports.

(b) Rolling supports.

Fig. 2.13 Two different types of supports used to test their contribution to the develop- ment of the load oscillations in the plastic regime during bending: (a) rigid support (no rotation allowed); (b) rolling support (rotation allowed).

A three-point bending test was performed using a dummy sample (stainless-steel bar) to examine the functionality of the new support. The resulted load-displacement curve is given in Fig. 2.14 in black. As expected, no load drops were observed, resulting to a continuous sample deflection without any abrupt sliding. However, the load oscillations were still occurring in the plastic region , even after the change of the loading axis and related ball-bearings, although with a relatively lower amplitude compared to the previous setup. These results were not suitable to provide a clear understanding of the origin of the oscillations, since it could be due to a misalignment of the load-cell sensor or to the device's metallic frame relaxation (related to its stiffness) or from an uneven axis rotation.

In efforts to understand and minimize the uncertainties and further optimize the testing configuration, a new pair of supports was developed. The new design is shown in Fig. 2.13b and it incorporates a rotational rounded surface where the sample lies upon. Rolling-element bearings are used, as shown in the sectioned side-view in Fig. 2.16, to restrict any relative movement between the sample rod and the support during testing conditions. Therefore, the sample doesn't slide on the support, but the support rotates following the movement of the rod. This fact eliminates the friction coefficient parameter, which is also desirable for the model simplification in the numerical analysis of the experimental results.

To investigate the performance of the new supports, a new test was performed using again the same type of sample as before (stainless-steel bar). The results are given in Fig. 2.14, red curve, and show that the amplitude of the oscillations was significantly reduced. The enlarged graph of a part of the plastic regime illustrates the difference on the performance between the two support types. The oscillations are still present; however, their amplitude has a much smaller effect on the shape of the recorded load curve.

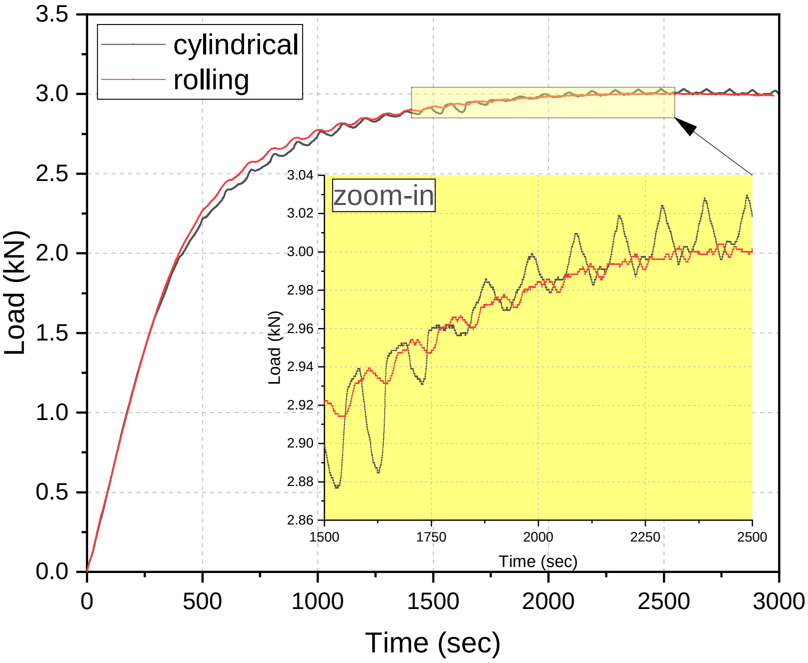

Fig. 2.14 Comparison of two different support systems for the assessment of the load instabilities in the plastic region during bending test.

No further investigations was deemed not worth pursuing to further minimize the oscillations observed in the load curve. Their affect had been significantly reduced, compared to initial results given in Fig. 2.11, after changing the loading axis and supports. Any further alteration to the device would require a considerable amount of time until final implementation (order of months), due to the different development phases, i.e. designing, machining, testing and performance analysis of each part.

Finally, the last device improvements focused on the geometrical characteristics and the selection of component materials. The first version of this setup was made of hard copper and is shown in Fig. 2.15. Two similar parts of equal diameters (60 mm) and different lengths were designed and machined to allow achieving different maximum bending angles (refer to Fig. 2.7). These parts, being 15 mm different in length, can provide maximum sample deflection (at the symmetry axis) of 60 mm or 75 mm. Considering the geometrical characteristics of the bending device these deflections are translated to approximately $\alpha = 100^\circ$ or $\alpha = 115^\circ$ maximum bending angles (see Fig. 2.2).

There were two issues associated with the operation of the former. The first one has to do with the hardness of the material, which is relatively low compared to the hardness of the samples under examination. As a result, the former's was found to have deformed after some tests. This is undesirable, since the test repeatability cannot be ensured. The second issue is related to the geometrical characteristics of the former's concave shape. In particular, the former's diameter was a limiting factor to reach higher bending angles. After a certain deformation, the samples were detaching from the internal concave surface and the load was consequently applied only at the two outermost extremities. Therefore, the test configuration could not be preserved at high bending angles, and the associated results were not representative of the samples' properties under bending loads.

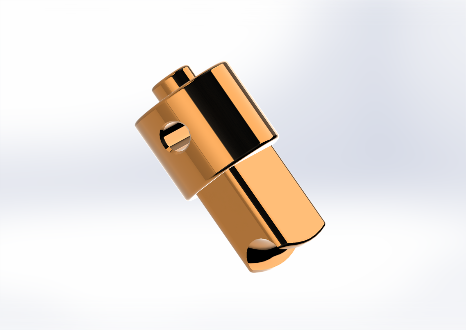

Fig. 2.15 First version of bending former made of hard copper.

2.2.3 Final geometrical characteristics

A 3D presentation along with the mechanical drawing of the support depicting the main geometrical characteristics is given in Fig. 2.16. The working principle of the new "rolling" supports is described in section 2.2.2. Their concave surface has a diameter of 10.75 mm, enabling the use of both BWR and PWR fuel rod segments. The effective diameter of the support is 29.25 mm and the effective distance between the center of the supports used for the experiments reported here is 140 mm, as shown in Fig. 2.6.

To improve and optimize the functionality of the former, a new version has been designed, shown in Fig. 2.17. Stainless steel was used, instead of copper, to provide sufficient hardness and prevent the component's permanent deformation after extensive use. To avoid clamping during the test and stretch forming of the sample, the former diameter has been reduced by half to 30 mm and the edges have been smoothed. Again, the new set included two formers, one longer than the other by 15 mm.

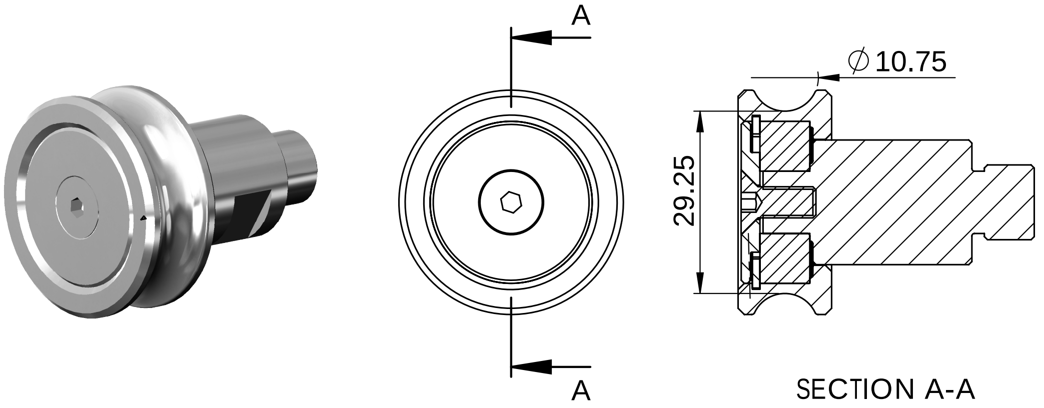

Fig. 2.16 Technical drawing of the final version of the rolling supports used for the three-point bending tests.

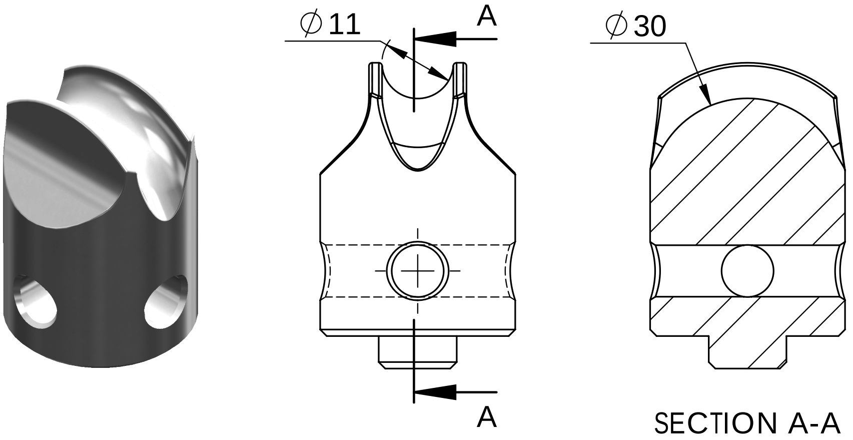

Fig. 2.17 Technical drawing of the final version of the former used for the three-point bending tests.

Table 2.1 provides the main dimensions of the major components and the symbols and designations associated with the bending test results.

Table 2.1 Main dimensions and description of symbols used for the three-point bending test.

Symbol	**Designation**	**Dimension**	**Unit**
D_b	Diameter of the former	30	mm
R_b	Radius of the supports	15	mm
l_b	Min distance between supports	140	mm
k	Distance step increase between supports	20	mm
a	Diameter of the test piece	*t.d.*[1]	mm
L_b	Length of the test piece		mm
a_b	Angle of bend		degrees
f_b	Displacement of the former		mm

2.2.4 Instrumentation and data acquisition

The three-point bending is a displacement driven test in which quasi-static loads are applied at the middle-span of the sample to deflect it until fracture. It is of paramount importance to measure, as accurately as possible, the applied load and the sample's deflection. By all means, the measurement techniques and associated instrumentation should be compatible with the hot-cell operational constraints, where remote handling is required, and the apparatus is subjected to high-radiation environment. As much as feasible, the use of the electronics within the hot-cell should be avoided in order to prolong the lifespan of the instrumentation. Fig. 2.18 shows an overview of the setup configuration, where the locations of the sensors are noted. The experimental setup has been equipped with three sensors for the recording of the:

1. applied load at the rodlet's middle-span ;
2. deflection of the sample;
3. internal pressure of the rodlet.

A load cell model, from the Burster 8435 series [77], is used to record the load applied onto the sample as the central axis moves at a constant rate (see Fig. 2.7). The sensor can measure both static and dynamic forces in tension and compression, it has small dimensions,

---

[1] where, $t.d.$: test depended

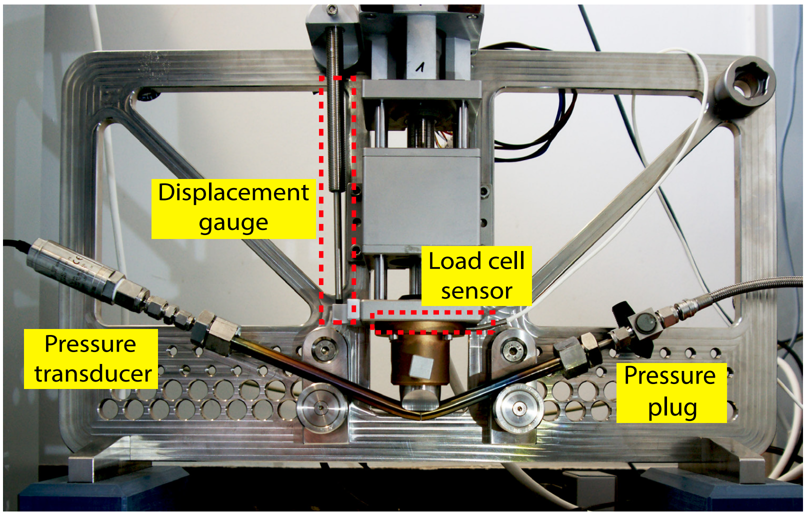

Fig. 2.18 Overview of a typical three-point bending test configuration illustrating sensors' positioning.

it is made of stainless steel and is ideal for installation in such loading machines. Its measuring principle relies upon the strain gauge technology. The sensor operates with the aid of a spring element. Its purpose is to convert the applied force into a linear extension. A horizontally mounted elastic membrane is used as spring element. Upon a force, the elastic membrane is deflected, and its deflection is measured by strain gauges. Since the elastic properties of the membrane are known, the force can be determined indirectly.

To achieve high measurement accuracy the force has to be applied in a direction perpendicular to the sensor, exactly along its symmetry axis as shown in Fig. 2.19a. Therefore the sensor is placed flat on the mounting surface using three screws as shown in Fig. 2.19b. This metallic surface is better shown in Fig. 2.7, where ball-bearing are used to connect and allow the free rotation of the axis. Therefore, the oscillations observed and described on the load signal (refer to section 2.2.2) could originate from any possible misalignment at the applied force direction.

As described in the previous section, the three-point bending test device has been significantly modified compared to its first version (refer to Fig. 2.3). Initially, the sample deflection (at the symmetry plane) was measured by following the central axis displacement, as this was provided manually via the torque wrench. This resulted in inconsistencies in the displacement rate, as shown in Fig. 2.4. To provide a constant and adjustable displacement rate of the central axis, a step-motor was installed to replace the torque wrench, as shown in Fig. 2.5. The sample deflection can now be assessed by following the electric pulses of the motor. In this way, the displacement rate of the axis will be determined as constant. Based

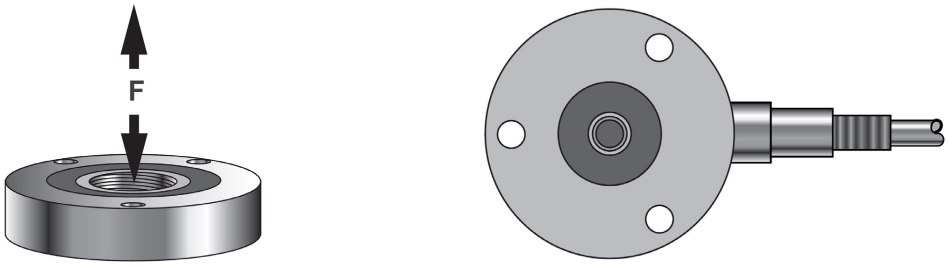

(a) Applied force direction.

(b) Mounting system.

Fig. 2.19 Force application direction (a) and mounting system (b) of the used load cell sensor.

on this approach, any possible deviation from the ideal case, that could be originated from numerous reasons, would be concealed.

As a result, a precision gauge head was installed, in order to measure indirectly the “real” axis speed, by following the displacement of the bottom plate where the load cell is fixed. An extra part has been attached to the bottom plate, where the tip of the gauge head is placed, as shown in Fig. 2.20. A GCA-121-2000 series gauge head model [78] was used, made up of stainless steel and whose electronics components are hermetically sealed. This gauge provides ruggedness, long life cycle, and very high reliability, even when operated in hostile environments, such as a hot-cell. The gauge head is fixed at the top of the metallic frame of the device, as shown in Fig. 2.20.

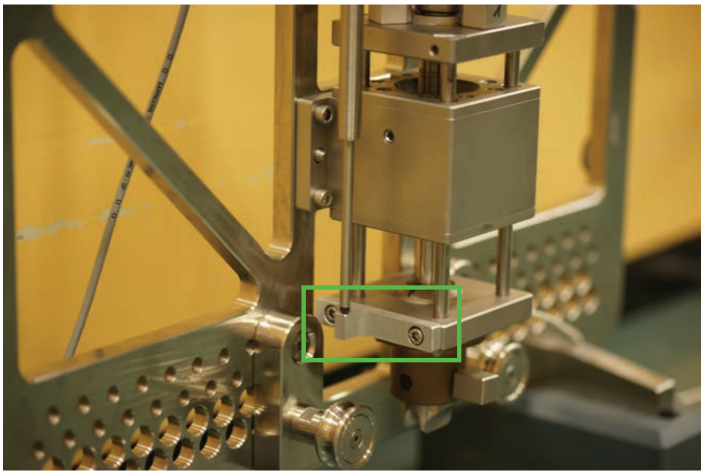

Fig. 2.20 The sample’s deflection is measured indirectly, by following the displacement of the bottom metallic plate where the sensor is located.

A pressure transducer is used to measure the internal pressure of the samples. Two end-plugs were fixed to both sides of the rodlet, as shown in Fig. 2.21. A valve was connected to one side in order to introduce and seal the gas used for the pressurization. At the other end, a pressure transducer (GE UNIK 5000 [79]) was installed in order to monitor the internal pressure. Its stainless steel construction, along with its simplicity and high frequency response, made it suitable for reliable online measurements and durability within hot-cell conditions. An overview of the set-up is given in Fig. 2.18.

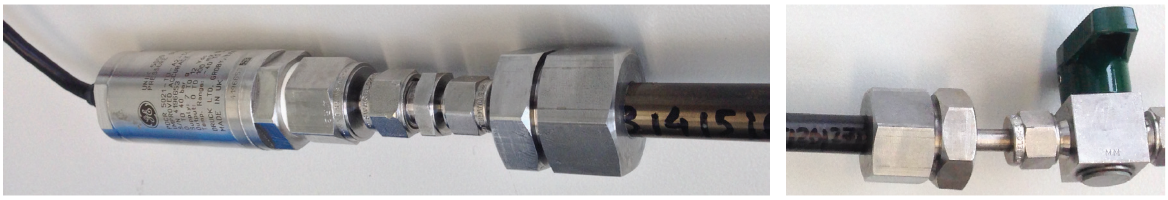

Fig. 2.21 Use of end-plugs to pressurize and seal (right) the rodlets and to measure the internal pressure (left).

An attempt was also made to install an acoustic sensor, aiming to capture the occurrence of pellet fragmentation. In the preliminary experiments during the device's development phase, the sound of surrogate pellet cracking was apparent. The intention was to determine the time, deflection and load needed to initiate the fracturing of the pellets and possibly correlate this with the overall mechanical response of the sample. Unfortunately, after installing and testing, the background noise prevented the clear identification of the pellet cracking, therefore such sensor was never used in practice.

A schematic representation of the data acquisition system of the bending apparatus is given in Fig. 2.22, where the process used to acquire the data is illustrated. The PC is connected to a powerful controller which processes the sensors' signals and controls the step-motor. The "Compact RIO" platform [80] features a range of embedded controllers with two processing targets; a real-time processor for communication and signal processing and a user-programmable FPGA to implement high-speed control and custom timing and triggering directly in hardware. This eliminates the need for separate subsystems by connecting directly to sensors and motors and takes advantage of powerful development and run-time software.

A LabVIEW program was developed to control the test process and acquire high-frequency data from the sensors. The development environment has a graphical programming syntax, which makes it simple to visualize and uses code engineering systems [81]. Fig. 2.23a shows the front panel which serves as a graphical user interface for the test sequence. It provides a real-time observation of the measured values and gives the possibility to immediately terminate the test as safety measure. The sensor signals for the applied load, displacement and pressure, as well as the electric pulses of the step-motor are displayed in four enlarged graphs. This gives the opportunity to follow the test in real-time and detect any possible

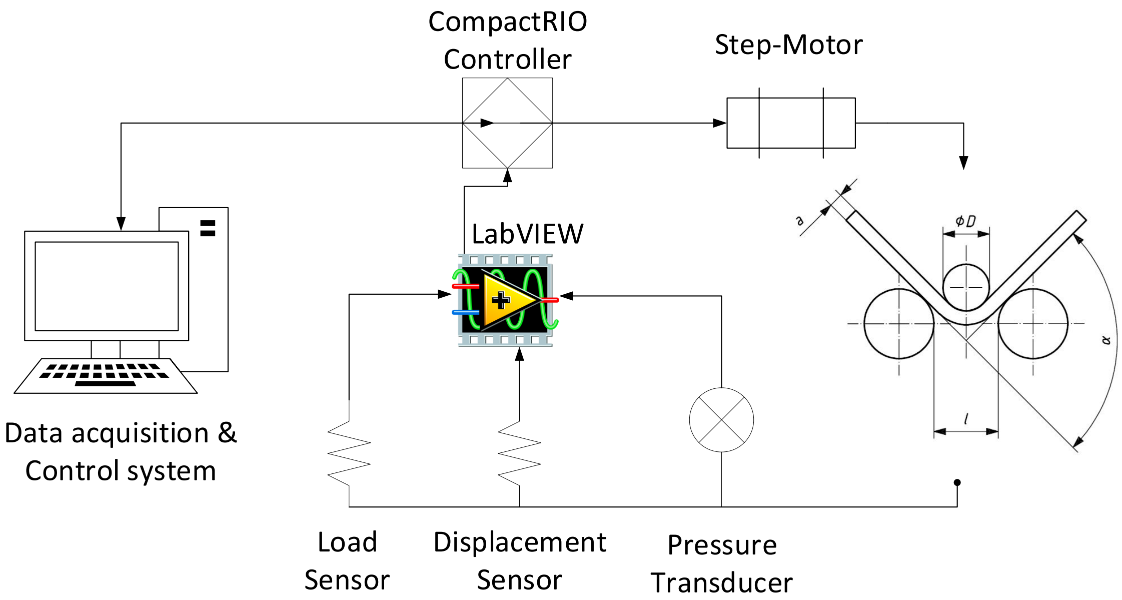
CompactRIO
Controller
Step-Motor
LabVIEW
Data acquisition &
Control system
a
ϕD
α
l
Load
Sensor
Displacement
Sensor
Pressure
Transducer

Fig. 2.22 Schematic representation of the test-rig and data acquisition process for the three-point bending test.

irregularities. All issues that could relate to test failure are also displayed as error message windows.

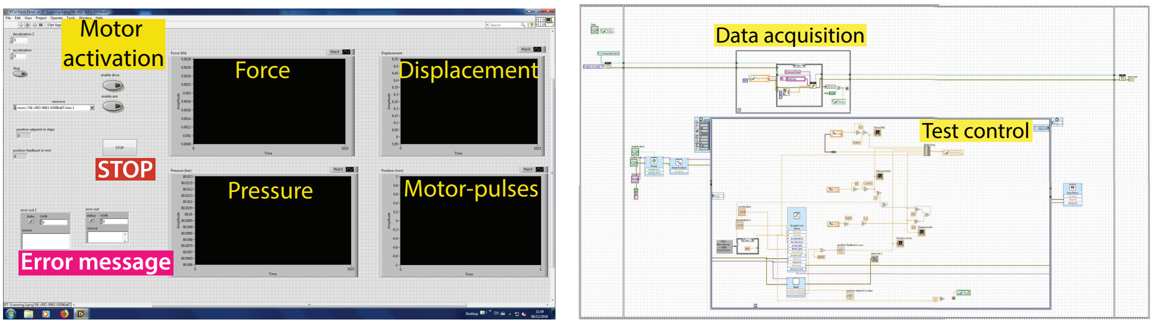
Motor
activation
Force
Displacement
STOP
Pressure
Motor-pulses
Error message
Data acquisition
Test control

(a) LabVIEW Front Panel.

(b) LabVIEW block diagram.

Fig. 2.23 LabVIEW program used to control the test process of the three-point bending test and acquire high-frequency data from the sensors.

Fig. 2.23b shows the block diagram developed for the three-point bending test, which contains the graphical source code. In this part, everything related to test procedure, data acquisition, sensor calibration is programmed. From the block diagram we can activate the step-motor and control its frequency and consequently the displacement velocity of the loading point. The frequency of the step-motor was also linked to the online force, displacement and pressure measurements. Therefore, the central axis motion can be deactivated once the sample is fractured (load and pressure drop drastically) or when the displacement reaches the device's hardware limitations (safety measure).

2.2.5 Experimental method - Simple beam theory

The raw data of the experimental test describing the flexural behavior of a sample consists of the load-displacement curve. This data represents neither the flexural mechanical properties of the cladding material nor of the fuel pellets, but of the composite SNF rod as both the cladding and the pellets contribute simultaneously to the bending response of the sample. As a result, the analysis of acquired data becomes very complex and demands further assumptions in order to characterize its flexural behavior. The analysis of the experimental data is based on the simple beam theory (or Euler-Bernoulli theory), where upon a series of assumptions about the stress-strain behavior of the samples can be made.

A simple beam is defined as a horizontal member (bar or structural member) that rests on two supports at its ends and all of the parts between these supports have free movement in a vertical plane under the influence of vertical loads. When the beam bends, the fibers on the concave side (upper) are shortened as compressive stresses are acting on them; the fibers on the convex side (bottom) are lengthened as tensile stresses are acting on them. In addition, shear stresses are developed along the beam cross-section. The change in the spacing of the ideal lines on each surface is a measure of the strain and consequently the stress to which the surface is subjected to. The simple theory of bending relies on a series of assumptions to derive a formula, which relates the stress in the surface of the beam to the value of the bending moment applied and the amount of curvature developed. These simplifying assumptions are as follow:

1. the elastic limit is not exceeded;
2. the beam is straight and unstressed before bending;
3. the beam's material is homogeneous and isotropic (same elastic properties and density throughout);
4. the elastic modulus is the same in tension and compression;
5. every beam's cross-section is symmetrical to the plane of bending;
6. there is no resultant force perpendicular to any cross-section.

As a result, the range of validity of this theory lies within the elastic region of the material and it cannot be used to accurately describe the relation of flexural stress-strain developed during plastic deformation. Moreover, the SNF rods are composite beams consisting of metallic cladding tubes and ceramic pellets, which have different material properties and are significantly heterogeneous (especially the irradiated fuel). Therefore, the application of the simple beam theory in our case will simply provide information on the effective (fictitious) mechanical properties of a homogeneous beam, which deforms identically to the SNF rod. Although this analysis may not directly investigate the mechanical properties of the cladding and the pellets, it still provides valuable information, which can be used either in analytical or numerical approaches when investigating the SNF response under bending loads.

The simple beam theory of elastic bending states that:

$$\frac{M}{I} = \frac{\sigma}{y} = \frac{E}{\rho} \tag{2.3}$$

where I is the moment of inertia of the beam cross-section about the neutral axis, M is the applied bending moment, σ is the flexural stress at distance y from the neutral axis, E is the Young's modulus of elasticity for the beam material and ρ is the radius of curvature of the neutral axis at the section. Fig. 2.24 gives a schematic representation of a beam subjected to pure bending (initially unstressed and constant bending moment applied along its length) which bends to a radius ρ.

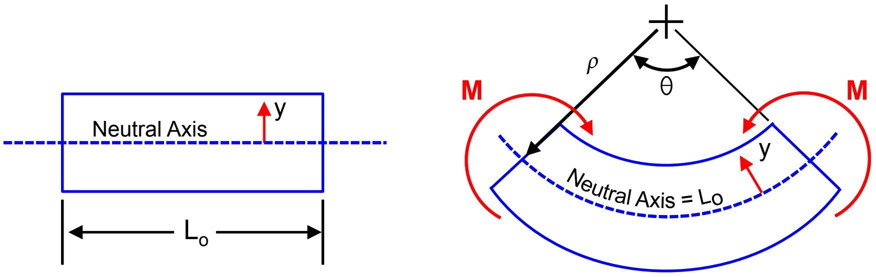

Fig. 2.24 Beam subjected to pure bending before and after the bending moment has been applied.

As a result, the flexural strain can be derived as:

$$\varepsilon = \frac{y}{\rho} \tag{2.4}$$

From Eq. 2.3 it can be noticed that if the bending moment is constant and the beam is of homogeneous material and uniform cross-section, the values of I, E and M remain constant and consequently the radius of curvature will also be constant. Under these assumptions of pure bending the radius of curvature to which any beam is bend under an applied bending moment M is given by:

$$\rho = \frac{EI}{M} \tag{2.5}$$

Therefore, ρ is directly related to the value of the quantity EI, often stated as flexural rigidity or flexural stiffness of the beam. This can provide an indication on the degree of flexibility of the beam, therefore the relative stiffnesses of beam sections can be compared to their EI values.

It has to be noted that the above derivation includes the assumption of pure bending without any shear, something that in most practical beam loading applications is not valid since they both occur together at most points [82]. However, for the three-point bending case where the load is centrally applied the shear, R, is always zero when the bending moment is at maximum, as shown in the shear and moment diagram in Fig. 2.25.

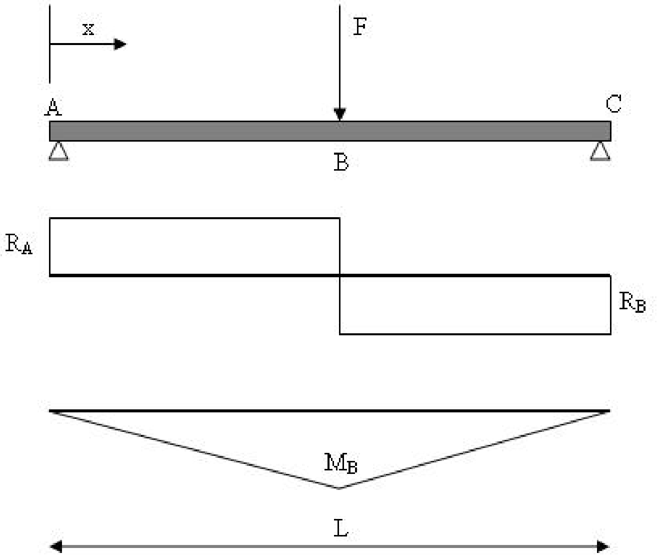

Fig. 2.25 Shear and moment diagrams for simply supported beam with central point load.

The stresses (compressive or tensile) of a beam subjected to bending are computed from the specimen thickness, the bending moment and the moment of inertia of the cross-section as:

$$\sigma = \frac{My}{I} \tag{2.6}$$

In the current study, two different beam cross-sections will be considered; the hollow circular and the circular cross-section as shown in Fig. 2.26. In both cases, the stress analysis will be performed assuming that a uniform material with the given cross-section can represent the flexural properties of the samples (surrogate or SNF) under the assumptions of the simple beam theory.

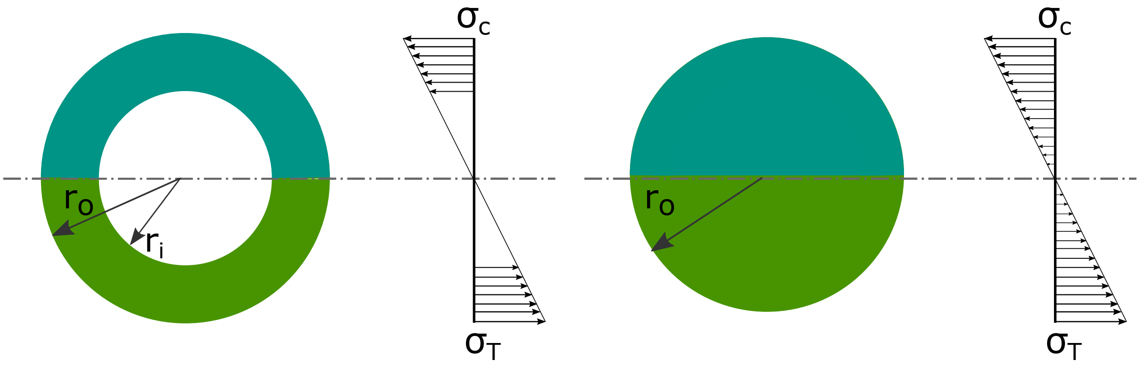

(a) (b)

Fig. 2.26 Bending stress distribution (compressive σ_c or tensile σ_T) for a) hollow-circular and b) circular cross-sections.

The moments of inertia is the sum of the products of each elementary area of the cross section multiplied by the square of the distance of the area from the assumed axis of rotation and is given as [83]:

$$I = \sum r^2 \delta A = \int r^2 dA \tag{2.7}$$

The moment of inertia for the hollow-circular and circular cross-sections along the neutral axis are given in Eqs. 2.8a and 2.8b, respectively.

$$\text{hollow-circular} \quad I_x = I_y = \pi \frac{({r_o}^4 - {r_i}^4)}{4} \tag{2.8a}$$

$$\text{circular} \quad I_x = I_y = \pi \frac{r^4}{4} \tag{2.8b}$$

The maximum tensile stress exists at the bottom specimen surface directly below the point of load application. At this point, the bending moment is equal to:

$$M = \frac{FL}{4} \tag{2.9}$$

The maximum flexural stress can be derived by substituting the bending moment and moment of inertia from Eqs. 2.6, 2.9 and 2.8.

$$\sigma_{max} = \frac{FLr_o}{4I} \tag{2.10}$$

From Eqs. 2.3 and 2.10, the maximum deflection of the beam is given as:

$$\delta_{max} = \frac{FL^3}{48EI} \tag{2.11}$$

The maximum strain at the point of maximum tensile stress can be derived from Eqs. 2.3 and 2.11 as:

$$\varepsilon = \frac{12\delta r_o}{L^2} \tag{2.12}$$

where δ is the maximum deflection of the beam or the displacement of the loading axis during the three-point bending test.

The area under the $\sigma - \varepsilon$ curve up to a given value of strain is the total mechanical energy per unit volume consumed by the material in straining it to that value, shown as follows [84]:

$$U^* = \frac{1}{V}\int F\,dL = \int_0^L \frac{F}{A_0}\frac{dL}{L_0} = \int_0^\varepsilon \sigma\,d\varepsilon \tag{2.13}$$

The area up to the yield point is termed the modulus of resilience, and the total area up to fracture is termed the modulus of toughness. The term "resilience" refers to the capacity of the material to absorb energy when it deforms elastically and upon unloading to have this energy recovered. This material property is the modulus of resilience, U_r, which is the amount of energy required to stress an unloaded beam up to the point of yielding. The modulus of resilience is derived from the triangular area under the curve up to yield point as:

$$U_r = \int_0^{\varepsilon_\gamma} \sigma\,d\varepsilon = \frac{1}{2}\sigma_\gamma\varepsilon_\gamma = \frac{1}{2}\sigma_\gamma\left(\frac{\sigma_\gamma}{E}\right) = \frac{\sigma_\gamma^2}{2E} \tag{2.14}$$

where σ_γ and ε_γ are the yield stress and yield strain, respectively. Therefore, resilient materials are those who have high yield strengths and low moduli of elasticity.

Toughness is the ability of a material to absorb energy and plastically deform up to the fracture point. For low strain rate applications, the modulus of toughness, U_T, can be derived from the area under the stress-strain curve up to the point of fracture [83]. The units are the same as the resilience (i.e. energy per unit volume of the material). A tough material is the one that shows both high strength and ductility, which is defined as the ability of a material to have its shape changed (as by being drawn out into wire or thread) without losing strength or breaking.

Finally, the energy absorbed by the sample up to fracture can be calculated from the integral of the load-displacement curve, as given in Eq.2.15. This gives the work or the energy transferred to the sample via the application of the force along its deflection.

$$W = \int_0^{\delta_f} F\, d\delta \tag{2.15}$$

Under the assumptions of the simple beam theory, the flexural stress-strain curves can be calculated with the use of the force-displacement data for given beam cross-sections. Fig. 2.27 is used as example to illustrate the type of results that will be derived to characterize the flexural response of a sample under bending loads.

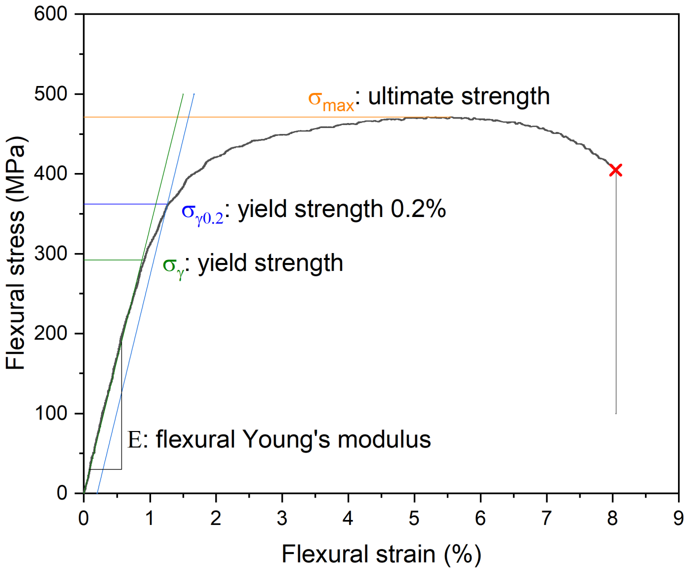

Fig. 2.27 Typical flexural stress–strain behavior to fracture for fresh Zry-4 cladding tube.

To establish a better understanding of the measurement results and derived quantities, it is of paramount importance to quantify the uncertainty associated with each measured value. Further details on the uncertainty analysis performed is given in Appendix B.

2.3 Impact or dynamic three-point bending test

Impacting is the second type of test used to investigate the mechanical properties of SNF rodlets. This experimental technique is used to study the response of SNF rods to impact loading, which is relevant to assess safety issues in various stages of the spent fuel management after discharge from the reactor. Specifically, it can be used to determine the radiologic consequences associated with an accident during SNF handling or transportation that involves fuel rod fracture and dispersion out of the cladding. A better understanding on the extent of the fuel release upon loss of cladding's integrity is relevant for the assessment of numerous postulated accident scenarios.

In 2008, the first experimental activities investigating rupture events under transient impact load were carried out at the Joint Research Centre - Institute for Transuranium Elements (JRC-ITU). A series of impact tests on irradiated SNF rod depressurized segments had been performed [15–17]. The tests were carried out in a hot-cell at ambient temperature and pressure conditions. The main objective was the assessment of the SNF rod fracturing behavior under transversal impact load conditions and the measurement of the amount of fuel material released in case of rod fracture. In particular, a possible correlation between the mass release and the burnup was examined. These first studies could address all the aforementioned subjects; however, further examination on the mechanical behavior of the SNF rodlets was not performed.

The present PhD research programme has been dedicated to further develop the experimental apparatus and to optimize the testing procedure for the study of SNF mechanical response under dynamic loads adopting a more consistent and insightful methodology. The development of a new experimental device, as well as the establishment and calibration of a new testing procedure are described in the following sections.

2.3.1 Early version of the impact tower

The first impact studies of SNF rods were carried out with the device shown schematically in Fig. 2.28. A hammer was dropped through a vertical guide tube onto a SNF rodlet fixed at its extremities on a stable metallic block. The hammer was locked at the top of the column and released by actuating the holding clamps. Two other capture clamps at the bottom of the guide tube were used to block and prevent the hammer from bouncing back after the first strike, to avoid repeated hitting onto the sample. The impact was recorded by a high-speed camera placed outside of the hot-cell. The fuel mass release was determined by weighing the sample before and after the experiment.

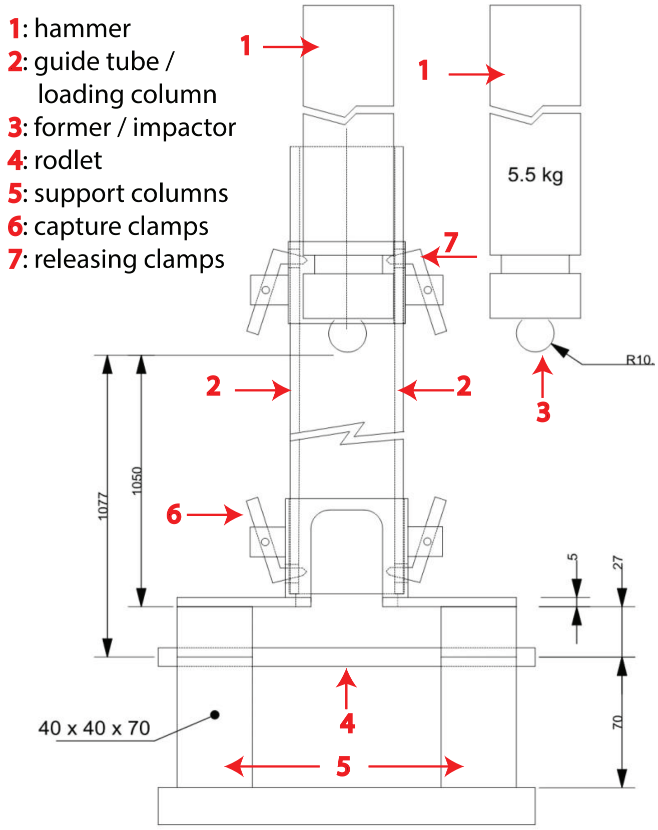
1: hammer
2: guide tube / loading column
3: former / impactor
4: rodlet
5: support columns
6: capture clamps
7: releasing clamps
1
1
5.5 kg
7
R10
2
2
3
1077
1050
6
5
27
70
40 x 40 x 70
4
5

Fig. 2.28 Schematic representation of the first version of the impact tower used in [15–17].

The photograph in Fig. 2.29 shows the experimental apparatus installed in the hot-cell. It must be noted that the image is a collage of two individual photographs; the optical parallaxes gives the impression, that the guiding tube was broken and tilted, but in reality it was straight and perfectly perpendicular to the specimen axis. The main parts of the device are highlighted. For that campaign, a hammer of 5.5 kg was used; the guide tube was made of a hollow Plexiglas cylinder of outer diameter 6 cm; the height of the column was 107.7 cm resulting to a maximum impact velocity of approximately 4.59 m/sec; the maximum frame frequency of the high-speed camera was 5000 Hz.

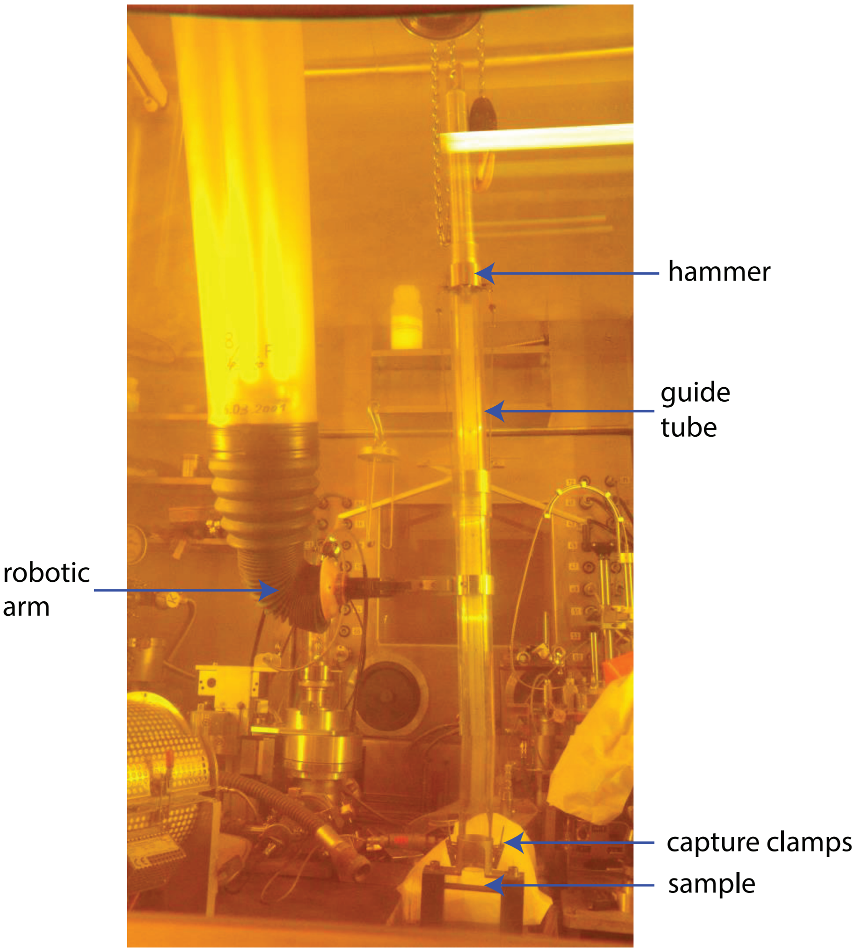

Fig. 2.29 First version of the impact tower operated at the hot-cell facilities of JRC-Karlsruhe. The optical parallaxes effect gives the impression, that the guiding tube was broken and tilted, but in reality it was straight and perfectly perpendicular to the specimen axis.

The experimental campaigned included tests on 3 PWR and 1 BWR UO_2 SNF rods, with burnup ranging from 19 to 74 GWd/tHM. Fig. 2.30 depicts selected photograms from the test performed on the sample with the highest burnup. These tests revealed some important results, extensively reported in [15–17] and briefly discussed in section 1.2.1. This campaign exposed the capabilities, potentials and possible improvements of the experimental setup for a better exploitation of this type of test. In short, two areas of improvements were identified for a possible extension and better exploitation of the test outcomes including an optimization of the testing procedure.

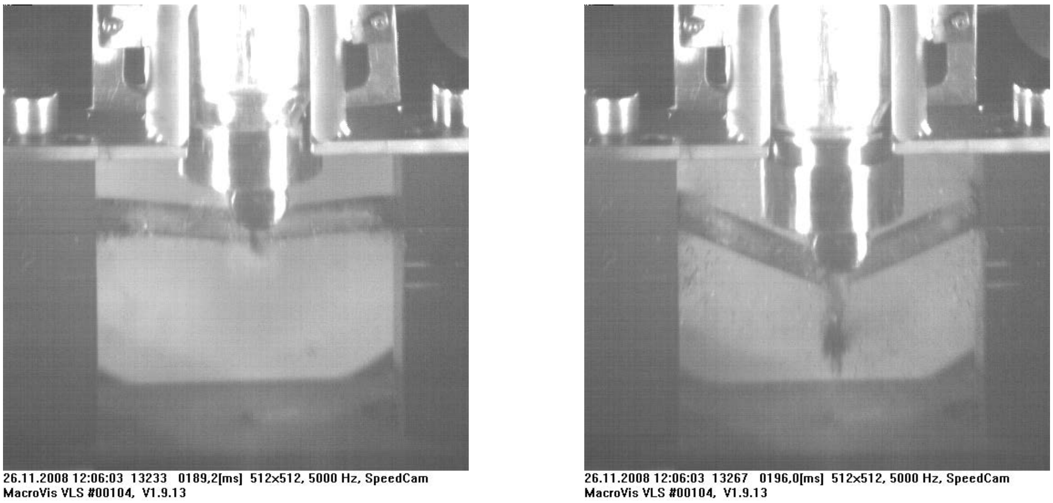
26.11.2008 12:06:03 13233 0189,2[ms] 512x512, 5000 Hz, SpeedCam
MacroVis VLS #00104, V1.9.13
26.11.2008 12:06:03 13267 0196,0[ms] 512x512, 5000 Hz, SpeedCam
MacroVis VLS #00104, V1.9.13

(a) Sample bending and first fracture.

(b) Fracture and fuel release in tree points.

Fig. 2.30 Photograms from the high-speed camera video illustrating the impact fracture of a 74 GWd/tHM PWR fuel rodlet, using the first version of the impact tower [15–17].

The first improvement refers to establishing more quantitative measurement capabilities. The first testing results consisted of the "indirect" estimation of the fuel mass release (sample weighted before and after testing), and of the visual inspection of the sample's response via the high-speed camera recording. In comparison to the three-point bending tests, there is not an explicit investigation of the mechanical response of the samples with the use of dedicated sensors or any other method that could facilitate this type of analysis. Moreover, although the use of the high-speed camera outside of the hot-cell simplified the testing procedure, the resulting images were of relatively low quality. Thus, the collected photograms could simply offer a qualitative visual inspection of the sample's response, restricting their use for a possible IA.

The second improvement area was about simplifying and optimizing some parts of the device for the use in hot cell. In particular, the need to construct a "closed" chamber to accommodate the fragments released by sample fracture was highlighted. In this way, the collection of the released mass could be maximized and the spread of the fuel fragments within the hot-cell could be avoided. Moreover, the size of the impact tower, and specifically the length of the guide column could be improved by modular design, thus facilitating the manipulation and operation of the setup using tele-manipulators.

2.3.2 Upgrade and development of a new impact device

In order to implement the improvements on the impact testing procedure and analysis, a new impact tower was constructed. The new development aimed at conducting of a series of impact tests on SNF rods for the current PhD thesis programme.

The principle of the test sequence did not change; however, all parts were modified. An overview of the new impact device is shown in Fig. 2.31. In comparison to the previous version, the impact takes place in a closed chamber and it is recorded with the use of a high-speed camera, mounted just outside of the chamber, inside the hot cell. New systems were designed to facilitate the use of the impact tower within the hot-cell, including handles for the guide tube and a release mechanism for the hammer. The bouncing of the hammer after the test is prevented with the use of a new mechanism (safety breaks). Finally, the new tower includes integrated systems for the collection of the fuel fragments and fine particles (aerosol) after each test.

Fig. 2.32 gives a better illustration of the closed chamber's geometry and of the working principle of the new impact tower, by means of a perspective view, cross-sectioned at the symmetry plane. The mounting plane for the high-speed camera offers the possibility to adjust the camera at different distances and angles. LED lights are placed inside the chamber at the left and right corners of the high speed camera window, facing the sample and providing high luminosity as needed for the recording of the impact test. The sample is mounted rigidly using two supports/holders (bottom and top). The bottom part of the chamber has a conical shape to accommodate the deflection of the sample and to facilitate the collection of heavy released fragments. Upon sample's fracture, the coarse fuel and cladding fragments are collected at the bottom of the chamber. This part is removable allowing easy retrieval and measurement of the released material. At the back, the chamber is connected to an aspiration system through particulate filters with different mesh size, where the fine particles are deposited.

Similarly to the previous device, the testing procedure consists of releasing the free-falling impactor through a vertical guide column. The impactor (or hammer) is released from the top of the column and impacts the sample laterally. A representative image illustrating the closed chamber geometry and the testing principle is given in Fig. 2.33. This is a typical view as recorded by the high-speed camera video, from an impact test performed on an unirradiated and untreated zircaloy rodlet containing alumina dummy pellets. The whole length of the sample can be observed, allowing the visual inspection of the sample's reaction and fracture point initiation and propagation both at the middle-span (under impactor), as well as at the

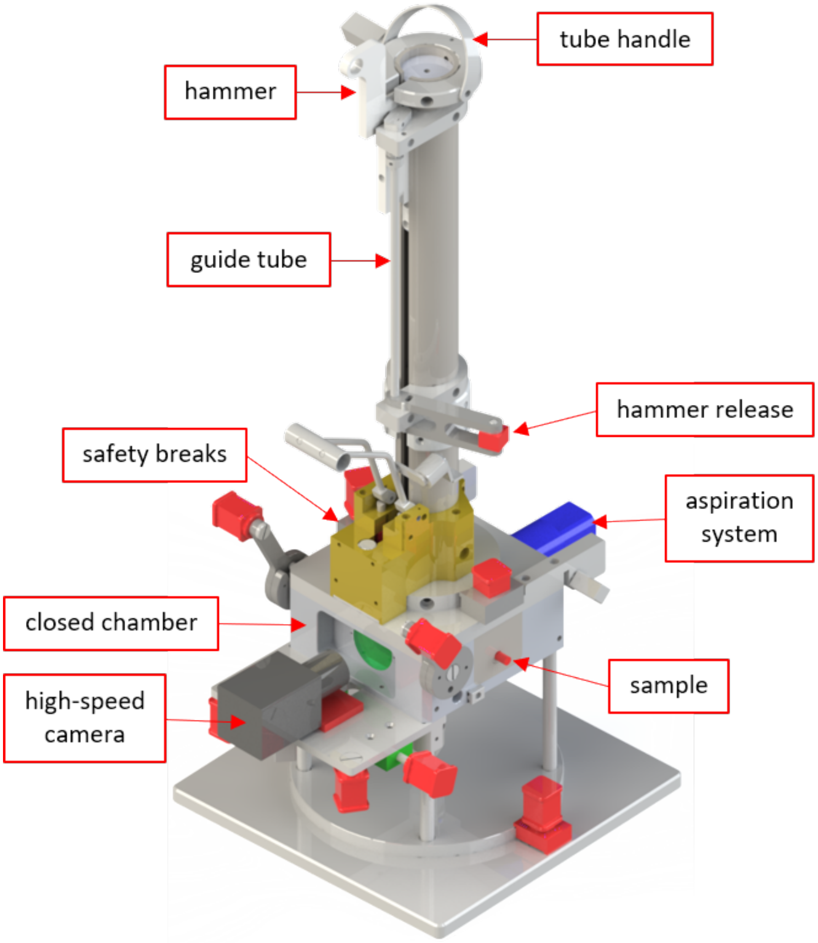
tube handle
hammer
guide tube
hammer release
safety breaks
aspiration system
closed chamber
sample
high-speed camera

Fig. 2.31 Overview (CAD model) of the impact device used for the present campaigns.

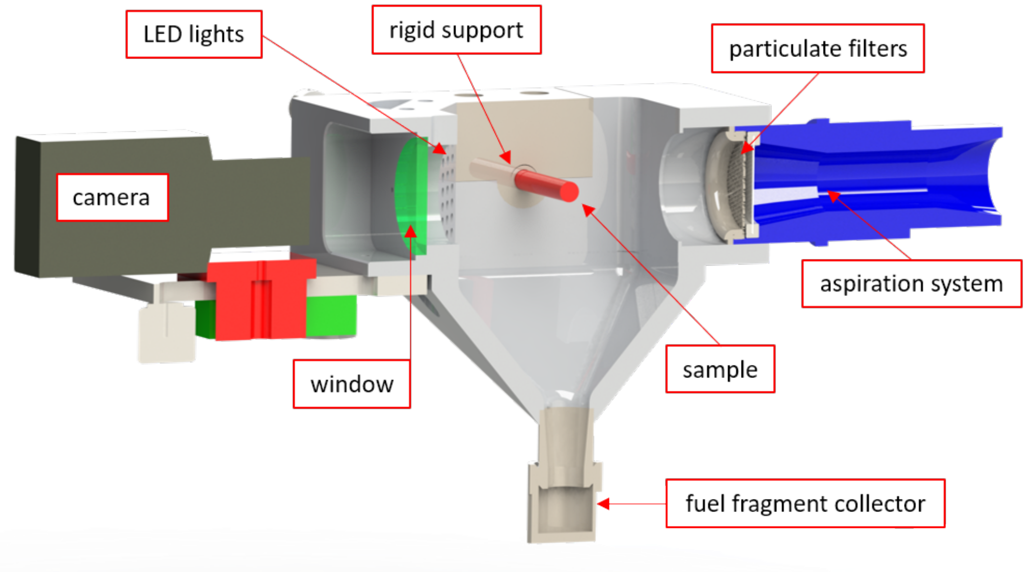
LED lights
rigid support
particulate filters
camera
aspiration system
window
sample
fuel fragment collector

Fig. 2.32 Cross section view (CAD model) of the closed chamber, illustrating the working principle of the new impact tower.

sides (fixed supports). The initial purpose of these tests was the visual demonstration of the SNF rod's response under dynamic loads and the study of the fuel mass release. Therefore, no dedicated methodology for evaluating the rod's behavior was implemented.

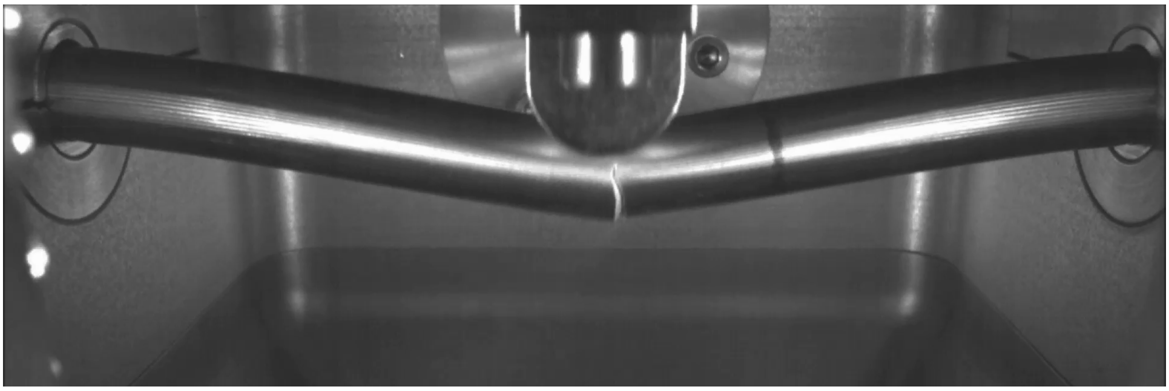

Fig. 2.33 Selected frame from a high-speed camera video illustrating the closed chamber geometry and the testing principle. The hammer impacts onto an unirradiated untreated zircaloy cladding tube containing dummy alumina pellets.

The most critical parameter in the impact test is the maximum load that can be applied, since this affects the sample's mechanical response. Although the mechanical properties of each sample differ, the objective of each experiment is to:

- reach the fracture point of each sample

- while keeping the kinetic energy of the hammer as low as possible.

In this way, the sample would break by absorbing most of the hammer's kinetic energy, resulting to a significant decrease of the hammer's velocity. This deceleration facilitates the analysis of the sample's response either when visually inspecting the recorded images or when using dedicated IA methods.

The maximum impact load (or hammer's kinetic energy) is determined by the effective drop length for the hammer's free fall and by its mass. In comparison to the previous impact device, the length of the guide column has been decreased to facilitate convenient use in the hot-cell. The effective distance between the impactor's tip and the sample is 690 mm, resulting to an impact velocity of 3.7 m/sec. Since the height was reduced, the hammer's mass had to be increased in order to obtain the sample fracturing in each experiment.

To this purpose, a sensitivity study was performed to determine the suitable fracturing mass range for both ductile and brittle materials. Surrogates of cladding tubes filled with alumina pellets (refer to section 3.1) were used for this purpose. The outcome of these tests was the introduction of a hammer with mass 3 kg higher compared to the previous design, which allows the investigation of rodlets of different properties and ductility. The new hammer has a mass of 8.55 kg corresponding to a maximum kinetic energy of 57 J at the striking moment.

The distance between the sample holders (or the effective length of the sample) is 120 mm, the same as in the previous design. The minimization of this distance allows the use of smaller samples, which is of the highest importance when working with "expensive and limited" materials, such as SNF. The impactor's diameter was changed to meet the testing requirements [12] and set equal to 15 mm. Dimensions and layout relevant for the impact test are given in Fig. 2.34, where two cross-section views and the symmetry planes are shown to illustrate the working principle of the test.

2.3.3 Revising the concept of the impact tests

In contrast to the 3-point bending apparatus, where sensors are used to record the applied load and sample's deflection, no sensors are used for the data acquisition in the impact test. The initial purpose of those tests was the visual demonstration of the SNF rod's response under dynamic loads and the study of the fuel mass release. Therefore, in the initial setup there no methodology for evaluating the rod's behavior in quantitative and systematic terms

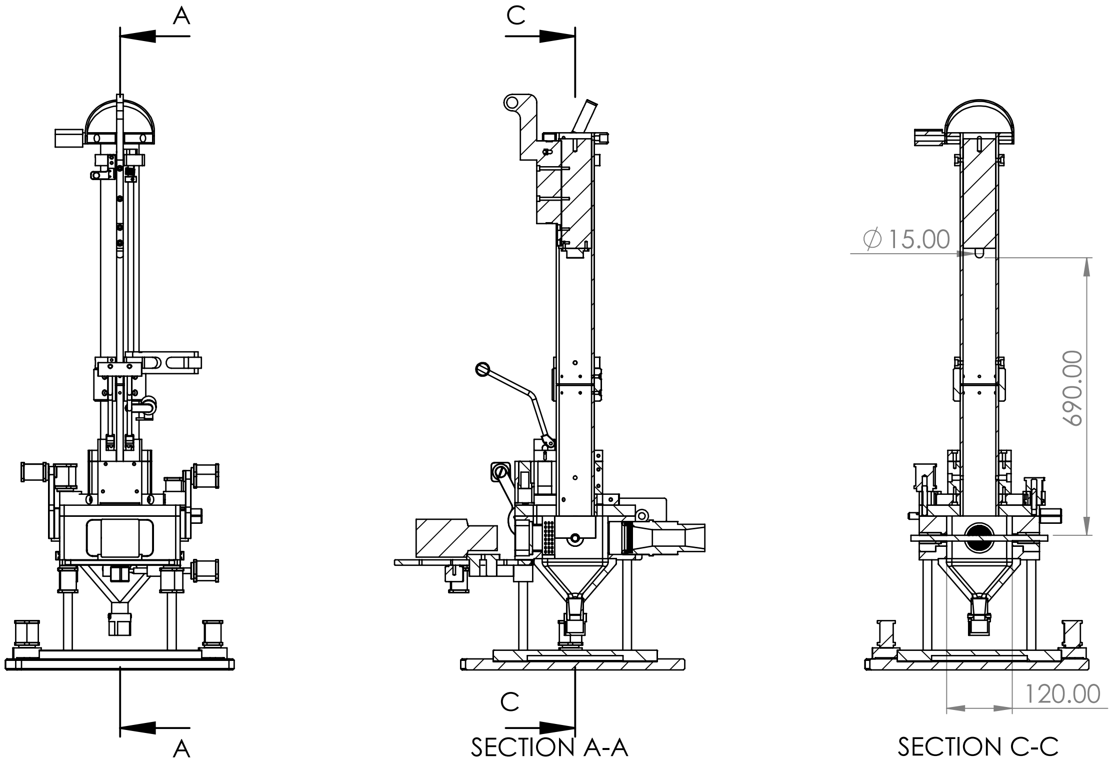
A
A
C
C
SECTION A-A
SECTION C-C
∅15.00
690.00
120.00

Fig. 2.34 Cross section view of the impact test device at the symmetry planes, illustrating the test working principle and main dimensions.

was implemented. Establishing such approach was one of the objectives of the present experimental campaign, in particular to:

1. investigate a possible correlation between quasi-static and dynamic loads;
2. develop a methodology to translate the visual representation of the rod's response into data of interest such as sample's deflection and absorbed energy.

The rationale for the first objective was to couple the 3-point bending tests with the impact tests. Since there is only a limited number of experiments that could be performed in the hot cells, the goal was to maximize the level of information produced by each test. The aim was to adopt similar (geometrical) configurations in both tests, to facilitate comparisons and allow the investigation of potential correlation (if any) affecting various material properties of the composite fuel/cladding system, such as the Young's modulus, the yield stress, etc. This was achieved by redesigning the closed chamber configuration of the impact tower.

The second objective was to provide a solid scientific basis for evaluating the sample's response by utilizing the capabilities of the available device. Due to the fact that in contrast to the 3-point bending test setup no sensor is used, the development of a methodology to perform image analysis of the obtained video during the impact sequence was prioritized. Implementing such analysis was a challenging task due to various reasons, including the fact that such an analysis was not initially foreseen and both hardware setup and camera specifications were not optimized for it.

In order to establish a direct comparison of the experimental results between the three-point bending and the impact test, the closed chamber geometry was modified. In particular, the top and bottom holders (or half ring clamps) providing the fixed support to the sample have been replaced with new ones, which reproduce the geometric characteristics of the three-point bending test. Fig. 2.35 gives a cross-sectioned view of the new chamber using a 3D CAD model. New rounded supports have been placed at the sides of the chamber allowing free moving of the sample, similarly to the three-point bending test. In order to "seal" the new chamber, two rubber plates have been fixed at the sides of the chamber; however, they have been sectioned to allow the axial movement of the sample upon/during deforming/impacting.

The new type of rounded supports used, is shown in detail in Fig. 2.36. The support has a concave surface, upon which the sample is placed. The diameter of this surface is 11 mm to accommodate samples from both PWR and BWR SNF rods. The effective diameter of the support is 30 mm, the same as in the three-point bending device.

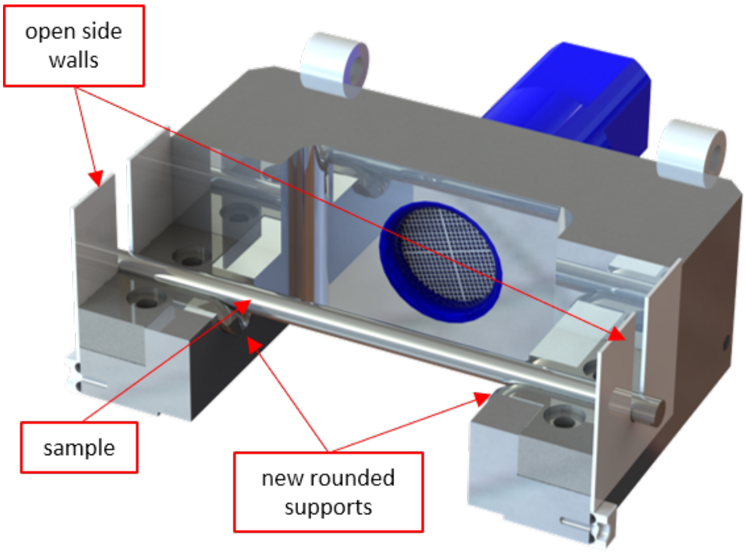
open side walls
sample
new rounded supports

Fig. 2.35 Cross section view (CAD model) of the modified chamber, highlighting the new rounded supports and side walls.

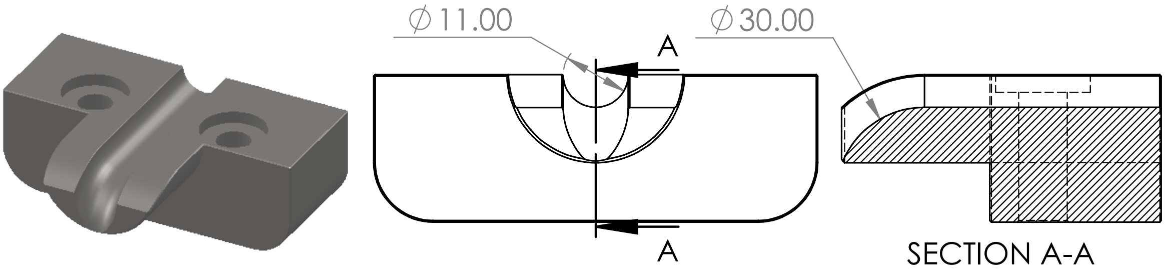
∅ 11.00
∅ 30.00
A
A
SECTION A-A

Fig. 2.36 Technical drawing of the new rounded support, highlighting its main dimensions.

Fig. 2.37 shows the front-view of the new chamber, using a cross section at the symmetry plane of the sample to illustrate the main dimensions of the new impact-loading configuration. With the new supports, the new effective length of the sample increases to 10 mm, similarly to the three-point bending test. As a result, both tests are sharing the same loading geometrical configuration, which enables the direct comparison of the experimental results. Therefore, it is now possible to investigate a possible correlation on the flexural properties of the composite fuel/cladding system under quasi-static (bending) and dynamic (impact) loading conditions. The main dimensions of the new impact tower are given in Fig. 2.38.

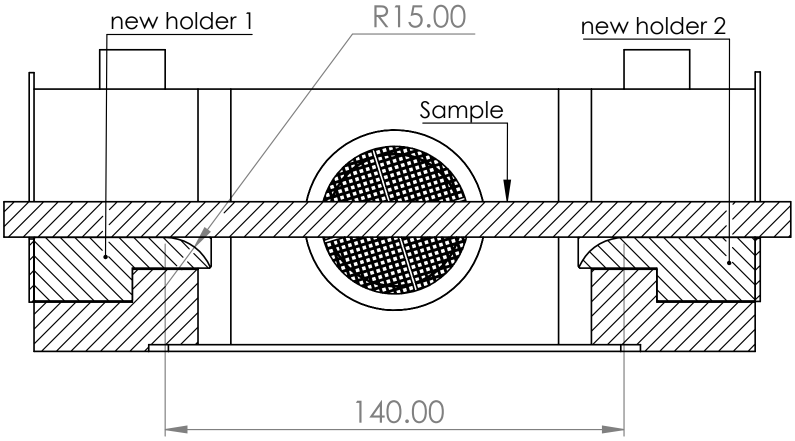

Fig. 2.37 Cross-section view of the new chamber, at the symmetry plane of the sample, illustrating the main dimensions of the new loading configuration.

Although the loading configuration was altered, the objective of the impact test remains the same, which is to reach the fracture point by transmitting as low kinetic energy as possible from the hammer to the sample. The effective height of the guide tube and the diameter of the impactor did not change; therefore, the only parameter that could affect the response of the sample is the mass of the hammer.

For this reason, a new sensitivity study was conducted using surrogate cladding tubes filled with alumina pellets to determine the suitable mass range for both, ductile and brittle samples. Only a limited number of tests were performed, since the device was already installed in the hot-cell. Nevertheless, it was observed that higher impact energy is needed in order to deflect and fracture the samples in the new setup. This is attributed to the fact that the energy is now transmitted over the whole length of the sample and not only to its effective length as before using rigid supports. In particular, the ends of the sample with the attached end-plugs extruding from the testing chamber will move upwards upon impacting. For this reason, the mass of the hammer had to be increased.

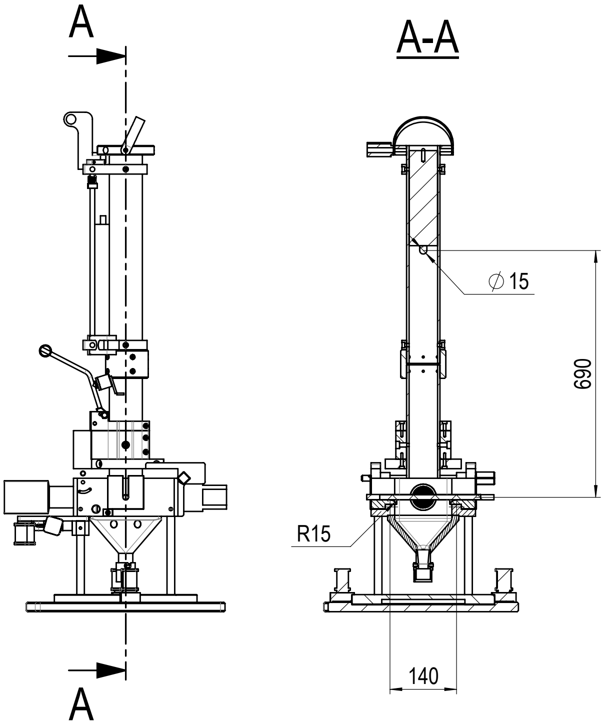

Fig. 2.38 2D drawing and main dimensions illustration of the revised impact tower.

The outcome of this campaign was the development of new hammer with a modular design, where its mass can be varied. The new hammer could be adjusted to either 8.5 kg, the same mass as used in the previous version, or to 10.5 kg. This results to a maximum impact energy of 73 J and impact velocity of 3.7 m/sec. The following Table 2.1 provides the main dimensions of the major components and the symbols and designations associated with the bending test results.

2.3.4 High speed camera monitoring and image analysis

The new impact loading geometry is matching the geometrical characteristics of the three-point bending test device, allowing studying the flexural properties of SNF rods at different strain rates. A high-speed camera yields a sequence of high-resolution images over a total collection time of around 1 s. The recorded video illustrates the sample's response in the impact tests. An example of an image sequence during impact is shown in Fig. 2.39. A set of frames is selected to illustrate the deflection and fracture of a SNF rod segment [24].

---

[2] where, $t.d.$: test dependent

Table 2.2 Main dimensions and description of symbols used for the impact test.

Symbol	Designation	Dimension	Unit
D_i	Diameter of the former	15	mm
R_i	Radius of the supports	15	mm
l_i	Min distance between supports	140	mm
M_1	Mass of the hammer 1	8.5	kg
M_2	Mass of the hammer 2	10.5	kg
H	Free-fall height of hammer	690	mm
a	Diameter of the test piece	$t.d.^2$	mm
L_i	Length of the test piece		mm
a_i	Angle of bend		degrees
f_i	Displacement of the former		mm

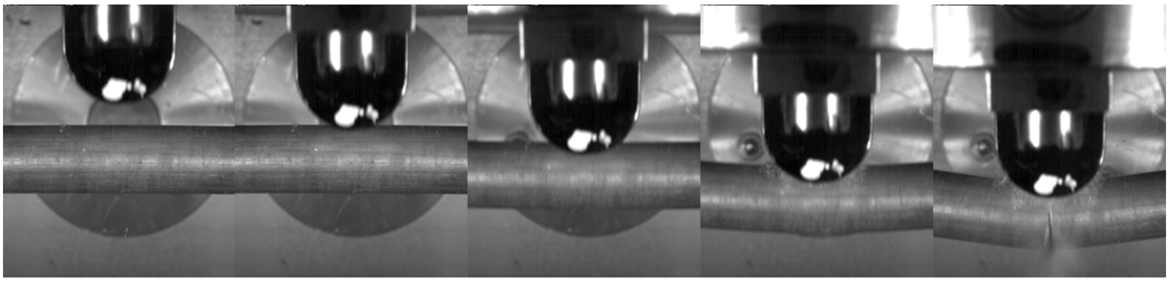

Frame 1 Frame 2 Frame 3 Frame 5 Frame 6

Fig. 2.39 Representative selected frames of the image sequence during an impact test.

From the observation of the sample deflection under dynamic loads, a valuable understanding of various phenomena is possible [85]. Nevertheless, an IA methodology was developed to convert the obtained video/images into convenient data, namely instantaneous sample deflection and impactor velocity per frame (i.e. time). Such analysis is of paramount importance since it provides (a) the means to compare material properties of SNF rods against strain rate (correlation to quasi-static case) and (b) the essential input needed for the FEM calibration against the experimental results.

The development of the IA methodology demanded an unconventional effort, as it was not initially foreseen [15], therefore, both hardware setup and camera specifications were not fully optimized for this type of data extraction. Concomitant deficiencies had to be overcome by other means. The following paragraphs describe the assumptions made in the development of the IA methodology.

The image analysis of the video frames is divided in two separates, but equally important, domains:

1. Spatial calibration of the impact sequence images.
2. Object tracking performed through dedicated image analysis software.

The obtained images provide a 2D projection of the 3D space. Thus, a correlation has to be defined to map geometrically each point onto the image plane. This process is referred as image calibration and provides a correlation between pixel position and “real-world” dimensions of the experimental device.

The object tracking gives the position of the impactor in each single frame. The procedure consists of applying a sequence of filters on the selected frames to be examined, as needed to enhance the visibility/contrast of the tracking object on the image. Both procedures can be performed independently; but both are essential to derive quantitative results.

Image calibration

To perform the image calibration, the so called “pinhole camera model” has been used. This basic model, based on the perspective projection principle, which obtains u coordinates of an image point as a non-linear function of the point in the 3D global coordinates system and the extrinsic and intrinsic parameters, is given in Eq.2.16:

$$u = P(X, \theta) \tag{2.16}$$

where $u = (u, v)^T$ are the point coordinates in the 2D image coordinate system, $X = (x, z, y)^T$ the point coordinates in the 3D global coordinate system and $\theta = (\theta_{int}, \theta_{ext})^T$ a vector with the intrinsic and extrinsic camera parameters. In brief, the intrinsic parameters allow a mapping of camera coordinates and pixel coordinates in the image frame. The matrix of intrinsic parameters does not depend on the scene viewed. So, once estimated, it can be re-used as long as the focal length is fixed (in case of zoom lens). The extrinsic parameters define the location and orientation of the camera with respect to the world frame. It is used to describe the camera motion around a static scene, or vice versa, rigid motion of an object in front of a still camera [86]. The perspective projection principle for camera modeling is shown in Fig. 2.40.

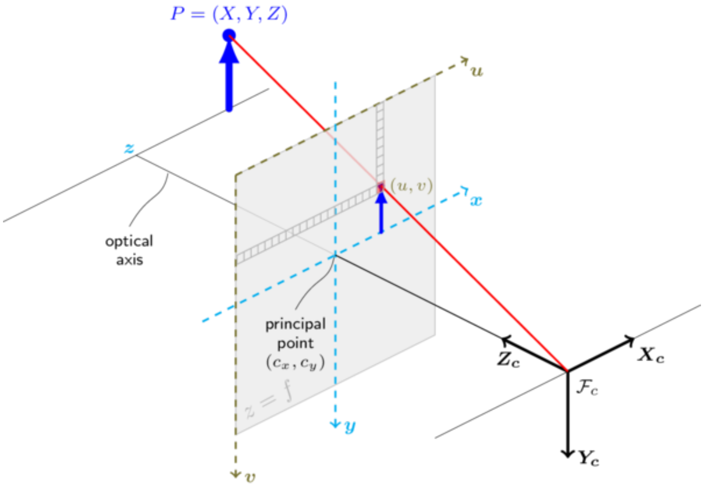

Fig. 2.40 Perspective projection of pin-hole camera model without distortion [18].

From Fig. 2.40 the coordinates of an image point may be expressed by means of Eq.2.17 and Eq.2.18 [86].

$$u(px) = X_p \cdot dx(\frac{px}{mm}) + C_x(px) \tag{2.17}$$

$$v(px) = Y_p \cdot dy(\frac{px}{mm}) + C_y(px) \tag{2.18}$$

These equations are used to calibrate the high-speed camera and evaluate the displacement of the hammer in each frame. In principle, the equations can formulate the well-known expression of the pin-hole camera model in homogeneous coordinates [87] as shown in Eq.2.19, where PTM is known as the perspective transformation matrix. The terms of this matrix are a linear combination of the considered intrinsic and extrinsic parameters, as shown in Eq.2.20 [86]. Eq.2.20 allows us to obtain the 2D screen coordinates that correspond to a 3D point, the coordinates of which can be known in the global coordinate system.

$$s\begin{bmatrix} u \\ v \\ 1 \end{bmatrix} = PTM \begin{bmatrix} Z \\ Y \\ Z \\ 1 \end{bmatrix} \tag{2.19}$$

$$PTM = A\left[R|t\right] = \begin{bmatrix} a_u r_{11} + u_0 r_{31} & a_u r_{12} + u_0 r_{32} & a_u r_{13} + u_0 r_{33} & a_u t_x + u_0 t_z \\ a_v r_{21} + v_0 r_{31} & a_v r_{22} + v_0 r_{32} & a_v r_{23} + v_0 r_{33} & a_v t_y + v_0 t_z \\ r_{31} & r_{32} & r_{33} & t_z \end{bmatrix} \tag{2.20}$$

A way to derive the PTM is to calibrate the camera using dedicated software. Camera calibration is the process of estimating this matrix using images of a special calibration pattern. One of the most common examples is to use the "Camera Calibrator" application of MATLAB [88]. This application basically selects a number of images (usually 10-20) in which a pattern of black/white squares of known dimensions are placed in the space in different orientations. The application can recognize the checkerboard pattern and by giving the dimension of each square, the PTM can be estimated.

In our case, this pattern could be attached to the impactor and several images could be acquired by recording a video of the impactor's drop without having a sample in the closed chamber. Then, the camera parameters could be used to remove lens distortion effects from the images and measure planar objects, allowing an accurate calculation of the sample's deflection or impactor's displacement. An example of a distorted and non-distorted image is given in Fig. 2.41.

Unfortunately, since the test rig was already installed at the hot-cell and the potential of image analysis was not foreseen, the application of standard calibration methods was essentially impossible necessitating the development of an alternative method to generate the image calibration of the recorded videos. In addition, since the PTM is related to parameters,

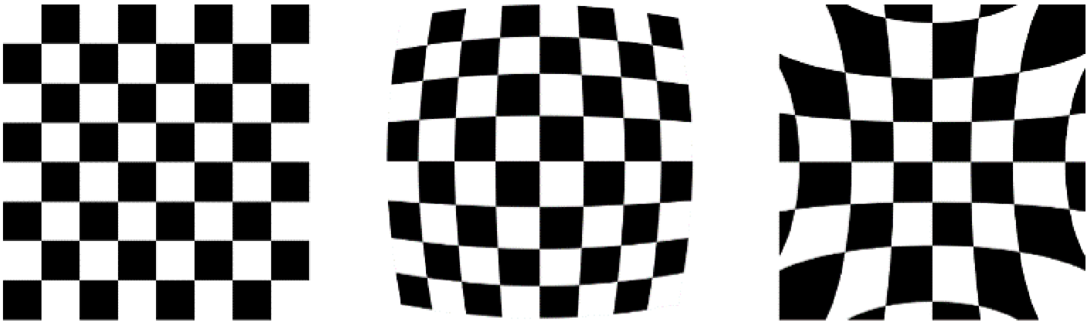

(a) no distortion (b) positive radial distortion (c) negative radial distortion

Fig. 2.41 Comparison of non-distorted image against images of common type of radial distortions.

such as the camera position, orientation and focus, this method cannot be applied retroactively to tests that had already been performed.

Applied image analysis

The following paragraphs describe the methodology developed and applied for the high-speed imaging spatial calibration, aiming to correlate each pixel to real word coordinates. This method is based on the principle of utilizing the perspective projection effect of objects with known dimensions in different positions within the acquired images.

In other words, since the camera position for each single test is fixed, the camera parameters can be derived from the dimensions of well-known/measurable object sizes in the images. Considering their length variation with regard to their position in the image and since all images have the same dimension and camera view, perspective effects are determined and used to correct the original images.

In our case, as shown in Fig. 2.39, for each impact test a sequence of images is obtained, which show the impactor position as it moves along the vertical axis defined by the guiding tube, but also include other static objects. To perceive the impactor's position in "pixel" coordinates, the side view of the closed chamber as provided by a cross-section at the symmetry plane of the sample, is shown in Fig. 2.42. Three axes are highlighted in black, red and blue, giving the movement of two different planes of the impactor and of the sample's symmetry plane. To interpret those three planes, a drawing of the impactor along with its main dimensions is shown in Fig. 2.43.

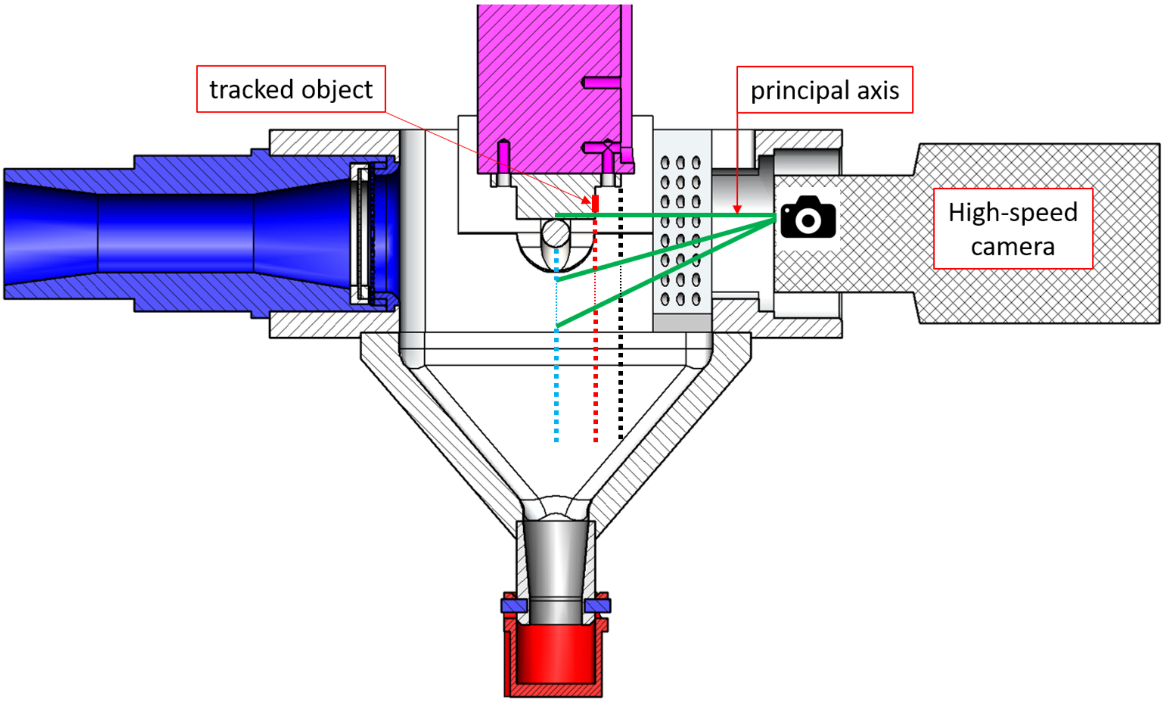
tracked object
principal axis
High-speed camera

Fig. 2.42 Sectional side view of the geometrical configuration of the impacting chamber showing a cross-section on the symmetry plane. The effect of the impactor's prospective projection is shown by highlighting axes, along which the object with known dimensions moves (in red and black).

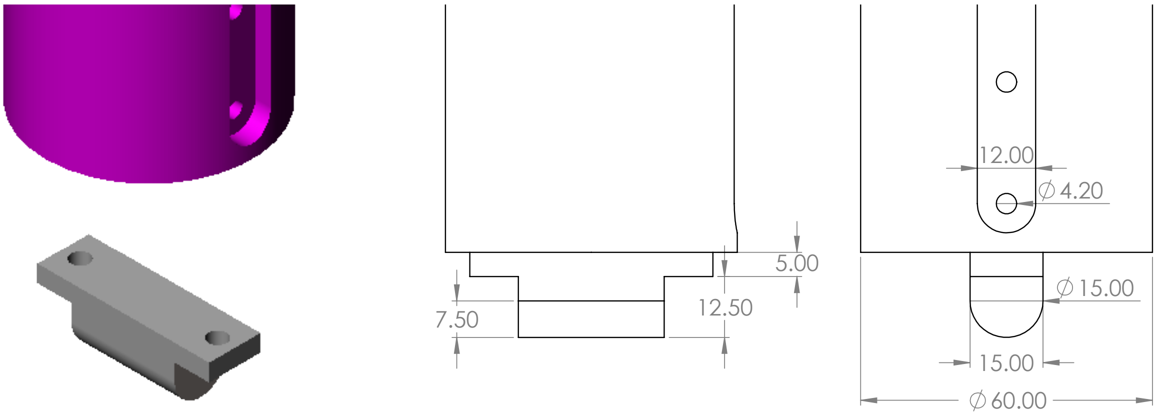
5.00
7.50
12.50
12.00
∅ 4.20
∅ 15.00
15.00
∅ 60.00

Fig. 2.43 Technical drawing of the impactor including basic dimensions.

The sample's deflection could be calculated by tracking a distinct object, namely a designated mark at the front view of the impactor, as shown in Fig. 2.44. This object is hand-drawn, it has an irregular white shape against a black background, and it is located on the red plane indicated in Fig. 2.42.

This approach relies on a major, realistic assumption that:

> the sample moves/deflects (at the symmetry plane) at the same rate as the object on the impactor, independently of its position with regard to the symmetry plane.

This approach also assumes stress equilibrium along the sample, which might not be valid for stiff materials (such as SNF rods) and at the early stages of high strain deformations (which occur during an impact test). In the reality, this approach calculates the impactor's displacement rather than the sample's deflection. Recent studies have proven that the loading point velocity and the velocities of points along the symmetry plane of the sample (e.g. points A and B as shown in Fig. 2.44) can vary slightly [89], but the frequency used to acquire the images is relatively low and the assumption of established stress equilibrium should be valid.

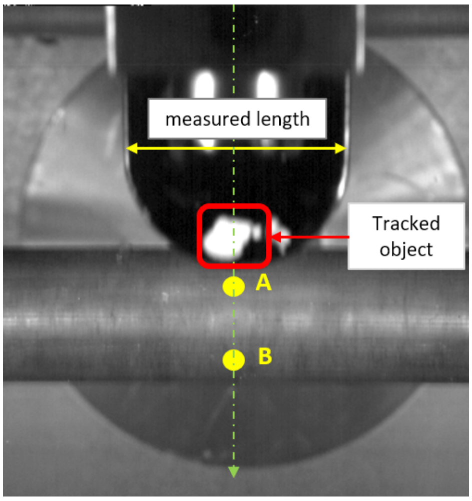

Fig. 2.44 Basic principles on which the image analysis methodology was built. The loading point velocity is calculated by tracking an object drawn at the front view of the impactor. In addition, points A and B are considered to have same directional velocities.

Applied spatial calibration

The calibration is performed by measuring the length variation in each frame of the lower horizontal axis of the impactor. This is the plane where the tracked objected is drawn which moves along the “red” highlighted axis shown in Fig. 2.42. The measured section is indicated in Fig. 2.44 and calculated in different axial position along the movement of the impactor.

Fig. 2.45a gives the length of the measured section in different axial positions, expressed in units of pixel. It is observed that the length reduces as the hammer moves towards lower axial positions which indicates that the impact takes place below the principal axis (refer to Fig. 2.42). In other words, the distance between the impactor and the high-speed camera increases from the time that impact takes place. A linear fit is used to get the section length variation within the selected range of interest.

The transformation of the pixel size into units of length can be performed by dividing the measured values to the known length of this section (refer to Fig. 2.43). Fig. 2.45b gives the spatial calibration of the image, where the pixel size is derived in units of mm, at different axial positions. This calibration is valid and can be applied on the pixel size at the close vicinity of the impactor’s symmetry plane. Since the high-speed camera is positioned on this plane, any radial distortion effects are canceling out when working within this region. For this reason, this calibration can be used upon applying the object tracking method, which gives the centroid position of the followed object in different axial position, but along or very close to the impactor’s symmetry plane.

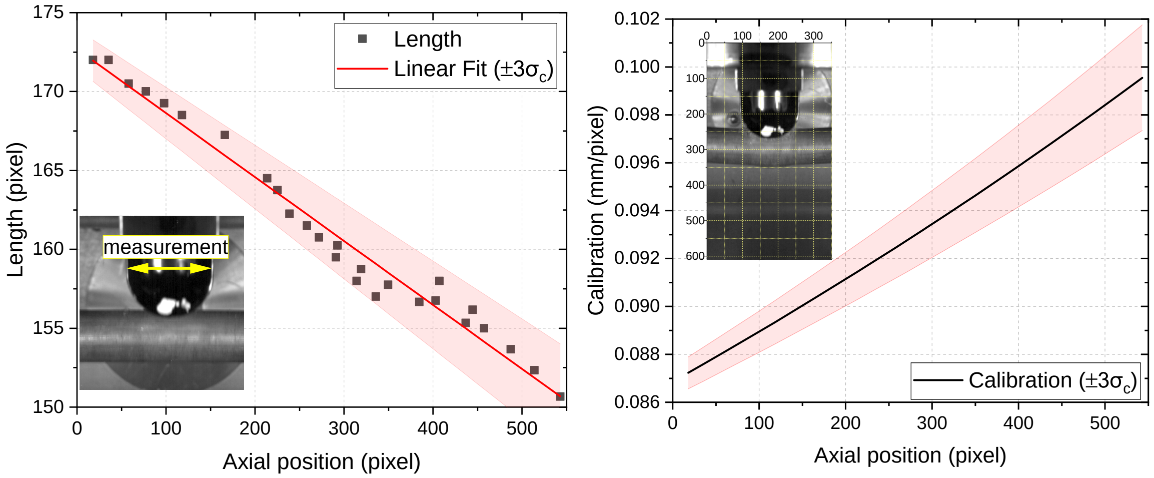

(a) (b)

Fig. 2.45 Spatial calibration process of frames acquired from the high-speed camera. (a) Linear fit of measured section lengths in different axial positions. (b) Transformation of pixel sizes, along the symmetry and in different axial positions, to “real-world” dimensions (mm).

Object tracking

The Image-PRO software [90] is used to track the object drawn on the impactor. The process followed for this purpose is given in Fig. 2.46. The concept relies on the application of a series of filters on the images in order to isolate and enhance the visibility of the tracked object (Fig. 2.46b). Consequently, the centroid position of the object can be determined in units of pixel in each frame (Fig. 2.46c). The connected green dots give the position of the object in all selected frames during the impact sequence. The thin line in Fig. 2.46d shows the trajectory of the object which moves along the symmetry plane of the impactor and, therefore, legitimates the application of the spatial calibration method.

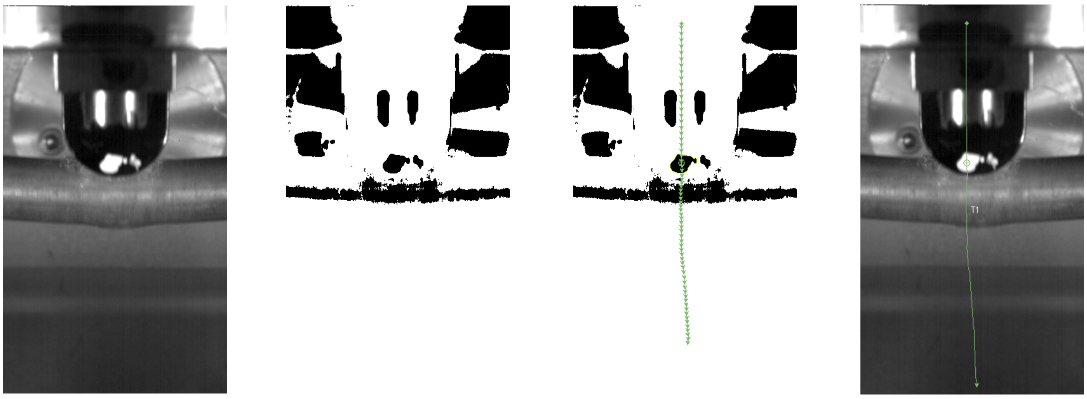

(a) (b) (c) (d)

Fig. 2.46 Object tracking procedure, from the raw data to the final result, obtained with the use of Image-PRO.

Applied image analysis results

Typical results of the developed IA methodology are presented in Fig. 2.47. In Fig.2.47a, the data points in black represent the axial position of the tracked object's position per frame before the application of the spatial calibration (pixel unit length), while the red data point show the information converted into "real-world dimensions (mm unit length). Subsequently, characteristic quantities can be further derived from these data, i.e. the hammer's instantaneous kinetic energy, acceleration and impact load.

Fig. 2.47b provides the same information, plotted in normalized units. This representation of the data highlights the effect of the spatial calibration and gives an indication about the axial position of the principal axis (refer to Fig. 2.42). A point exists where the relative changes of the raw and transformed data are matched. The impact takes place after this point, which facilitates the IA analysis, since the distance of the tracked object will always be increasing from the camera.

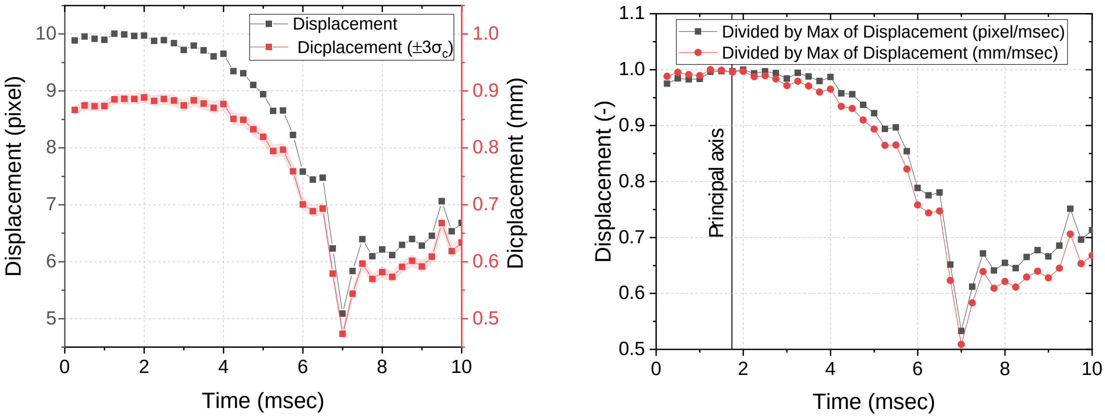

(a) (b)

Fig. 2.47 (a) Application of spatial calibration upon object tracking results and (b) normalized IA results highlighting the impact of the spatial calibration.

An indication on the validity of the results is provided in Fig. 2.48, where the velocity of the loading point in each frame is plotted. Considering the effective height of the hammer's free-fall (refer to Table 2.2), the theoretical maximum velocity at the point of contact with the rodlet is 3.68 m/sec. The calculated velocity upon application of the IA methodology is derived as 3.55 mm/sec, and is considered to be realistic when taking into account the friction between the hammer and the guide tube. The two vertical blue lines delimit the time range where the impact takes place. From the time of contact, the velocity decreases until a minimum value when the cladding cracks. After this point the resistance of the sample decreases and consequently the hammer's velocity increases. The kinetic energy loss of the hammer or the critical fracture energy can be calculated from the integral of the curve at this highlighted range.

To sum up, the new IA methodology has been successfully developed and applied to analyze the mechanical response of samples in impact tests. A preliminary validation has been demonstrated; however, a short experimental campaign was designed to provide a better understanding and to validate the experimental results as derived from the IA methodology (refer to section C).

2.4 Summary

In the current chapter, the design of the experimental campaign and setup for the study of the mechanical performance of surrogates and SNF rodlets was presented. The development pro-

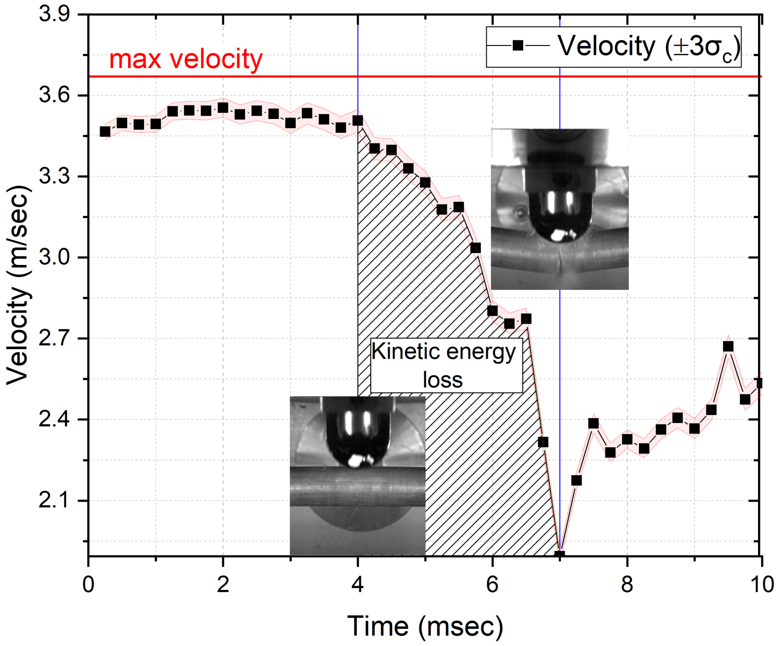

Fig. 2.48 Typical result of the application of the IA methodology, describing the impactor's loading point velocity per frame.

cess of the three-point bending test device was described. Efforts were made to automate the testing process and eliminate systematic errors observed in the resulting data. Three sensors were installed for the online measurement of the sample's internal pressure, applied load and deflection. The raw data consist of load-displacement curves providing a fundamental insight on the flexural properties of the fuel/cladding system under quasi-static loads.

The development of the impact test device was also described. The objectives for the redesign and construction of a new experimental apparatus were to facilitate the testing process within the hot-cell and to expand the acquisition capabilities of the device. An important improvement of the current experimental campaign, compared to former tests, is the acquisition of the capability for investi- gation of various material properties of the composite fuel/cladding system, comparing and integrating between quasi-static and dynamic loads. This was achieved by introducing a closed impact chamber configuration at the bottom of the impact tower, by redesigning the sample support system (by replacing the former rigid holders with rounded supports) and by having the same support radius and sample's effective length as in the three-point bending test apparatus.

Finally, the development of a new methodology was presented, which translates the visual representation of the rod's response into quantitative experimental data such as sample's instant deflection and absorbed energy. The analysis is based on IA principles and a first partial validation was demonstrated. The resulting data are of paramount importance, since they provide not only a direct comparison against the quasi-static results, but also the necessary information for the development and validation of numerical models (refer to section 5).

Chapter 3

Experimental investigations on surrogate samples

Abstract *The first phase of the experimental campaign consists of analogue tests on surrogate samples. The objectives of those tests are to investigate the mechanical properties of hydrogenated Zry-4 claddings and to further develop and optimize the experimental devices. The sample characteristics and their preparation for the conduction of the tests are presented. In addition, the flexural response of as-received and hydrogenated Zry-4 claddings from three-point bending testing is described. The Euler-Bernoulli beam theory is used to derive flexural stress-strain curves for different beam cross-sections. Finally, the main findings from two impact tests on fresh and hydrogenated claddings are discussed.*

3.1 Surrogate samples properties

The objectives concerning the sample selection for the analogue tests with surrogate rods are:

- to eliminate geometrical and material uncertainties to facilitate testing calibration and
- to investigate the influence of the hydride content and orientation on the mechanical performance of the cladding.

The surrogate rods consist of fresh and hydrogenated Zry-4 cladding tubes filled with high purity aluminium oxide (alumina) pellets. The initial mechanical properties and impurities' concentration of all cladding tubes are known before they undergo hydrogenation. A schematic representation of the surrogate rodlet, annotated with the main sample dimensions, is given in Fig. 3.1. The Zry-4 cladding tubes used in the present study had an outer diameter (OD) of 10.75 mm with wall thickness of 0.725 mm and length of 298 mm.

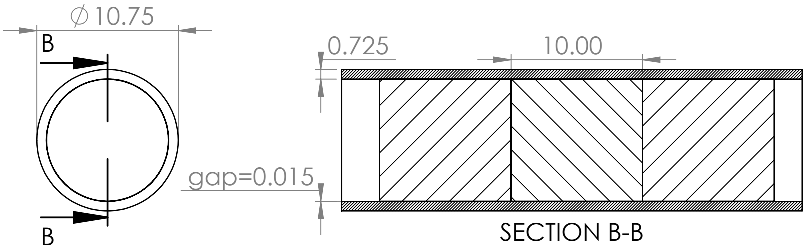

Fig. 3.1 Technical drawing illustrating main dimensions of the surrogate rodlets used in the analogue studies.

The alumina pellets, being ceramic material, share common properties with the uranium dioxide (asymmetrical strength in the plane of principal axes [91]) and have also been used in different studies to model the pellet behavior [92, 16]. Pellets of two different dimensions have been used to reproduce geometrical characteristics of irradiated rods by creating gaps of different sizes. Smaller and bigger pellets with diameter of 9.15 mm and 9.27 mm respectively, were used to simulate gaps corresponding to fresh (or low burnup) and medium-high burnups fuel rods. An overview of the pellet and cladding dimensions is provided in Table 3.1.

Table 3.1 Geometric dimensions of the surrogate samples consisting of pellets and cladding used in analogue studies.

Component	**Designation**	**Dimension**	**Unit**
Pellet	Length	10	mm
	Diameter 1	9.27	mm
	Diameter 2	9.15	mm
Cladding	Length	280	mm
	Outer diameter	10.75	mm
	Inner diameter	9.30	mm
	Gap 1	0.015	mm
	Gap 2	0.075	mm

The main material properties of the dummy pellets and claddings (before hydrogenation) are known. Although the alumina pellets do not share the exact same properties as unirradiated UO_2pellets, they lie within the same range. Knowing the material properties of the samples is of paramount importance, since they provide the reference values for the test calibration. In addition, this is essential for the calibration of the numerical models, which are to be performed with the use of the surrogate samples in order to eliminate this source of uncertainty. The main mechanical properties of the cladding and pellets are listed in Table 3.2.

Table 3.2 Mechanical properties of cladding and pellet samples used in analogue studies.

Mechanical properties	**Specific value (actual value)**	**Unit**	**Comments**
Pellets			
Bending Strength	350	MPa	DIN EN 843-1
Compressive Strength	3500	MPa	
Young’s Modulus (static)	380	GPa	
Poisson’s Ratio	0.22		
Zry-4 Cladding (fresh)			
0.2-Yield Strength	≥350 (502)	N/mm^2	
Tensile Strength	≥480 (663)	N/mm^2	ASTM-E 21-92
Elongation A5O mm	≥15 (23)	%	

The hydrogenated cladding samples were provided by the Institute of Applied Materials (IAM) of the Karlsruhe Institute of Technology (KIT). The hydrogenation method is described in [93]. In short, the sample enters into a furnace (LORA furnace hydrogenation facility [94]). The hydrogenation process occurs in a mixture of hydrogen/argon with hydrogen partial pressure at 0.1bar. The initial temperature and cooling rate applied in the furnace varies depending on the final desired hydride concentration and orientation. The hydrogenation duration is 2 to 12 min. After this process the specimen is withdrawn and cooled in atmospheric conditions.

The samples used for the analogue studies have been hydrogenated at temperatures of 550°C, 650°C and 750°C, respectively. Fig. 3.2 shows the hydride orientation of two samples with identical hydrogen content, but different hydrogenation conditions. At higher temperature, more randomly oriented hydrides could be formed.

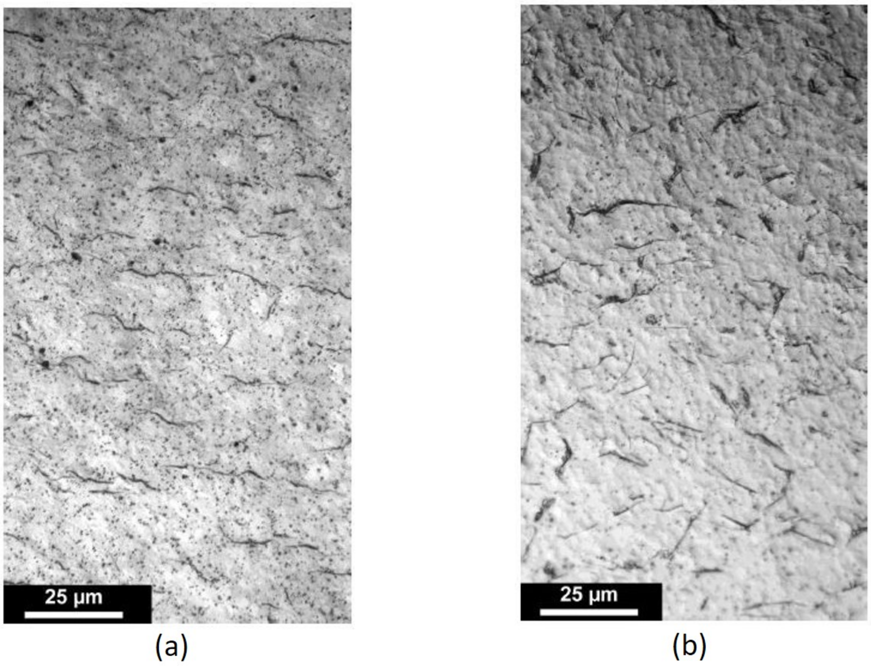

Fig. 3.2 Influence of hydrogenation process on Zr hydride orientation; a) 550°C, $t_{hydrogenation}$= 60 s, hydrogen 330 wppm: circumferential orientation of hydrides, b) 750°C, $t_{hydrogenation}$= 30 s, $t_{annealing}$ =600 s, hydrogen 330 wppm: random hydride orientation.

3.2 Sample preparation

The main concept of the sample preparation for the cold test campaign was to investigate the surrogate material performance by attempting to reproduce similar working conditions as in the case of the real irradiated rodlets. In addition, all parameters that could potentially influence the mechanical performance of the surrogate rodlets were kept constant, in order to perform a parametric study on the relative importance of the hydrogen content/orientation on the cladding's response.

Fig. 3.3 gives a not to scale schematic representation of the surrogate samples as prepared for the cold test campaign. The hydrogenated cladding tubes were filled with alumina pellets and a spring was used at one end, to fix the pellets and accommodate the stresses resulting from the pellet movement during bending.

All samples were pressurized to 40 bar with helium gas and sealed at both ends with end-plugs. The selection of this internal pressure of the samples is based on experience accumulated at the JRC-KA through numerous puncture test measurements on irradiated commercial fuel rods. In addition, it is based on the end-of-life (EOL) rod internal pressure

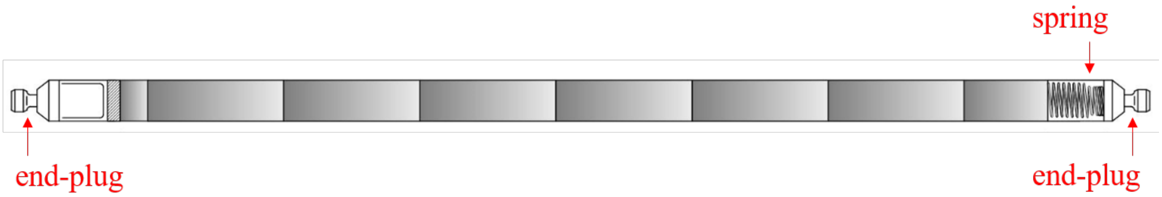

Fig. 3.3 Not to scale schematic representation of a surrogate rodlet.

study in PWR SNF, performed by ANATECH Corporation for the US Electric Power Research Institute (EPRI) [95]. This study attempted to predict the internal pressure of the rod based on statistical analysis of publicly available experimental data. As a result, the selection of 40 bar can well represent the average burnup of a Swiss PWR SNF assembly of around 50 GWd/tHM.

There were in total 46 hydrogenated cladding tubes with known hydrogen concentration, which varies lengthwise. For all samples the hydrogen profile was not constant along the length, due to the hydrogenation process resulting from a non-homogeneous axial temperature in the oven where the samples were treated.Such inhomogeneity of the hydrogen concentration is not problematic for the test, since only small regions of relatively constant hydrogen concentration were selected for the three-point bending tests. The local axial hydrogen content was estimated from the tube diameter variation, measured by means of laser scanning with an axial step of 2 mm and circumferential step of 1 degree. The average circumferential value of the tube diameter was used to determine the hydrogen concentration at each axial measured location.

Fig. 3.4 shows a typical hydrogenated pressurized Zry-4 cladding sample. In order to correlate the axial hydrogen concentration profile to each sample, the cladding tubes were marked with numbers with a step of 1 cm, as indicated in Fig. 3.4 (left). An example of a pressurized surrogate rodlet before testing is provided in Fig. 3.4 (right). The pressure sensor is attached to the left end of the sample and the valve controlling the inlet of the He gas for the pressurization is attached to the right.

3.3 Three-point bending tests

The present experiments aimed mainly at demonstrating and optimizing the capabilities of the testing setup in view of its application to characterize deformation and failure behavior of spent fuel rods. It is well known that the hydrogen content in spent fuel cladding is a key

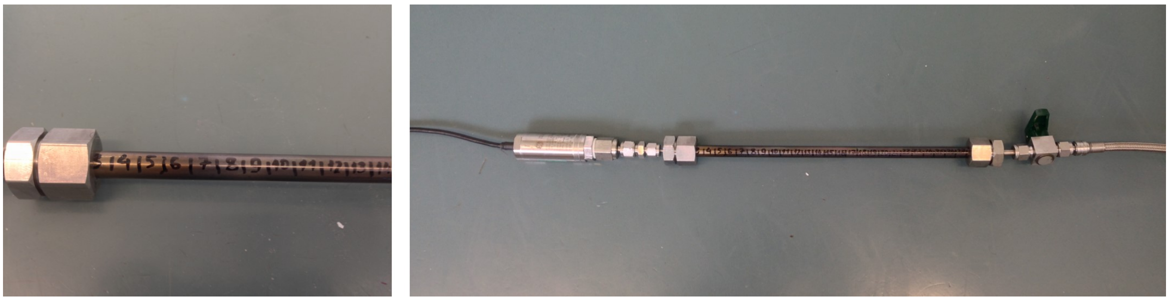

Fig. 3.4 Pressurized hydrogenated Zry-4 cladding tube used of the three-point bending experiments.

factor affecting the response of the fuel rod to mechanical solicitations and loading, which may occur during the various stages of spent fuel management. To verify the effectiveness of the bending setup in characterizing such effects, the cold test campaign covered a wide range of local hydrogen concentration levels, ranging from untreated cladding to extremely high hydrogen concentration levels (>2000 ppm).

In total, 23 three-point bending test experiments have been conducted on fresh and pre-hydrogenated samples for the present analogue campaign. The pressure, the applied load and the deflection of the samples at the loading point were acquired for each experiment .

Fig. 3.5 depicts the experimental setup for the three-point bending test investigations with the use of surrogate samples. The bending device is positioned vertically, on top of two block-supports which provide enough space to allow the sample's deformation. The controller is installed directly next to the three-point bending test device, where it is also possible to observe the measured values of pressure, load and displacement in real-time.

The testing conditions for the experiments performed on hydrogenated samples are provided in Table 3.3. All samples were pressurized[1] to 40 bar, the loading rate was set to 1 mm min^{-1} and the data frequency was set to 20 Hz. The internal pressure was kept constant for all experiments to eliminate its relative influence at the results. The data were acquired at very high frequency allowing detailed observation of the data evolution during the test.

Table 3.3 Testing conditions for the three-point bending tests on surrogate rodlets.

Testing conditions	Value	Unit
Internal pressure	40	bar
Loading rate	1	mm/min
Data frequency	20	Hz

---

[1] No internal pressure used for two tests on fresh Zry-4 cladding tubes (refer to section 3.3.1).

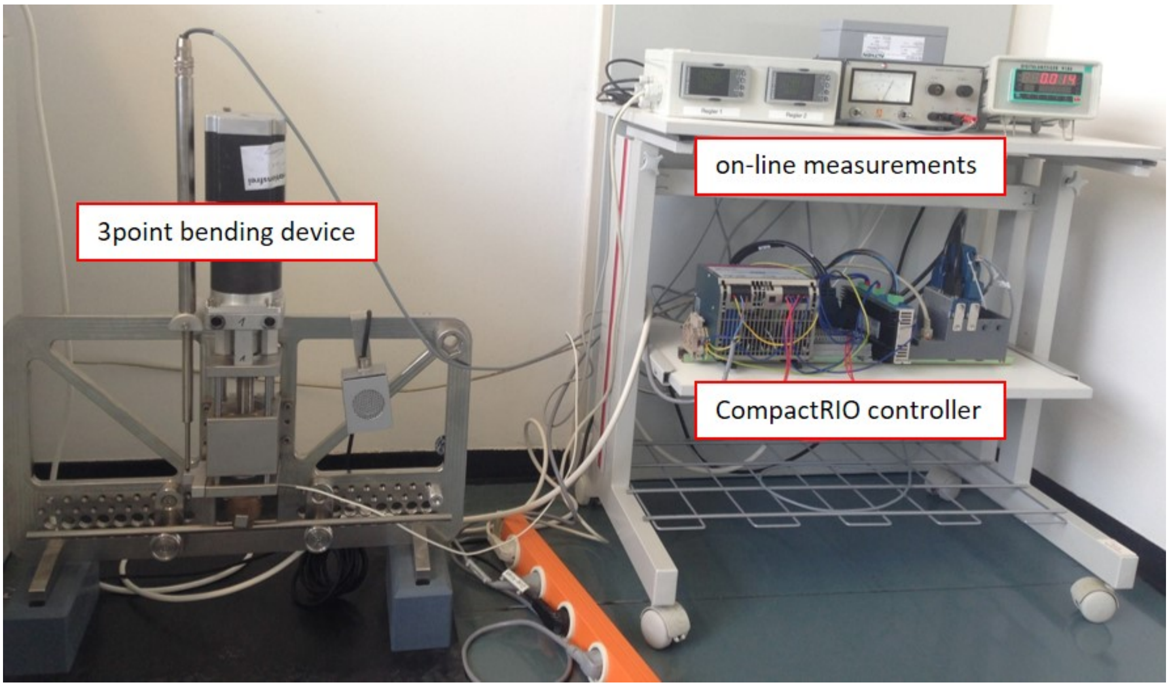

Fig. 3.5 Setup for three-point bending tests on surrogate rodlets under cold conditions.

3.3.1 Use of fresh Zry-4 cladding tubes

Two three-point bending tests were performed on fresh[2] Zry-4 cladding tube, with and without the presence of the alumina pellets. The objective was to study the cladding's response before hydrogenation, to develop a better understanding on the effects due to the pellets presence on the rodlet's bending behavior, as well as to facilitate the FEM calibration, since the mechanical parameters for the fresh cladding are known (refer to section 5.4). In addition, for these tests no internal pressure was applied to eliminate another parameter that could influence the FEM calibration. Fig. 3.6 shows the load-displacement curves for the two cases depicting the elastoplastic behavior of the samples.

The first important observation is that the bending modulus of elasticity (or Young's modulus) is similar in both tests, indicating that the pellets have insignificant effect on the elastic flexural properties of the composite cladding/pellet material. In other words, the elastic regime reveals the elastic properties of the cladding material. This could be explained by the fact that in very low flexural strains, there is no significant deformation of the cladding, therefore the pellets do not experience any significant stresses.

---

[2] Hydrogen content $\leq$25 ppm as provided from manufacturer material information.

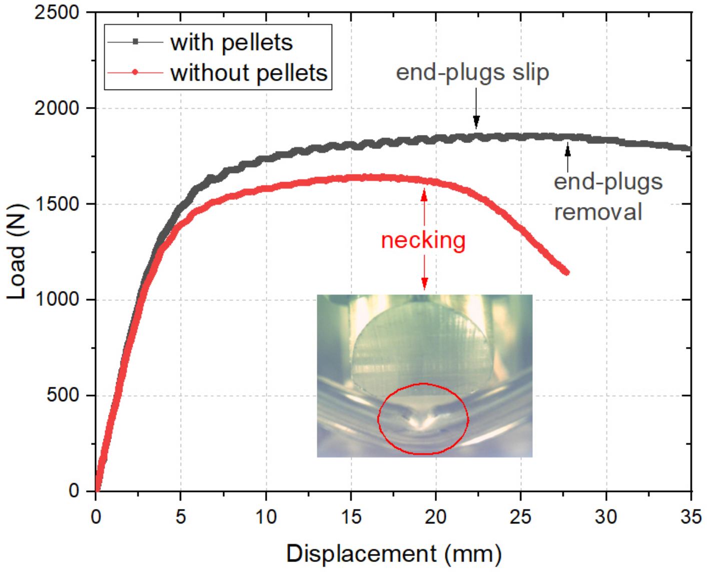

Fig. 3.6 Load-displacement curves for fresh Zry-4 cladding tubes with (black) and without (red) alumina pellets.

As a result, one can derive the flexural elastic behavior of cladding tubes, even in cases where the cladding tube is not empty. This is particularly helpful for the case of irradiated rods, where the samples are not mechanically defueled. Therefore, the flexural elastic behavior of claddings of irradiated spent fuel rods can be derived directly from the experimental results. It should be noted that for these experiments on surrogate rods, there is no bonding between pellets and cladding: therefore its contribution to the flexural properties of the rods cannot be examined.

In addition, the Yield stress is very close (essentially identical) for the two cases. A difference lies at the development of the plastic regime where, the pellet contribution becomes apparent, showing an increase in the bending strength during plastic deformation. Following the elastic regime, the pellets start to take up part of the bending stresses as the cladding deforms. At the displacement of 15 mm, the load difference between the two cases is approximately 11%, which shows the additional bending strength that the pellets contribute to the mechanical performance of the composite cladding/pellet system.

The plastic deformation for the case of the hollow tube is clearly divided between two regions: the strain hardening region where the load increases up to a maximum value and the necking region where the load drops. At the point of transition, the cladding tube deforms locally, as shown in the inset in Fig. 3.6. At this point, the strain concentrates at the location of highest stress which, eventually, causes even more concentration of strain, leading to an instability that produces the formation of a neck. This is a geometric instability caused by a macroscopic decrease in the cross-sectional area of the cladding. The experiment was stopped after a significant drop in load, since no useful information could be derived after that point.

The necking behavior is not observed for the case of cladding with pellets and the rodlet was able to undergo significant plastic deformation before rupture (high ductility). However, an irregular behavior is noticed on the development of the plastic regime for displacement greater than 22 mm. Around this point, the periodic oscillations detected during plastic deformation start to smooth out and eventually disappear. During the test it was noticed that at this point the end-plugs used to fix tightly the pellets within the cladding start to slip out. Fig. 3.7a illustrates the cladding, pellet and end-plug used for this test. The fixation of the pellets differs compared to the end-plugs used in all the other experiments with the use of hydrogenated cladding tubes. No spring was used, but a soft material (sponge-like) was placed between the pellets and the end-plugs.

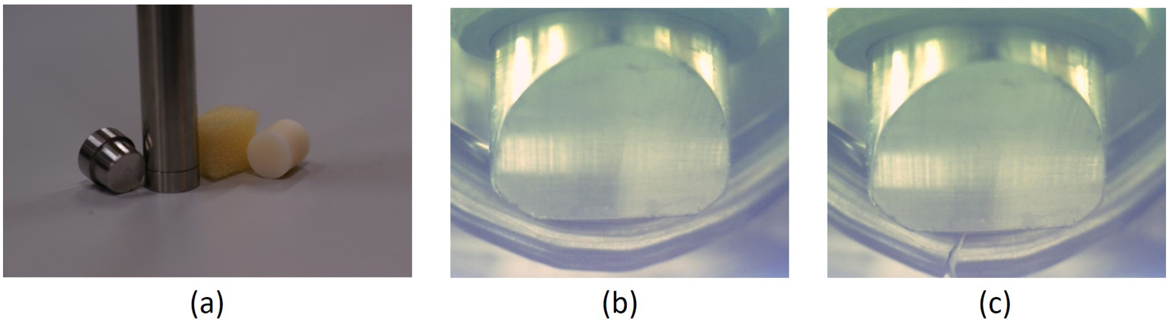
(a) (b) (c)

Fig. 3.7 a) photograph showing the fresh cladding tube, alumina pellet, sponge filler and end-plug used for the sample preparation, b) rod deflection before fracture shaped based on pellets' positioning and c) cladding fracture under tension (bottom area) at the pellet-cladding interface closest to the loading axis.

In the plastic region (higher flexural strains) the pellets are also subjected to bending and stresses that develop are pushing the pellets outwards. The end-plugs used for this test could not hold this pressure and eventually slipped out. This made the system less stiff since the pellets had the freedom to move axially and this is the reason why the observed oscillations smoothed out and the load slightly dropped.

Figs. 3.7b and 3.7c depict the cladding deformation before and after fracture initiation. The fresh Zry-4 cladding tube, being highly ductile, becomes shaped according to the pellet therein. The rupture of the cladding initiated at the bottom region of the cladding, which is subjected to tension, and at the pellet-cladding interface closest to the loading (vertical) axis. This point revealed the development of higher stresses leading to crack initiation. Similar behavior was also observed in the bending tests with hydrogenated Zry-4 cladding tubes (refer to section 3.3.2 as well as in the numerical studies in section 5.4).

3.3.2 Use of hydrogenated Zry-4 cladding tubes

The data acquired during the tests provide information from the first contact to the point in time when the cladding tube cracks and the pressure and applied load drop. Fig. 3.8 illustrates typical results from one experiment, performed on a sample with local hydrogen content of approximately 184 ppm; in the graph, load and internal pressure are plotted as a function of deflection [96]. The strain energy transmitted by the loading device to the sample can be calculated by integrating the area under the curve; the critical energy until fracture can be also estimated. Furthermore, the ultimate and fracture strength can be calculated.

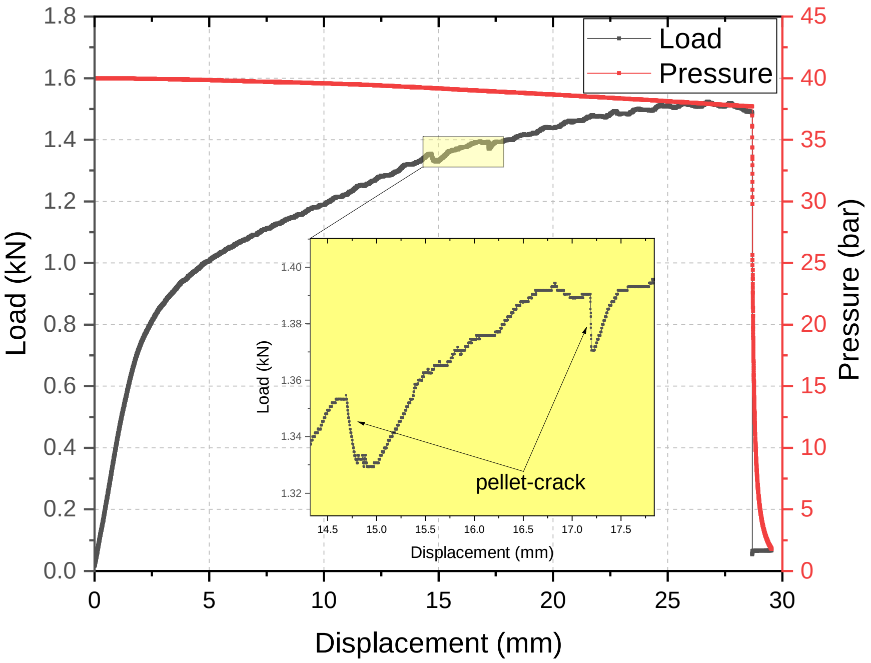

Fig. 3.8 Three-point bending experiments on pressurized hydrogenated Zry-4 cladding tube.

The slow pressure decrease is a consequence of the slight volume increase of the sample during bending, associated to cladding elongation. The elastic and plastic regions can clearly be distinguished. Similarly to the fresh cladding results, a ductile behavior of the surrogate rodlet can also be observed here. During plastic deformation the load increases and the cladding fractures at around 27 mm of displacement, which corresponds to a smaller bending angle compared to the fresh cladding case. This is expected since the hydrogen absorbed in the Zry-4 degrades the bending performance of the cladding. At the fracture point, the load and the internal pressure drop instantly. Finally, sudden load drops appear during plastic deformation, as in the yellow highlighted region in Fig. 3.8. The relatively small drops of the load can be attributed to cracking occurring in the alumina pellets under the applied load. Such cracking could be heard during the tests.

The local hydrogen content at the fracture point is determined after the completion of the test. Fig. 3.9 shows the hydrogen concentration along the cladding's length for one of the examined samples. A snapshot of the fractured cladding shows the region where the cracking occurred. The local hydrogen content at this point is determined by averaging the hydrogen concentration in this region, as indicated with the two red vertical lines in Fig. 3.9.

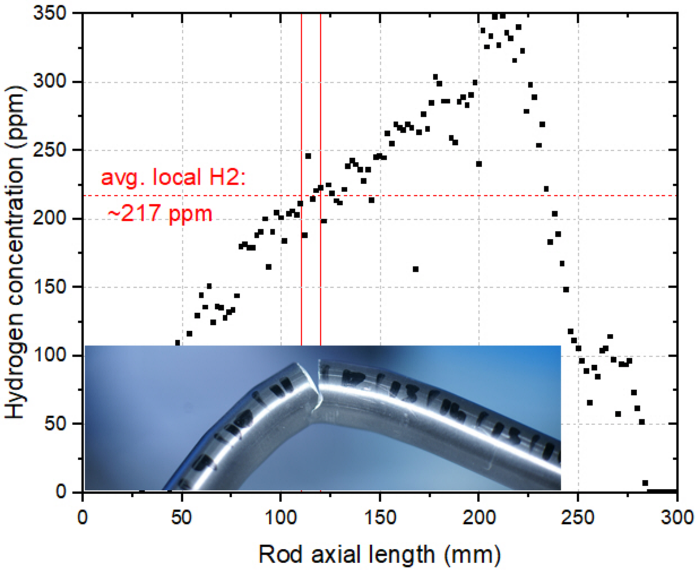

Fig. 3.9 Hydrogen axial distribution in the pressurized hydrogenated Zry-4 cladding tube used for the three-point bending experiments. The position markers on the cladding allow determining the local hydrogen content at the point of fracture.

An overview of the surrogate samples tested in this experimental campaign is given in Table 3.4. In total, 21 experiments with hydrogenated Zry-4 cladding tubes were performed, which could be categorized in four groups depending on the cladding's hydrogenation treatment and on the size of pellets used (refer to Table 3.1). The pellets with bigger diameter leave just a tiny gap compared to the pellets of smaller diameter.

The first group, which is considered as the group of reference, consists of samples with cladding tubes treated at 550 °C (hydrides randomly oriented) and pellets of bigger diameter. Most of the experiments were performed for surrogate samples with these characteristics. The local hydrogen content at the fracture point varied from low to extremely high values.

In order to compare the influence of the gap size to the sample's flexural behavior, a second group of test samples includes those with smaller pellet diameter. In order to examine the influence of the cladding's hydrogenation treatment, samples with different treatment temperatures were tested in the first, third and fourth group of samples. The third and fourth group include samples with big pellets, which have been treated at higher temperatures, at 650 °C and 750 °C. The higher temperatures in this case are expected to induce formation of some radial hydrides.

Table 3.4 Characteristics of hydrogenated surrogate samples used for bending tests.

Index	Sample ID	H2 at fracture [ppm]	Hydrogenation temperature [°C]	Hydride orientation	Pellet size [3]
1	H194Z4_59	125	550	radial	big
2	H172Z4_128	187	550	radial	big
3	H186Z4_214	260	550	radial	big
5	H175Z4_253	352	550	radial	big
6	H192Z4_286	374	550	radial	big
4	H195Z4_227	396	550	radial	big
7	H178Z4_192	462	550	radial	big
8	H182Z4_222	517	550	radial	big
9	H190Z4_445	643	550	radial	big
10	H177Z4_318	690	550	radial	big
11	H181Z4_509	1437	550	radial	big
12	H183Z4_925	2296	550	radial	big
13	H169Z4_69	85	550	radial	small
14	H185Z4_188	344	550	radial	small
15	H193Z4_302	645	550	radial	small
16	H176Z4_818	2160	550	radial	small
17	H117Z4_280	113	650	random	big
18	H159Z4_397	342	650	random	big
19	H112Z4_190	181	750	random	big
20	H105Z4_180	219	750	random	big
21	H116Z4_360	321	750	random	big

3.3.3 Experimental results

The experimental data from the three-point bending tests (Fig. 3.10) consists mainly of the load-displacement curves, depicting the flexural behavior of the surrogate rodlets and provide the displacement to fracture. In addition, the sample's internal pressure is measured during the test and upon fracture. The load-displacement curves for the analogue three-point bending test campaign are summarized in Figs 3.11 and 3.12. The legend of these graphs indicate the local hydrogen content of the sample at the fracture point along with the main characteristics of the sample group (either cladding hydrogenation temperature or pellet size).

Fig. 3.11a presents the load-displacement curves of the samples belonging to the first group of Table 3.4, as well as the two additional experiments performed on non-pressurized fresh Zry-4 cladding tubes with and without the presence of pellets. These cladding tubes were hydrogenated at 550 °C and filled with big alumina pellets. As expected the fresh/untreated cladding tube (highlighted in black) shows more ductile behavior compared to the hydrogenated Zry-4 samples, as it fractures at a deflection of approximately 35 mm. The elastic region in all tests is the same, indicating that the Young's modulus does not change based on the hydrogen content of the Zry-4 tubes, as it had also been previously observed in Ring Compression Test (RCT) on unirradiated Zry-4 claddings [97].

The hydrogen concentration affects the ductility of the sample, since samples with higher hydrogen content exhibit more brittle behavior and fracture at lower deflection. Fig. **??** presents snapshots from selected bending tests at the time of cladding fracture. Fig. **??**a shows the deformation of a non-hydrogenated cladding tube where an extensive deformation was required until fracture. The following figures show snapshots from samples with increasingly higher hydrogen content. The correlation between sample's ductility and cladding's hydrogen concentration is clearly observed as the bending angle to fracture decreases with higher hydrogen content.

Moreover, although there is no unequivocal correlation between the fracture strength and the hydrogen content, also due to the stochastic component associated with the axial positioning of the pellets inside the cladding tube (see below), samples with higher hydrogen content tend to have lower fracture strength, mainly due to the limited plastic deformation they undergo. Finally, although the yield stress appears to be similar in most cases, the transition to the plastic regime appears steeper for the samples with higher hydrogen content; nonetheless, this transition could also be influenced by the pellet positioning along the

---

[3] refer to Table 3.1.

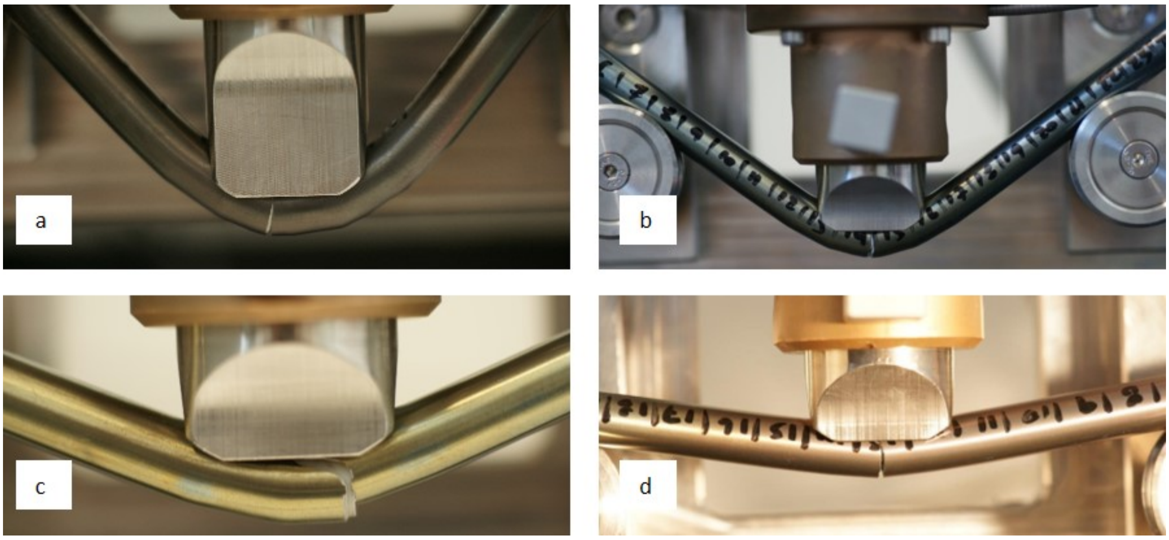

Fig. 3.10 Analogue bending tests; a) Bending test of non-hydrogenated sample. The rod shows very high ductility; b) Bending test of sample with intermediate Zr hydride content; c) Importance of the presence of pellets during the test. The sample breaks always at the pellet-pellet interface; d) Bending test in high Zr hydride content (> 700 ppm) sample. The rod shows brittle behavior (low deflection at fracture) when compared to the other rods.

symmetry axis. This parameter is stochastic since we cannot control the pellet position (in particular, the pellet-pellet interface locations) during sample preparation.

Fig. 3.11b shows the experimental results of the second group of samples from Table 3.4, which includes the same cladding tubes, however filled with alumina pellets of smaller diameter. Compared to the reference case (first group), considerably less experiments were performed. The motive was to test samples along a wide range of hydrogen content to investigate the influence of smaller pellets to the samples response. Again, the correlation of the sample's ductility to the cladding's hydrogen content is clearly observed. The samples with very high hydrogen content showed brittle behavior and fractured at around 10 mm of displacement, similarly to the reference case where bigger pellets were used. The two samples with lower hydrogen showed greater ductility and fractured in considerable higher displacements, if compared to the reference case. Moreover, a bucking behavior of the sample with the lowest hydrogen content at fracture point (85 ppm, highlighted in black) was observed, as the load decreased in higher displacements. This could indicate that the bigger gap (4 times higher than the reference case (refer to Table 3.1)) allowed the development of larger local deformations at the loading point, which in turn decreased the stiffness of the sample.

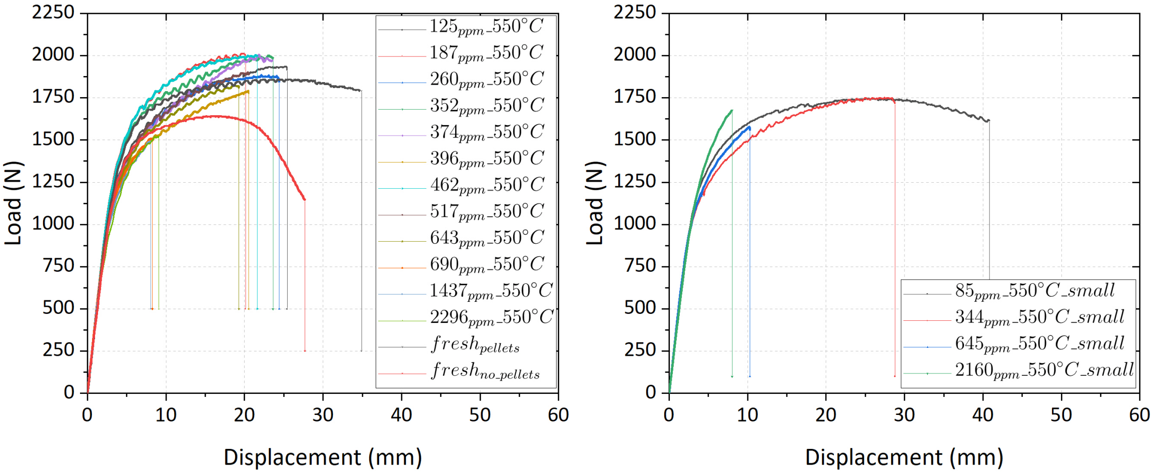

(a) (b)

Fig. 3.11 Load-displacement curves of surrogate samples from group 1 and 2, including Zry-4 cladding tubes hydrogenated at 550°C with the use of a) big and b) small alumina pellets.

Five additional bending tests were conducted on hydrogenated cladding tubes treated at higher temperature. Fig. 3.12a provides the experimental results of two samples consisting of Zry-4 cladding tubes treated at 650°C containing pellets with the bigger diameter. The samples showed much more ductile behavior compared to the reference case, as they fractured at displacement almost two times higher. Although both samples revealed higher bending toughness (higher energy required to fracture), they exhibited approximately 20% lower bending strength. This behavior has to be linked to the different hydrogenation process used for these samples. Further details on the hydride orientation are given in section 3.3.5. In both tests, there are discontinuities observed during plastic deformation. For the case of the sample with the lowest hydrogen content (highlighted in black), the test was interrupted in order to replace the former with a longer one (refer to section 2.2.3) since the initial bending setup had reached its maximum axis displacement. The second test was interrupted due to the popping out of one of the end-plugs, starting at around 16 mm of displacement and indicated by the smoothing of the plastic loads. Similarly to the experiment on the fresh Zry-4 cladding filled with alumina pellets (refer to Fig. 3.6), the sample became less stiff once the end-plug started to slip-out since the pellets were no longer axially constrained.

In Fig. 3.12b the experimental results on hydrogenated cladding tubes treated at 750°C and filled with big alumina pellets are given. Three tests were performed on hydrogen content ranging between 180 ppm and 320 ppm. The tests did not reveal any trend associating the hydrogen content and the critical displacement to fracture; however, all of them showed higher ductility compared to the reference case, which could be a result of a possible thermal annealing of the sample after its heat treatment.

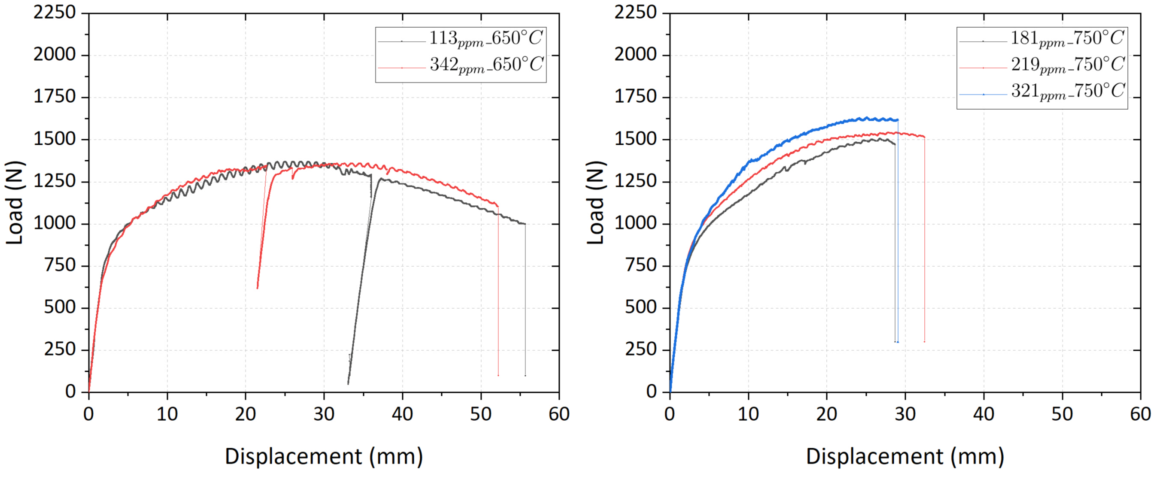

(a) (b)

Fig. 3.12 Load-displacement curves of surrogate samples including big pellets and Zry-4 cladding tubes hydrogenated at a) 650°C and b) 750°C.

The displacement and bending angle at which the samples fractured as a function of the local hydrogen content in the vicinity of the crack, are plotted in Figs. 3.13 and 3.14 for all three-point bending test experiments. The results can be categorized into 3 main groups as indicated in Fig. 3.13.

The first group refers to Zry-4 cladding with relatively low hydrogen content ($\leq$100 ppm) where all samples exhibited a great amount of plastic deformation and fractured at considerably higher bending angles. The alumina pellets proved to be the limiting factor to the sample's ductility, since no rupture was observed for Zry-4 cladding tubes with the same hydrogen content, but without pellets.

The second group refers to samples with hydrogen content above 100 ppm and up to approximately 650 ppm. This region includes the hydrogen content range to be expected in commercial spent fuel cladding after discharge from reactor. In this group, a nearly linear correlation could be observed between the local hydrogen content and the displacement to fracture for the reference experiments having Zry-4 cladding tubes hydrogenated at 550°C and alumina pellets with the bigger diameter, as shown in Fig. 3.14b. At higher hydrogen content (not representative of standard spent fuel rod conditions during dry storage), the samples break at the same deflection level independent of the local hydrogen content. The cladding material in this range can only withstand a deflection of around 9 mm until cracking.

Finally, these results are in line with reported trends of failure strains as function of hydrogen content, observed for irradiated PWR claddings during burst tests [98].

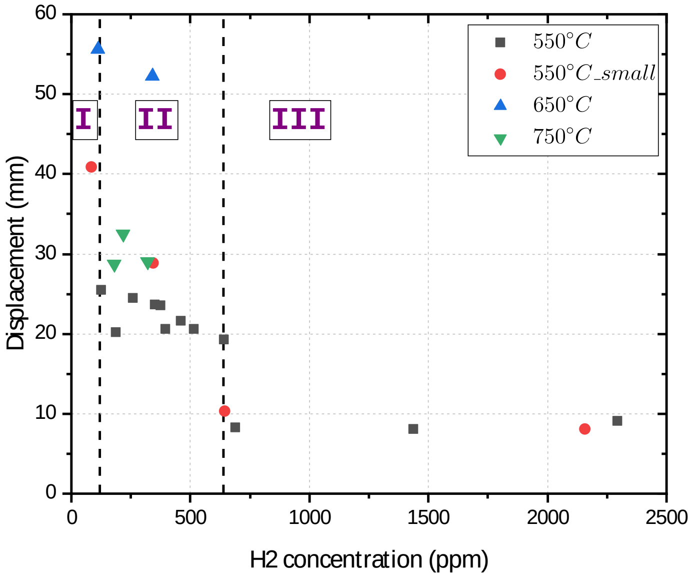

Fig. 3.13 Displacement to fracture of surrogate samples as a function of hydrogen concentration. Black, blue and green dots correspond to samples having experienced hydrogenation temperatures of 550°C, 650°C and 750°C, respectively. The red dots correspond to samples including pellets of smaller diameter. The displacement to fracture becomes independent of hydrogen content above 650 ppm.

A summary of the three-point bending test experimental results is given in Table 3.5. The bending angle and displacement to fracture are given, as well as the maximum recorded load during the tests. Moreover, the area under the load-displacement graphs is provided representing the work, or the energy transmitted to sample until fracture.

Additionally to the load-displacement data, the internal pressure of the samples was also recorded. During the test, the pressure slightly dropped due to the cladding elongation and associated sample volume increase, as shown in Fig. 3.8. At the point of fracture, the pressure instantly dropped, however the depressurization process differed based on the sample's ductility and pellet size.

Fig. 3.15 gives representative results of the depressurization process on selected samples. Upon cladding's fracture, the pressure drops instantly to atmospheric for the samples, which either showed brittle behavior or, included pellets with smaller diameter. On the other hand, samples which exhibited long plastic deformations and were filled with bigger alumina

Table 3.5 Summary of experimental results on surrogate rods.

Sample ID	H2 at fracture [ppm]	Displacement at fracture [mm]	Bending angle at fracture [$\circ$]	Load$_{max}$ [N]	Work [N*mm]
H194Z4_59	125	25.45	44.60	1935	40757
H172Z4_128	187	20.12	35.02	1751	32869
H186Z4_214	260	24.41	42.74	1883	38333
H192Z4_286	374	23.51	41.11	2004	37254
H175Z4_253	352	23.63	41.33	2002	38880
H195Z4_227	396	20.53	35.76	1790	29362
H178Z4_192	462	21.63	37.73	2002	35783
H182Z4_222	517	20.54	35.77	1901	31111
H190Z4_445	643	19.29	33.53	1822	28031
H177Z4_318	690	8.30	14.01	1509	8917
H181Z4_509	1437	8.07	13.61	1491	8403
H183Z4_925	2296	9.10	15.40	1524	9801
H117Z4_280	113	55.67	93.24	1371	65090
H159Z4_397	342	52.24	88.56	1360	62889
H112Z4_190	181	28.70	50.41	1507	34886
H105Z4_180	219	32.46	57.03	1543	42395
H116Z4_360	321	29.05	51.02	1631	39164
H169Z4_69	85	40.83	71.20	1746	63905
H185Z4_188	344	28.80	50.59	1751	42341
H193Z4_302	645	10.31	17.52	1578	11808
H176Z4_818	2160	8.03	13.55	1676	8893
fresh$_{pellets}$	≤ 25	34.90	60.09	1859	57992
fresh$_{no\_pellets}$	≤ 25	27.72	47.87	1642	39018

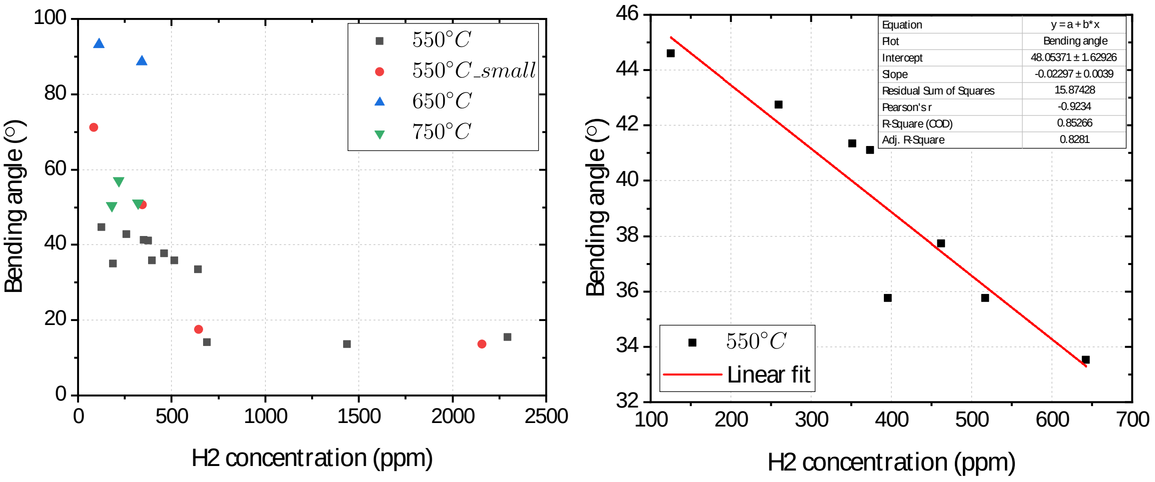

(a)

(b)

Fig. 3.14 a) Bending angle to fracture as a function of hydrogen concentration for surrogate samples under three-point bending test; b) linear fit of bending angle to fracture of the reference samples (group 1 on table 3.4) with hydrogen content between 100 ppm and 650 ppm.

pellets showed a much slower transition to atmospheric pressure. This is associated to the gap closure created by the cladding deformation, which was not observed for the samples including smaller pellet size. In any case, in both cases the time to ambient pressure is of the order of seconds.

3.3.4 Flexural properties of surrogate rods

The mechanical properties of the surrogate samples under bending loads are derived based on the simple beam theory, as described in section 2.2.5. The flexural properties are calculated for beam elements with circular and hollow-circular cross-sections with regard to the cladding's outer and inner diameter. The results provide the "effective" flexural properties of beam elements with a given cross section (under the assumptions/limitations of the simple beam theory) that could resemble the mechanical response of the surrogate samples under bending loads.

The flexural stress-strain curves as derived for beam elements with circular and hollow-circular cross-sections are given in Appendix A. The flexural modulus of elasticity is calculated from the slope of the elastic region along with the toughness of the samples (area under the curves) and is provided in Table 3.6.

Table 3.6 Flexural modulus of elasticity and toughness of surrogate samples assuming circular and hollow-circular cross-section.

Sample ID	H2 at fracture [ppm]	Flexural E_{mod}	Toughness [Mpa]	Flexural E_{mod}	Toughness [Mpa]
		hollow-circular		circular	
H194Z4_59	125	85.4	87.5	37.6	38.5
H172Z4_128	187	84.0	70.6	37.0	31.0
H186Z4_214	260	87.4	82.3	38.5	36.2
H175Z4_253	352	84.7	83.5	37.2	36.7
H192Z4_286	374	84.1	80.0	37.0	35.2
H195Z4_227	396	81.8	63.0	36.0	27.7
H178Z4_192	462	86.0	76.8	37.8	33.8
H182Z4_222	517	84.9	66.8	37.3	29.4
H190Z4_445	643	83.2	60.2	36.6	26.5
H177Z4_318	690	87.5	19.1	38.5	8.4
H181Z4_509	1437	84.7	18.0	37.3	7.9
H183Z4_925	2296	80.0	21.0	35.2	9.3
H117Z4_280	113	79.4	139.7	35.4	61.5
H159Z4_397	342	85.7	135.0	34.2	59.4
H112Z4_190	181	84.5	74.9	37.2	32.9
H105Z4_180	219	83.7	91.0	36.8	40.0
H116Z4_360	321	81.2	84.1	35.7	37.0
H169Z4_69	85	79.1	137.2	34.8	60.4
H185Z4_188	344	83.5	90.9	36.7	40.0
H193Z4_302	645	85.0	25.4	37.4	11.2
H176Z4_818	2160	79.6	19.1	35.0	8.4
fresh_pellets	25	97.2	124.5	42.7	54.8
fresh_nopellets	25	95.8	83.8	42.3	36.8

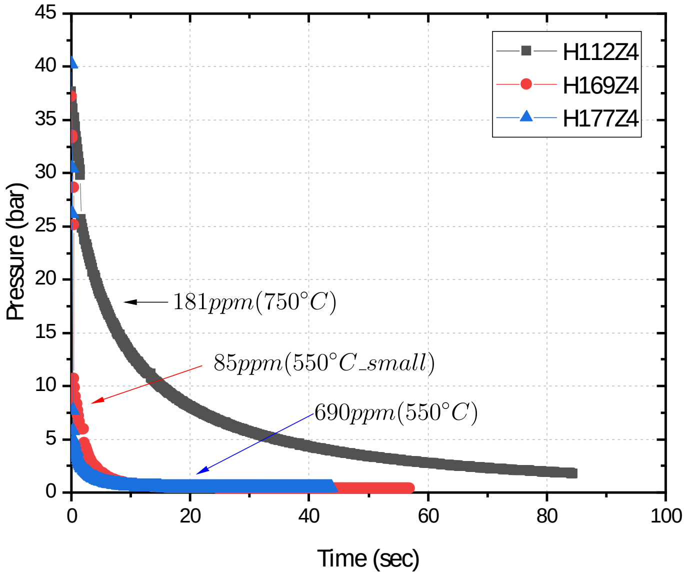

Fig. 3.15 Sample internal pressure drop after fracture vs. time.

As shown in Fig. 3.6, the slope of the elastic region in three-point bending tests for Zry-4 tubes with and without alumina pellets are identical. Therefore, the assumption of beam element with hollow-circular cross-section could well represent the elastic properties of the cladding material even in the cases where they are filled with ceramic pellets. Therefore, the Young's modulus of the cladding can be estimated from the derived stress-strain curves for this specific cross-section.

Fig. 3.16 gives the flexural modulus of elasticity for beam elements with hollow-circular cross section. The calculated values of fresh Zry-4 range between 95.8 and 97.2 GPa which are in very good agreement with observations from different studies [99–101, 55]. All hydrogenated samples showed decreased values of flexural modulus of $\sim 12\%$, ranging between 79.1 and 87.4 GPa.

3.3.5 Fracture behavior and crack initiation

The large number of experiments on the surrogate samples allowed the observation of the cladding's fracture behavior and failure modes. The most important outcome is that the crack always initiates at the bottom side of the cladding which is subjected to tension and at the pellet-pellet interface (PPI) closest to the axis of loading (or symmetry axis), as shown e.g. in Fig. 3.17a. At this point, higher local plastic stresses and strains are developed as the

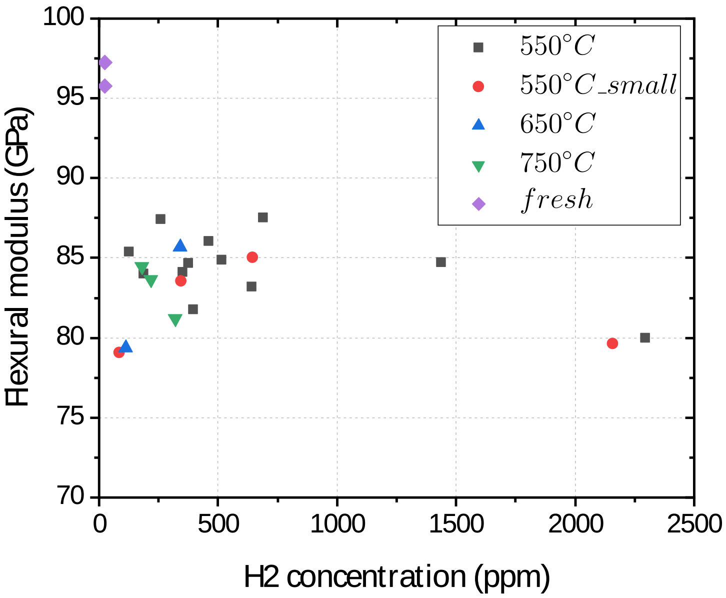

Fig. 3.16 Flexural modulus of hydrogenated and fresh Zry-4 cladding tubes.

pellet transmits forces to the cladding. The cladding fails in a typical tensile failure mode, however the crack propagates following a mixed failure mode (tension and shear), as shown in Figs. 3.17 and 3.18.

The pellets positioned under the loading axis follow the deformation of the cladding and are therefore subjected to bending. At the bottom part the pellets are detaching, whereas at the top part the pellets are pushed together increasing their contact pressure, as highlighted in Fig. 3.17. It was observed that the alumina pellets cracked at the top part and depending on the amount of deflection (or cladding deformation) the cracking pattern could increase.

The cladding always failed after a considerable amount of deformation, except for the samples with extremely high content of hydrides. In all cases, higher local strains were developed at the cladding span below the former, where during bending the cladding became shaped based on the pellet positioning (refer to Fig. **??**a). In this region, the small gap between the pellets and the cladding was closed and the pellets were bonded tightly to the cladding. Upon cladding failure, the cracked alumina pieces at the PPI are the only ones that could potentially be released. As a result, the total amount of alumina pellet release never exceeded the mass of one pellet, as shown in Fig.3.18.

The depressurization data could also provide valuable information on the potential fuel mass release upon loss of cladding's integrity. In case of abrupt drop of the internal pressure,

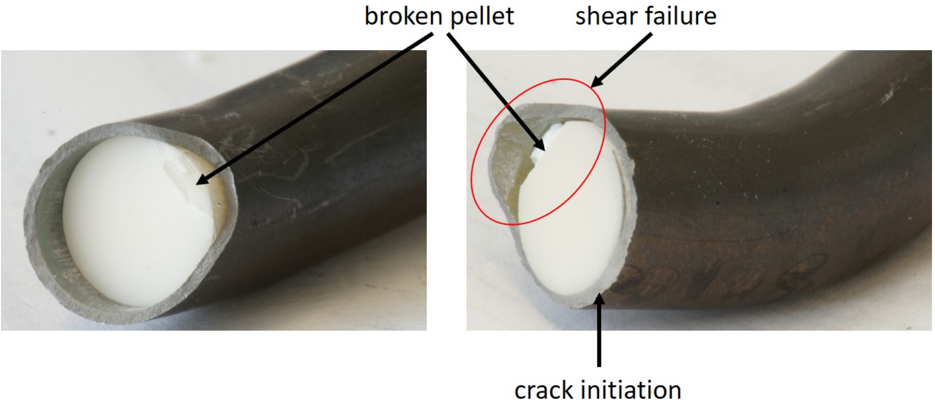

Fig. 3.17 Cladding failure initiation and crack propagation in surrogate samples.

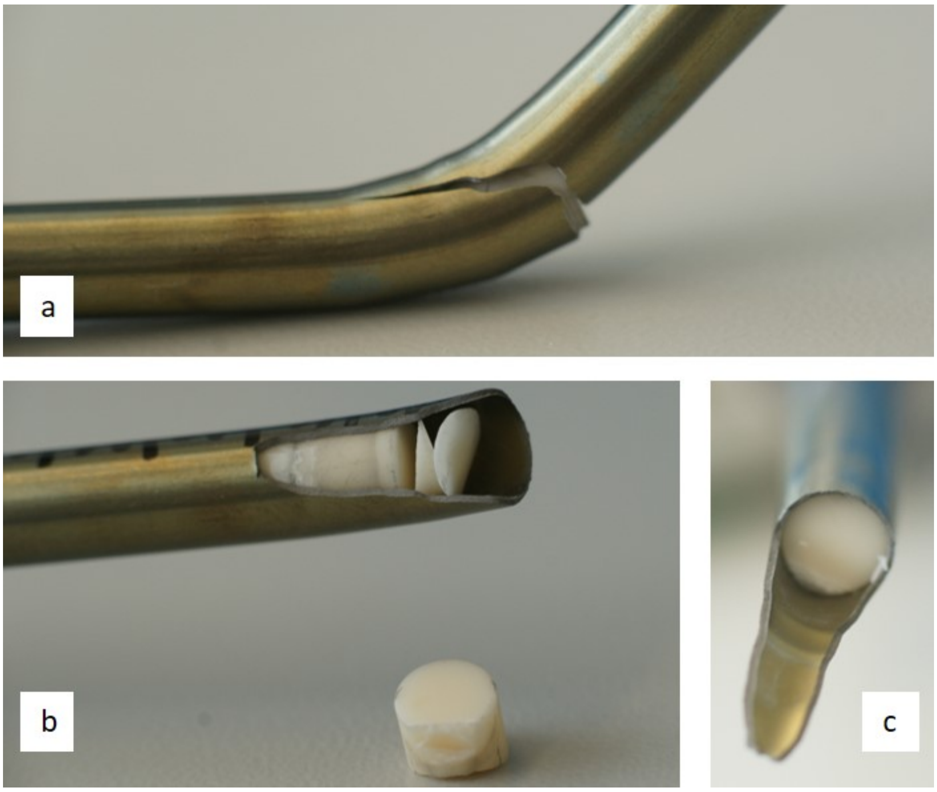

Fig. 3.18 Typical observations of cladding failure and pellet release of hydrogenated samples after three-point bending tests. The tensile and shear failure modes are seen in a), whereas the cracked pellets and mass release are shown in b) and c).

the pellets will also experience axial forces with direction towards the crack. For samples with highly brittle behavior (limited plastic deformation) and pellets potentially free to move (open gap) this could potentially lead to an extensive loss of fuel mass, as shown in Fig. 3.19. The local hydrogen content at the loading point for this sample was appropriately 2500 ppm (not realistic for commercially irradiated SNF) and the cladding broke at a very low bending angle. The cladding exhibited only limited plastic deformation and had a brittle failure, allowing the pellets to escape under the influence of the internal pressure.

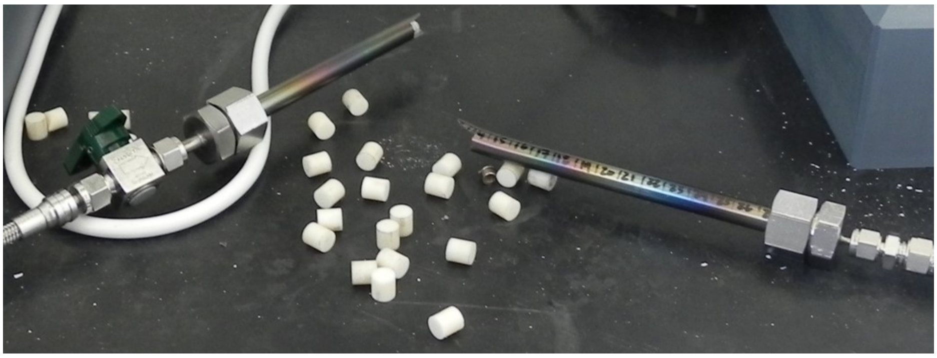

Fig. 3.19 Extensive pellet release upon cladding's brittle failure for sample with extremely high hydrogen content (2500 ppm).

3.3.6 Post-test examinations

The post-test examination after the three-point bending tests on surrogate samples were limited to a few samples and focused on the investigation of the cladding's hydrogen content and hydride formation and orientation. Hydrogen measurements with the method of hot gas extraction was carried out on selected samples at the point of fracture to determine the local hydrogen concentration. The results confirmed the nominal content, as estimated from the hydrogen profiles along cladding's length (refer to Fig. 3.9), and supported the conclusions derived from the observed trends.

Metallography was employed to investigate the zirconium hydride orientation. Fig. 3.20 shows images taken for Zry-4 samples with $\sim$ 350 ppm hydrogen content, hydrogenated at temperatures of 550°C (Fig. 3.20a,b), 650°C (Fig. 3.20c,d) and 750°C (Fig. 3.20e,f). At 550°C, mainly circumferential hydrides are formed, whereas randomly oriented hydrides are observed in the sample hydrogenated at the higher temperatures.

Since the sample has a high hydrogen concentration ($\sim$ 350 ppm), at low magnification it is difficult to distinguish between hydrides and grain boundaries after etching. Figs. 3.20b,d,f provide a zoomed-in section of Figs. 3.20a,c,e. The hydride orientation can be better distinguished in these figures where circumferential and random orientations are shown for the case of Fig. 3.20b and Fig. 3.20d,f, respectively. It should be pointed out that the morphology of the hydrides in an irradiated cladding usually differs significantly.

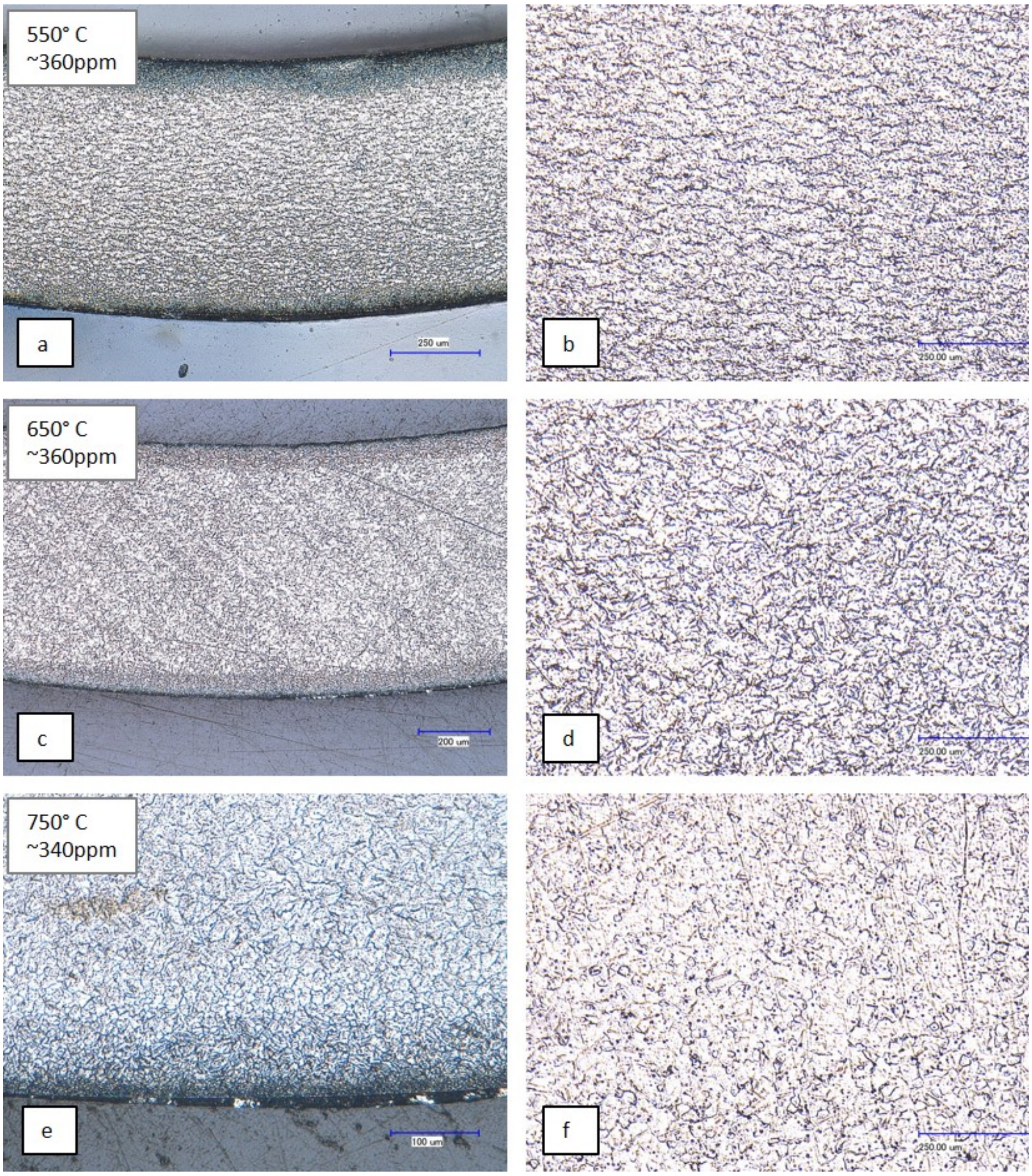
550° C
~360ppm
a
250 um
b
250.00 um
650° C
~360ppm
c
200 um
d
250.00 um
750° C
~340ppm
e
100 um
f
250.00 um

Fig. 3.20 Metallographic images illustrating the hydride orientation in Zry-4 cladding samples with $\sim$ 350 ppm hydrogen content, hydrogenated at different temperatures; circumferential orientation prevails at 550°C, while randomly oriented hydrides formed at 650°C and 750°C.

3.4 Impact tests

In contrast to the analogue three-point bending test studies, no extensive investigation on surrogate samples was performed for the case of the impact tests. The shortage of hydrogenated Zry-4 samples, the limited acquisition capabilities of the first version of the impact device (no IA, refer to section 2.3.2) and the urgent need to setup the device in the hot-cell were the main reasons for limiting the scope of this experimental campaign.

In cold conditions, two tests were performed on fresh and hydrogenated Zry-4 cladding tubes filled with alumina pellets, with the use of the first version of the impact tower. Three additional tests were conducted once the device was inserted in the hot-cells, aiming to study the performance of the final version of the impact tower (refer to section 2.3.3) and to optimize its acquisition capabilities.

3.4.1 Use of fresh and hydrogenated Zry-4 samples

The first test was performed on fresh Zry-4 cladding tube filled with big alumina pellets and pressurized to 35 bar with He gas. The impact device included the fixed supports where no rotation was allowed at the mounting locations.

Fig. 3.21 shows representative images of the evolution of cracking during the experiment. The new high-speed camera position gives the opportunity to have a deeper view of the chamber to follow the evolution of the segment fracture. The second frame shows the moment when the first crack occurred in the middle of the rod. The sample exhibits some significant deformation before fracturing. Moreover, the mounting points of the sample at the ends did not break, showing ductile behaviour. A relatively small release of material from the cladding is visible upon full fracturing.

The second test performed with the use of hydrogenated Zry-4 filled with small alumina pellets and pressurized to 35 bar. The cladding had an average hydride concentration of 590 ppm with a standard deviation of ± 152 ppm, which is quite high in comparison to a PWR spent fuel rod. Fig. 3.22 presents the crack evolution during this impact test. The specimen cracked immediately in the middle showing its brittle behaviour (hardly any plastic behaviour before fracture), as expected since the hydride content is high.

A significant outcome of this experiment was the influence of the fast internal depressurization on the amount of material released from the tube. With open and relatively large gap, the aluminium oxide pellets were free to move. When the fracture occurred, the pressure dropped rapidly forcing the pellets to move towards the middle area. However, it must be pointed out that such high hydrogen content and large gap between the fuel and the cladding is not a realistic configuration for a spent fuel rod.

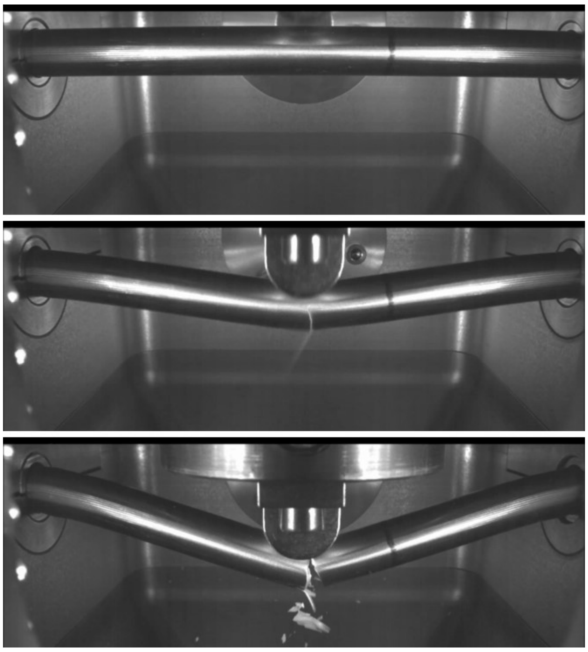

Fig. 3.21 Impact test on pressurized non-hydrogenated Zry-4 sample filled with alumina pellets. Sample breaks under the loading point, but not at the fixed ends illustrating high ductile behavior.

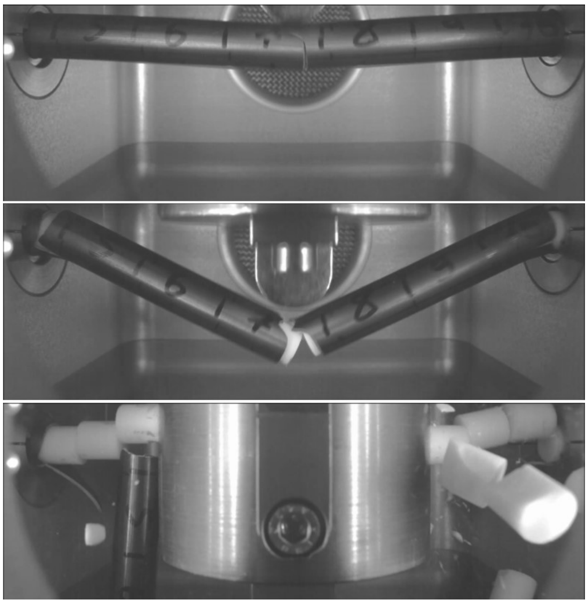

Fig. 3.22 Impact test on a pressurized hydrogenated Zry-4 cladding tube filled with small alumina pellets. High speed camera photograms illustrate the additional cracking at the sample holders under the impacting hammer, as well as the extensive pellet release due to open gap.

3.4.2 Post-test examinations

There was not a particular interest to perform post-test examinations, since no extensive investigations were performed on surrogate samples under impact tests. Nevertheless, this limited number of experiments offered the opportunity to test the performance of the filtration system installed in the closed chamber, which aims to capture the fine particulates and aerosol released upon fracture. In addition, carbon filters used to sweep the closed chamber were analysed to examine the remaining contamination upon fracture.

The carbon filter was analysed in a Focused Ion Beam (FIB) setup to identify the size distribution and the elemental composition of the particulates. The scope of this examination was to test its feasibility for future experiments on SNF rodlets. Some representative images of those examinations are presented in Figs. 3.23a and 3.23b. Fig. 3.23a gives an overview of the particulates dispersed on the carbon filter at a magnification of 62x provided by SEM analysis. Fig. 3.23b shows colour mapping from EDX analysis of the alumina particulates deposited on the filter.

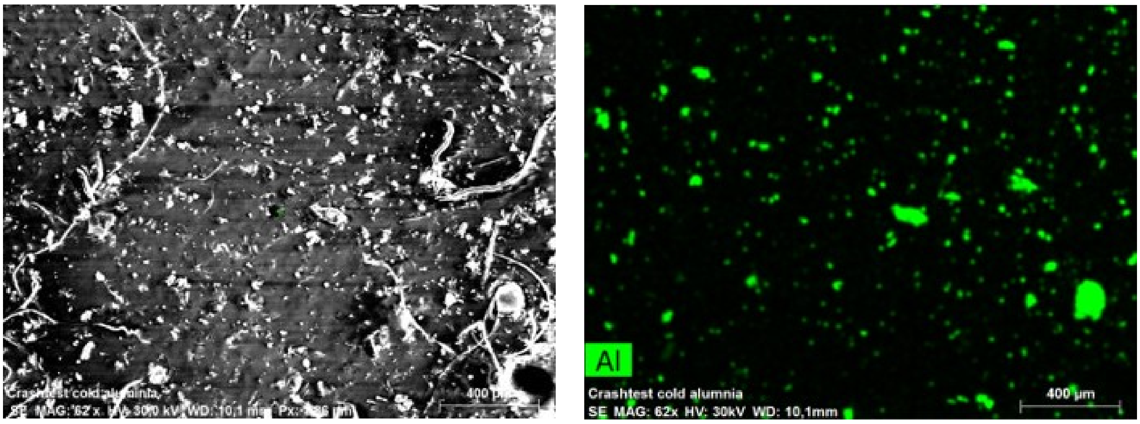

(a)

(b)

Fig. 3.23 a) SEM analysis of dispersed aluminium oxide particulates on a carbon filter and b) colour mapping of the alumina particulates dispersed on the carbon filter by EDX analysis.

A selected micrograph from BSE analysis performed on the filter coupled with the chamber's aspiration system, is presented in Fig. 3.24. Particles with different atomic mass number are depicted with different brightness levels. Brighter BSE intensity correlates with greater average atomic number, thus both Zry-4 and alumina particles can be detected.

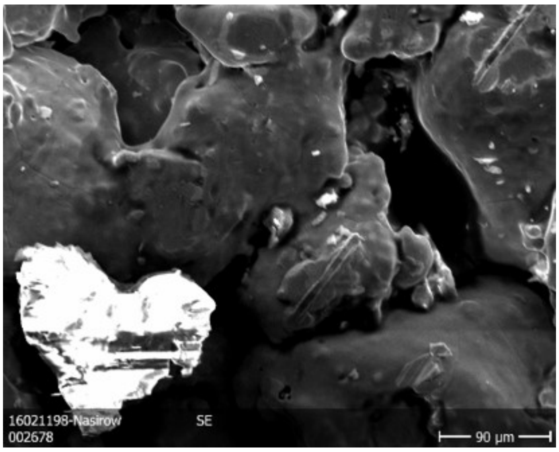

Fig. 3.24 BSE micrograph of fine particulates and aerosol deposited on the filter coupled to the aspiration device connected to the impact testing chamber after fracture of the surrogate sample.

3.5 Summary

The analogue experimental campaign on surrogate rods was presented in this chapter. The samples consisted of untreated and hydrogenated Zry-4 cladding tubes, filled with alumina pellets and pressurized to 40 bar. Various sample groups were tested by three-point bending, including cladding tubes with different hydride orientation and dummy pellets of different sizes.

The first important observation was on the linear region of the load-displacement curves of the different samples, which did not significantly change depending on the cladding's hydrogen content or the pellet size. The Euler-Bernoulli beam theory was used to derive the flexural response of the sample. The flexural modulus of the claddings was calculated using beam elements with hollow-circular cross section. Values similar to what reported in literature were obtained for fresh Zry-4 claddings. Hydrogenated claddings revealed slightly lower values on the flexural modulus of elasticity, without any dependence on the hydrogen content.

In addition, the dependence of the sample's ductility as function of the cladding's hydrogen content was presented. Cladding tubes with low hydrogen content showed high ductility. At higher hydrogen concentrations ($\sim$100 ppm) the ductility showed a linear decrease up to around 650 ppm. Samples with higher hydrogen content exhibited a brittle behavior and fractured at low bending angles, of around 15° independently from the hydrogen content. Moreover, the cladding fracture behavior was discussed. The crack initiated always at the bottom cladding region subjected to tension and at the PPI interphase closest to the loading axis. The cladding failed in a typical tensile mode and propagated in a mixed mode (tension and shear).

Finally, two impact tests were presented on fresh and hydrogenated cladding tubes mounted rigidly in the closed chamber (refer to section 2.3.2). The main observation refers to the amount of pellet release upon fracture. The fresh sample showed high ductility, as expected, and only a fraction of 1 pellet was released after loss of cladding's integrity. The hydrogenated sample showed almost no plastic deformation and extensive pellet release, which was associated to the depressurization process and the open pellet-cladding gap. This behavior is not representative since the cladding had extremely high hydrogen content and contained small alumina pellets; such configuration is not present in irradiated SNF rods, where the gap is closed and the pellets are bonded to cladding after a few irradiation cycles.

Chapter 4

Experimental investigation on irradiated samples

Abstract *The second phase of the experimental campaign consisted of the mechanical tests on irradiated PWR UO2 samples. The objectives of these tests are to macroscopically investigate the flexural mechanical properties of the composite cladding/fuel samples and to examine the fuel mass release in case of cladding integrity loss. The sample characteristics and preparation for the conduction of three-point bending and impact tests are described. The simple beam theory and the developed image analysis methodology are applied for the analysis of the samples' response in three-point bending and impact tests, respectively. Finally, a series of post-test examinations is performed to examine the cladding failure modes and to characterize the hydrogen concentration and hydride morphology of the claddings.*

4.1 Spent nuclear fuel samples

The samples used for the hot-test campaign consist of commercial spent fuel rods irradiated in PWR NPPs. The campaign was designed in the frame of a collaboration between JRC-Karlsruhe and Nagra, upon agreement with KKG and Framatome GmbH, who kindly allowed using the Framatome spent fuel rods, which had been irradiated in KKG and were temporarily stored in JRC-Karlsruhe for this study. The results from an additional PWR fuel rod, irradiated in KWG, have also been included in this study with permission from JRC-Karlsruhe.

Table 4.1 provides an overview of the main characteristics of these spent fuel rods. The rods consists of $UO_2$with duplex cladding with outer liner (DXD4).

Table 4.1 Characteristics of spent fuel rods used in this study.

Fuel rod ID	Fuel type	Cladding type	Avg. burnup [GWd/tHM]	Irradiation cycles	End of irradiation
KKG D02	UO2	DX Zr2.5Nb	100.5	10	08.06.2002
KKG D08	UO2	DX D4	46.9	3	02.06.2007
KKG A07	UO2	DX D4	58.6	4	31.05.2008
KKG A11	UO2	DX D4	18.3	1	31.05.2008
KWG A16-5	UO2	Duplex Zry-4	67.0	5	03.2001

The cladding DXD4 (widely employed in Swiss PWRs) consists of two layers, an outer thin one, which is highly corrosion resistant (low-tin and high-iron zirconium alloy D4), and a thicker inner layer of Zry-4, which forms the bulk of the cladding and provides most of the mechanical strength. Previous studies [102, 103] have shown that DXD4, compared to other cladding formulations from the same vendor, is more resistant to hydrogen pick-up and to corrosion, and shows better creep behavior. The hydrogen pick-up and potential hydride formation that could deteriorate the mechanical integrity of the cladding are the most important aspects relevant to the current study. The cladding of the KWG sample consists of two components; an inner Zry-4 component providing good mechanical properties, and an outer layer of Zr with relatively small additions of alloying elements (e.g. low Sn concentration) [104].

The criteria for selecting the rods to be tested was to include SNF rods having a wide range of burnup with the same type of cladding. The burnup variation of the selected group of rods offers the possibility to investigate its possible influence on their mechanical properties. The investigation will be extended to MOX rods (not included in the present study), being this a technical gap in the international experimental database [31]. The publication of the experimental data on the MOX fuel rod integrity investigations will take place within the EURAD project [105].

Concerning the samples from both SNF groups examined in this study, nominal dimensions of cladding and pellets are given in Fig. 4.2. The outer diameter of the claddings is 10.75 mm and the cladding thickness is 0.725 mm.

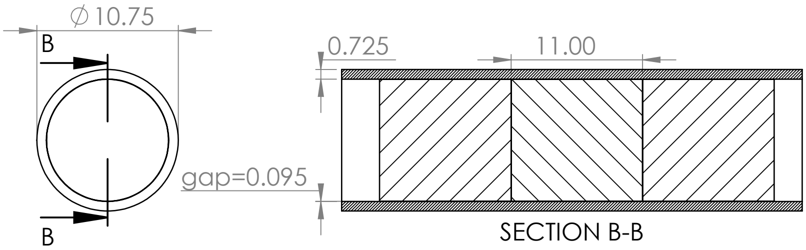

Fig. 4.1 Nominal dimensions for cladding and pellets of the SNF rods used in the current study.

The selected rods have different discharge dates, with cooling time up to the experiments ranging from 9 to 16 years. The SFAs have undergone a drying process in order to be encapsulated and transferred to the hot-cell facilities of JRC-KA. The heating caused by the drying process was not followed by a very slow cooling rate, similar to the conditions that SFAs are experiencing during dry-storage in TSC. Therefore, the hydride formation process would not be fully representative of SNF during standard dry storage conditions. More information on the hydrogen content and hydride orientation is given in section 4.6.

4.1.1 Post irradiation examinations

The following non-destructive PIE had been performed for the majority of the spent fuel rods for previous studies[1] [15–17]:

- visual inspection of the rod to identify noticeable defects;
- profilometry measurements to measure the fuel rod diameter along its length;
- eddy current testing for cladding defect detection;
- oxide film thickness measurements with the eddy current method;
- gamma spectra acquisition for leak-tight testing/cladding integrity control;
- gamma scanning of Cs-137 along the fuel rod length to acquire the axial burnup profile.

The PIEs have been performed in two phases. At first, each rod was inserted into a long hot-cell, where all the non-destructive examinations were conducted. Subsequently, the rods were introduced into a neighbouring α-β-γ hot-cell, where a series of destructive PIE was

---

[1] The results on KKG SNF rods belong to Framatome GmbH

performed. At first, each fuel rod was punctured to determine the rod internal pressure as well as the isotopic composition of the fission gases. Thereafter, the rods were segmented in segments of approximately 480 mm. Selected parts of these segments were used to perform hydrogen concentration measurements in the cladding; optical microscopy was performed using metallography and ceramography analyses for the cladding and the fuel, respectively. Part of these data have been used by JRC-Karlsruhe and Nagra for the development of the experimental campaign, with the agreement of Framatome GmbH and KKG.

4.2 Sample selection and preparation

Concerning the design of the three-point bending and impact tests conducted in this study, one main condition was to perform mechanical loading in regions of the rodlets that exhibit a rather constant burnup. The process for identifying such regions was based on results from the aforementioned gamma-scanning and profilometry measurements on the rods.

Fig. 4.2 shows an example of such results (in normalized units) from both types of measurements obtained for the rod with ID KKG-A07. At the bottom of the graph a drawing of the rod is given, where the position of each segment is highlighted. The significant drop that is repeatedly observed in both, counts and rod diameter due to locally lower burnup and smaller oxide layer, respectively, indicates the positions of the spacer grids.

As mentioned earlier, a well-suited segment for the purpose of this study should show a rather constant burnup profile, which can be observed for segments lying in the middle of the rod. Taking also into account the availability of segments, since some of them had already been used in previous destructive studies, segment 6 was considered to fulfill the criteria, and it was the segment selected from every rod used in this test campaign. It should also be noted that the region where segment 6 lies, the upper half of the rods, shows increased oxidation and is thus even more interesting for being examined in the context of this study.

At first, the selected segments were subjected to three-point bending and after fracture the remaining of the segment was used for impact test. The sample preparation for the spent fuel rod segments is mainly the same as that for the cold-test campaign (see chapter 3). A significant difference is that the SNF samples were re-pressurized with helium to the rod internal pressure (RIP) as measured at room temperature by puncture tests, as given in Table 4.2. Moreover, end-plugs were used to seal the segment with no spring placed at one end, as in the case of the surrogate samples.

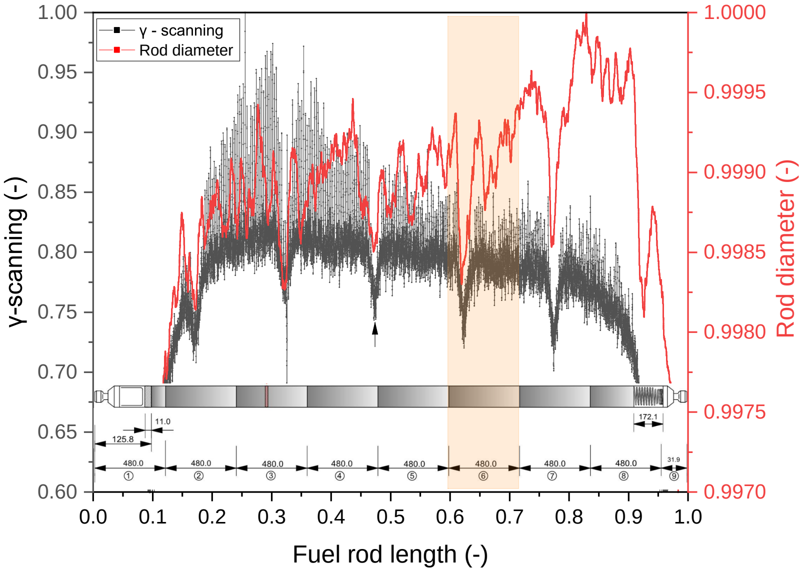

Fig. 4.2 Gamma scanning and profilometry measurements on a KKG spent fuel rod. Segment number 6, highlighted in orange, was used from each rod to perform the mechanical tests.

Table 4.2 Rod internal pressure of SNF rods, measured with puncture tests at room temperature.

Fuel rod ID	Average burnup [GWd/tHM]	RIP [bar]
KKG A11	18.3	29.4
KKG D08	46.9	39.3
KKG A07	58.6	68.4
KKG D02	100.5	105.9
KWG A16-5	67.0	70.0

4.3 Three-point bending tests

For the conduction of the three-point bending tests on SNF rodlets, the parts of the experimental setup were inserted separately and reassembled in the hot-cell, whereas the controller was installed outside the cell to protect it from radiation damage. Fig. 4.3 show the testing of a SNF sample in the hot-cell.

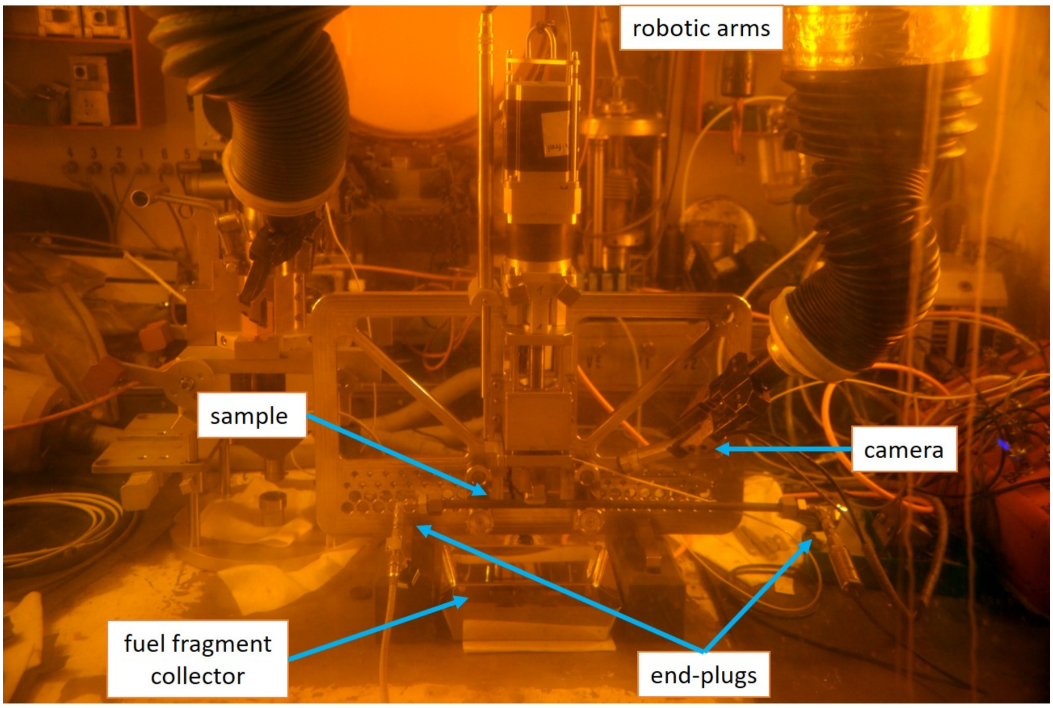

Fig. 4.3 Three-point bending device installed in hot-cell at JRC-Karlsruhe.

Each sample was weighted before and after the test to determine the mass release upon fracture. In addition, the heavier fuel fragments were collected at the bottom of the device. The small mass difference between the two measurements refers to aerosol and fine particulates that were not deposited onto the fuel fragment collector. The bending response of the sample was also captured with a camera, placed in front of the sample by the robotic arms.

Similarly to the analogue tests on surrogate samples, applied load, rod internal pressure and displacement were recorded. The loading rate and data frequency were set to $1\,\mathrm{mm\,min^{-1}}$ and $20\,\mathrm{Hz}$, respectively. In contrast to the analogue tests, each sample was pressurized to its measured RIP at room temperature, as given in Table 4.2. Different end-plugs had to be used in order to achieve internal pressure of more than 40 bar. The first bending test on sample

KKG A07 was performed with RIP of 32 bar (instead of 68.4 bar), since the end-plugs had not yet been replaced by that time.

Fig. 4.4 illustrates the typical response of an SNF rodlet (KKG A07) subjected to three-point bending test, showing a sequence of photograms as recorded by the camera inside the hot-cell. The visual inspection of the sample's response provides useful qualitative information on its ductility and on the overall performance of the test (i.e. sample alignment, cross-head movement, etc.). The recording of the sample's bending response with the use of the camera is the first step of a thorough analysis and series of post-test examinations that were used to characterize the fracture behavior and the cladding material (refer to section 4.6).

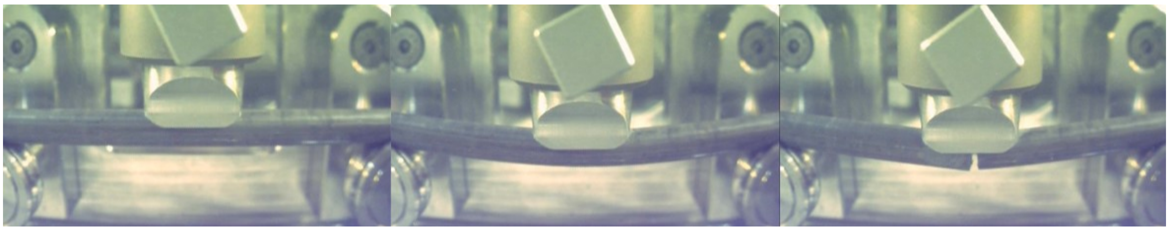

Fig. 4.4 Bending response of the irradiated sample KKG A07 as recorded by the camera inside the hot-cell.

4.3.1 Experimental results

Fig. 4.5 shows the load-displacement curves from bending tests performed on the SNF rod selected segments. For the sake of comparison, the results from the two tests performed on fresh Zry-4, with and without the presence of alumina pellets, are also plotted in the same graph. SNF samples showed higher bending strength due to irradiation hardening. In addition, the slope of the elastic region increases with the burnup of the rods (e.g. among samples A11 and A07). Different factors might contribute to this increasing trend, such as the slightly different cladding elastic properties due to different burnup (or irradiation time) [100], and the slight difference in the SNF cross-section due to increased oxide layer thickness in higher burnup rods.

All samples fractured under plastic deformation; the low burnup rodlet showed much higher ductility compared to the higher burnup samples, but smaller ductility if compared to fresh Zry-4 claddings. In comparison to the fresh claddings, the yield point of the low burnup sample was slightly higher (approximately 10%), however the development of the plastic region was similar. This indicates that the relative contribution of the pellets to the

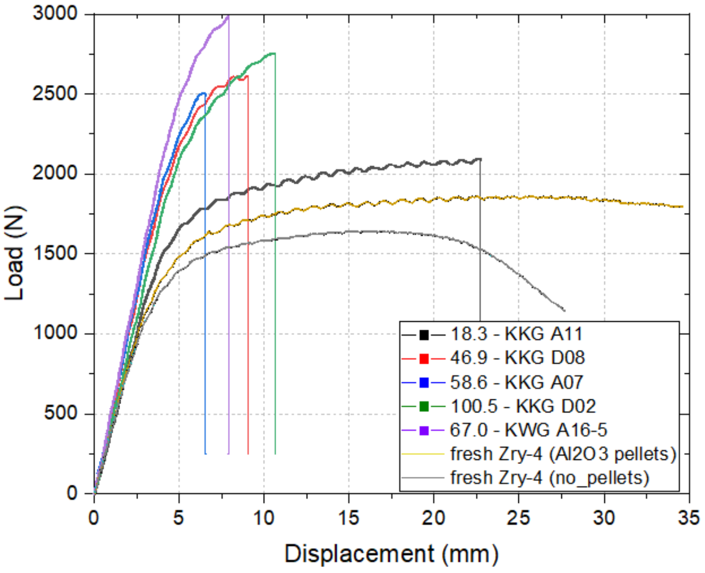

Fig. 4.5 Load-displacement curves from bending tests on SNF rodlets and fresh Zry-4 samples.

bending strength of the samples is comparable. Moreover, the low burnup sample showed lower bending strength compared to the higher burnup samples, which fractured at 25-50% higher loads. Finally, the KWG sample fractured at ∼10% higher load, which was probably caused from the difference in the cladding and rod fabrication process compared to the other samples.

Table 4.3 gives the experimental results on displacement, bending angle and load at fracture point along with the associated uncertainties (refer to section B). In addition, the work or the energy absorbed from the sample unit fracture is given, calculated from the integral of the load-displacement curve.

Table 4.3 Experimental results of three-point bending tests on irradiated PWR rodlets.

Sample ID	**Burnup [GWd/tHM]**	**Displacement at fracture [mm]**	$3U_\delta$ **[mm]**	**Bending angle at fracture [°]**	$3U_\alpha$ **[°]**	**Load at fracture [N]**	$3U_F$ **[N]**	**Work [Nmm]**
KKG A11	18.3	22.7	0.4	39.7	0.9	2088	14	39 420
KKG D08	46.9	9.1	0.4	15.4	0.8	2611	14	15 890
KKG A07	58.6	6.6	0.4	11.0	0.7	2489	14	9119
KKG D02	100.5	10.7	0.4	18.1	0.8	2749	14	18 304
KWG A16-5	67.0	7.9	0.4	13.3	0.8	2984	14	13 296

Fig.4.6a illustrates the bending angle and load at fracture point as function of burnup. Samples A11, D08 and A07, being rodlets from SNF rods with Zry-4 cladding irradiated at KKG, show a nearly linear correlation on the bending angle to fracture against burnup, as highlighted in Fig. 4.6b. The correlation of the fracture angle to burnup is performed qualitatively and is subjected to several error sources since the fracture of an irradiated sample depends on various physical and geometrical parameters such as the local hydrogen content of the cladding, the hydride morphology and orientation, the cladding and oxide layer thickness, the pellet positioning, the RIP etc. All these variables can influence the local plastic strains developed in the cladding, which, in turn, limit the ductility of the material. The identification of a correlation between sample's ductility and rod's average burnup can be attributed to the commonalities characterizing these samples, since they share the same fuel rod type with similar nominal geometrical/mechanical properties and the same axial position.

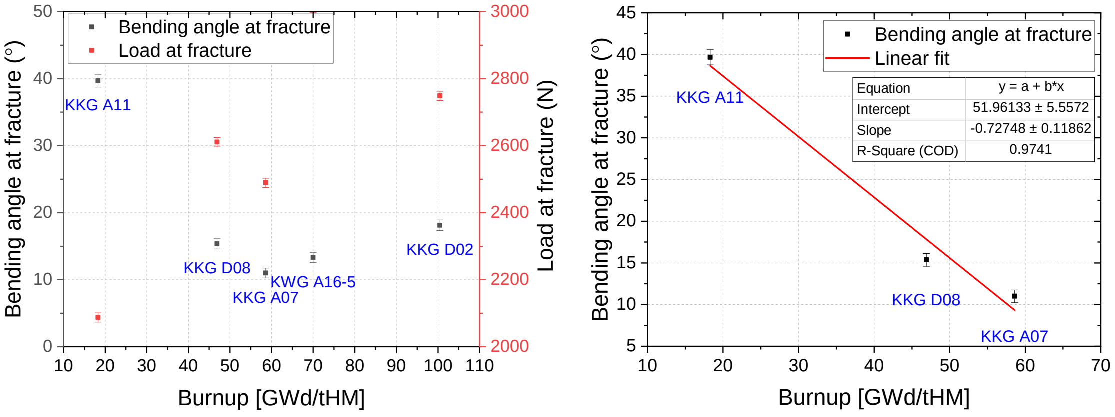

(a) (b)

Fig. 4.6 a) Bending angle and load to fracture as a function of burnup under three-point bending test; b) linear fit of bending angle to fracture as function of bunup for the KKG samples with Zry-4.

Therefore, the flexural ductility, under quasi-static loading, of the considered KKG fuel rods can be expressed as a linear correlation of the bending angle to fracture to the rod's average burnup as:

$$\alpha_f = 51.96 - 0.73x \tag{4.1}$$

,where α_f is the bending angle to fracture and x is the rod's average burnup. This correlation can be considered for samples' burnup ranging from 18.3 to 58.6 GWd/tHM.

To evaluate the rod's response beyond this burnup range, the results obtained on surrogate materials from three-point bending tests could be used. Concerning samples of lower burnup their behavior is expected to be softer and bounded by the results obtained for the fresh Zry-4, as presented in Fig. 4.5, characterized by higher plastic deformation and lower yield strength.

The behavior of samples with burnup higher than the tested rodlets, could be assessed by closely examining the results of the hot and cold tests. At first, the sample KKG A07, being the one of the highest burnup including DXD4 cladding, has shown very limited plastic deformation fracturing at only 6.6 mm of displacement. Considering this result, a significant further decrease of the ductility in higher burnup samples is not expected. Moreover, results generated from three-point bending tests on the hydrogenated Zry-4 samples (refer to section 3.3.3) showed that after a certain hydrogen concentration ($\sim$650 ppm) the flexural response of the surrogate samples reached a plateau and fractured at similar bending angles of around 14°. Based on this observation, the sample KKG A07 (highest burnup and hydrogen concentration (see section 4.6.3)), which fractured at bending angle of 11°, can be considered as a limiting case on the flexural response of irradiated rods. Taking also into account results from previous studies showing that the hydrogen content of irradiated Zry-4 increases with increasing burnup [106], it can be assumed that samples with higher burnup (compared to KKG A07) would exhibit similar flexural behavior as the KKG A07 sample.

The RIP was also recorded during the experiments. Fig. 4.7 presents the depressurization process of the irradiated samples upon fracture. The time to ambient pressure is very small (of the order of seconds) for all samples. The pressure drops immediately after fracture, but the depressurisation becomes slower as burnup increases, since the gap between pellet and cladding closes. Taking into account the results from tests on surrogate rods (refer to section 3.3.3) and the effect of the depressurization process, one could infer that in terms of potential mass release, the lower burnup samples could represent more severe cases. However, the fast depressurization did not cause an extensive fuel release, even for the case of the low burnup sample. More details are given in section 4.6.2.

It must be noted that the gas permeability data could be relevant in other assessments concerning the safety of spent fuel rods, e. g. in the assessment of drying procedures of defective pins.

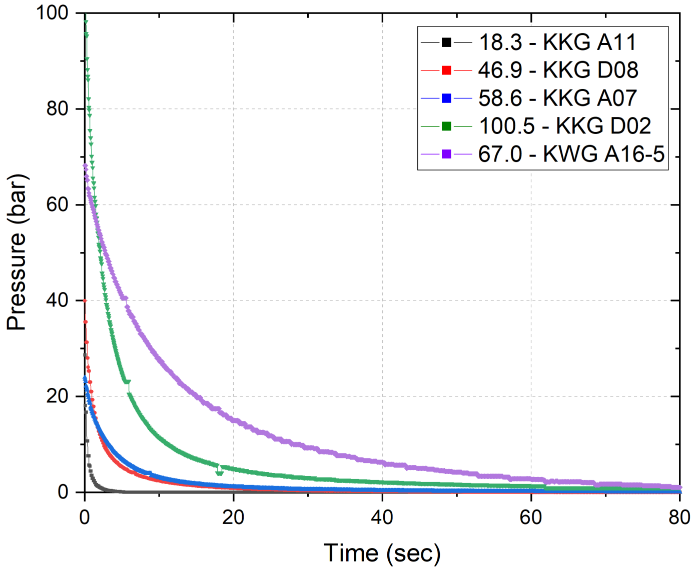

Fig. 4.7 Segment pressure drop after fracture as function of time.

4.4 Impact tests

Fig. 4.8 shows the impact test device installed in the hot-cell, where its main features are highlighted. The high-speed camera is stored in a glove-box, outside of the hot-cell to be protected from radiation exposure. The guide tube of the device is handled by the robotic arms and a crane. In this way, the "closed-chamber" can be opened to place and remove the samples and the hammer.

Two different loading geometries have been used for the conduction of the impact tests. The first includes fixed supports (or rigid sample holders, refer to section 2.3.2), whereas the second includes simple supports, allowing the sample to rotate, similarly to the three-point bending tests (refer to section 2.3.3). Modifications in the loading geometry of this setup were performed during this study, and after the initiation of the experimental campaign. The first test was performed on the KWG fuel rod with the use of fixed supports, where IA could not be applied. The following tests on the KKG rod segments have been conducted on the final version of the device including the simple supports.

The objective of the further development/optimization of the impact device was to allow a direct comparison of experimental results between three-point bending and impact tests by considering similar loading configuration in both cases (more details in section 2.3.3). Minor

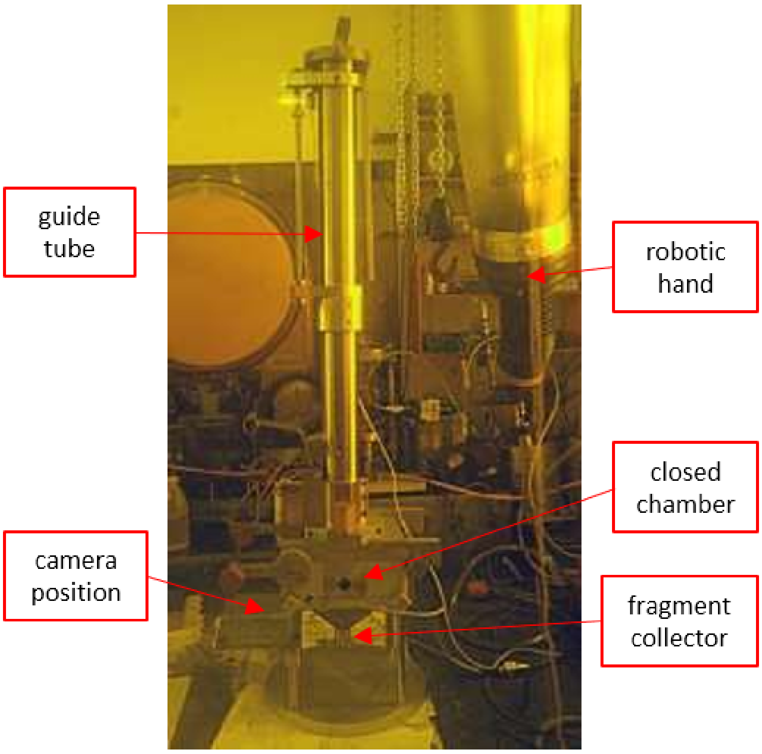

Fig. 4.8 Side view of the impact test device installed at the hot-cell.

modifications on the loading point allowed the analysis of the sample's dynamic response with the use of dedicated IA techniques (refer to section 2.3.4). Thereafter, the influence of the strain rate to the sample's flexural response could be investigated.

The sample preparation was similar to the three-point bending test as the end-plugs were used to repressurize and seal the sample to the desired internal pressure (refer to section 4.2). The end-plugs had no influence on the bending tests, where quasi-static loads are applied. However, these parts change the mass and geometry of the sample, and could therefore influence its flexural response, since inertia effects are relevant for impact loadings. Such effects are discussed in Appendix C.

4.4.1 First test on old impact setup

The first test was performed on a sample from the KWG rod [107, 85]. The fuel rod segment was pressurized to 40 bar, different than the nominal internal pressure (being approximately 70 bar), since by that time the sealing end-plugs available could not withstand pressure higher than 40 bar. For this test, the sample was mounted rigidly on a stable metallic block near the column bottom end and a 8.5 kg hammer was used. The frequency of the high speed camera was set to 2000 Hz. Fig. 4.9 shows a sequence of photograms recorded by the high speed camera illustrating different moments preceding, during and after the impact on the rodlet.

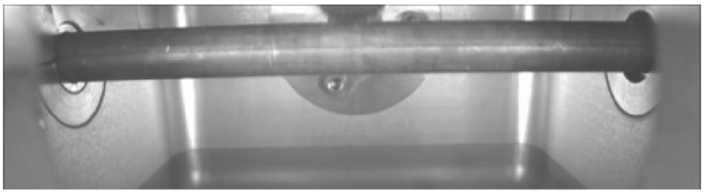

(a) Photogram showing the rodlet immediately prior to the impact with the falling hammer.

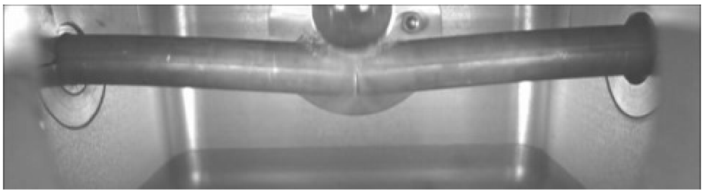

(b) Photogram illustrating the outer oxide layer removal and the first cracking and depressurization under the impacting hammer.

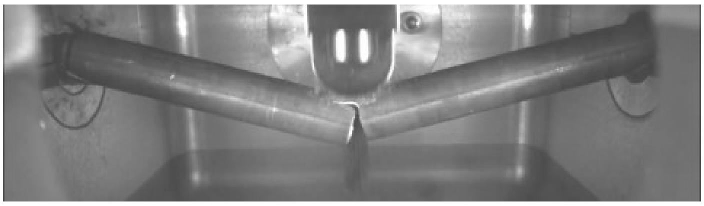

(c) Photogram illustrating the additional cracking at the sample mount locations under the impacting hammer and the fuel release from the fractured rodlet.

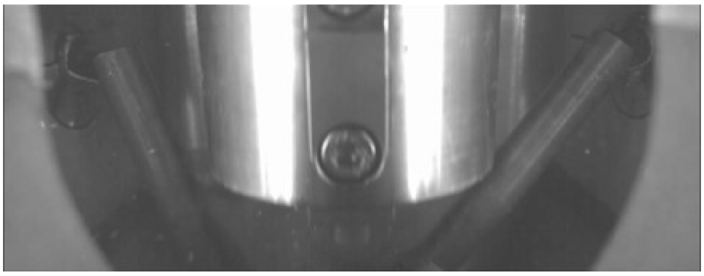

(d) Photogram illustrating fuel and cladding particulate floating in the chamber after the rodlet fracture.

Fig. 4.9 Representative photograms illustrating the dynamic response under impact of a pressurized PWR UO2 rodlet irradiated to a burnup of 67 GWd/tHM at KWG.

The first effect of the impact is the shattering of the outer oxide layer in the vicinity of the hammer rodlet contact region, as shown in Fig. 4.9b. The sample initially cracks in the middle span under the impact of the hammer. The failure modes and subsequent fuel release are evident in Fig. 4.9c. The sample broke at the bottom surface subjected to tension and the crack propagated in a typical tensile mode. At the top surface it can be noticed that the crack direction is horizontal indicating mixed failure mode (shear and tension). In addition, the sample breaks also at the support locations, since it is rigidly mounted. Fig. 4.9c shows also the broken pieces of the rodlet floating in the chamber and the dispersion of the fine particulates released.

4.4.2 Impact test campaign using the new setup

The following impact tests were performed on the KKG and KWG samples (A11, D08, A07, D02 and A16-5) repressurized to their nominal rod internal pressure at room temperature (refer to Table 4.2). For these tests, the rigid sample holders were replaced with the simple rounded supports, similarly to the three-point bending case, as shown in Fig. 2.35. In addition, the heavier 10.5 kg hammer was used in comparison to the first test performed on the KWG, since higher impact energy was required for the new loading configuration (refer to section 2.3.3).

The frequency of the high-speed camera was set to 4000 Hz, except for the test on sample KKG-A11 which was set to 2500 Hz. In order to achieve that, the view of the high-speed camera was shrunk to focus on the movement of the hammer's cross head. Fig. 4.10 shows the dynamic response of the samples subjected to impact testing with the use of representative frames before and after the samples' rupture.

Typically, the sample deforms under dynamic loading and the oxide layer around the hammer area, being the region with the highest local strain, detaches from the rodlet. The sample cracks at the bottom surface subjected to tension and the depressurization of the sample is visible as fine particulates from the fuel and cladding are floating in the closed chamber. Once the crack has propagated and the rupture is established at the sample's midspan, larger fuel fragments are released from the area at the close vicinity of the crack. The big fragments are collected at the bottom of the closed chamber, while the fine particulates and aerosol are captured by the micro-filters connected to the chamber's aspiration system or are deposited on the inner walls of the testing chamber.

The ductility of the samples can be evaluated from the amount of deformation undergone before fracture. A first qualitative indication is given by a direct comparison from the frames in which the first crack is observed. To this extent, Fig. 4.11a is used where the image size from all frames was adjusted to the rod size and, subsequently, the samples have been aligned. The red line indicates the upper position of the rodlet or the moment that the hammer touches the sample. In Fig. 4.11b the frames when the first crack occurred for each sample are shown. The relative ductility of the samples can be estimated from their displacement to fracture. Similarly to the three-point bending tests, the first three samples, having the same type of cladding DXD4, showed decreased ductility with higher burnup. The fourth sample, being

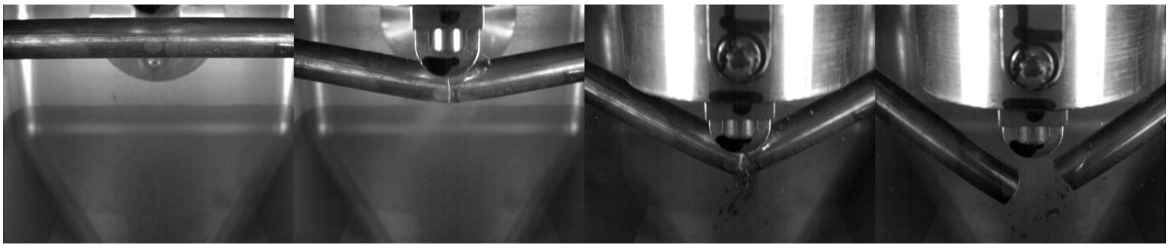

(a) Selected frame sequence illustrating dynamic response of sample KKG A11.

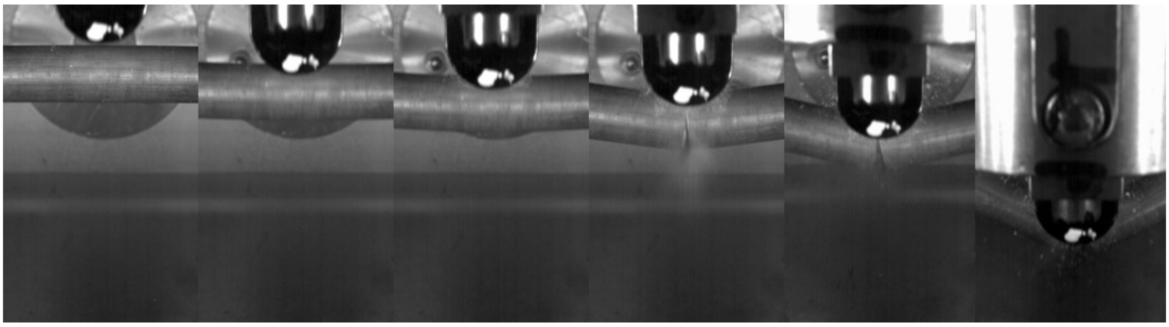

(b) Selected frame sequence illustrating dynamic response of sample KKG D08.

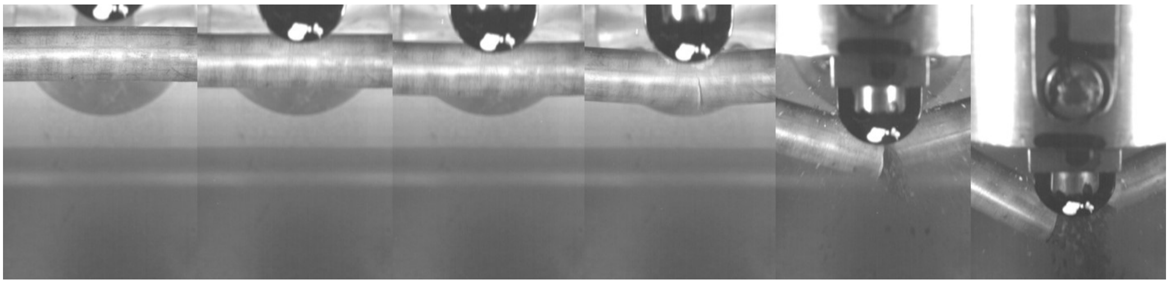

(c) Selected frame sequence illustrating dynamic response of sample KKG A07.

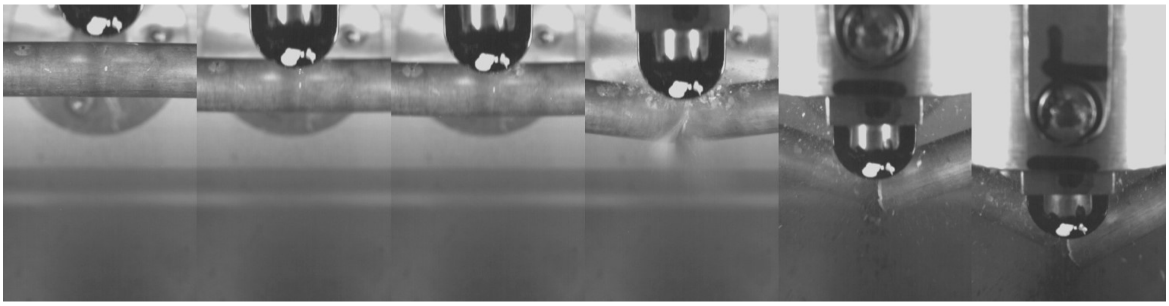

(d) Selected frame sequence illustrating dynamic response of sample KKG D02.

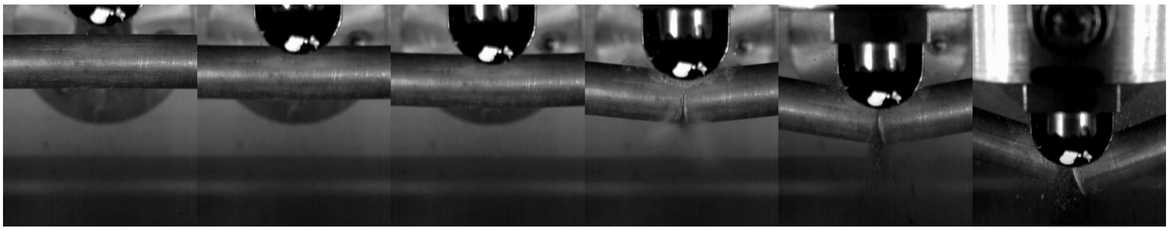

(e) Selected frame sequence illustrating dynamic response of sample KWG A16-5.

Fig. 4.10 Representative photograms illustrating the dynamic response under impact of pressurized PWR UO2 rodlets.

of the highest burnup, exhibited larger deformation until fracture compared to the other two samples of high burnup, as observed in the three-point bending test.

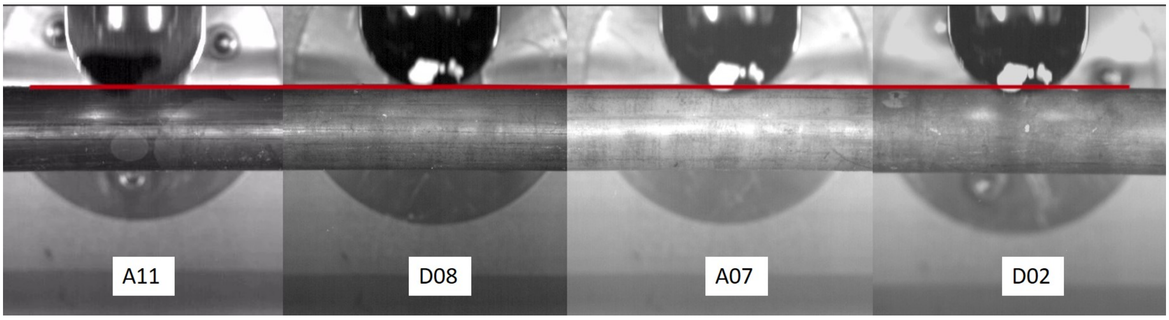

(a) Selected frames before impact loading adjusted to rod size for all KKG samples.

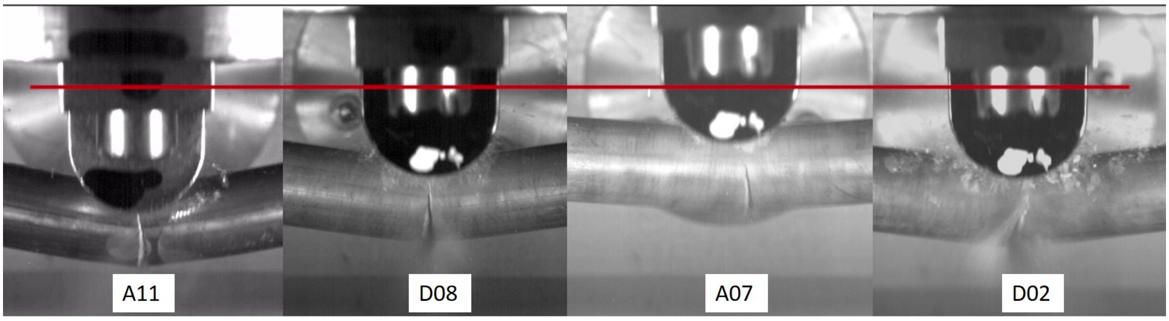

(b) Frame when first crack observed for all KKG samples.

Fig. 4.11 Qualitative indication of KKG samples' ductility as function of burnup from direct comparison of their deformation to fracture.

These results provide valuable information on the samples' ductility as function of burnup. In addition, they provide proof that plastic deformation occurs even in cases of higher strain rates, such as the impact loading. Nevertheless, in order to quantify the resulting deformations IA is required.

4.4.3 Results from Image Analysis

Image analysis has been applied to the impact test performed on KKG and KWG rods, following the methodology described in section 2.3.4. Initially, spatial calibration of the acquired images was performed for every experiment by measuring the pixel length variation along the symmetry axis (vertical) of the lower horizontal axis of the impactor (refer to Fig. 2.45a). Since the real length of this axis is known, the dimension of the pixels in mm was derived for each axial position (refer to Fig. 2.45b).

Subsequently, the Image-PRO software was used to track the object drawn on the impactor. The process relies on the application of a series of filters in order to enhance the contrast of the images and isolate the object. Consequently, the centre of mass was derived for each frame, as shown in Fig. 2.46. By applying the spatial calibration as resulted for each test, the hammer's or the tracked object velocity can be calculated.

The final results of the IA methodology are shown in Fig. 4.12. The velocity of the tracked object (namely the hammer) for each frame is plotted against time. In addition, the first and last frame (at rod failure) of the impact are highlighted in each graph. The impact duration was in range of 1.25 to 4 ms, depending on the ductility of the sample. In all tests, the velocity of the loading point was found to be slightly lower than the hammer's theoretical free-fall velocity, confirming the validity of the method.

The energy absorbed from the sample until fracture can be derived from the difference of the hammer's kinetic energy before impact until the point of first crack (or complete rupture). In addition, the displacement to fracture can be calculated from the cumulative distance of the loading point at these frames. Finally, the error is estimated as the combined uncertainty resulting from the spatial calibration and geometrical characteristics of the impact loading and the sample. The uncertainty resulting from the object tracking method was not considered since it cannot be quantified. The following tables provide the results of the impact tests on KKG fuel rodlets upon application of the IA methodology. The displacement, bending angle and work are given with regard to the first crack and complete sample rupture in Tables 4.4 and 4.5, respectively.

Table 4.4 Impact test results until sample crack initiation for the KKG fuel rodlets.

Sample ID	**Burnup [GWd/tHM]**	**Displacement at first crack [mm]**	$3U_\delta$ **[mm]**	**Bending angle at first crack [°]**	$3U_\alpha$ **[°]**	**Work at first crack [Nmm]**	$3U_W$ **[Nmm]**
KKG A11	18.3	11.25	0.05	19.0	0.3	43.6	2.1
KKG D08	46.9	8.66	0.05	14.5	0.2	23.2	2.5
KKG A07	58.6	4.34	0.15	7.2	0.3	6.3	6.9
KKG D02	100.5	7.42	0.15	12.4	0.3	17.0	5.5
KWG A16-5	67.0	6.40	0.05	10.7	0.2	14.7	3.8

To put these results into perspective and better understand the effect of the strain rate, the following figures provide a comparison of the derived quantities in bending and impact tests. Figs. 4.13a and 4.13b show the displacement and bending angle to fracture for both tests. The low burnup sample (KKG A11) achieved approximately two times higher deformation (or bending angle) until fracture in three-point bending compared to impact test. On the other

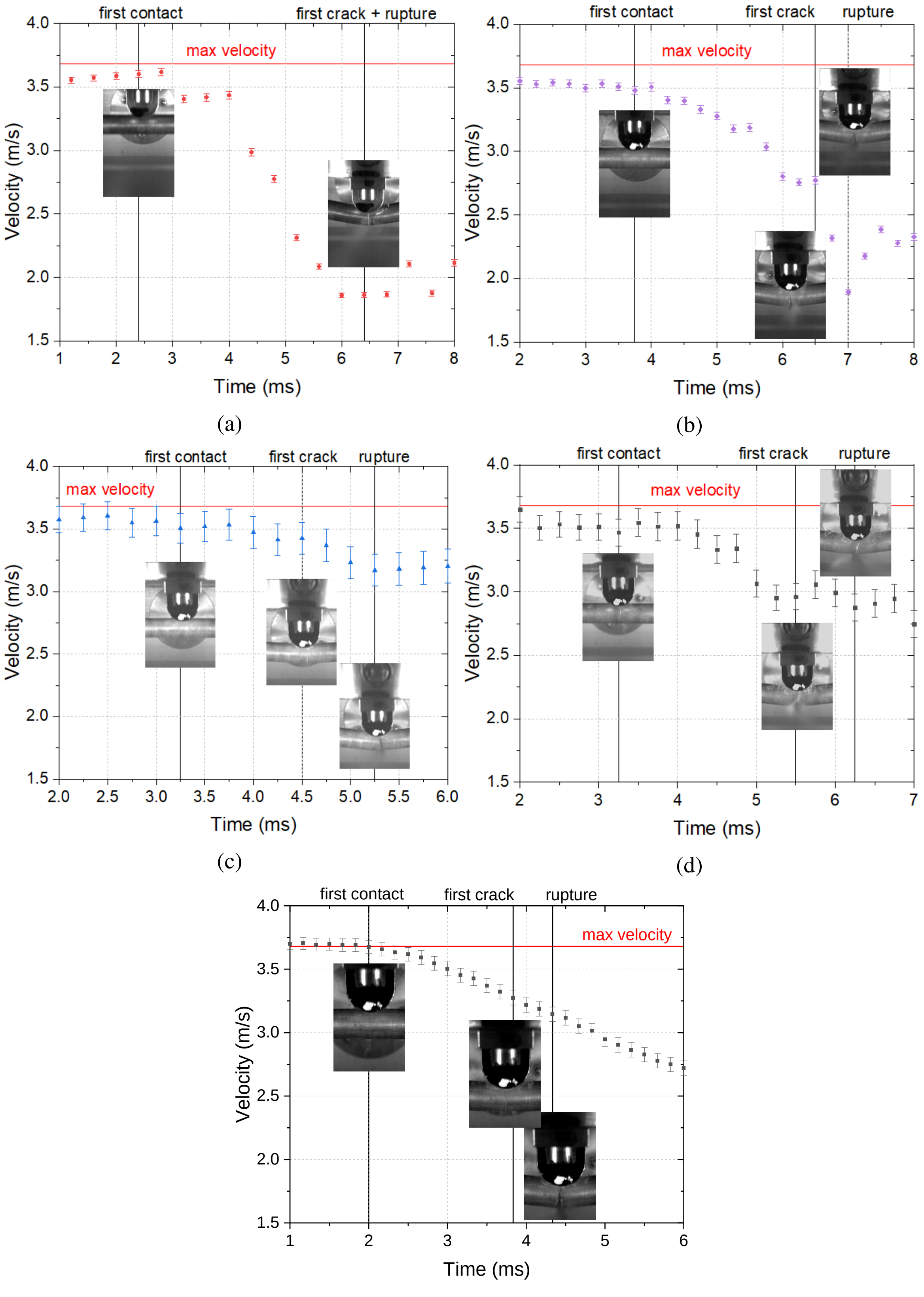

(a)

(b)

(c)

(d)

(e)

Fig. 4.12 Hammer’s velocity as derived from IA for the impact test on samples a) KKG A11, b) KKG D08, c) KKG A07, d) KKG D02 and e) A16-5.

Table 4.5 Impact test results until sample rupture for the KKG fuel rodlets.

Sample ID	Burnup [GWd/tHM]	Displacement at fracture [mm]	$3U_\delta$ [mm]	Bending angle at fracture [°]	$3U_\alpha$ [°]	Work at fracture [Nmm]	$3U_W$ [Nmm]
KKG A11	18.3	11.25	0.05	19.0	0.3	43.6	2.1
KKG D08	46.9	9.71	0.04	16.3	0.2	44.8	2.2
KKG A07	58.6	6.79	0.16	11.3	0.3	13.5	6.7
KKG D02	100.5	9.65	0.15	16.2	0.3	19.7	5.4
KWG A16-5	67.0	7.99	0.05	13.4	0.2	19.0	3.7

hand, the high burnup samples exhibited similar behavior in both tests. The displacement and bending angle to fracture were slightly smaller for the impact case; however, they were comparable for all samples. As a result, the ductility of the samples is less dependent on the burnup under higher strain rates.

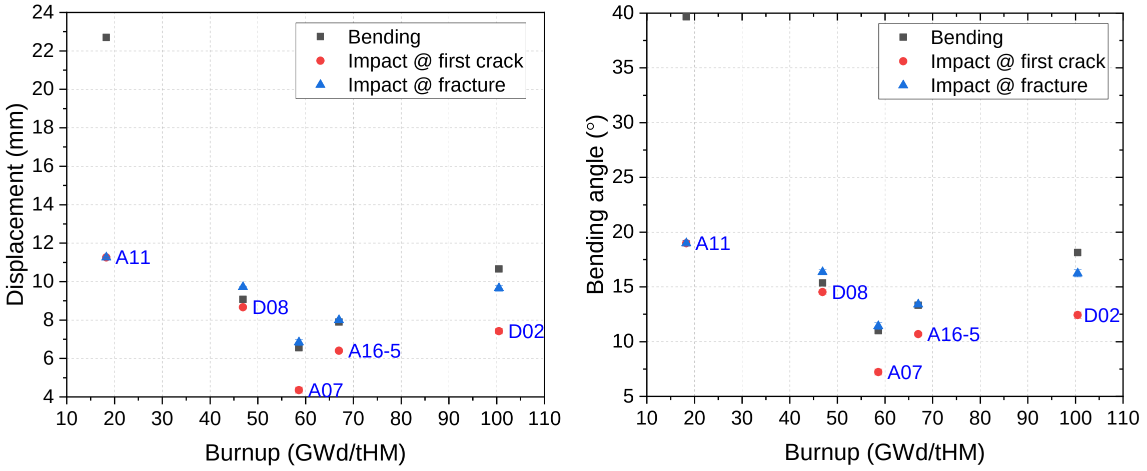

(a) (b)

Fig. 4.13 Comparison of samples' ductility in bending and impact test as function of their a) displacement and b) bending angle to fracture.

The work or energy absorbed from the sample until fracture is plotted in Fig. 4.14. The results of the impact tests are similar to those from the three-point bending tests, showing higher energy requirements to cause sample fracture as burnup decreases. For the first three samples, which have the same cladding type, the energy depends linearly on burnup. The work in impact tests was found to be slightly higher (approximately 5-10%); however, this might be a consequence of the end-plugs use, which changed the sample geometry and total mass. Since inertia effects are relevant in dynamic loadings, the use of end-plugs affects the derived quantities. A thorough analysis on the sensitivity of these results is given in Appendix C.

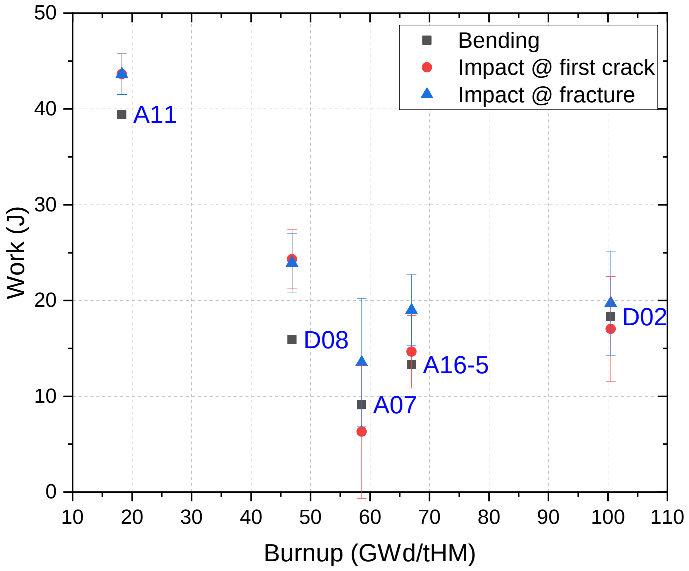

Fig. 4.14 Work of absorbed energy until fracture of the SNF rodlets subjected to three-point bending and impact.

4.5 Static flexural properties of irradiated PWR rods

The flexural properties of the irradiated PWR SNF samples were derived from the three-point bending test results, based on the assumptions of the simple beam theory, as described in section 2.2.5. The flexural stress-strain curves for beam elements with circular and hollow-circular cross-sections are provided in Figs. 4.15a and 4.15b, respectively.

The mechanical properties with the corresponding uncertainty (refer to Appendix B) describing the flexural behavior of the samples are given in Tables 4.6 and 4.7 considering a beam element with hollow-circular and circular cross-sections, respectively. The elastic regime is described with the flexural modulus and yield strength. The yield strength implies the level of flexural stress at which the material under load ceases to behave elastically and begins to yield. The identification of this point includes a level of uncertainty, since this transition is not always apparent. For this reason, the 0.2% offset yield strength is also

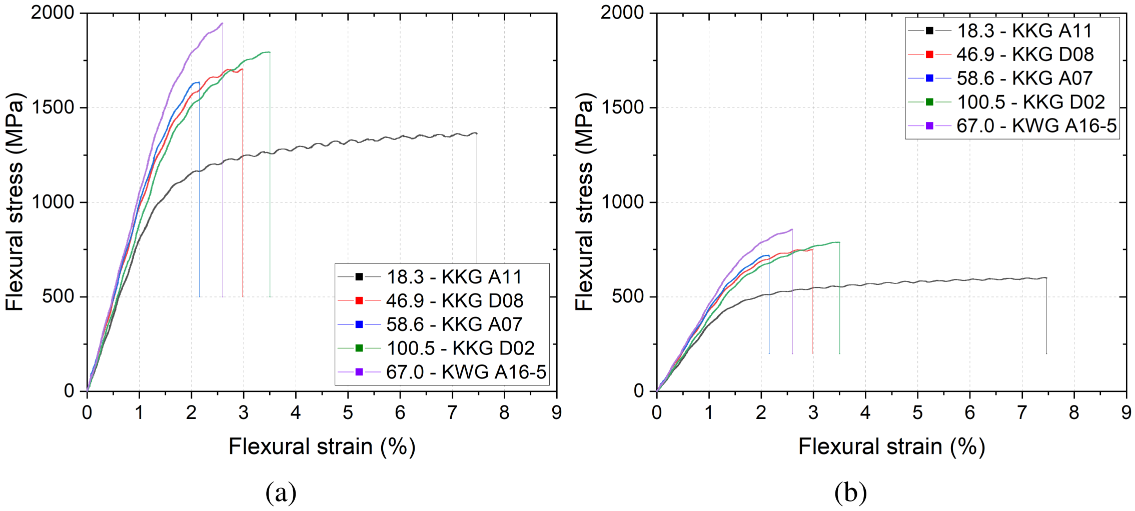

(a) (b)

Fig. 4.15 Flexural stress-strain curves for beam elements with a) hollow-circular and b) circular cross-sections derived from three-point bending tests on pressurized SNF rodlets.

provided corresponding to the amount of stress that will result in a plastic strain of 0.2%. In addition, the ultimate flexural strength, flexural strain to failure and toughness are given.

Table 4.6 Flexural mechanical properties of beam elements with hollow-circular cross-sections derived from the three-point bending results.

Sample ID	Flexural modulus [MPa]	u_E [MPa]	Yield strength [MPa]	u_{σ_γ} [MPa]	0.2 Yield strength [MPa]	$u_{\sigma_{\gamma_{0.2}}}$ [MPa]	Ultimate strength [MPa]	$u_{\sigma_{max}}$ [MPa]	Failure strain [-]	$\varepsilon_{\sigma_{fail}}$ [-]	Toughness [MPa]
A11	81140	4042	930	24	1095	29	1440	38	0.075	8.0E-04	85.1
D08	101097	5034	1158	30	1512	40	1794	47	0.030	5.4E-04	34.1
A07	104131	4854	1188	31	1572	41	1721	45	0.022	5.1E-04	20.9
D02	91409	3482	1299	34	1519	40	1891	49	0.035	5.6E-04	42.0
A16-5	109487	4443	1479	39	1795	47	2049	53	0.026	5.3E-04	31.1

Table 4.7 Flexural mechanical properties of beam elements with circular cross-sections derived from the three-point bending results.

Sample ID	Flexural modulus [MPa]	u_E [MPa]	Yield strength [MPa]	u_{σ_γ} [MPa]	0.2 Yield strength [MPa]	$u_{\sigma_{\gamma_{0.2}}}$ [MPa]	Ultimate strength [MPa]	$u_{\sigma_{max}}$ [MPa]	Failure strain [-]	$\varepsilon_{\sigma_{fail}}$ [-]	Toughness [MPa]
A11	33905	1458	388.8	3.8	457.8	1.8	601.8	5.6	0.075	8.0E-04	37.4
D08	42244	1815	484.0	4.6	631.9	2.1	749.6	6.9	0.030	5.4E-04	15.0
A07	43512	1735	496.3	4.7	656.3	2.2	719.3	6.6	0.022	5.1E-04	9.2
D02	38196	1160	543.0	5.1	634.9	2.1	790.0	7.3	0.035	5.6E-04	18.5
A16-5	45750	1511	618.1	5.7	750.9	2.4	856.3	7.9	0.026	5.3E-04	13.7

The cladding flexural elastic properties were derived assuming that beam elements with hollow-circular cross-section can well describe its elastic flexural behavior (refer to section 3.3.3). Fig. 4.16a shows the cladding Young's modulus of the different SNF samples calculated based on the three-point bending test results. These values are in very good agreement with observations from different studies [99–101, 55]. The first four data points refer to DXD4 claddings showing a nearly linear increase with burnup. This increase could possibly originate from the difference in the oxide layer and bulk Zry-4 material thickness in different burnup. The Young's modulus of the oxide layer is significantly higher compared to Zry-4, therefore as its thickness increases with burnup, this could result in higher average elastic modulus of the claddings. These values are in very good agreement with observations from different studies [99–101, 55].

Finally, the yield strength and 0.2% offset yield strength are shown in Fig. 4.16b. These results reveal the higher toughness of higher burnup samples, as consequence of the higher irradiation damage. In addition, the difference between these quantities for each sample could indirectly indicate the steepness of the transition to plastic deformation. Higher values represent less ductile behavior and the resulting differences confirm the observations of the samples' flexural response, as shown in Fig. 4.15a.

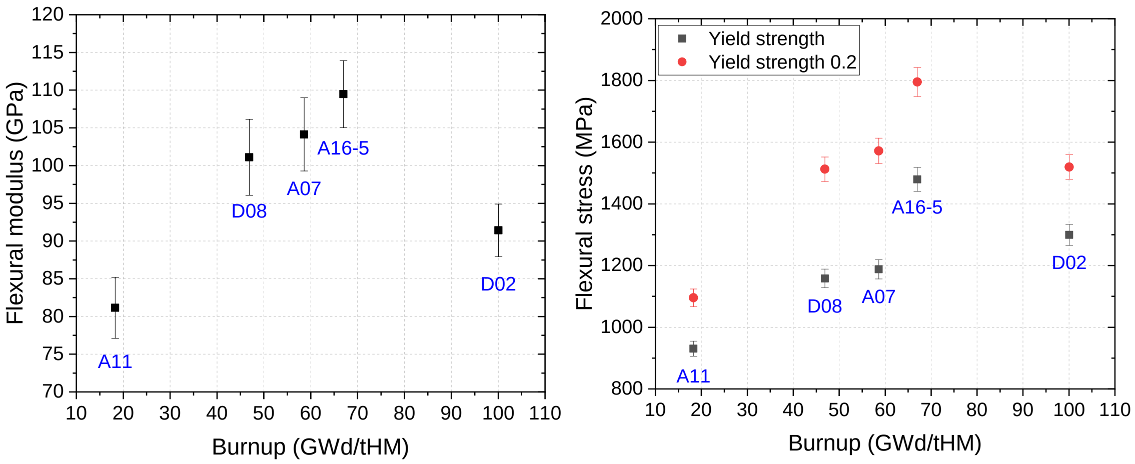

(a) (b)

Fig. 4.16 a) Flexural modulus of elasticity and b) yield strength and 0.2% offset yield strength derived from three-point bending results for beam elements with hollow-circular cross-section.

4.6 Post-test examinations

A series of post-test examinations has been performed in order to characterize the state of the fuel rodlet upon fracture, the cladding material in terms of hydrogen concentration and hydride morphology, and the fuel mass release in terms of mass and size distribution. The following section describes the methods used and provides the corresponding results for all SNF rods tested under three-point bending and impact.

4.6.1 Fracture behavior

After the completion of the mechanical tests, the resulting broken pieces were visually inspected to examine the cladding failure modes and to qualitatively assess the fuel mass release. Figs. 4.17 and 4.18 provide representative photograms of the two pieces of the fractured rodlet samples after bending and impact tests, respectively.

The first and most important outcome is that defueling was not observed in any of the tests. The release was only limited to the volume directly affected by the loading point at the fracture area. The bonding between the pellet and cladding was found to be the most significant mechanism preventing any excess fuel release. That was particularly important for the high burnup fuel samples, which exhibited less ductile behavior. Moreover, the higher extent of plastic deformation of the low burnup samples also restrained fuel release, since the gap was somewhat closed by deformed cladding, as shown in Fig. 4.17a.

In addition, similarly to the cold tests, the crack initiation occurred at the bottom cladding surface subjected to tension and preferentially at the pellet-pellet interphase closest to the loading axis. In this region the cladding failed due to higher local plastic strain. The pellet directly under the loading point appears to be fractured and part of it was released upon cladding failure. The neighbouring pellet appears to have remained intact, as clearly illustrated in Figs. 4.17a, 4.17c and 4.18a.

Transverse fractures at the rod cross-section were observed in all samples after the bending tests. The cladding surfaces at the crack initiation fractured at an angle indicating shear failure, as shown in Figs. 4.17a and 4.18b. On the contrary, there were cases where the crack propagated in a mixed failure mode under impact loads. This type of fracture exposed higher region of the pellet, as it can be seen in Fig. 4.18b, which in turn could lead to additional fuel release in case of pellet fragmentation.

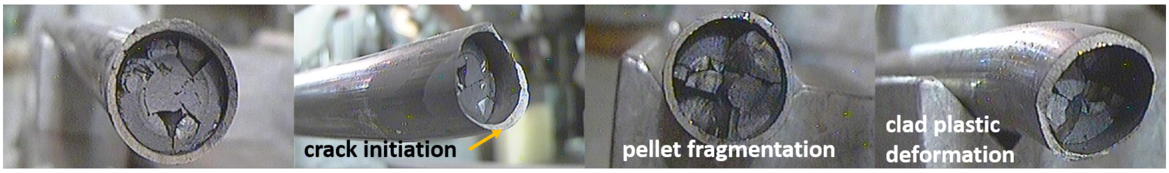
crack initiation
pellet fragmentation
clad plastic deformation

(a) Fracture surfaces after bending test of sample KKG A11.

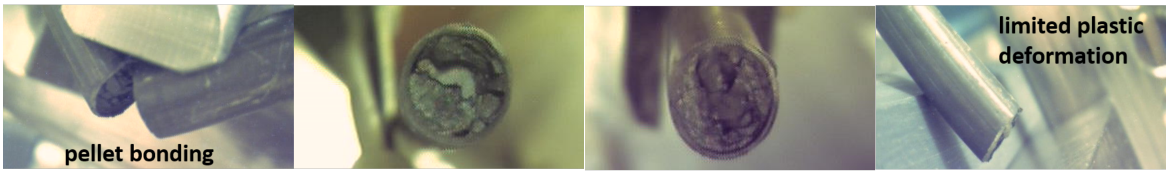
pellet bonding
limited plastic deformation

(b) Fracture surfaces after bending test of sample KKG D08.

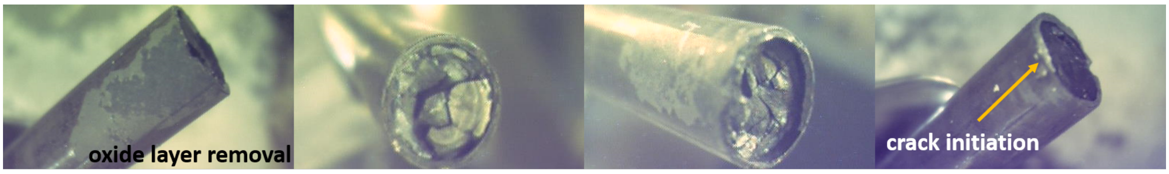
oxide layer removal
crack initiation

(c) Fracture surfaces after bending test of sample KKG A07.

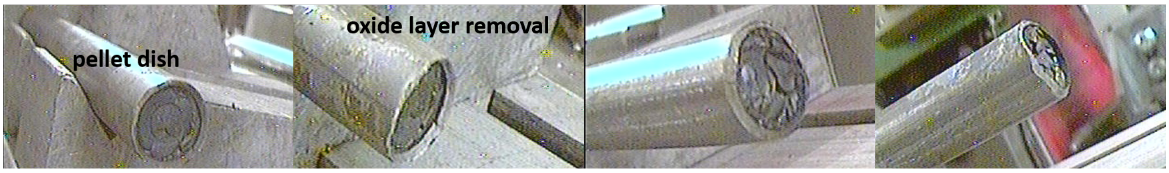
pellet dish
oxide layer removal

(d) Fracture surfaces after bending test of sample KWG A16-5.

Fig. 4.17 Failure profiles of SNF rodlets subjected to three-point bending test.

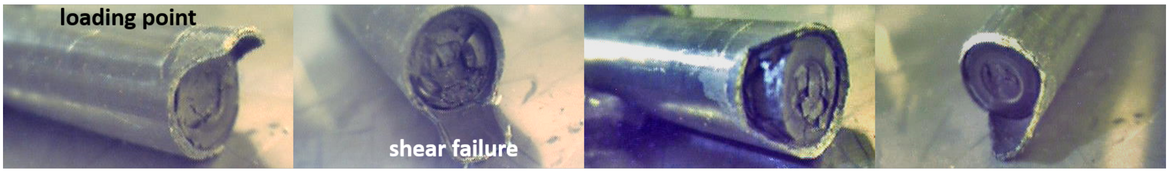
loading point
shear failure

(a) Fracture surfaces after impact test of sample KWG A16-5.

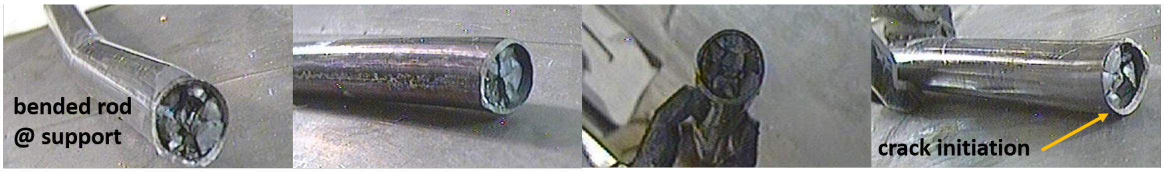
bended rod
@ support
crack initiation

(b) Fracture surfaces after impact test of sample KKG A11.

Fig. 4.18 Failure profiles of SNF rodlets subjected to impact test.

Finally, the removal of the oxide layer at regions close to the fracture points was observed. This had already been noticed in impact tests from the high-speed camera photograms; however the same behavior was observed in bending tests, as shown in Figs. 4.17a, 4.17c and 4.18a. At these areas, the local strains at the cladding exceed the yield point and the thin oxide layer that was formed during irradiation is detached from the cladding.

4.6.2 Fuel mass release

The released fuel was collected upon completion of the mechanical tests, in order to be weighted and characterized. The total release was indirectly measured from the mass difference between the weight of the original sample and the sum of the weight of the resulting broken pieces upon fracture. Bigger fragments, mainly resulting from the pellet cracking, were captured at the bottom of the three-point bending device and of the impact device closed chamber. The fine particulates and aerosols released after impact were captured onto 3 µm and 8 µm filters, which were installed in the aspiration system of the impact testing chamber.

Table 4.8 gives the fuel mass release per fracture for the tested SNF rodlets after impact and bending tests. In all cases the total mass per fracture was less than one pellet confirming that no excessive fuel release occurred during these tests. That was also observed from the photograms shown in Fig. 4.17, where the dish of the fuel pellet is shown at one fracture side and only a part of the pellet at the other fracture side.

Table 4.8 Fuel mass release per fracture resulting from three-point bending and impact tests on SNF rodlets.

Sample ID	Average burnup [GWd/tHM]	Bending fuel release [g]	Impact fuel release [g]
KKG A11	18.3	1.64	2.55
KKG D08	46.9	1.06	1.59
KKG A07	58.6	1.18	2.09
KKG D02	100.5	4.20	4.54
KWG A16-5	67.0	0.99	2.33

Fig. 4.19 summarises the results of the previous table, showing tendencies between fuel burnup and fuel mass release per fracture for bending and impact conditions. At first, the release was always higher in impact tests indicating that the higher strain rate affected bigger part of the pellets positioned directly under the cross-head. Moreover, the low burnup fuel

sample showed higher release compared to the two higher burnup samples, due to the open (or not well established) gap between the pellets and the cladding. Concerning the high burnup samples, the fuel release increased with increasing burnup. The overall fuel release behavior of the samples in bending and impact, or in static and dynamic loadings, could be estimated with the use of a second order polynomial fit, simply to highlight the trend without having any physical explanation, as:

$$m_r = A + B1x + B2x^2 \tag{4.2}$$

,where x is the rod's average burnup and the fitting parameters for impact and bending are given in Table 4.9.

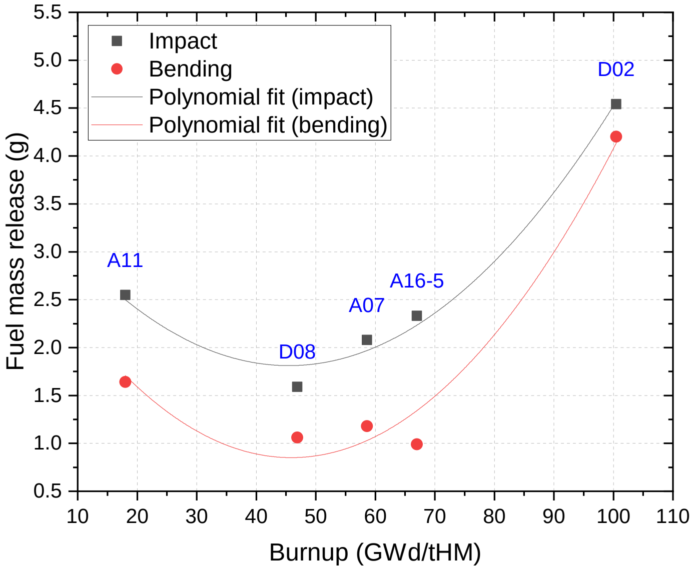

Fig. 4.19 Fuel mass release per fracture of SNF rod samples under impact and bending tests.

Table 4.9 Fit parameters of second order polynomial Eq.4.2 estimating fuel mass release per fracture in bending and impact.

Test type	A	A	B1	B1	B2	B2	Statistics
	Value	Standard Error	Value	Standard Error	Value	Standard Error	Adj. R-Square
Impact	3.6977	0.36929	-0.08295	0.0133	9.12E-04	1.08E-04	0.97072
Bending	3.1721	0.60051	-0.10115	0.02163	1.10E-03	1.76E-04	0.94614

The heavy fuel particles collected after the impact tests at the bottom of the impact chamber were sieved and classified based on their size. The mass of the collected fragments was approximately 99.5% of the total mass release. Fig. 4.20 shows the fractional size distribution of the sieved particles. After sieving, the particles were classified in five classes based on their size. Most of the particles (in terms of volume fraction) were larger than 1000 µm. In all cases, similar density for each class (especially for the KKG samples) was observed.

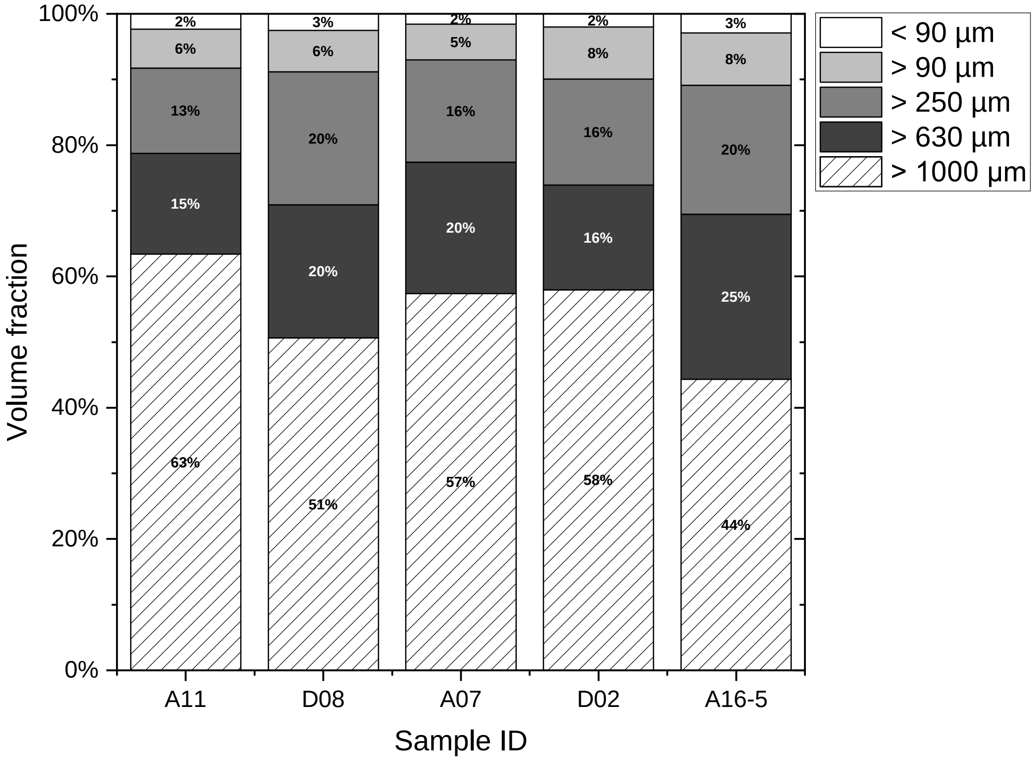

Fig. 4.20 Fractional size distribution of the heavy particles collected at the bottom of the testing chamber after impact tests.

The missing fraction of 0.5% corresponds to the aerosol and fine particulates deposited on the inner walls of the testing chamber or collected on the filters coupled with the aspiration pump, which "vacuumed" the test chamber before, during and after the impact experiment (this mass includes also released fission gases and He used to pressurize the spent fuel segment).

Fig. 4.21 shows SEM micrographs of the fine particulates that deposited onto the filters after impact tests. Figs. 4.21b and 4.21b give representative SEM micrographs collected on the 8 µm filter, at different magnification levels, after the impact test on sample KWG A16-5. Figs. 4.21b and 4.21b. Figs. 4.21c and 4.21c show a representative micrograph after SEM and BSE analysis on the 3 µm filter after the impact test on sample KKG A07. EDX analysis performed on the selected micrographs indicates that the majority of the particles are fuel fragments with a small fraction originating from the cladding.

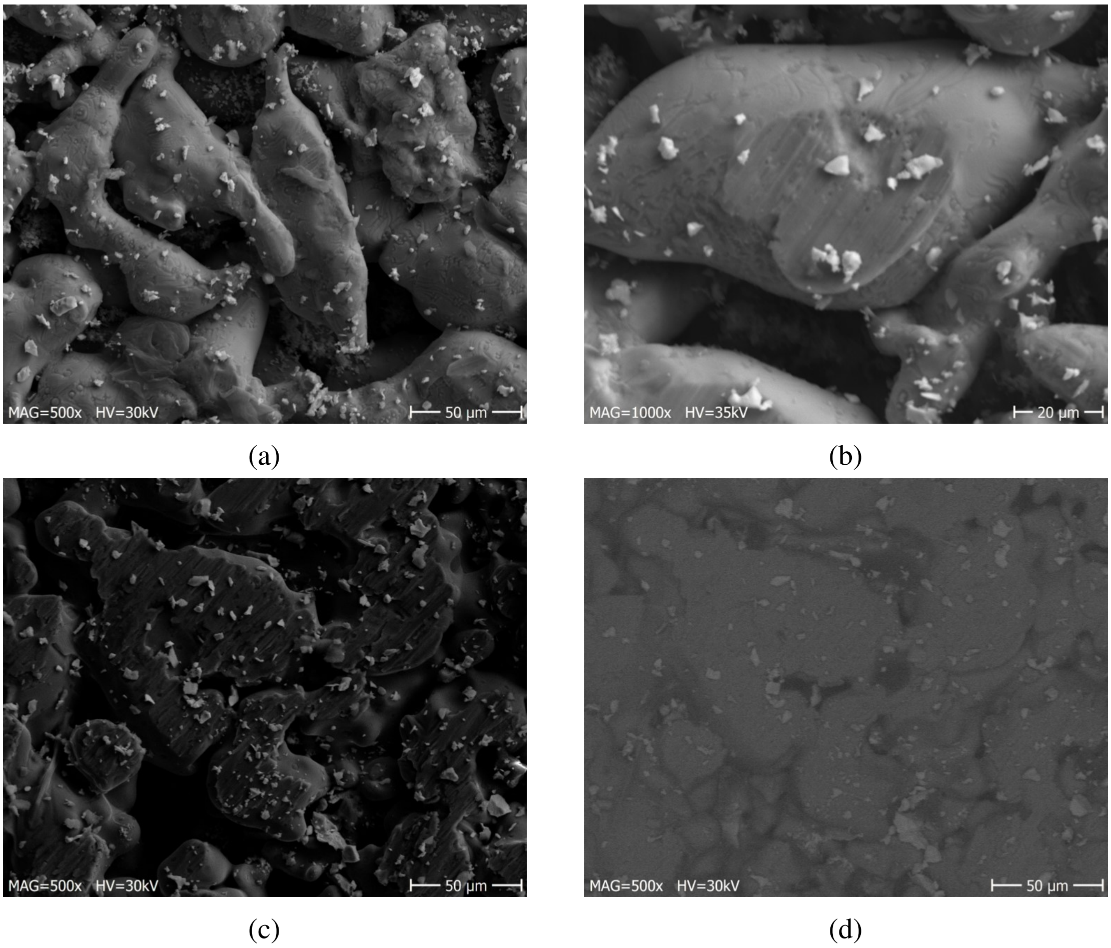

(a) (b) (c) (d)

Fig. 4.21 SEM micrographs showing fine fuel particles filtered through a) & b) 8 µm, and c) & d) 3 µm mesh filters coupled with the aspiration device connected to the impact testing chamber after the impact test on samples a) & b)KWG A16-5, and c) & d) KKG A07.

The particles deposited on the inner walls of the testing chamber were also characterized by SEM-EDX. These particles were obtained by swiping the walls with adhesive conductive tapes. This allowed obtaining information on the morphology and the origin of the released particles. Fig.4.22 shows SEM micrographs of the fine particulates collected on the carbon filter, at different magnification levels, after impact test of the sample KWG A16-5. The fuel particles reveal a variety of morphologies, as they originate from different radial locations of the fuel pellet, as shown in Figs. 4.22b and 4.22d.

The presence of relatively large (up to tens of microns in size) particles, as shown in Fig. 4.22c, having the typical morphology of the high burn-up structure (HBS) confirms that restructured fuel in HBS regions does not necessarily fragment into individual grains, but follows rather discrete cracking patterns. Nevertheless, numerous sub-micron grains were also found.

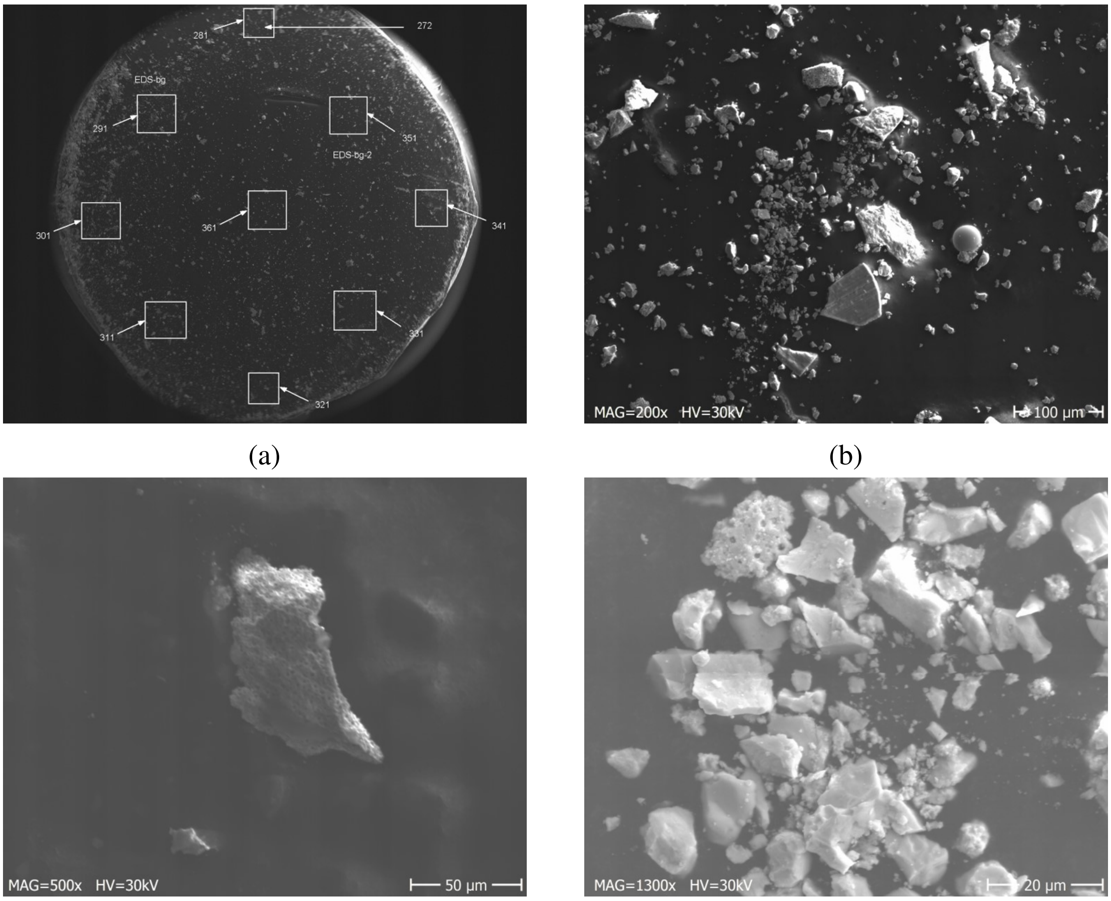

(a) (b)

(c) (d)

Fig. 4.22 SEM micrographs of particles collected from a swipe of the lower inner walls of the testing chamber after impact test on fuel KWG A16-5.

The micrographs were processed to classify the particles according to their Equivalent Circle Diameter (ECD). Cladding oxide particles were also detected, as they were distinguished in the micrographs with the BSE technique, but were excluded from the analysis. Indicatively, the process followed for this classification is illustrated in Fig. 4.23 showing an SEM micrograph resulting after the impact test on sample KKG A07. Image analysis was used to isolate the fuel particles and their size was classified based on their ECD, as indicated by different colour coding in Fig. 4.23c.

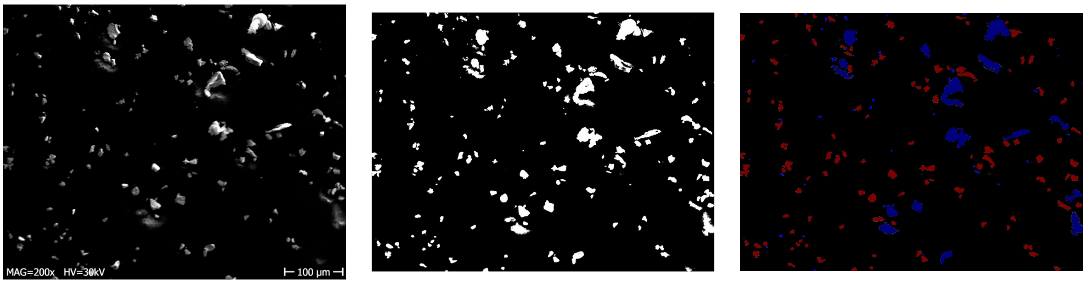

(a) (b) (c)

Fig. 4.23 Classification of fuel particles based on their ECD from SEM photographs resulting from impact test on sample KKG A07.

The resulting histograms in Fig. 4.24 represent the average number of particles (or fractional size) of each ECD size class. The histograms indicate log-normal distributions and the average particle size for each measurement is shown in the graph. Finally, in all cases a considerable amount the samples is constituted of sub-micron particles.

4.6.3 Hydrogen concentration at fracture

The hot-gas extraction method was used to measure the hydrogen content at the fracture surfaces of the cladding after impact and bending. Carrier gas hot extraction (CGHE) is a commonly applied technique for determination of hydrogen in claddings based on the accelerated hydrogen effusion due to thermal activation at elevated temperatures. Fig. 4.25 shows the process for the preparation of the cladding samples used for CGHE hydrogen measurements. For this purpose, small cladding rings were cut at the fracture side from the broken samples resulting after rupture.

A new method for the hydrogen measurement calibration is proposed in this study. A detailed description of this methodology is given in Appendix D. Fig. 4.26 provides the average hydrogen concentration measured for the different SNF samples after impact (black dots) or bending (red dots) tests. As expected, the hydrogen content of the first three Zry-4 samples from KKG, A11, D08 and A07 increases with higher burnup. The fourth KKG sample D02 with the highest burnup has lower hydrogen content due to the different cladding material (DX Zr2.5Nb). Finally, the KWG A16-5 sample from a different vendor has lower hydrogen content compared to the high burnup samples D08 and A07 from KKG.

It can be clearly observed that the sample's ductility, as explained in section 4.4.3, is strongly related to the cladding's hydrogen content. Concerning the KKG samples with DXD4 cladding (A11, D08 and A07), there is a clear correlation between the cladding's

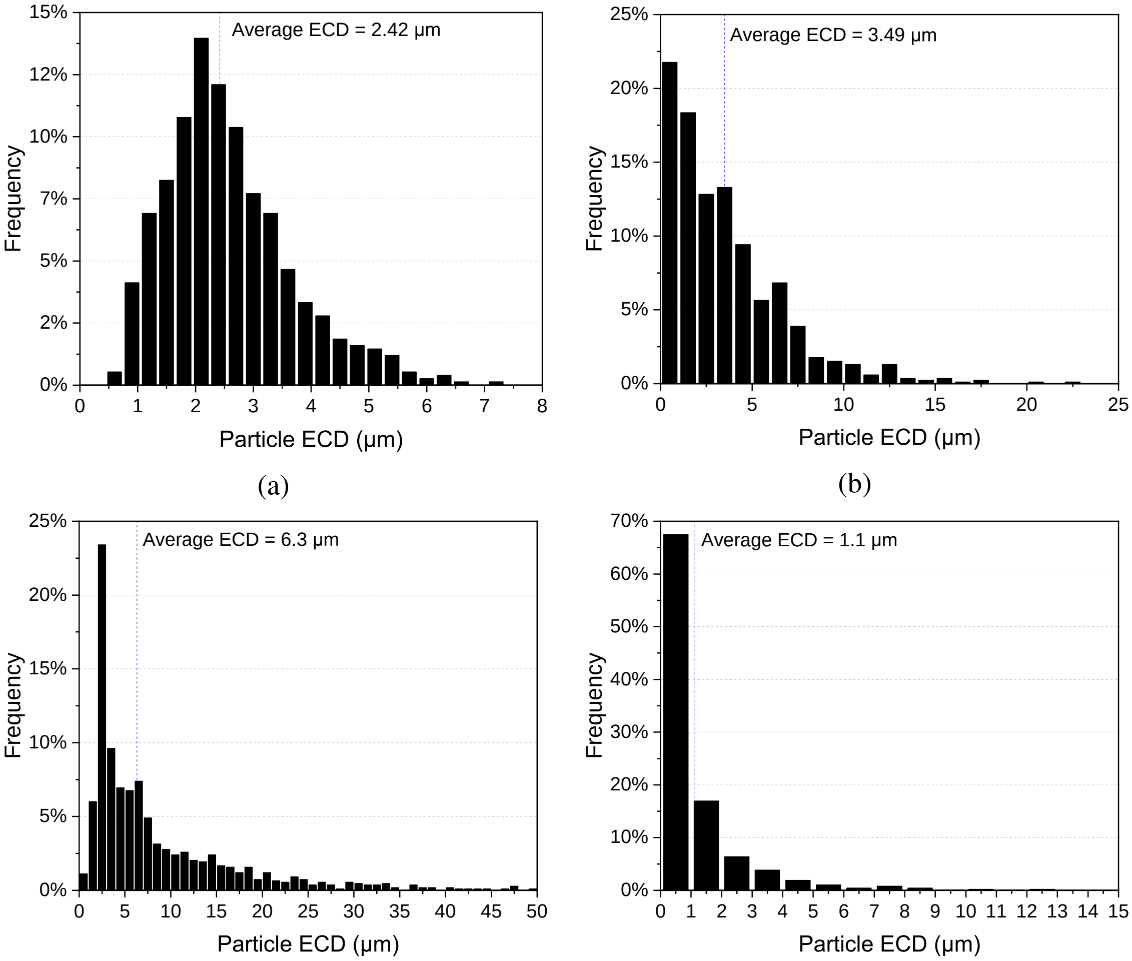

(a) (b)

(c) (d)

Fig. 4.24 Fractional size distribution of particles deposited on a) 8 µm vacuum filter after impact on sample KWG A16-5 and on carbon filters after impact on samples b) KKG A11, c)KKG A07and d) KKG D02.

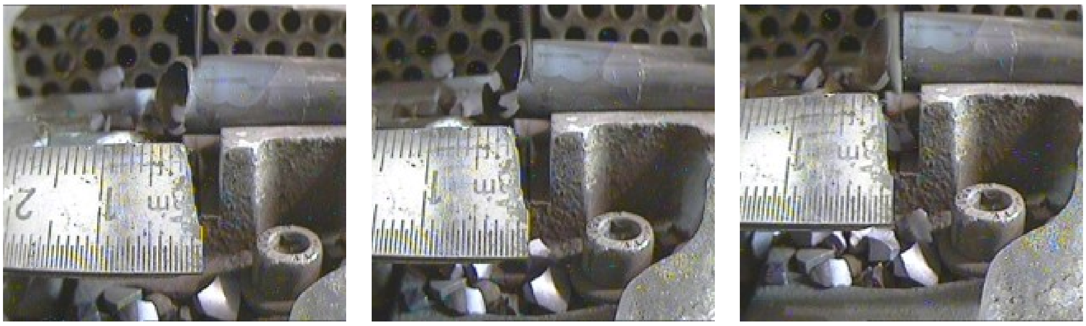

(a) (b) (c)

Fig. 4.25 SNF rodlet cutting for sample preparation to perform cladding hydrogen concentration measurements.

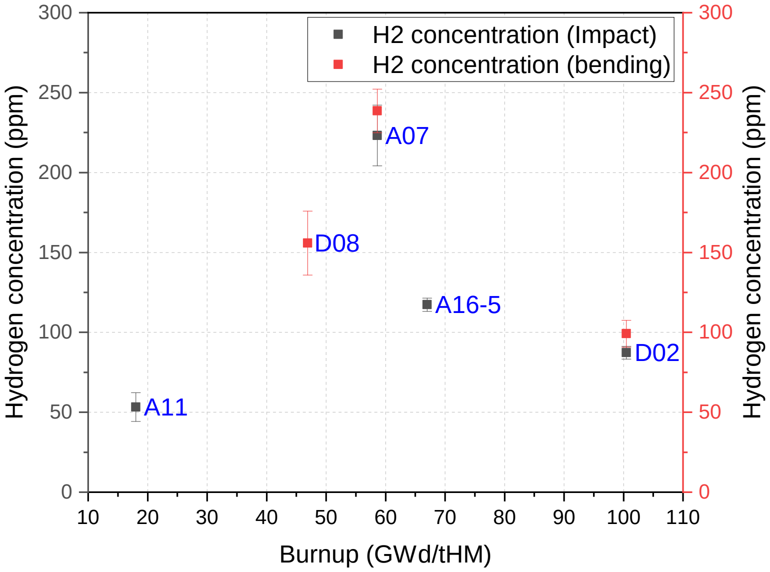

Fig. 4.26 Hydrogen concentration at cladding fracture region as measured with the hot-gas extraction method.

hydrogen content and the rod's average burnup. Fig. 4.27a shows the relation between these two quantities, which could be very well described by a second order polynomial fit, in the form given in Eq.4.2. In addition, the bending angle to fracture as function of the cladding's hydrogen content is given in Fig. 4.27b. Higher hydrogen content results in lower sample's ductility or lower bending angle to fracture. This behaviour can also be well described by a second order polynomial fit. The fitted parameters with their corresponding error are given in both graphs.

4.6.4 Hydride morphology

Small samples of approximately 5 mm in length were cut at the direct vicinity of the fracture point after each mechanical test. The samples were embedded in sample holders and after polishing and chemical etching, they were submitted to the optical microscope for examination of the hydrides population, characterization of their morphology and measurement of the geometrical characteristics of the cladding.

Fig. 4.28 gives an overview of the metallographic examinations performed on each sample, except for sample KWG A16-5. Angular positions (noted in sample KKG D02) are

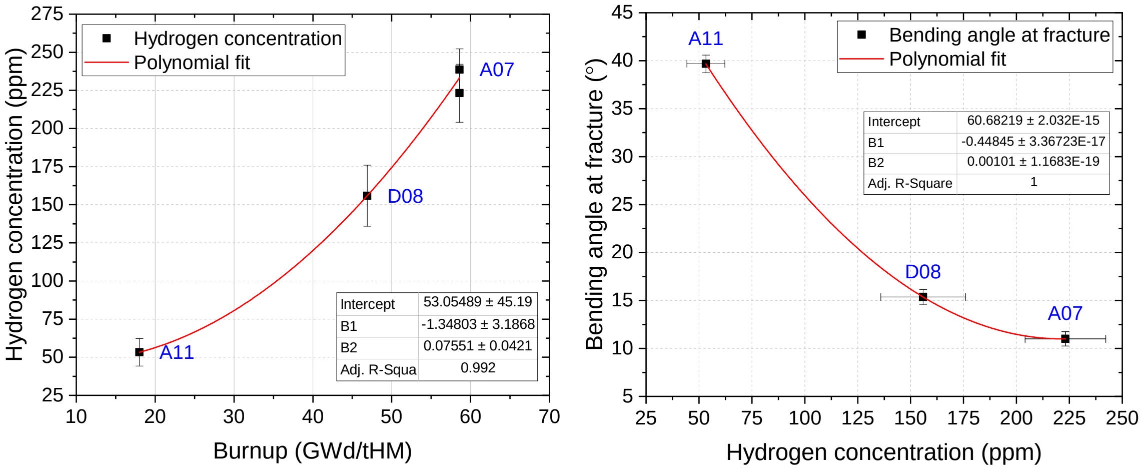

(a) (b)

Fig. 4.27 a) Hydrogen content as function of burnup and b) bending angle to fracture as function of hydrogen content of the Zry-4 KKG samples.

used as reference to indicate the location of the cladding micrographs, which are shown on the right.

Higher hydride precipitation at the outer liner was observed in all samples, as also shown in [108]. In addition, most samples included long circumferential hydrides, which precipitated preferably in the inner half of the cladding. On the contrary, samples KKG A11 and KKG D02, being the ones with the lowest hydrogen concentration, did not reveal any precipitation of circumferential hydrides. However, cross-shaped hydrides of smaller size were formed through the bulk of Zry-4 cladding. These smaller hydrides have irregular orientation, including both circumferential and radial directions, and are also present in samples KKG D08 and KWG A16-5.

The pellet-cladding gap was well established and closed in samples KKG D08-6 and KKG A07; this was not the case for the low-burnup sample KKG A11. The geometrical dimensions of the cladding characteristics are provided in Table 4.10. The cladding diameter and thickness were found to be close to their nominal dimensions. The samples with the highest and lowest cladding thickness were KWG A16-5 and KKG A11, respectively. The outer oxide layer for the low-burnup KKG A11 sample was partially removed after the mechanical test and the machining of the metallography sample. Table 4.10 reports the maximum values observed for the inner and outer oxide layers.

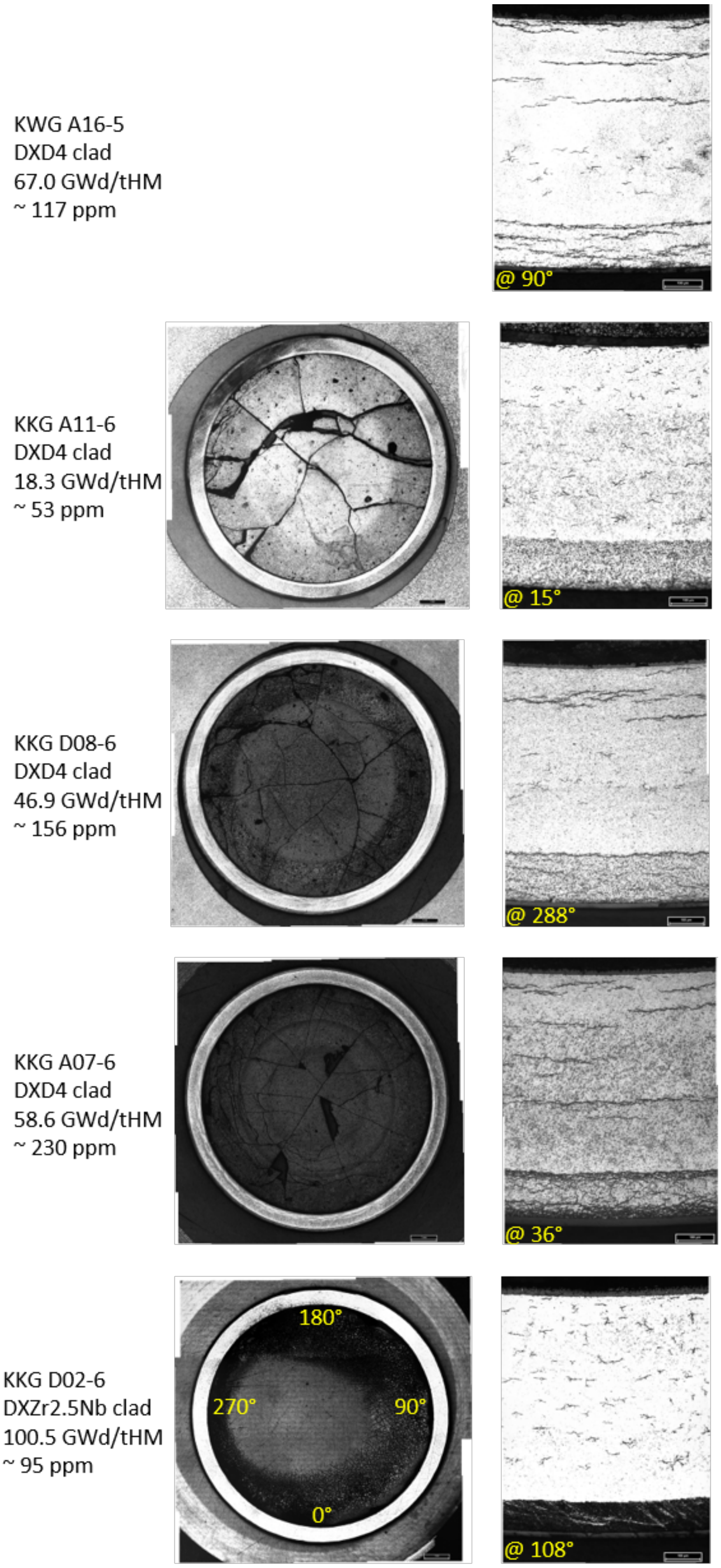
KWG A16-5
DXD4 clad
67.0 GWd/tHM
~ 117 ppm
@ 90°
KKG A11-6
DXD4 clad
18.3 GWd/tHM
~ 53 ppm
@ 15°
KKG D08-6
DXD4 clad
46.9 GWd/tHM
~ 156 ppm
@ 288°
KKG A07-6
DXD4 clad
58.6 GWd/tHM
~ 230 ppm
@ 36°
KKG D02-6
DXZr2.5Nb clad
100.5 GWd/tHM
~ 95 ppm
180°
270°
90°
0°
@ 108°

Fig. 4.28 Microscopic examination of metallography samples from the tested SNF rodlets. Left: macrographs of the full cross section; right: micrographs showing the hydride distribution and orientation. The angular positions of the micrographs are indicated at the bottom of each image.

Table 4.10 Geometrical dimensions irradiated of cladding.

Sample ID	Cladding diameter [mm]	Cladding thickness [mm]	Liner thickness [mm]	Inner oxide layer [mm]	Outer oxide layer [mm]
KKG A11	10.776	0.713	0.146	0.009	0.004
KKG D08	10.753	0.730	0.145	0.011	0.015
KKG A07	10.743	0.730	0.131	0.010	0.023
KKG D02	10.720	0.722	0.091	0.016	0.014
KWG A16-5		0.742	0.127	0.017	0.016

4.7 Summary

The experimental campaign on the irradiated PWR UO2 rodlets was presented in this chapter. Five samples were tested having a wide range of burnup, from low to extremely high, and cooling times from 9 to 16 years. The samples were selected from the same region of the rod and they were pressurized to their measured rod internal pressure at room temperature. Four samples were irradiated at KKG and one at KWG. The KKGfuel rods had Zry-4 duplex cladding with outer liner (DX D4), except from the highest burnup rod which had 2.5% of Nb at the outer liner (DX Zr2.5Nb). The KWGfuel rods had Zry-4 duplex cladding with outer low-alloyed Zr-based layer. Both impact and three-point bending tests were performed at room temperature.

The three-point bending tests revealed the flexural performance of the samples in quasi-static bending loads. Higher burnup samples showed less ductile behavior by fracturing at lower bending angles, however some plastic deformation still occurred. In addition, the toughness of the samples increased with burnup due to irradiation damage on the cladding. The image analysis methodology developed in the current study was successfully applied for the analysis of the samples' response in impact test. The displacement (or bending angle) and the energy absorbed from the sample until fracture was calculated and compared against the three-point bending test results. The difference in strain rate seemed to have a bigger effect in the case of low burnup sample, which fractured under impact loads in approximately half of the displacement compared to bending. Overall, the trends observed in the bending and impact tests were quite similar; this confirmed the effectiveness of the testing optimization effort implemented (especially on the impact test setup) during the cold test campaigns on the analogue samples (see chapter 3).

A series of post-test examinations was performed to characterize the state of the fuel rodlet upon fracture, the cladding material in terms of hydrogen concentration and hydride morphology, as well as the fuel mass release in terms of mass and size distribution. The location of the cladding crack initiation was systematically at the bottom side subjected to tension and at the pellet-pellet interphase closest to the loading axis. In all cases, the fuel mass release per fracture was limited to less than one pellet and was always relatively higher in impact tests compared to three-point bending. In addition, the fuel fragments were characterized based on their size distribution; most of the released mass consisted of fragments larger than 1 mm. The fine particulates and aerosol that were captured after impact tests at the filter system connected to the aspiration device, were analysed with SEM and BSE. Image analysis was performed to determine the equivalent circular diameter of these particulates.

Moreover, the hydrogen concentration of the cladding at the fracture surfaces was measured with the hot-gas extraction method. The hydrogen content of the samples ranged from approximately 50 ppm to 240 ppm, showing an increasing trend in higher burnup samples. Furthermore, metallographic examinations were performed at the vicinity of the cladding fracture to examine the hydride distribution and morphology. The photographs showed increased hydride precipitation at the outer liner, with long circumferential hydrides and almost no radial hydrides observed.

Finally, the flexural properties of the irradiated samples were derived under the assumptions of the simple beam theory. Beam element with hollow-circular and circular cross sections were used for this purpose. The analysis was performed on the three-point bending results and revealed the flexural mechanical properties of the composite cladding/fuel samples. The hollow-circular beam element approach was used to derive the elastic flexural properties of the cladding, where higher yield strength values were derived for higher burnup samples due to irradiation hardening of the cladding. The flexural modulus of elasticity for the samples with DX D4 claddings showed a nearly linear increase with burnup, and the results are in good agreement with values reported in previous studies. This slight increase could possibly originate from the higher oxide layer thickness in high burnup samples.

Chapter 5

Numerical investigation of SNF rodlet performance under flexural loads

Abstract *The numerical studies aim to complement the experimental investigations and concentrate on modelling the bending behavior and the mechanical properties of the examined spent nuclear fuel (SNF) rods. With the use of Finite Element Analysis (FEA) it is attempted to gain a better understanding of the observed experimental results, to investigate the mechanical properties of the SNF rod materials and to extend the examination of the rod's integrity to conditions and configurations outside the domain defined by the experimental studies themselves. This chapter focuses on the development of Finite Element Models (FEMs) on SNF rod segments under static bending loading conditions. ANSYS Mechanical was used to develop and run the models and an extensive sensitivity analysis is presented aiming to investigate the relative importance of many parameters on the model. The calibration process of the FEMs is described, based on the the three-point bending experimental results. Finally, the calculated effective mechanical properties of the cladding are presented and a comparison against the experimental values is performed.*

5.1 Introduction

In this chapter, the study of the mechanical properties and response of SNF rods under bending loads is attempted with the use of FEA. The numerical investigations constitute the second part of this project and aim to examine the structural integrity of the SNF rods and assemblies in various loading types and conditions. The use of FEMs to simulate normal and/or accident scenarios is necessary since the experimental data are limited and the loading configurations that could be examined are varying significantly. The first step towards this goal is the development of small-scale models that would be suitable to study the flexural response of spent fuel rodlets. Within the scope of this PhD, a study aimed to develop, optimize and calibrate small scale FEMs using the experimental results from the mechanical tests on SNF rod samples (refer to chapter 4) integrates and complements the first phase of the work based on measurements and tests in hot cells.

For this purpose, ANSYS Mechanical was used to develop a 3D implicit static structural FEM, which simulates the sample deflection under three-point bending conditions. In this model, several aspects had to be defined, such as the geometry and material properties of the sample, the contacts between the different parts, the meshing of the geometry and finally the boundary conditions that constrain the model. In the bending case, the boundary conditions mainly refer to the fixed supports where the sample lies upon and to the loading application on the sample via the former. The accurate description of these parameters for the case of the irradiated samples is a highly challenging task mostly due to the great number of uncertainties related to the geometry and material property, as well as the contact definition between the cladding and the pellets.

The surrogate samples and the associated experimental results were used for the model development since many modeling uncertainties could be eliminated due to the much simpler geometry and known/homogeneous mechanical properties of the fresh Zry-4 cladding and alumina pellets. Based on this model, an extensive sensitivity analysis was performed to evaluate the relative importance of numerous parameters on the solution quality and computational time. The objective of this study was to understand the relevance of different modeling approaches and to derive the necessary simplifications and assumptions that are required for the construction of an FEM simulating the flexural response of a spent nuclear fuel rod.

In addition, the sensitivity studies revealed the most important parameters of the FEM, which affect the flexural response of the rod under bending. As explained in detail in the following sections, these parameters refer to the mechanical properties of the cladding.

Therefore, the mechanical properties of the cladding were derived by validating the final FEM against the experimental results on irradiated samples. This FEM validation was performed through an optimization process, which minimized the difference between the experimental and the numerical load-displacement curves by varying the values of the cladding parameters. The cladding properties were derived as function of burnup and reflect the "effective" properties that are valid under the assumed modeling simplifications.

5.2 FEA of bending setup

The first step towards the numerical investigations of the mechanical properties of SNF rods was to examine a possible influence of the three-point bending device onto the recorded experimental data. The aim was to estimate the stiffness of the device or the amount of deformation occurring at each part of the device during the mechanical loading of the samples.

For this purpose, the behavior of the test-rig was modelled under "worst-case" simplified boundary conditions using static structural analysis in ANSYS Mechanical. Half symmetry was applied and the model was coarsely meshed (10 mm quadratic element size) to reduce the computational time, as shown in Fig. 5.1. The mesh quality was of relatively low importance since no stress evaluation was required (second order results); however, finer meshing was applied at the areas of interest, namely the former and the supports (1.5 mm quadratic element size). The step-motor was modelled as a point mass positioned at its center of mass and remotely attached to the upper plate of the loading column. Finally, the material properties of each part were assigned based on pre-defined material data provided in ANSYS Mechanical.

The reaction forces occurring in the device are modelled with simplified boundary conditions, as shown in Fig. 5.1a. Fixed support was applied at the bottom surface of the device to establish its vertical position throughout the testing procedure. The largest possible reaction force of 5 kN was applied to the former and support, which is defined by the torque of the step-motor. This force is significantly higher compared to the recorded loads during the three-point bending tests on surrogate and irradiated samples.

The results of the analysis are shown in Fig.5.2, where the total deformation is given for the maximum applied load of 5 kN. The total deformation at the former was found to be insignificant taking also into account that the results vary linearly with the applied load. Therefore, it can be assumed that the experimental apparatus did not have any significant

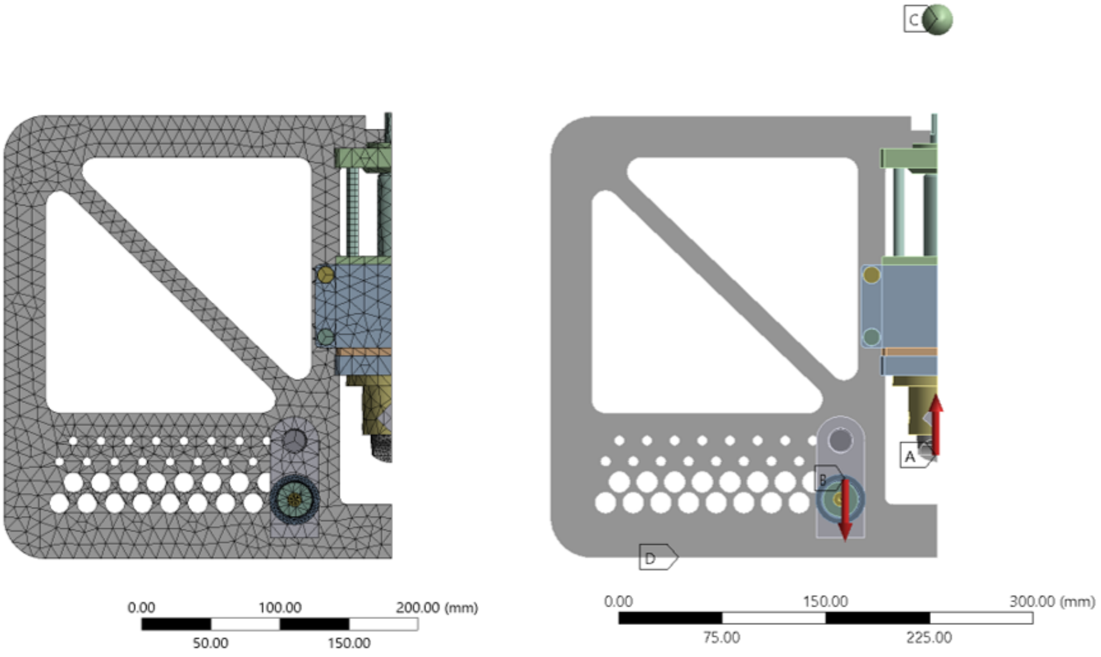
C
A
B
D
0.00
100.00
200.00 (mm)
50.00
150.00
0.00
150.00
300.00 (mm)
75.00
225.00

(a) (b)

Fig. 5.1 a) Mesh of an FEM of the three-point bending device and b) boundary conditions considered for investigating the stiffness behavior of the device.

influence on the derived load data. In addition, the support is stiff enough and does not deform even under the maximum applied load.

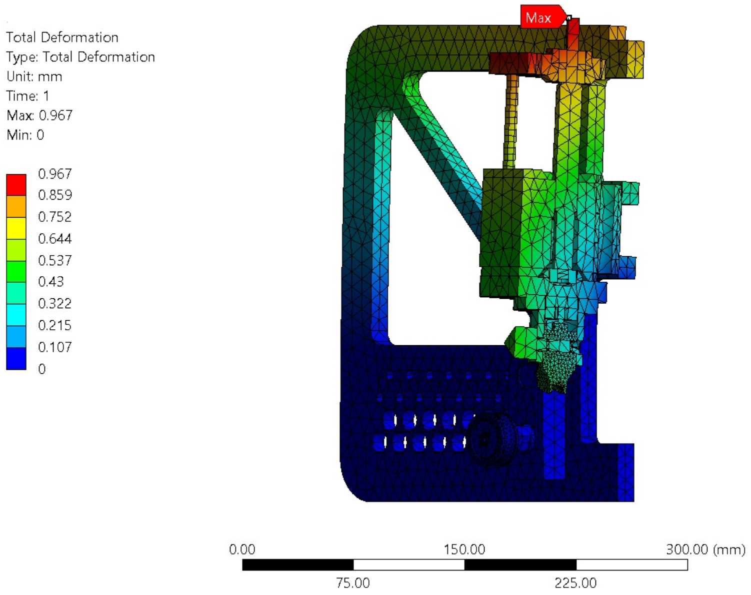
Total Deformation
Type: Total Deformation
Unit: mm
Time: 1
Max: 0.967
Min: 0
0.967
0.859
0.752
0.644
0.537
0.43
0.322
0.215
0.107
0
Max
0.00
150.00
300.00 (mm)
75.00
225.00

Fig. 5.2 Total deformation at maximum applied load of 5 kN.

5.3 Development of fuel rod FEM under bending loads

The development of a 3D FEM representing a fuel rod segment is a challenging task, since it includes large deformations with non-linear behavior and undefined geometry of the cladding, pellets and their interaction. As discussed in section 5.1, the development of the preliminary FEMs were based on the results from the three-point bending on the surrogate samples. In this case, the geometrical characteristics and mechanical properties of the pellets and cladding are known, in comparison to the irradiated samples, therefore the number of modeling uncertainties can be significantly reduced.

Fig. 5.3 shows an overview of an FEM of a fuel rod segment simulating a surrogate rodlet in three-point bending test. The pellets and cladding are modelled as solid elements with a flexible stiffness behaviour. The nominal mechanical and geometrical properties were used, as provided in Tables 3.1 and 3.2. The model exploits one fourth symmetry to reduce its size (or number of elements) and minimize the computational time. The symmetry planes are along the loading axis and at the pellets' mid-section (or at y and x axes). The former and the support are modeled as shell elements with rigid behavior, which does not allow their deformation. Finer mesh was employed at the areas of interest, being the pellet and cladding at the loading point and at the former and support contact areas.

A series of boundary conditions were used to represent the experimental settings. The pellets were retained with the use of a spring attached at the end-pellet, as shown in Fig. 5.3b. Frictionless contact was applied between the cladding and the support to simulate its rotation. Frictional contacts were used for the pellet-pellet, pellet-cladding and former-cladding interactions. In addition, the sample's internal pressure was simulated with a uniform pressure acting on the internal surface of the cladding. Moreover, a fixed support was placed at the shell element representing the support. Finally, loads are applied by assigning a maximum displacement at the former as determined in the experimental results (fracture point).

5.3.1 Material parameters

A principal difficulty in Finite Element Modeling is the use of correct properties for the materials involved. Often, the analysis is performed with material data available from the literature, however this can lead to results that are not representative for the actual material. For the case of the three-point bending test, the FEA becomes more challenging when the analysis moves from the linear or elastic behavior where the deformation of

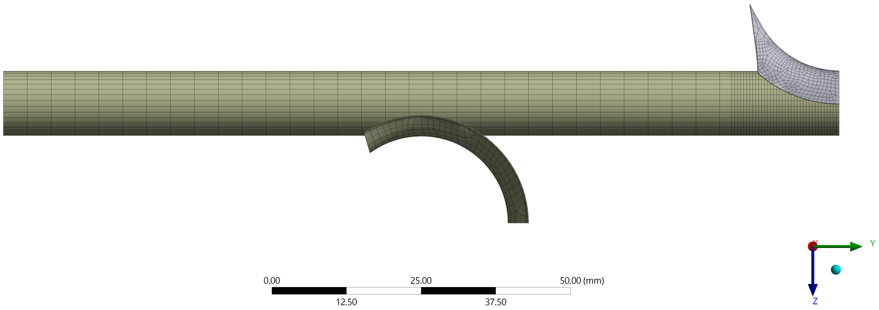

(a) Mesh elements of cladding and former/support.

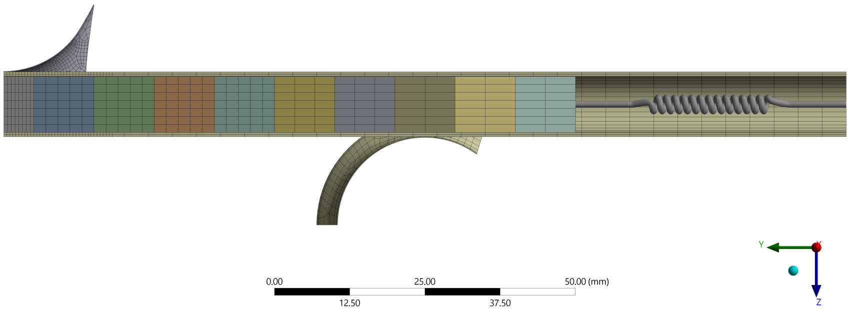

(b) Mesh elements of pellets and spring attachment.

Fig. 5.3 3D implicit FEM simulating the bending behavior of a fuel rodlet under three-point bending test.

the sample is proportional to the load, to non-linear or plastic behavior where the sample undergoes permanent deformation. Additionally, the combination of large deformations and high number of contacts leads to a highly complex numerical problem, which demands considerable computational and theoretical effort to be solved. In this situation, the proper characterization of the mechanical behavior of the material is fundamental. For this purpose, different material laws were used to describe the elasto-plastic behavior of the pellets and cladding in order to investigate the FEM performance.

At first, two different material laws were used for the pellets, namely the Bilinear Isotropic Harding (BISO) and the cast-iron plasticity model. BISO option uses the von Mises yield criteria coupled with an isotropic work hardening assumption. It is called bilinear because just two lines define the stress-strain curve; one to describe the linear elastic region and another to describe the plastic.

In addition, the cast-iron plasticity model was used to describe the plastic response of the pellets. This material law is widely used for modelling ceramic materials as it accounts for different plastic yield and hardening in tension and compression, while still assuming isotropic elastic behaviour. Fig. 5.4a shows a graphical representation of the stress-strain relation in the cast-iron model. The compressive behavior is defined by the compressive yield strength along with the compressive plastic modulus. The limited material strength in tension is considered with the tensile yield strength, which is defined by dividing the compressive yield strength by a constant called compression-to-tension (CtT) coefficient. The pellet cracking is indirectly modeled by defining very low values for the compressive and tensile plastic modulus. In other words, if the pellet yields under any type of load, then the pellet cannot transmit higher stresses under further deformation.

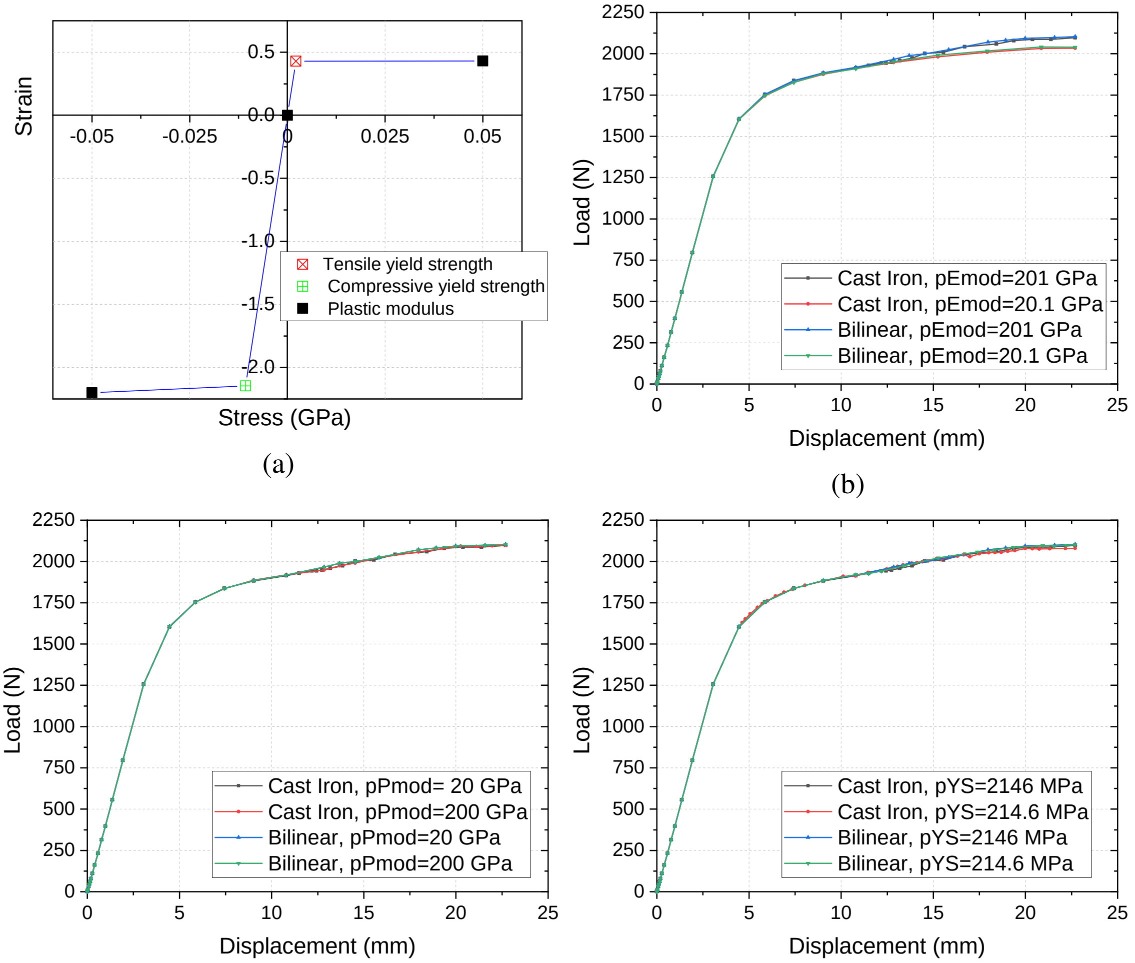

(a)

(b)

(c)

(d)

Fig. 5.4 a) Cast iron plasticity model assigned to pellets; Pellet material model comparison between cast-iron and BISO for different b) Young's modulus, c) plastic modulus and d) yield stress values.

A series of simulations was run to investigate the relative importance of the different material laws and of the most important mechanical properties on the numerical results, namely the load-displacement curves. The results are given in Figs. 5.4b, 5.4c and 5.4d and show no difference on the resulting load-displacement curves between the cast-iron and the

BISO model. The results indicate that the pellet properties are not of the highest importance for the bending response of the sample, under the current modeling approach and up to the considered maximum sample displacement. Indeed, the model showed that the pellets do not yield (apart from the point of PPI bellow the former), therefore the use of different plasticity models does not influence the results.

Different values for the pellet Young's modulus, yield stress and plastic modulus were used in order to find their relative importance to the results. As expected, there is hardly no difference on the derived load-displacement curves. Small differences appear when the Young's modulus is changed by one order of magnitude, as shown in Fig. 5.4b. The differences appear in the plastic deformation of the sample, where higher values of the Young's modulus slightly increase the bending stiffness of the sample. This also indicates that under plastic deformation and at around 12.5 mm of sample's displacement, the pellet start to contribute to the flexural response of the sample.

The cladding plasticity was described with the use of the Voce model to account for non-linear isotropic hardening. This model has also been used in previous studies for the description of the cladding properties [109]. Voce hardening law is a variation of bilinear isotropic hardening where an exponential saturation hardening term is added to the linear term (based on assumption that hardening eventually reaches the maximum stress). A graphical representation of the plastic stress-strain relation in Voce law is given in Fig. 5.5 and its mathematical formulation is described in the following expression:

$$\sigma = \sigma_0 + R_0 \varepsilon_{pl} + R_{inf} \left(1 - e^{-b\varepsilon_{pl}}\right) \tag{5.1}$$

where σ_0 is the yield stress, ε_{pl} is the equivalent plastic strain, and R_0, R_{inf} and b are the material parameters characterizing the isotropic hardening behavior of the pellets. R_0 is the initial value of isotropic hardening, R_{inf} is the asymptotic value of isotropic hardening (matching the stable cycle regime), while b describes the rate of the cycle stabilization. Fig. 5.5 gives a graphical representation of the Voce hardening law.

The effect of each parameter on the resulting load-displacement curve was investigated and presented in Fig. 5.6. The load-displacement curve is more sensitive to the change of some of the parameters of the cladding material definition. The cladding yield stress is the most important parameter affecting the bending response of the sample, as shown in Fig. 5.6a, where a change of around 50% in the yield stress leads to a change of work (area under the curve) of appropriately 29%.

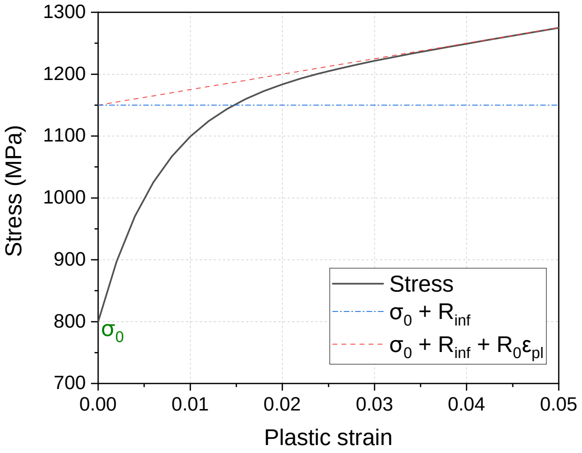

Fig. 5.5 Voce non-linear isotropic hardening model used in cladding.

A change in the linear coefficient, R_0 does not strongly affect the load-displacement curve, as it can be observed in Fig. 5.6c; however, it affects the buckling behaviour of the sample. If R_0 is reduced then buckling occurs and negative stiffness is observed in the load-displacement curve (as the force does not monotonically increase with higher displacements). For higher R_0 values the buckling occurrence is delayed to higher displacements. Therefore, in cases where the FEM has to be run for higher displacements (i.e. fresh Zry-4 of very low burnup samples), then R_0 could become more important for the proper characterization of the cladding properties. In any other case (i.e. intermediate and high burnup), R_0 is of no importance since this parameter affects the plasticity region only after stress saturation. Thus, in a structure in which failure occurs at an early stage of yielding the contribution of R_0 becomes very limited.

Fig. 5.6b shows that the exponential coefficient (R_{inf}) affects the results by shifting the whole plasticity regime. Nonetheless, the dependency of the load-displacement curve on R_{inf} is weaker than in the case of the yield stress (a 73% change leads to a change in the curve of 16%). R_{inf} affects just the non-linear plastic part of the curve in which stress saturation occurs, therefore if the structure is rather brittle and it collapses at an early stage of the plasticity regime it might be that a change of R_{inf} would not affect significantly the results.

Finally, the effect of a change of the exponential saturation parameter (b) is shown in Fig. 5.6d. As expected, the effect is confined to the saturation region of the curve. However, if the structure is brittle, the plastic part of force-displacement curve will be limited to the saturation region, hence b might become a bigger contributor for a correct matching of the experimental curve with the FEM, in other words the relative integral difference might become bigger [110].

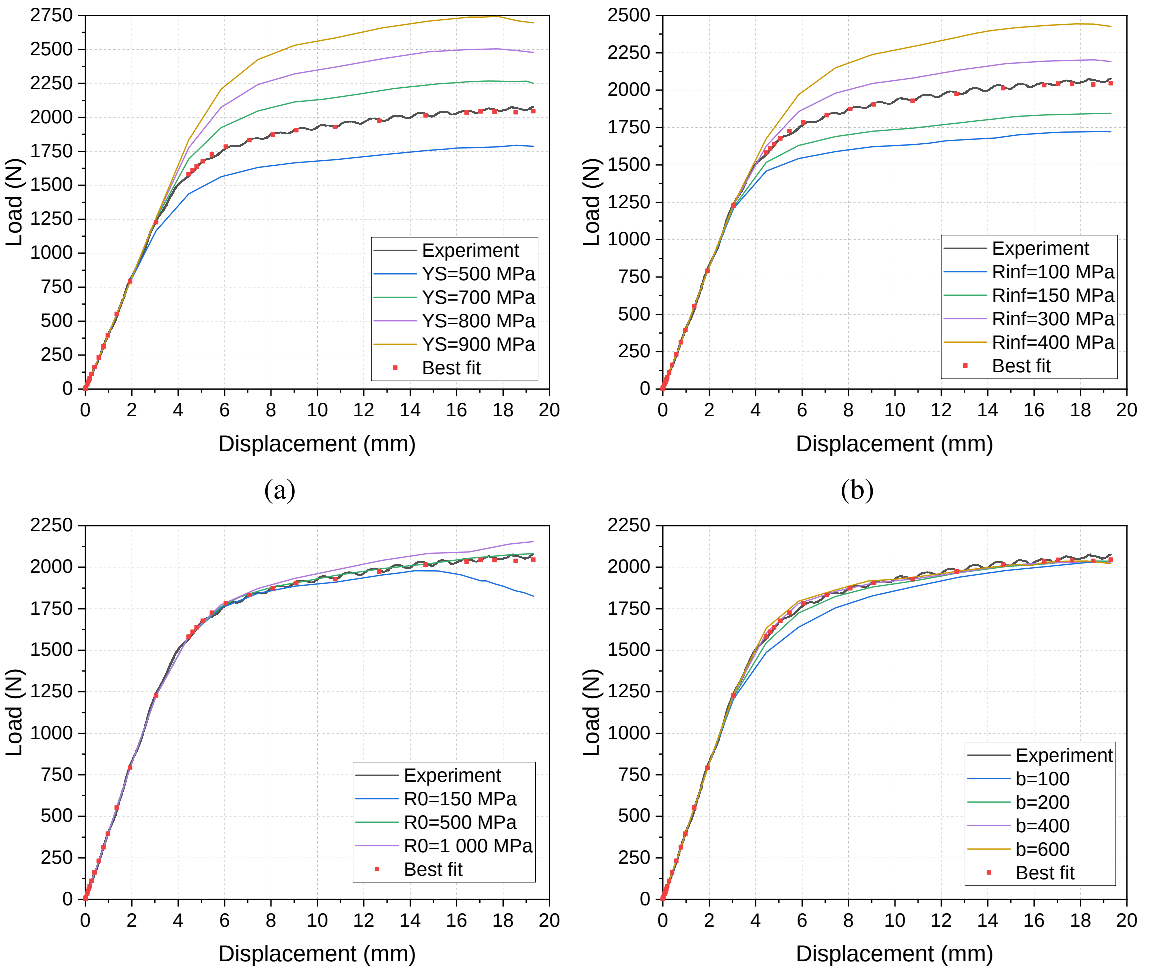

(a) (b)

(c) (d)

Fig. 5.6 Results of the sensitivity studies performed on the Voce parameters of the 3D reference model. The effect of different a) yield stress, b) R_{inf}, c) R_0 and d) b values on the laod-displacement curve of the simulation is presented. The red dots represent response of the reference FEM.

5.3.2 Sensitivity analysis on various parameters of FEM

The following sections provide a thorough investigation on the relative importance of various numerical parameters and modeling approaches on the derived numerical results, namely the load-displacement curve of a sample under three-point bending test. The objective is to develop a better understanding of the model simplifications and assumptions and finally, to construct a model, which can provide reliable results in relatively short computational time.

At this stage the sensitivity of the modelling approach has been evaluated for variations of seven different factors using the experimental data. These factors include the CPU time, the maximum stresses at cladding and pellets, the force at maximum displacement, the maximum contact pressure and penetration, and the derived load-displacement curves. These results do not have the same importance or validity, since e.g. the stress values cannot be compared against experimental data. In addition, the FEM includes a series of geometrical and numerical approximations that prevents the high confidence and validity for direct use of second order results (such as the derived stresses). On the contrary, the derived load-displacement curves and the CPU time are of the highest importance. These data assess the bending behavior of the sample during the whole range of deformation, as well as the model's applicability for further use, since minimization of the computational time is highly relevant for model optimization against the experimental results (refer to section 5.4).

For this purpose, a *reference* 3D FEM was used, which was built upon the nominal mechanical and geometrical properties of the surrogate samples. The aim was to select an experimental load-displacement curve with high plastic deformation in order to study the influence of each modeling approach in that area, where non-linear effects are present. Consequently, the reference model was calibrated against the results of the sample "H1960_Z4" (refer to Tables 3.4 and 3.5), as shown in Fig. 5.7 for illustration purposes. Therefore, all simulations were run for a maximum displacement of 19.3 mm. Further details on the construction of the reference model are given in Appendix E along with the hardware specifications of the computer system used to run the ANSYS simulations.

Indicative results from the simulations are given in Fig. 5.8. The Von Mises stresses on cladding and pellets are shown in Figs. 5.8a and 5.8c. The maximum stresses at the cladding are observed at the bottom surface subjected to tension and at the pellet pellet-pellet interface closest to the symmetry axis. At this location, the maximum equivalent plastic strain was also observed, as shown in Fig. 5.8b. Moreover, the maximum stresses at the pellets were observed at the PPI closest to the symmetry axis and at the top side, where

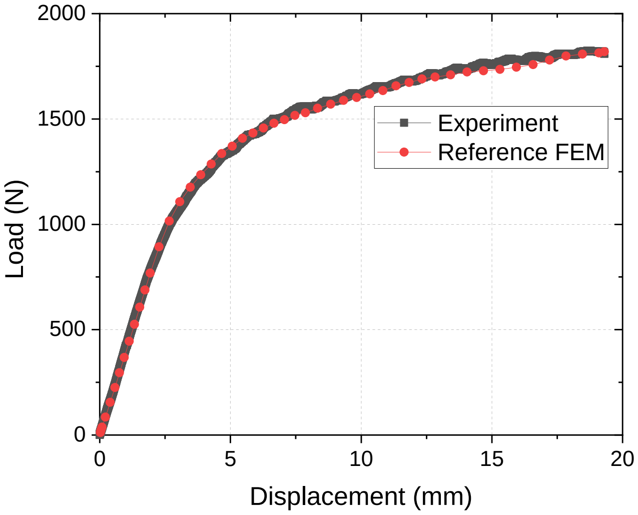

Fig. 5.7 Load-displacement curve of the reference 3D static structural model calibrated against three-point bending test experiment on surrogate sample "H1960_Z4".

compressive stresses are developed due to higher contact pressure between the pellets, as shown in Fig. 5.8d.

In addition, the contact status and penetration between the pellets are shown in Figs. 5.8e and 5.8f, since these were the most numerically challenging areas for the FEM convergence. At these points, the status of the contacts is changing dynamically as the sample bends and the pellets closest to the symmetry axis are losing contact ("near" status), while higher penetrations are observed to the rest of the pellets (closed contact or "sticking" status). At the same time all pellets are constrained from the spring application and pushed out due to bending and high contact pressure close to the symmetry axis.

5.3.3 Symmetry and pellet positioning

The *reference* model includes 10 pellets, which are constrained at the end with the use of a spring. Two additional pellets were included after the support to consider the sample sliding. In reality, there were 14 pellets in total, which were not modeled in order to reduce the computational time of the simulation. To investigate the influence of the pellet removal, another model was created (named "*all pellets*") filled with four additional pellets up to the end of the cladding.

Moreover, the effect of symmetry was studied with a model including half symmetry (named "*half symmetry spring*"), as shown in Fig. 5.9a. In addition, the reference model considers half pellet at the symmetry plane, which is the equivalent of having the middle

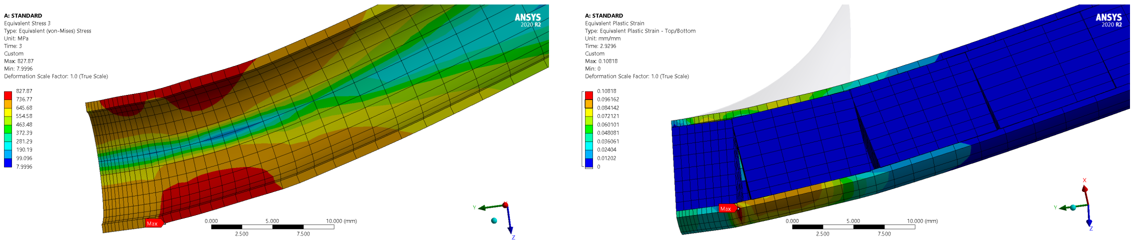
A: STANDARD
Equivalent Stress 3
Type: Equivalent (von-Mises) Stress
Unit: MPa
Time: 3
Custom
Max: 827.87
Min: 7.9996
Deformation Scale Factor: 1.0 (True Scale)
827.87
736.77
645.68
554.58
463.48
372.39
281.29
190.19
99.096
7.9996
Max
ANSYS
2020 R2
0.000
5.000
10.000 (mm)
2.500
7.500
Y
Z
A: STANDARD
Equivalent Plastic Strain
Type: Equivalent Plastic Strain - Top/Bottom
Unit: mm/mm
Time: 2.9296
Custom
Max: 0.10818
Min: 0
Deformation Scale Factor: 1.0 (True Scale)
0.10818
0.096162
0.084142
0.072121
0.060101
0.048081
0.036061
0.02404
0.01202
0
Max
ANSYS
2020 R2
0.000
5.000
10.000 (mm)
2.500
7.500
X
Y
Z

(a) Cladding stress distribution (MPa) (b) Plastic strain (mm/mm)

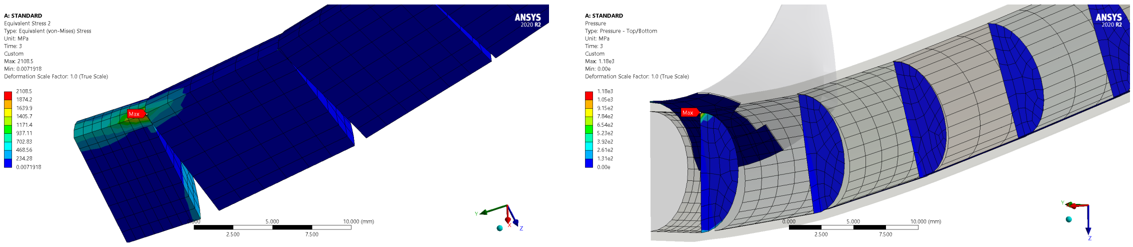
A: STANDARD
Equivalent Stress 2
Type: Equivalent (von-Mises) Stress
Unit: MPa
Time: 3
Custom
Max: 2108.5
Min: 0.0071918
Deformation Scale Factor: 1.0 (True Scale)
2108.5
1874.2
1639.9
1405.7
1171.4
937.11
702.83
468.56
234.28
0.0071918
Max
ANSYS
2020 R2
5.000
10.000 (mm)
2.500
7.500
Y
Z
A: STANDARD
Pressure
Type: Pressure - Top/Bottom
Unit: MPa
Time: 3
Custom
Max: 1.18e3
Min: 0.00e
Deformation Scale Factor: 1.0 (True Scale)
1.18e3
1.05e3
9.15e2
7.84e2
6.54e2
5.23e2
3.92e2
2.61e2
1.31e2
0.00e
Max
ANSYS
2020 R2
0.000
5.000
10.000 (mm)
2.500
7.500
Y
Z

(c) Pellet stress distribution (MPa) (d) Contact pressure (MPa)

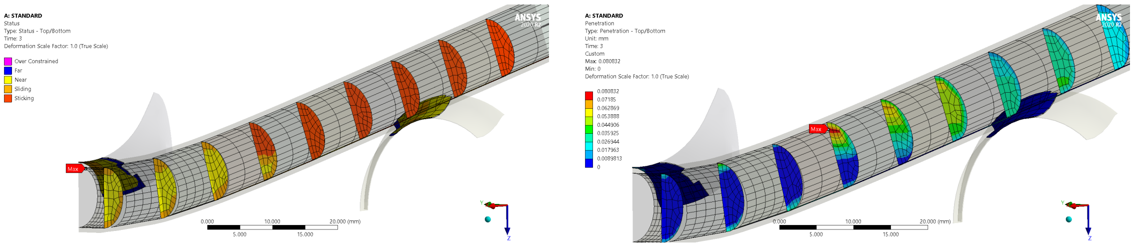
A: STANDARD
Status
Type: Status - Top/Bottom
Time: 3
Deformation Scale Factor: 1.0 (True Scale)
Over Constrained
Far
Near
Sliding
Sticking
Max
ANSYS
2020 R2
0.000
10.000
20.000 (mm)
5.000
15.000
Y
Z
A: STANDARD
Penetration
Type: Penetration - Top/Bottom
Unit: mm
Time: 3
Custom
Max: 0.080832
Min: 0
Deformation Scale Factor: 1.0 (True Scale)
0.080832
0.07185
0.062869
0.053888
0.044906
0.035925
0.026944
0.017963
0.0089813
0
Max
ANSYS
2020 R2
0.000
10.000
20.000 (mm)
5.000
15.000
Y
Z

(e) Contact status (f) Penetration (mm)

Fig. 5.8 Representative results from reference FEM at max displacement.

of a pellet positioned under the former. To study the influence of the pellet positioning another model was created (named "*half symmetry full pellet*"), where the first pellet was fully modeled in order to have the PPI exactly at the symmetry plane. This model represents the other extreme in terms of pellet with regards to the load application. For this purpose, the half symmetry model was modified to adjust the pellet positioning. Finally, the half symmetry model simply mirrors the reference case with a spring placed at both ends. In reality, the other end was constrained by the pressure plug; the latter is modelled as bonded contact to the cladding in a new model (named "*half symmetry bonded*"), as shown in Fig. 5.9b.

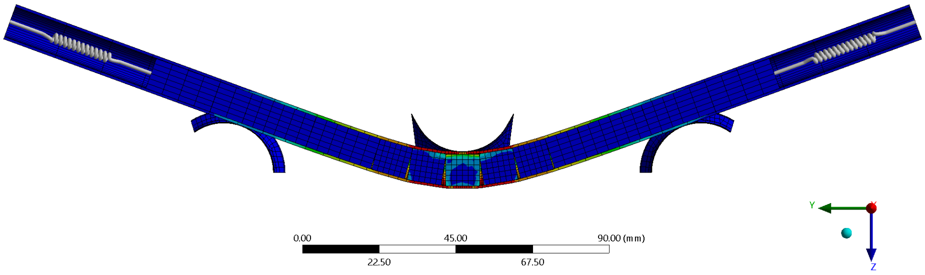

(a) Half symmetry model with springs used at both ends.

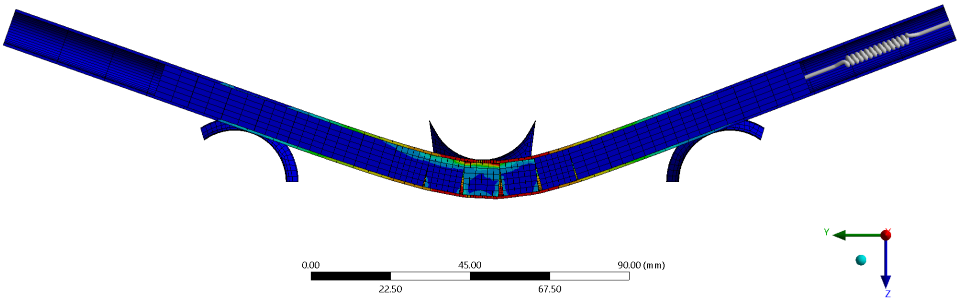

(b) Half symmetry model with bonded pellet at one end (left).

Fig. 5.9 Equivalent (Von Mises) stress at maximum displacement of a) half symmetry model with bonded pellet at one end (left) to constrain the pellets and b) half symmetry model with bonded pellet at one end.

The load-displacement curves are given in Fig. 5.10 and a summary of the results is provided in Table 5.1. All models showed exactly the same behavior in the elastic region and small differences in loads became apparent in higher displacements. The model including all pellets is approximately 50% slower and slightly stiffer (but not significantly), since all pellets are contributing to the sample deformation. The load development in the plastic region is slightly higher, however the maximum difference is less than 1.7% and therefore not significant.

The half symmetry models are approximately 3-4 times slower. The resulting load-displacement curves showed similar behavior to the reference model with only exception

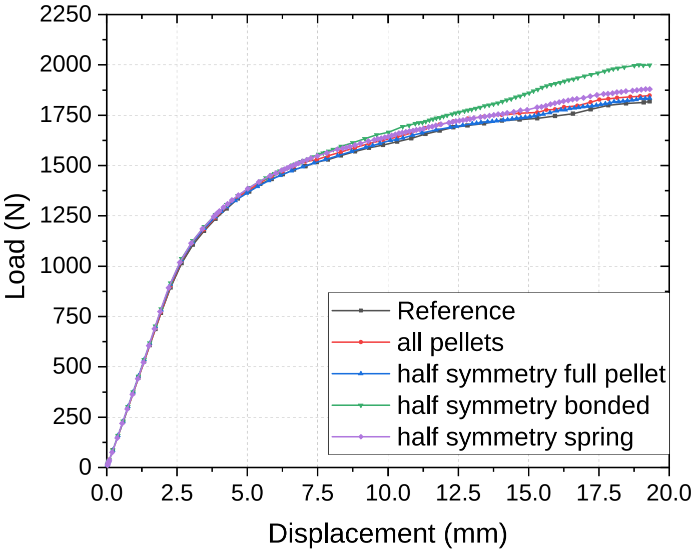

Fig. 5.10 Load-displacement curves of FEMs with different modeling approaches.

Table 5.1 Summery of representative results at maximum sample deflection from different modeling approaches.

Model	CPU time [s]	$\sigma_{clad_{max}}$ [Mpa]	$\sigma_{pellet_{max}}$ [Mpa]	$F_{fracture}$ [N]	max contact pressure [MPa]	max penetration [mm]
reference	230	828	2109	1818	1176	0.081
all pellets	348	838	1656	1848	766	0.052
half symmetry spring	1020	813	720	1880	322	0.071
half symmetry full pellet	743	876	772	1834	395	0.071
half symmetry bonded	822	827	1034	1999	515	0.096

being the model having one end bonded to the cladding. In this case, the differences in the load development are becoming more significant as the displacement increases, reaching a value of 10% at maximum displacement. In this case, the pellets are contributing more to the stiffness of the sample since there is no spring at one end to accommodate the contact pressure increase due to bending.

The difference between the spring and the bonded-end can be appreciated in Fig 5.11, where the contact penetration is given for the PPI along the sample length. It can be clearly observed that higher contact penetrations are developed at the left half of the sample, where the end pellet is bonded and does not allow further relaxation of the sample. As a result, the bending behavior becomes stiffer at higher displacements, where the contact pressure at PPI increases.

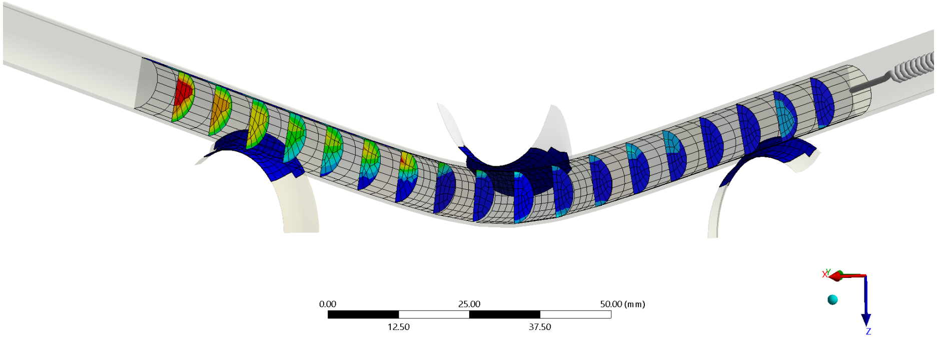

Fig. 5.11 Penetration at PPI of half symmetry model with bonded pellet at one end (left).

5.3.4 Cladding modeling approach

The cladding can be modeled either as body element or as surface element with virtual thickness equivalent to its real dimension. The main difference is given by the meshing elements adopted in the two cases; solid elements for the former (SOLID185, 8 nodes with 3 Degrees of Freedom (DoF) each) and shell elements (SHELL181, 4 nodes with 6 DoF each) for the latter. For each case, the cladding could be meshed in the radial direction to account for stress and strain gradients that could develop locally between the inner and outer surface.

The reference model included the cladding as body element with only one mesh element over its thickness. Two additional simulations were run with two and three meshing elements over the thickness to examine the differences on the results. To investigate the performance of each approach an additional FEM was created by modeling the cladding as surface element. In this case, five meshing elements were used over the cladding thickness.

The resulting load-displacement curves are given in Fig. 5.12, showing no significant differences. The major difference between these approaches lies at the CPU time, which is proportional to the number of mesh elements used. A summary of the results is provided in Table 5.2. The models with two and three body elements through the cladding thickness are approximately 4 and 7 times slower, respectively. However, they provide a much better representation of the plastic strain development at the region of the crack initiation, as shown in Fig. 5.13. Since the plastic strain can be used to derive failure criteria of the cladding, the model with 2 mesh elements through the thickness was selected as the best compromise between computational time and accuracy. The model with the surface cladding element approach was discarded, since it required relatively high computational time and also showed convergence problems.

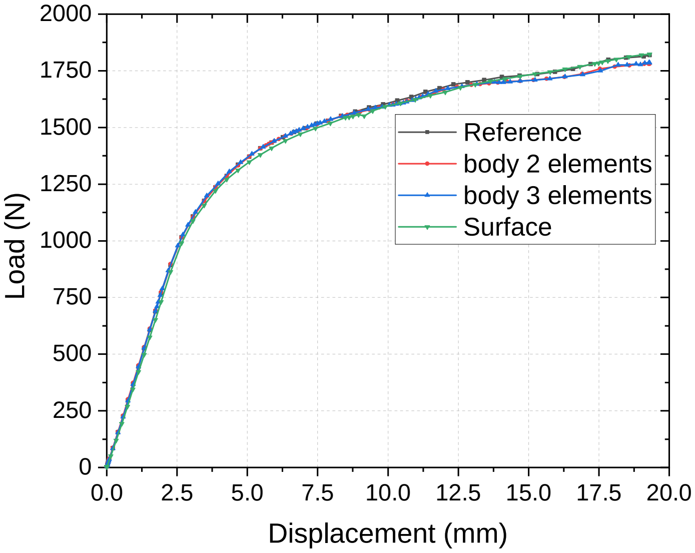

Fig. 5.12 Load-displacement curves of FEMs with different cladding modeling approaches.

Table 5.2 Representative results at maximum sample deflection from different cladding modeling approaches.

Model	Mesh elements	CPU time [s]	$\sigma_{clad_{max}}$ [Mpa]	$\sigma_{pellet_{max}}$ [Mpa]	$F_{fracture}$ [N]	max contact pressure [MPa]	max penetration [mm]
Reference	2270	230	828	2109	1818	1176	0.081
body 2 elements	3220	854	817	1115	1781	486	0.078
body 3 elements	4320	1550	813	1086	1785	479	0.147
Surface	1414	446	853	1445	1824	608	0.085

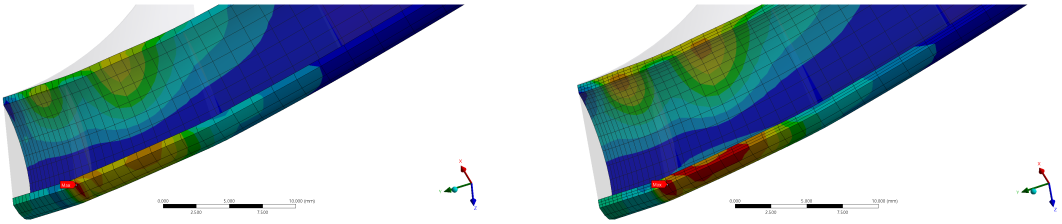

(a) (b)

Fig. 5.13 Equivalent plastic strain at cladding with a) one and b) 3 mesh elements through its thickness.

5.3.5 End-pellet boundary condition

An important boundary condition refers to the axial constraint of the pellets within the cladding, since they tend to be pushed out as the sample bends. This is caused from the contact pressure that the central pellets at the vicinity of the loading point are acting on the neighboring pellets during the cladding deformation.

In the reference FEM the pellets are constrained by the use of a spring element of 2 N/mm stiffness. Several runs were performed with higher values of stiffness in order to investigate its influence on the bending behavior of the sample. In addition, another type of boundary condition was applied by replacing the spring with a constant force acting along the axial direction on the last pellet. Two runs with different force values were performed for this purpose.

A summary of the results is given in Fig. 5.14, where the load-displacement curves for each scenario are plotted. It can be observed that the elastic region is identical for every case; therefore, the end-pellet boundary condition is irrelevant for the elastic regime. In the plastic region, the simulations revealed higher bending stiffness of the samples as the stiffness of the spring increased. The maximum difference of the load at the fracture point against the reference FEM was approximately 10%. The simulation with a force of 500 N on the end-pellet showed completely different results. In this case, since the force is acting normal to the pellet-direction, it actually facilitates the bending of the sample. For this reason, the reaction force registered at the former is significantly lower. As a result, the use of this boundary condition was rejected. A summary of the simulation results is given in Table 5.3.

The effects of the spring stiffness were further investigated by means of a sensitivity analysis on the resulting maximum force and stresses on the cladding and pellets at the point of maximum displacement. Fig. 5.15 gives the dependency of this value with regards to the spring stiffness. It can be observed that both the calculated load and stress on the cladding

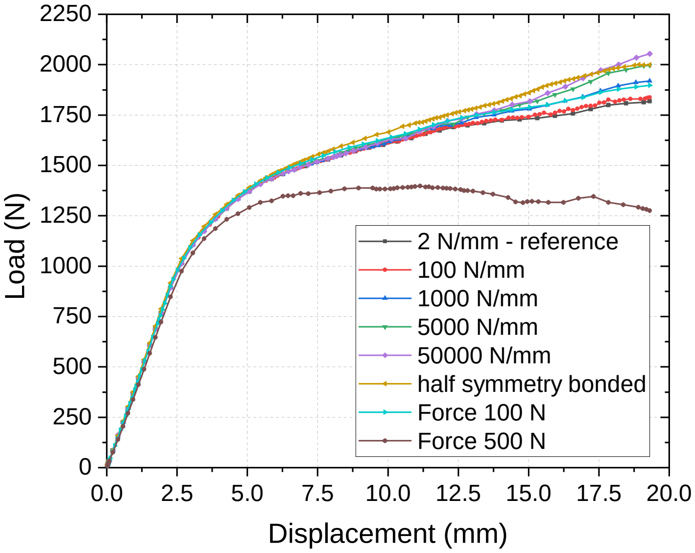

Fig. 5.14 Load-displacement curves of FEMs with different modeling approaches on the end-pellet boundary condition.

Table 5.3 Representative results at maximum sample deflection from different modeling approaches on the end-pellet boundary condition.

Model	CPU time [s]	$\sigma_{clad_{max}}$ [Mpa]	$\sigma_{pellet_{max}}$ [Mpa]	$F_{fracture}$ [N]	max contact pressure [MPa]	max penetration [mm]
Spring: 2 N/mm (reference)	230	828	2109	1818	1176	0.081
Spring: 100 N/mm	1065	832	2173	1837	1224	0.182
Spring: 1000 N/mm	327	851	2981	1919	1753	0.153
Force: 100 N	373	839	2285	1897	1224	0.051
Force: 500 N	357	841	3787	1276	2375	0.160

increase with increasing spring stiffness and in exactly the same manner. This increase is much steeper for spring stiffness values between 2 N/mm and 500 N/mm. Nevertheless, the maximum difference between the two extremes is less than 10%. Similar behavior can also be observed for the maximum stresses on the pellets; however, second order results, such as the stresses, cannot be considered as reliable under these modelling assumptions and simplifications.

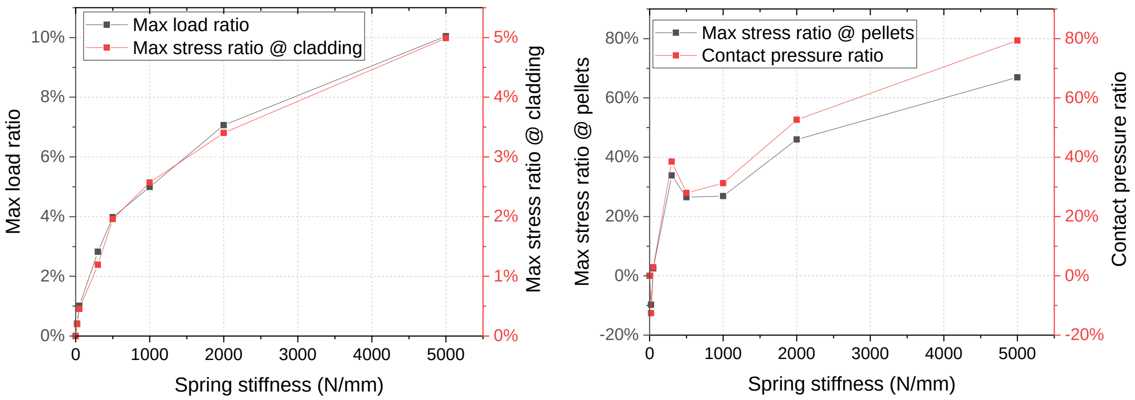

(a) (b)

Fig. 5.15 Sensitivity study on the end-pellet boundary condition with the use of spring; a) maximum load and cladding stress (Von Misses) difference and b) maximum pellet stress (Von Mises) and pellet contact pressure at maximum displacement for different spring stiffness factors.

5.3.6 Rod internal pressure

The effect of the internal pressure applied to the cladding was examined with a series of simulations using different pressure values. Fig. 5.16a gives the resulting load-displacement curves showing that the sample's stiffness increases with decreasing internal pressure values. Again, no difference was observed in the elastic region, whereas the deviations in the plastic regime increased with higher displacement. Higher values of internal pressure facilitate the bending of the sample since additional forces are acting normal to the cladding surface.

Fig. 5.16b shows the relative change of the load and the maximum stress at the cladding and pellets at the point of maximum sample displacement as a function of internal pressure. It can be clearly seen that the load decreases linearly with increasing pressure, varying approximately 11% over a range of 4 MPa. The maximum stress in cladding was only slightly affected, in contrast to the stress in pellets that decreased by approximately 25% over this range. This could originate from the fact that under these modeling assumptions the cladding's internal diameter had marginally increased. Therefore, the stresses acting on the pellets were reduced, since under the same bending deformation the pellets were less restrained.

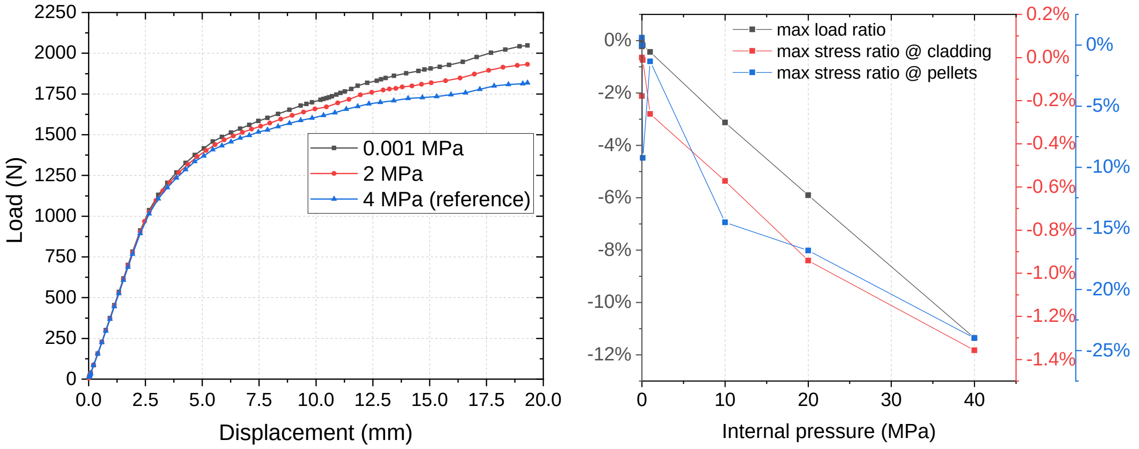

(a) (b)

Fig. 5.16 Sensitivity study on the bending response of the model with regard to the internal pressure; a) resulting load-displacement curves and b) maximum load and pellet/cladding stress (Von Misses) differences for various internal pressure values.

5.3.7 Contact formulation

One of the most important aspects in the modeling of the sample's bending was to understand the effect of the contact formulation between the different bodies. This includes the contact type formulation, the contact stiffness factors and the friction coefficients.

Initially, a sensitivity analysis was performed on the contact types using Pure Penalty, Augmented Lagrange and Normal Lagrange. All three are penalty-based methods, in which a spring is virtually considered between the contact nodes. Whenever penetration occurs, the spring applies a force to the nodes, which is proportional to the penetration. The proportionality factor is the contact stiffness. In the Augmented Lagrange method a constant is added for the force calculation.

$$F = k\chi + c \tag{5.2}$$

In the Normal Lagrange method an additional DoF, i.e. contact pressure, is considered at the contact nodes. Penetration is avoided by guaranteeing contact pressure equilibrium between contact nodes, so no stiffness definition is required. This formulation requires a direct instead of iterative solver, therefore it is more computationally expensive.

Table 5.4 Representative results at max sample deflection from different modeling approaches on contact formulations.

Model	CPU time [s]	$\sigma_{clad_{max}}$ [Mpa]	$\sigma_{pellet_{max}}$ [Mpa]	$F_{fracture}$ [N]	max contact pressure [MPa]	max penetration [mm]
Reference	230	828	2109	1818	1176	0.081
Pure Penalty	285	829	1314	1813	583	0.137
Augmented Lagrange	273	829	1899	1820	1029	0.107
Normal Lagrange	728	855	4033	2037	1548	0.037

The results of the simulations are given in Table 5.4 and the load-displacement curves are shown in Fig. 5.17.

The reference model (where Pure Penalty is used) and the model with Augmented Lagrange formulations showed identical behavior in the bending response of the sample. On the contrary, the Normal Lagrange model provided a much stiffer bending response, which prevented any penetration between the PPI. However, the computational time required was approximately 3 times longer compared to the other models.

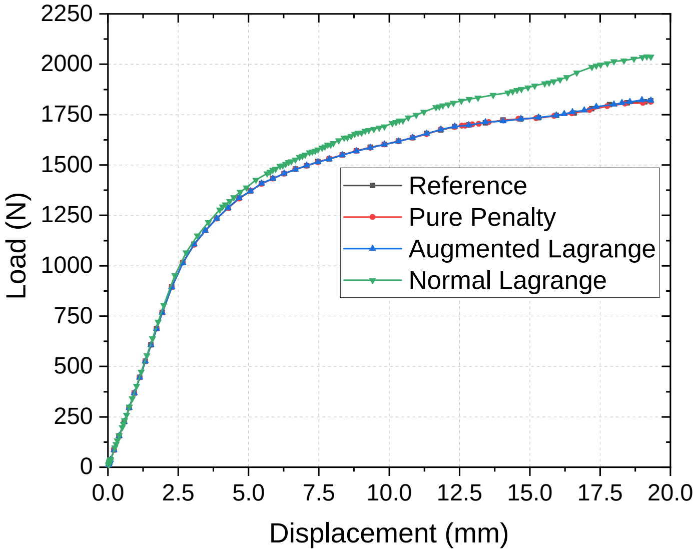

Fig. 5.17 Load-displacement curves of FEMs with different modeling approaches for the contact formulation.

Subsequently, the friction coefficients of pellet to pellet and pellet to cladding contacts were examined. Fig.5.18 shows the load-displacement curves from the sensitivity study on this parameter. It is evident that the pellet to pellet friction coefficient does not affect the resulting load-displacement curve of the simulation, whereas the pellet to cladding friction coefficient affects the slope of the plastic region. Based on the experimental results from tests on irradiated rodlets, where the plastic deformation of the samples (especially for higher burnup) was limited compared to the surrogate cladding tests, it can be assumed that the effect of the pellet to cladding friction coefficient becomes much less significant in the case of irradiated fuel testing.

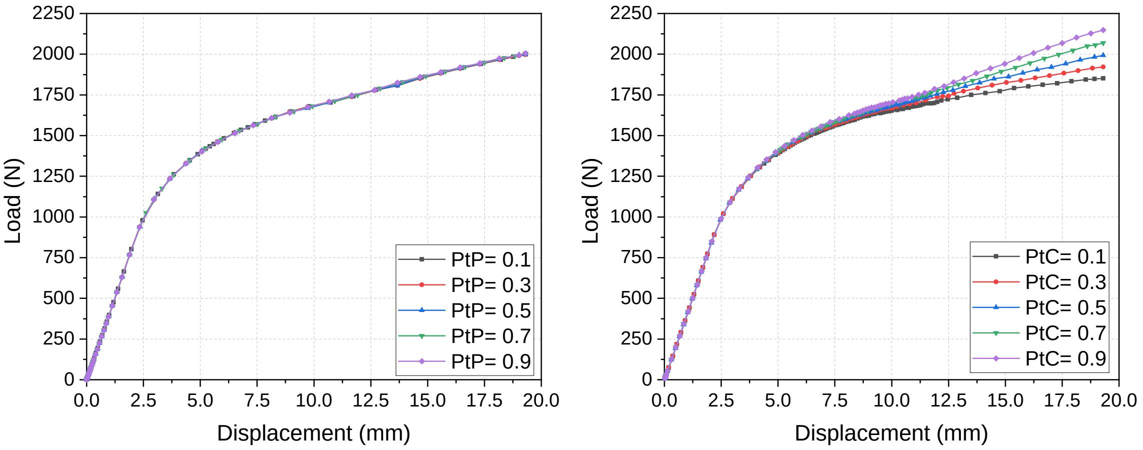

(a) (b)

Fig. 5.18 Friction coefficients sensitivity studies performed on the reference 3D model; resulting load-displacement curves for the a) pellet to pellet friction coefficient study and b) pellet to cladding friction coefficient study.

Finally, the effect of the contact stiffness factor was studied by investigating the sample response for values ranging from 0.1 to 300. The results showed no dependence on either the pellet to pellet or pellet to cladding contact stiffness.

5.3.8 Mesh independence

A sensitivity study was performed to determine the dependence of the results on the mesh density. For this purpose, a coarser and a finer mesh were generated based on the reference model. Then, two additional FEMs were created, where the element order was changed from linear to quadratic elements and from linear to tetrahedral elements. The generated number of nodes and elements, along with the simulation results, are given in Table 5.5. In addition, the resulting load-displacement curves are shown in Fig. 5.19a, where the bending response was found to be identical for all models except for the model with the coarse mesh, which showed softer behavior. Moreover, the computational time of the models (except of the coarser) was increased by 3 to 4 times compared to the reference model.

Table 5.5 Representative results at max sample deflection from different mesh densities and options of the FEM.

Model	Mesh nodes	Mesh elements	CPU time [s]	$\sigma_{clad_{max}}$ [Mpa]	$\sigma_{pellet_{max}}$ [Mpa]	$F_{fracture}$ [N]	max contact pressure [MPa]	max penetration [mm]
Reference	4072	2270	230	828	2109	1818	1176	0.081
Coarse	2062	1096	237	818	403	1713	189	0.09
Fine	7596	4493	695	848	1591	1783	832	0.046
Quadratic	4072	2270	965	817	1583	1798	700	0.105
Tetrahedral	3690	10569	781	804	311	1791	351	0.127

Since most of the approaches provided similar results in terms of load-displacement, the dependence of the load at maximum displacement on mesh density was investigated with the use of the reference 3D model. Fig. 5.19b gives the ratio of the calculated loads for different mesh densities. As expected, the load is underestimated for the models with coarser mesh (<1500 elements), indicating a softer sample behavior as shown in Fig. 5.19a. The load seems to be independent from the mesh density for a number of elements higher than 3000.

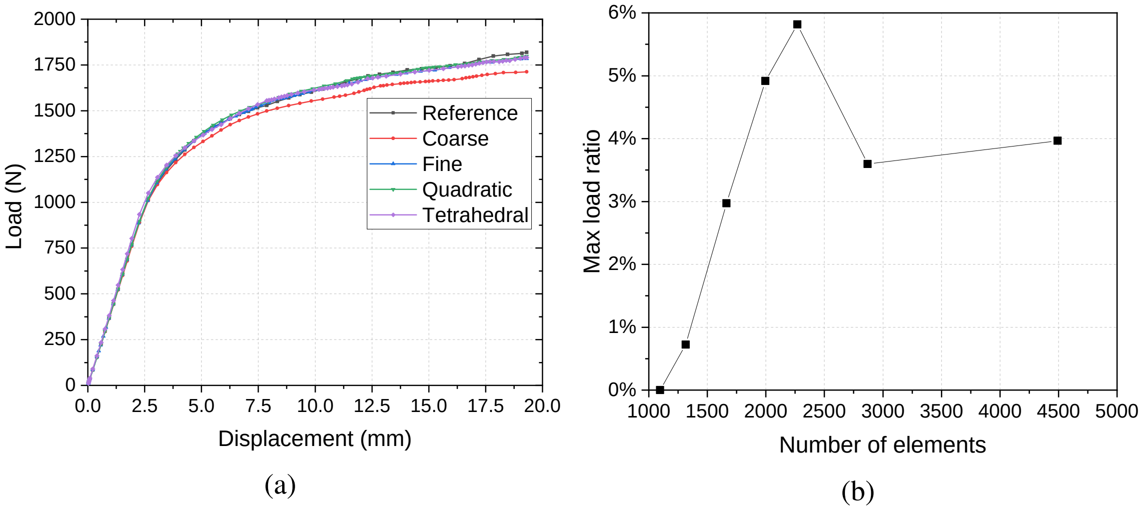

(a) (b)

Fig. 5.19 Mesh independence study of the FEM; a) load-displacement curves for different mesh densities and elements and b) load at maximum displacement for different mesh densities of the 3D reference model.

5.3.9 Weak springs

In many cases the convergence of the FEM was challenged due to the high number of contacts and large deflections expected during the sample deformation. To enhance the numerical stability of the model the weak springs option was activated. The weak springs are a numerical expedient that can help convergence and can avoid rigid body motion. Since the weak springs have a low stiffness relative to the model stiffness, they will not have an effect on a properly constrained model. Nevertheless, their effect on the resulting load-displacement curves was investigated for different weak spring stiffness factors.

Fig. 5.20 shows the load-displacement curves for different weak springs options. When the weak springs option is activated, the program automatically adds weak springs in case of unstable contacts. The bending response of the models with and without the weak springs option showed identical behavior. Further simulations were run for higher values of weak springs stiffness factors. The resulting load-displacement curves showed stiffer bending responses for higher weak springs stiffness values. Again, the differences appeared in the plastic region, whereas the elastic regime was identical for all cases. Fig. 5.20b provides the differences of the load at maximum displacement for different stiffness factors, where a nearly linear correlation was demonstrated.

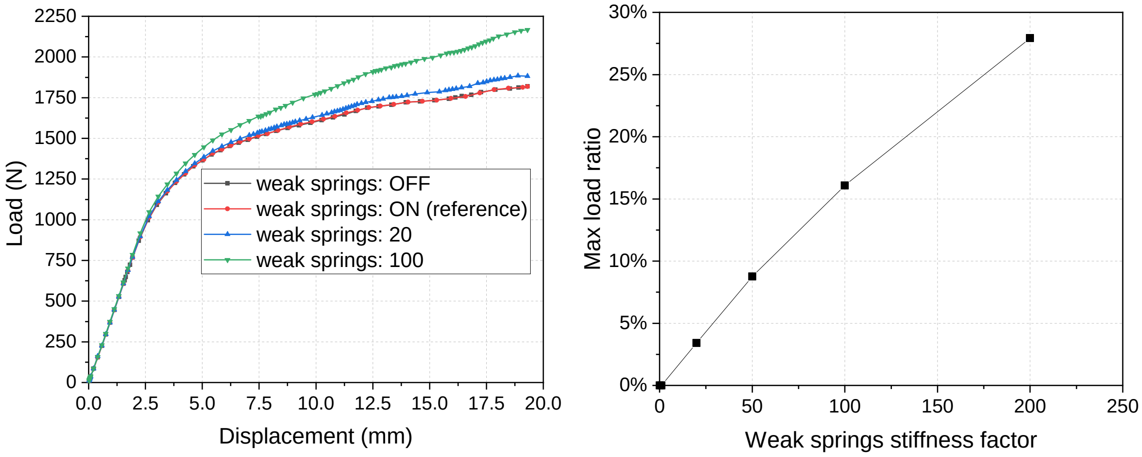

(a) (b)

Fig. 5.20 a) load-displacement curves for different weak springs options and b) load at maximum displacement for different values of the weak spring stiffness factor.

5.3.10 Conclusions and construction of final FEM version

An extensive sensitivity study on the modelling approach and use of several numerical parameters was performed on the reference 3D FEM. The objective of this study was to fully understand the influence and importance of the modelling simplifications on the resulting load-displacement curves. Based on this study the reference FEM was modified and a final version of the model was defined. The final model was the best compromise between solution quality, model convergence, and computational time required for the simulation. A detailed description of this model is given in Appendix E.

The most important modifications of the final FEM concern the meshing of the model, the contact formulation between the different bodies and the boundary conditions used for the end-pellet. The cladding was modelled as body element with two elements across its thickness, in order to accurately estimate the development of the plastic strains in higher deflections close to the loading region. In addition, much higher mesh density was used in the areas of interest, namely in the vicinity of the load application and at the contact between the cladding and support. Finally, a stiffer spring was used to constrain the end-pellet in order to artificially create a slightly stiffer response of the sample, as predicted from the half symmetry model (refer to Fig. 5.14).

One of the most significant simplifications was the use of nominal geometrical dimensions and mechanical properties for the pellets (refer to Appendix E). In this way, the bending strength contribution of the pellets was assumed to be the same and irrelevant of the sample burnup. Indeed, the sensitivity analysis on the FEM revealed that the cladding properties are significantly more important than those of the fuel for the bending response of the sample. In addition, the opposing effects of pellet fragmentation and swelling over sample stiffness, were considered by modelling the fuel pellets based on their nominal dimensions and not based on the internal diameter of the cladding. The latter condition under the aforementioned modelling assumptions could create a much stiffer model.

Another important outcome of the sensitivity study was that the bending response in all FEMs was similar in the elastic region. The resulting differences appeared in the plastic regime and mainly after a considerable amount of plastic deformation. In addition, the development of the plastic stresses and strains at theses points were governed from local effects introduced by the modeling simplifications (i.e. pellet geometry, contact formulations, etc.). Therefore, the results for these conditions are prone to singularities that might occur close to the loading region and at the pellet-pellet or pellet-cladding contacts. The results for these conditions (and after extensive plastic deformation) are of high importance, since they could be used for the derivation of cladding failure criteria of the low burnup samples. In order to improve the confidence and understanding of the results in these conditions, the use of the load-displacement experimental data is not sufficient and further experimental data are needed (e.g. bending radius of the sample in different locations, etc.).

Finally, the use of FEM helped towards the verification and/or better understanding of the qualitative assumptions on the sample's bending response made based on the experimental observations (refer to section 4.7). The following images provide a direct comparison between the experimental and the numerical results, where some of the most important outcomes on the sample's response are highlighted. On the cladding crack initiation, the numerical simulations confirmed that the cladding fractures in the area of highest plastic strains, which is developed at the pellet-pellet interface closest to the symmetry-loading axis, as shown in Fig. 5.21a. In addition, after extensive plastic deformation the cladding at the area of the loading is permanently bent, which prevents the possibility of extensive fuel mass release in case of fracture as shown in Fig. 5.21b. Lastly, the highest stresses on the pellets are developed at the pellet-pellet interface closest to loading point and in the pellet under the area of the former. In this region, the pellet cracks and the fragments are released after the cladding failure as illustrated in Fig. 5.21c.

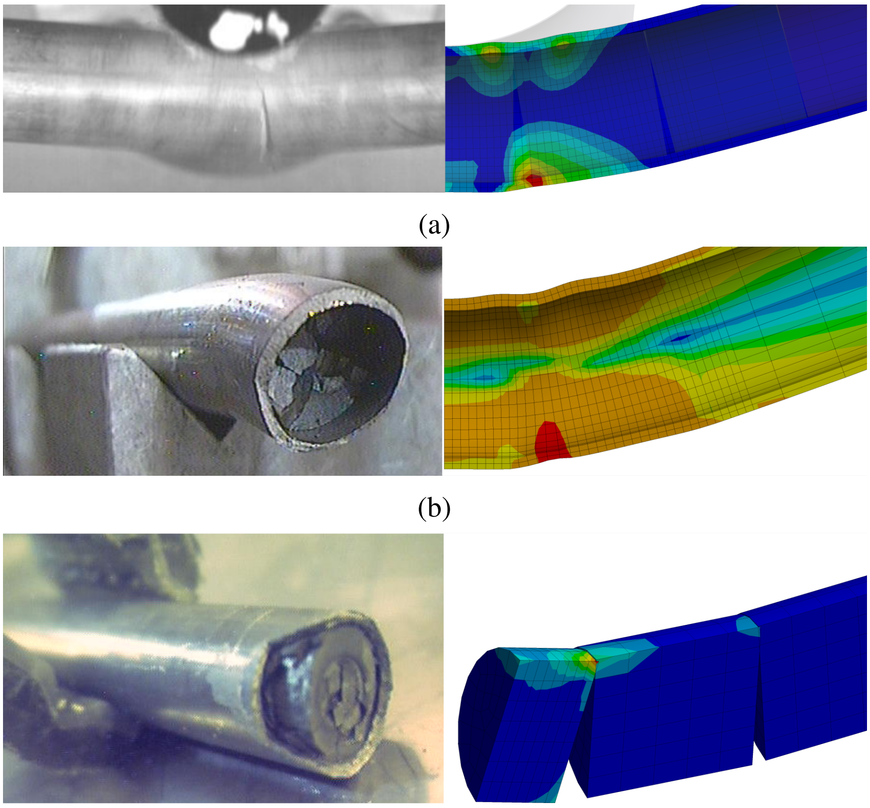

(a)

(b)

(c)

Fig. 5.21 a) cladding failure at point of highest plastic strain, b) permanent bending of cladding after long plastic deformation under the loading points and c) areas of highest stress development at the pellets.

5.4 FEM calibration based on experimental results

The calibration of the FEMs was performed on the 3-point bending experimental results with the use of "optiSLang", an ANSYS integrated software package for sensitivity analysis and optimization. In short, the FEMs were parametrized so that the variation of certain variables (i.e. material properties) could be used to explore their effect on the results. Then, the numerical results were compared to the experimental data by implementing an objective function, which calculates the sum of the squared errors (or differences between experimental and numerical data) over all time steps. Thus, optiSLang explored the cause of non-matching results, to understand the driving parameters, adjust the parameters for the numerical model and finally optimize the specific function of interest [111]. The calibration process of the FEMs is described in the following paragraphs.

At first, a range is given to each parameter of the material properties of the FE model. The range is selected by expert judging, on the basis of the experimental results and some preliminary trial runs. The parameters to which a range is assigned are simply referred to as variables. As a second step, sampling is performed on the variables' range to produce a set of models (design points) that will run in ANSYS. Latin hypercube sampling (LHS) is mostly used to sample the variables and to define the design points since it guarantees a good representation of the solution space with relatively few runs (in the order of hundreds).

The optimisation is defined through a minimisation function (hereafter called error function), which simply gives the difference between the integral under the load-displacement curves; specifically, it is the Euclidean norm difference of the vectors corresponding to the FE model load-displacement and the experimental load-displacement. An example of the generated models via the LHS sampling is given in Fig. 5.22. Figs. 5.22a and 5.22b provide the same information, where the range of each variable, the combinations of the values used for each model and the resulting error of each simulation are shown. In Fig. 5.22b, the simulations that have produced the lowest error values are highlighted. There, it can be observed that for the variables that have a strong influence on the resulting load-displacement curves (e.g. the cladding yield stress) the values that produce the best models are constrained in a small part of the variable range. This is not true for other variables (i.e. the exponential saturation coefficient of the Voce model), where practically any value in the given range can produce models with very small errors, since this variable has much lower importance on the bending response of the sample.

An example of simulation results generated from optiSLang by sampling the design variables is given in Fig. 5.23a. The load-displacement curves (or the reaction force at the

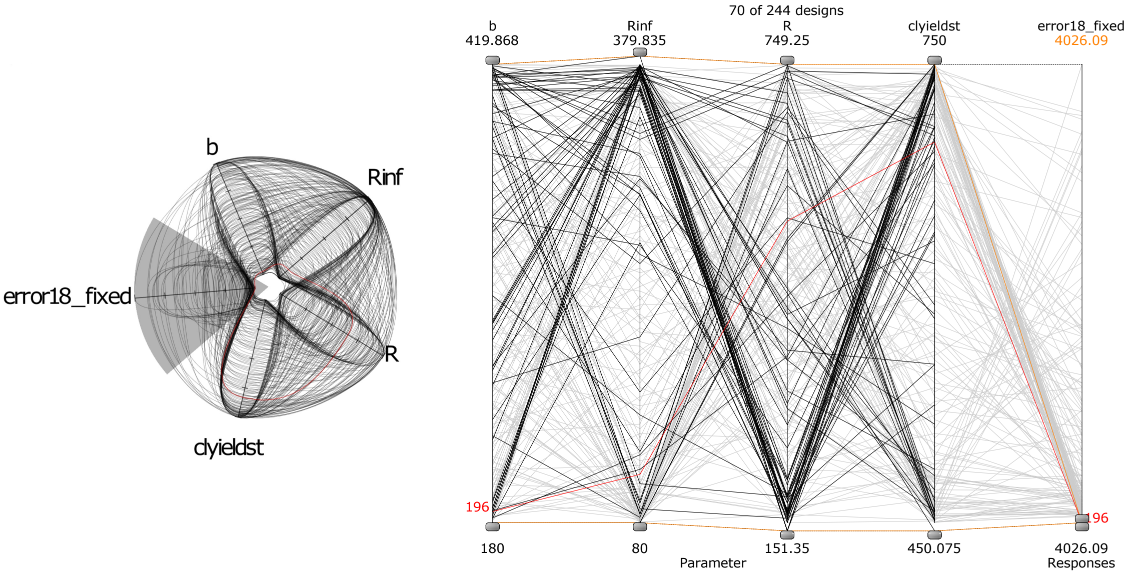

(a)

(b)

Fig. 5.22 a) Spider plot and b) parallel coordinates plot showing the value selection for the generated FEMs through LHR sampling.

former against its displacement) produced from each simulation are plotted in grey. The error of each simulation gives its deviation from the experimental result, which is plotted in black. The simulation that gives the lowest value of error is defined as the best design and it is highlighted in red.

Each simulation can be described from the value of the objective function (or the error). These values can be plotted as a function of the input variables to provide a visual representation of different solution spaces describing the optimization problem. OptiSLang produces a so-called MoP, which is a response surface as an explicit function based on the exploration of selected variables. In other words, the MoP is basically the fitted surface created by the response of the most decisive parameters (as estimated in optiSLang) of the FEM simulation. Fig. 5.23b shows an example of an MoP as derived after a sensitivity analysis on the material properties of the model. The data points in red represent how much the simulation deviates from experimental results and the MoP surface is generated using the Isotropic Kriging fitting approach. In this specific case, the effect of the cladding yield stress and Voce exponential coefficient (being the most important parameters in this model) are shown.

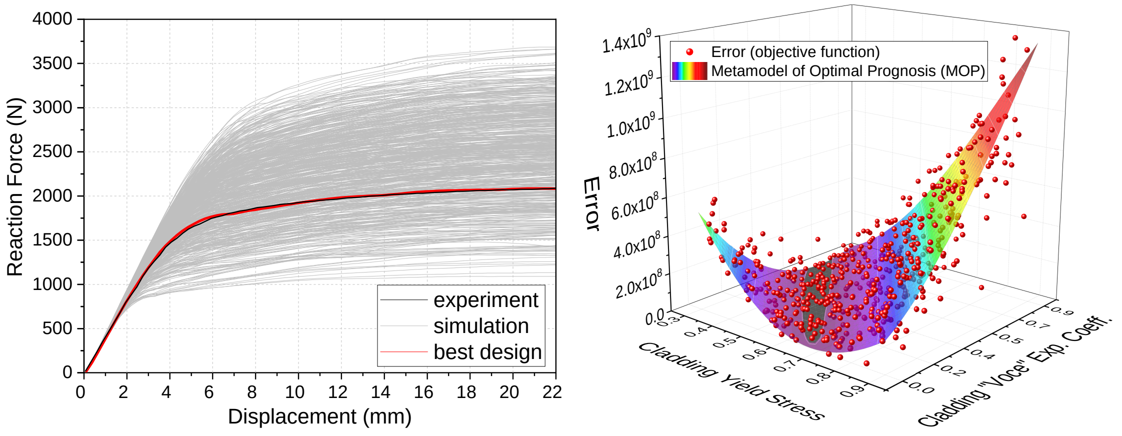

(a)

(b)

Fig. 5.23 a) Force-displacement curves of the generated design points obtained from sampling the variables' range with optiSLang and b) Metamodel of Optimal Prognosis (MOP) showing the result deviation or error of each simulation (red points) from the experimental results. The error is plotted as function of the most important parameters of the FEM being the cladding yield stress and the Voce exponential coefficient.

5.4.1 Optimization process

The objective in this study was to examine any possible dependence of mechanical properties of the cladding on the rod's average burnup. The results on the KKG SNF rods are presented since they refer to the same cladding type. OptiSLang was used for the model calibration and for the subsequent optimization process. The goal of the optimization was to find the best possible solution that describes the cladding mechanical properties by providing the lowest possible difference against the three-point bending experimental results from of each test.

OptiSLang uses a quality measure, called CoP, to evaluate the relative importance of the input variables and to optimize the selection of the MoP. The CoP actually describes the predictive quality of the MoP, where high values thereof ensure that the metamodel can be used reliably to explore the solution space, avoiding time-consuming FEM simulations. The CoP was also calculated for each variable as defined in the FEM simulations. High values of CoP indicate that the variable is of high importance with regard to the solution quality. The next step in the model calibration is to perform an optimisation using the MoP. In this case, the parameter range is readjusted (variables with low CoP values are excluded), and an optimization problem is applied once more to minimize the differences between the numerical and experimental results. The theoretical background for the derivation of these measures is given in the following paragraphs.

The selection of the best MoP (or the best method to fit the generated results) is based on the Coefficient of Performance (CoP). The CoP is a model-independent measure to evaluate the model quality and is defined as:

$$CoP = 1 - \frac{SSE_E^{prediction}}{SS_T} \tag{5.3}$$

, where $SSE_E^{prediction}$ is the sum of squared prediction errors [1], and SS_T is the total variation of the support points, i.e. the sum over all squared differences between the observations and their overall mean. In this work, SS_T is defined as the squared sum of the difference between the error value (which is the output value) in each specific support point and the average error of the support points:

$$SS_T = \sum_{sp=1}^{tot_{sp}} (error_{sp} - average\_error)^2 \tag{5.4}$$

, where sp stands for support point and tot_{sp} is the total number of support points, which is the total number of models run by ANSYS.

The CoP, when calculated for each variable ($CoP(X_i)$), assumes a second meaning of paramount importance both for better selecting the metamodel and for getting an understanding on the role that each variable plays in the final results (i.e. the load-displacement curves). The $CoP(X_i)$ is calculated as:

$$CoP(X_i) = CoP \times S_T^{MoP}(X_i) \tag{5.5}$$

, where $S_T^{MoP}(X_i)$ is the total sensitivity index for the MoP that for a generic metamodel is defined as:

$$S_T^M(X_i) = 1 - \frac{V(Y \mid X_{\sim i})}{V(Y)} \tag{5.6}$$

, where $V(Y \mid X_{\sim i})$ is the variance of Y (the metamodel output) caused by all variables excluding the variable of interest X_i, and $V(Y)$ is the unconditional variance of the model output. To better understand the idea behind the total sensitivity index and in turn behind the $CoP(X_i)$ it is worth explaining briefly the first-order sensitivity index, which is:

---

[1] Note that here errors are NOT meant to be the errors of the support points calculated through the error function, but are meant as the differences between the values of the error of the support points predicted by the fitting and the actual error values.

$$S^M(X_i) = \frac{V(Y \mid X_i)}{V(Y)} \tag{5.7}$$

, where $V(Y \mid X_i)$ is the variance of Y (the metamodel output) caused by a variation of the variable X_i only. In other words, $S^M(X_i)$ quantifies how much the variance of the metamodel is influenced by one of its variables. If $S^M(X_i)$ is equal to one means that only X_i influences the metamodel. With a different perspective, it means that just X_i is the variable that matters, the others are utterly unimportant for the metamodel output. If $S^M(X_i)$ is equal to zero means that X_i does not affect the results whatsoever. Now, $S^M_T(X_i)$ is the logical and natural extension of $S^M(X_i)$ in case the variables are covariant. Indeed $S^M(X_i)$ measures only the decoupled influence of each variable.

Fig. 5.24 is used as example to show the $CoP(X_i)$ results as derived in optiSLang for a three-point bending simulation. For this specific run, the software has cancelled out the pellet parameters, being the least important, and provides information for the cladding Voce parameters. High values indicate high importance of the parameters to determine the final results: the cladding yield stress and the exponential coefficient (R_{inf}) were found to be the most decisive parameters defining the bending response of the sample.

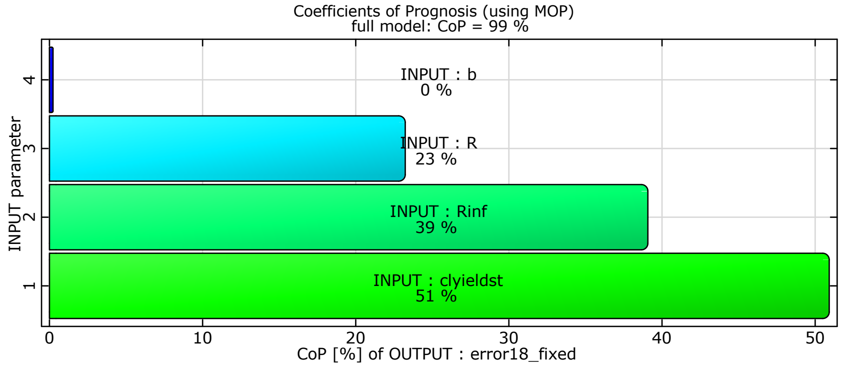

Fig. 5.24 Example from $CoP(X_i)$ resulting from the MoP generation.

5.4.1.1 Derivation of cladding's effective mechanical properties

Fig. 5.25 shows the load-displacement curves generated through the FEM calibration/optimization process for each model representing the three different samples. The best design point is highlighted in red; it is clearly seen that the model calibration has already provided very good results in comparison to the experimental data. To further minimize the resulting errors of the simulations an optimization process was performed for each case.

The cladding properties as derived from the best design point after the optimization are given in Table 5.6. In addition, the CoP values for each parameter are given along with the total CoP, which characterizes the quality of the MoP. Although the CoP values depend on many factors, it can be observed that the most decisive parameters of the CoPs are the Young's modulus and the yield strength (σ_0). This is particularly correct for the two high burnup samples, where there was only limited amount of plastic deformation. Consequently, the parameters describing the plastic stress development based on the Voce model are less important. These factors showed higher importance for the low burnup case, in particular the Voce exponential coefficient R_{inf}, as expected due to much higher plastic deformation.

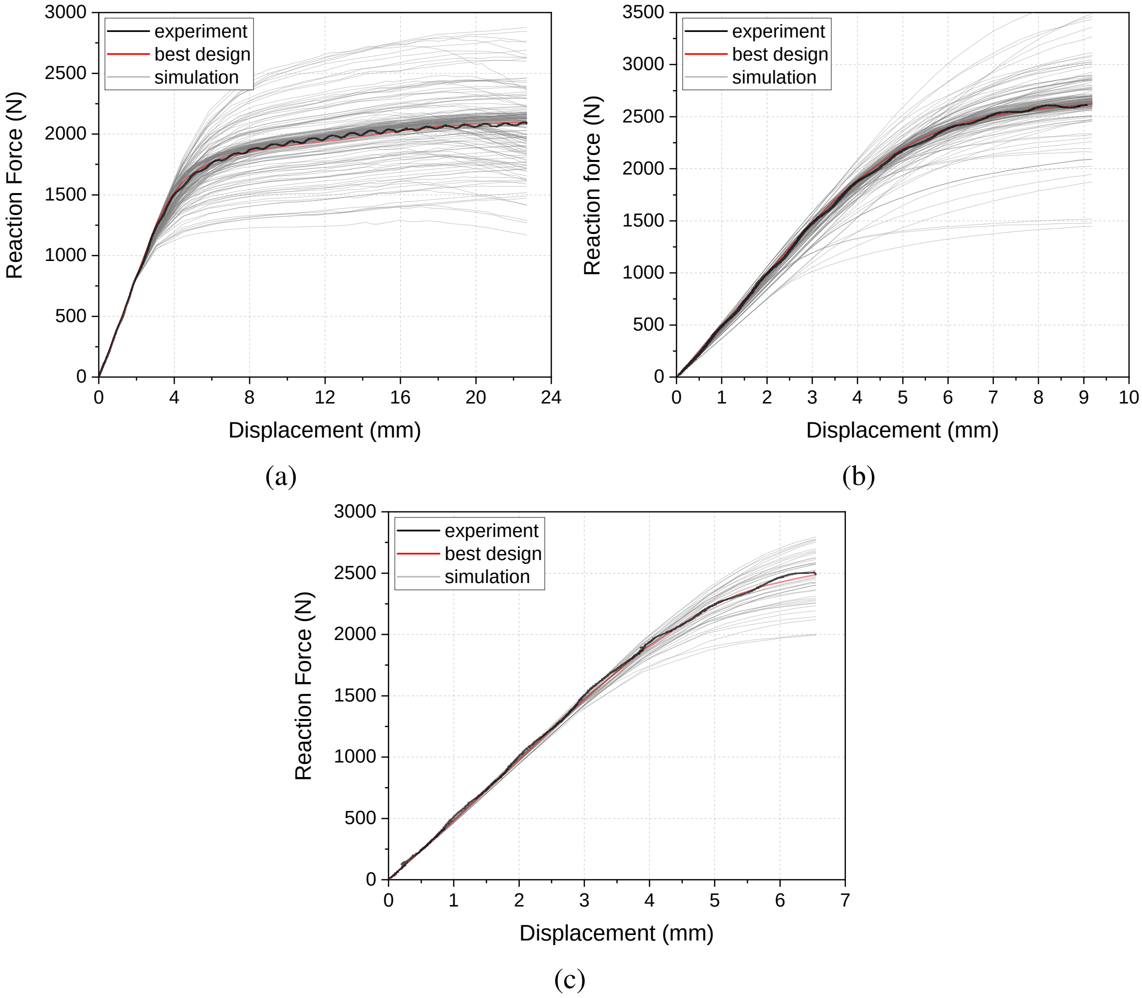

(a) (b)

(c)

Fig. 5.25 Load-displacement results of all the 3D model OptiSlang fittings for the a) 18.3 GWd/tHM (KKG-A11), b) 46.9 GWd/tHM (KKG-D08) and c) 58.6 GWd/tHM (KKG-A07) models compared to the corresponding experimental data. The best-fit is highlighted in red, whereas the experimental data curve is presented in black. The grey lines are the OptiSlang generated FEM simulations.

Table 5.6 Cladding properties and associated CoP values as calculated in optiSLang.

Sample	Parameter	Young's modulus (MPa)	Poisson's ratio	σ_0 (MPa)	R_0 (MPa)	R_{inf} (MPa)	b	Total CoP
18.3 GWd/tHM	Best-fit value	87050	0.38	699	545	112	186	
(KKG-A11)	CoP(X_i)	-	-	51%	23%	39%	0%	99%
46.9 GWd/tHM	Best-fit value	104762	0.40	776	717	364	407	
(KKG-D08)	glsCoP(X_i)	3%	0%	93%	0%	7%	5%	99%
58.6 GWd/tHM	Best-fit value	103500	0.48	800	138	350	660	
(KKG-A07)	CoP(X_i)	41%	0%	82%	0%	31%	5%	99%

In Fig. 5.26 the most important cladding properties as derived from the ANSYS simulations are compared to the respective experimental results. The graph in the left gives the results of the Young's modulus for the three different samples. Good agreement is observed between computed and experimental values showing that the derived flexural modulus could be used directly in the ANSYS models. A small difference was observed for the low burnup case; however, due to long plastic deformation of this sample the Young's modulus has lower importance.

It is also interesting to look at the comparison of the experimental flexural yield strength to the tensile yield strength as calculated in optiSLang from the FEM simulations. The experimental results, plotted in Fig. 5.26b, show higher values of the flexural properties, which a range between 30% and 50% compared to the tensile ANSYS properties. The difference between these values stems from the fact that in tensile loading the profile of the stresses is a horizontal line, compared to the stress distribution in bending (refer to Fig. 2.26a). This in turn means that all the "fibers" of the body have the same (maximum) stress in tensile loads, whereas in bending, stresses increase radially with the maximum stress located on the outer part of the body. Since there are more fibers under maximum stress in tensile loads, the chances of an imperfection existing in one of these parts (from which cracks or increased local stresses can start developing) is increased, thus resulting in a smaller yield strength value.

5.5 Summary

In this chapter, the numerical investigations on the mechanical response of SNF rods under static bending loads were presented. Finite Element Models (FEMs) were developed in ANSYS Mechanical to simulate the response of the samples. The models were calibrated

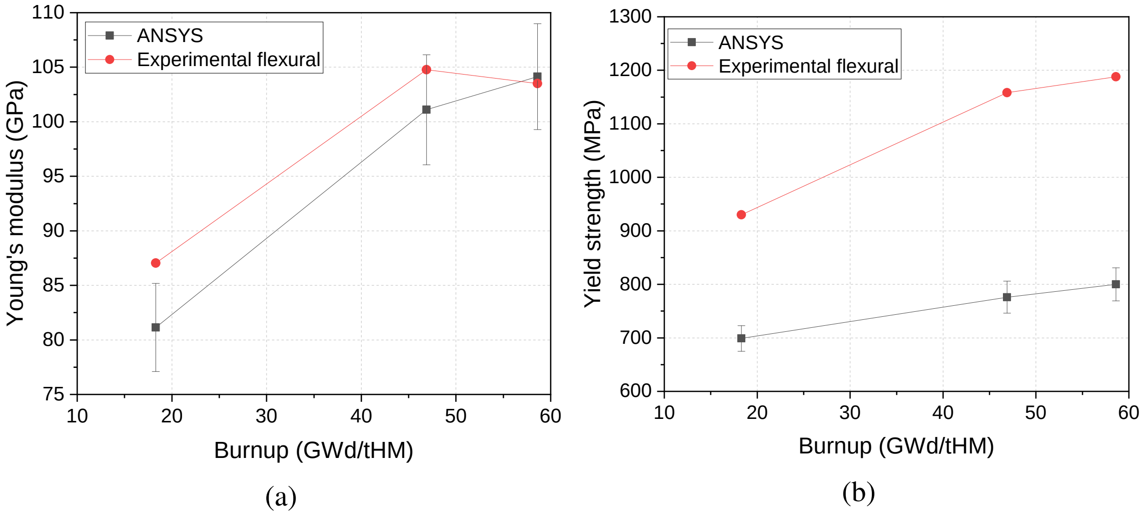

Fig. 5.26 Comparison of the a) Young's modulus and b) yield strength between the experimentally and numerically derived mechanical properties of the cladding.

against the experimental results from the three-point bending tests, namely the resulting load-displacement tests, since more experimental data were available compared to the impact testing. The objectives of the FEA in this study were to provide a better understanding of the observed experimental results and to investigate the mechanical properties of the SNF rods.

At first, the stiffness of the three-point bending device was examined in order to assess whether its response could possibly influence the experimental load-displacement data. To that extend, an FEM was developed representing the structure of the bending device and simple boundary conditions were applied to conservatively estimate the deformation of the loading point under the highest possible loading conditions. The results revealed that the stiffness of the device is adequately high and only limited amount of deformation was calculated at the tip of the former.

Subsequently, a FEM was constructed to simulate the three-point bending test conditions and samples used in the experimental campaign. Due to the high modelling complexity of the irradiated samples the first models were built upon the nominal geometrical dimensions and mechanical properties of the surrogate samples including fresh Zry-4 claddings and alumina pellets. Based on this model, an extensive sensitivity analysis was performed on numerous numerical and physical parameters in order to examine their relative importance on the results and the uncertainty that could be introduced based on different modeling approaches. A final version of the FEM was built upon the results of the sensitivity study, as the best compromise between computational time and solution quality.

In addition, a FEM representing the irradiated samples was constructed based on a series of assumptions. Their validity was investigated, and the FEM was used to simulate the mechanical response of the samples under three-point bending conditions. OptiSLang was used to calibrate the FEMs against the bending experimental results, to understand the most important parameters of the model and finally to derive the cladding mechanical properties. For this purpose, an optimization problem was solved aiming at reducing the differences in terms of load-displacement curves between numerical and experimental results. In addition, this process revealed and confirmed that the cladding properties are the decisive parameters of the FEM, having significantly greater importance compared to the fuel properties. As a result, the optimization problems were solved based on the cladding properties.

The final optimized FEMs provided the effective cladding mechanical properties under the considered modeling assumptions; their combination can simulate the mechanical response of the irradiated samples as recorded during the mechanical tests. The dependence of the most important cladding parameters on rod burnup was investigated and the results were in good agreement with the experimental observations. Finally, a comparison between experimentally and numerically derived effective cladding properties was performed. The results showed very good agreement on Young's modulus and a difference of 30%-50% (depending on the burnup) on the yield strength. Such differences were expected, since the experimental results reflect the flexural rather than the tensile properties of the cladding, as these were derived numerically in ANSYS.

Chapter 6

Conclusions and outlook

The main goal of this doctoral study was to investigate the structural response and the mechanical properties of spent nuclear fuel rods. To that extent, a twofold approach was followed including both experimental and numerical investigations. The experimental studies included a series of mechanical tests and post-test examinations on surrogate and irradiated SNF rodlets. The objectives were to examine the properties of the samples as a function of different parameters (e.g. burnup, hydrogen concentration, strain rate) and to better understand the process of rod failure and to evaluate its consequences (i.e. fuel mass release). The numerical studies concerned the development and validation of Finite Element Models (FEMs) to simulate the structural response of spent fuel rods under bending loads. The aim was to derive the mechanical properties of the cladding as function of burnup and to provide the means to describe the structural integrity of SNF rods under conditions and configurations that differ from those applied in the conducted experimental investigations.

The following paragraphs present the main achievements and key observations of this work. The conclusions resulting from the experimental and numerical studies are summarized in section 6.1. As this work constitutes the onset of a wide range of RD&D activities in the area of spent fuel integrity in Nagra [67], the last section 6.2 is used to provide some highlights and recommendations for future work and technical improvements.

6.1 Summary and main conclusions

The design of the experimental campaigns and the methodologies used to evaluate the structural response of the tested samples were described in Chapter 2. The experimental studies were conducted at the hot-cell facilities of JRC-Karlsruhe and followed previous experimental investigations that have been presented in previous publications [15–17]. The current study aimed at extending and deepening the understanding of the mechanical behaviour of the SNF by studying their structural response to external loads in a systematic way. For this purpose, two mechanical test devices were developed to perform three-point bending, and gravitational impact tests on surrogate and irradiated SNF rod samples. This approach has made it possible to examine macroscopically the flexural behavior of the rods at different strain rates. The development and optimization of the experimental devices focused on the exploitation of the testing capabilities, in particular by maximizing the comparability of the data from both types of test, and on the elimination of systematic errors affecting the obtained experimental data.

The two mechanical setups share the same geometrical characteristics in terms of the loading configuration of the sample. Both apply bending loads via a former onto the sample, with the latter lying upon circular supports. Their main difference is the load application or the strain rate. In three-point bending tests, a step-motor was used to apply constant (and very slow) displacement rate, which translates in quasi-static loading conditions. In impact tests, dynamic conditions are applied by the free-fall of a heavy ($\sim$10 kg) hammer on the sample. As a result of the device hardware optimization, the differences of the mechanical response of the samples subjected to different strain rates could be examined by comparing directly the experimental results from both tests; this constitutes the first major achievement of this study.

Another significant difference between the two test techniques is the data acquisition and analysis of the flexural response of the samples. In the 3-point bending apparatus, sensors are used to record applied load and sample's deflection. The raw data consist of load-displacement curves and the mechanical properties of the rods can be derived with the use and under the assumptions of the simple beam theory. In the impact tests on the other hand, a high- speed camera is used instead of sensors to capture the response of the samples during these tests. The analysis of the samples' flexural response was performed with Image Analysis (IA), which was used to translate the recorder images into tangible experimental data (i.e. sample's momentary deflection and absorbed energy). The development and validation of this new methodology was another major achievement of this work, which also enabled the direct comparison of the experimental results between the two tests.

The experimental campaign consisted of two phases; the first phase refers to the analogue studies performed on surrogate samples under cold laboratory conditions and the second phase includes experiments on commercial SNF rods. The analogue experimental campaign was presented in Chapter 3 and included mechanical testing on untreated and hydrogenated Zry-4 cladding tubes, filled with alumina pellets and pressurized to 40 bar. Both objectives of this initial phase, namely the development and optimisation of the devices, and investigation of the cladding's mechanical properties as function of the hydrogen content, were achieved. The first important conclusion was that the elastic properties of samples are governed solely from the cladding properties. With the use of the Euler-Bernoulli beam theory the flexural properties of the claddings were derived using beam elements with hollow-circular profile. Slightly lower values of the Young's modulus on hydrogenated claddings were measured compared to fresh Zry-4 cladding tubes, where the derived values were in accordance to literature data. This small decrease could be attributed to thermal treatment and annealing of the claddings during the hydrogenation process.

The samples with lower hydrogen concentration in the cladding (up to 100 - 150 ppm) showed higher ductility and fractured at higher bending angles. At higher hydrogen concentrations, in the range $\sim$150 - 650 ppm, the ductility decreased linearly. Samples with higher hydrogen content exhibited brittle behavior and failed at similar bending angles $\sim 15^\circ$ independently of the hydrogen content. The contribution of the fuel pellets on the bending response of the sample was determined. Their influence manifested during plastic deformation by increasing the bending stiffness of the sample and preventing the buckling of the cladding. Finally, another important observation concerns the fracture behavior of the cladding: the crack initiated always at the bottom region subjected to tension and at the PPI interface closest to the loading axis.

The experimental campaign on commercially irradiated PWR UO2 rodlets was presented in Chapter 4. The samples were selected from rods irradiated at KKG (4 rods) and at KWG (1 rod) NPPs and covered a wide range of burnup. All the rods had Zry-4 cladding. The KKG rods, from Framatome, had cladding with outer liner (DX D4), except the highest burnup rod, which had 2.5% of Nb at the outer liner (DX Zr2.5Nb). The KWG rod, from Westinghouse, had Duplex cladding. Both impact and three-point bending tests were performed at room temperature on samples pressurized to their initial nominal internal pressure.

The samples with lower burnup showed higher ductility both in three-point bending and in impact testing. The toughness of the samples was higher at higher burnup due to irradiation hardening of the cladding. The Young's modulus of the claddings showed good agreement with previous studies and a nearly linear increase with burnup was observed, mainly due to higher oxide layer thickness. The IA methodology was successfully applied to analyse the response of the samples in the impact tests and the displacement and energy absorbed from the sample until fracture were determined. The results were compared with the three-point bending tests data and showed that the difference in strain rate has a stronger effect on the displacement at fracture at lower burnup, as for this case the sample fractured at approximately half of the displacement in impact compared to bending.

Another important conclusion of this work concerns the extension of the description of the mechanical response of rods to lower and higher burnup compared to the burnup range of the fuel rods tested. Taking into account all the results from the three-point bending tests, both on surrogate and irradiated samples, it can be concluded that the trends and correlations observed and determined in the current experimental campaign can be extended to cover/bound the behavior of rods with lower or higher burnup. Lower burnup rods are expected to be softer and their expected behaviour can be interpolated between the obtained irradiated rods results and the values obtained for the fresh Zry-4. For higher burnup rods, the flexural response will be similar to the samples tested in the present campaign, which showed rupture levels becoming essentially burnup-independent at very high burnup, and quite limited plastic deformation.

Moreover, the mechanical tests were complemented by a series of post-test examinations, which were successfully performed to character- ize the overall state of the fuel rodlet upon fracture, the hydrogen concentration and hydride morphology in the cladding, as well as the fuel mass release, mainly in terms of mass and size distribution. Similarly to the analogue studies, the location of the cladding crack initiation was at the bottom side subjected to tension and at the PPI closest to the loading axis. The most important observation was on the fuel mass release, which in all cases was limited to less than a pellet per fracture and always systematically higher in impact tests (with both testing methods showing the same trends of mass release as a function of burnup). The release was limited over the whole burnup range of the samples tested due to the effectiveness of the pellet-cladding bonding (closed gap) at higher burnup and due to higher plastic deformation of the cladding lower burnup. Furthermore, the effect of the hydrogen embrittlement on the cladding performance was investigated. As expected, the cladding ductility decreased with higher hydrogen content. A correlation between the rod's burnup and the hydrogen concentration in DX D4 claddings was determined. Finally, the size distribution of the released fragments and fine particulates was studied, providing valuable information for accident scenario analysis and possible decontamination techniques.

The numerical investigations with the use of Finite Element Analysis (FEA) were presented in Chapter 5. The main objectives of this study were to provide a better understanding of the structural response of SNF under bending loads and to derive the mechanical properties of the cladding as function of the burnup. For this purpose, ANSYS Mechanical was used to develop and validate 3D static structural FEMs against the experimental three-point bending test results. An extensive sensitivity study on various modeling parameters was performed to investigate their importance on the derived results, namely on the load-displacement curves. Based on this study, a series of modelling simplifications and assumptions could be made in order to construct an FEM of a SNF rodlet, which can provide reliable results in reasonably low computational time.

The sensitivity study revealed the significance of the mechanical properties of the cladding regarding the bending response of the samples. On the other hand, the pellet properties do not have any significant influence (under the assumed modeling simplifications), confirming the experimental observations. Consequently, the calibration of the FEMs was performed by varying the cladding properties, aiming to minimize the difference between the experimental and the modeled numerical load-displacement curves. This optimization process was performed for the experimental data on the samples from KKG rods with the same cladding type. The results showed a dependence of the most important cladding parameters on the burnup, which were in accordance to the experimental observations. The experimental results represent the flexural properties of the sample, whereas the numerical represent the tensile ones. For this reason, the Young's modulus was found in very good agreement between both studies, in comparison to the yield strength, where higher values were observed in the experimental data (as expected). The development and validation of the FEM was another major achievement of this work since the structural response of SNF rods can now be investigated under more realistic loading conditions and configurations.

6.2 Future work recommendation

This study was the initiation of a collaborative agreement between Nagra and JRC-Karlsruhe, with the support by Framatome and KKG, on the investigation of the structural response and mechanical properties of SNF rods after long-term dry interim storage. The research aims to provide essential input on the operational safety related to storage, transportation and final disposal of SNF assemblies. To this extent, more data and numerical analysis are needed in order to understand the effect of various phenomena on the mechanical properties of SNF rods. Therefore, follow-up works should extend and exploit the outcomes of further experimental campaigns in order to improve the numerical models and minimize the uncertainties of the derived mechanical properties.

The first area of potential improvements is related to the characterisation of the mechanical response of SNF rods in dynamic loading conditions. An important effect that cannot be studied with the current experimental setup is the damping of the material. Damping in mechanical systems is the dissipation of mechanical energy from the motion in the system that attenuates oscillations due to internal resonances. This factor characterizes the material and its definition is of paramount importance for dynamic structural analysis with FEM. This effect could be studied by either improving the acquisition capabilities of the experimental device or by employing advanced methods of IA.

Fig. 6.1 shows the designs of a conceptual experimental impact test device with extended data acquisition capabilities that would facilitate the testing procedure in the hot-cell. In this case, a step-motor is used to raise the heavy hammer after each test without the need of using the crane. The actual impact energy could easily be adjusted by either changing the height of the hammer's positions (new mounting system design) or by varying the hammer's weight. The impact loads could be recorded with a high frequency load-cell sensor installed on top of the former, similarly to the three-point bending setup. In addition to the proposed device improvements, the flexural response of the sample could be analysed using ultra high-speed photography in conjunction with Digital Image Correlation (DIC) [112, 113]. This is a well-established state-of-the-art method to characterize the mechanical response of materials in high strain rates and could also be applied for the analysis of the impact tests on SNF samples.

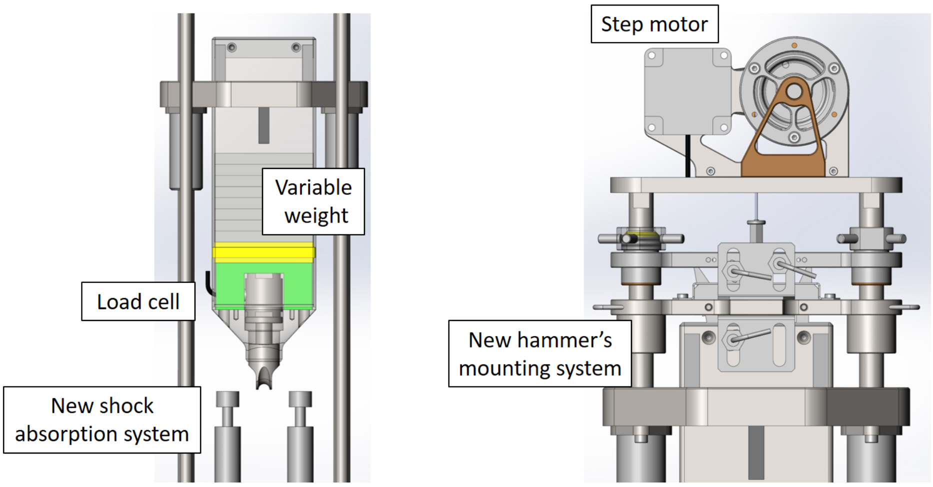

Fig. 6.1 Conceptual design of a new impact test setup aiming to extend the data acquisition capabilities and facilitate the test procedure within the hot-cells.

In addition, some aspects would have to be considered for the design of future experimental campaigns. For instance, the effect of internal pressure on the sample's flexural response was numerically investigated and analysed in this work (refer to Fig. 5.16). It was observed that the elastic response of the sample is not affected by variations in internal pressure, while bending stiffness increases for lower pressure values and the effect becomes more apparent after long plastic deformation. Having determined the role of internal pressure, allows for excluding it from future parametric experimental studies, not only for minimization of the required time for test conduction, but also for a direct comparison of experimentally derived cladding properties at different burnups. In addition, sample pressurization should be avoided since the end-plugs used for its sealing affect the sample geometry and weight, and as a result the dynamic response (damping factor) of the material.

The effect of the hydride re-orientation on the mechanical response of the samples could be investigated with additional tests. Samples from the same rods could be selected to undergo thermomechanical cycled treatment, causing the hydrides to dissolve and precipitate again in the radial direction. Mechanical tests on theses sample could reveal the relevance and influence of the hydride reorientation on the flexural response of SNF rods. In addition, the mechanical response of the SNF rods could be investigated as function of temperature. This would enable the evaluation of the rods response during dry interim storage or transportation in TSCs, where temperature conditions are expected to exceed room temperature. Furthermore, tests on either MOX or BWR SNF would be of great importance since experimental data from tests on these fuel types are extremely rare.

The last recommendations are related to the improvement of the FEA and to the possible future extension and use of the FEM. At first, in order to minimize the solution uncertainty, the validation of the models could be performed based on experimental results for more than one mechanical properties. For example, the bending radius of the sample in different axial locations could be measured and used to create a multi-objective optimization problem, aiming to minimize the difference of experiential and numerical results by varying the most important parameters of the model (i.e. cladding properties) [114]. Moreover, the validity of the assumptions/simplifications made for the construction of the FEM representing the SNF rods should be further investigated experimentally. For this purpose, simple experiments under cold laboratory conditions could be designed with the use of certified materials. For instance, the influence of pellet cracking and pellet-cladding bonding, could be studied by replacing the alumina pellets of surrogate samples with granular material of different sizes and packing densities. Finally, the investigation of the structural integrity of SFAs cannot be examined by simply extending the current 3D FEM since this would significantly increase the modeling complexity and result in long computational times. For this purpose, new FEMs have already been established by following beam modeling approaches [110, 115]. The models have already been calibrated against the experimental results and the following step would be to construct simplified SFA models by connecting the beam elements with simple boundary conditions.

References

[1] Efstathios Vlassopoulos. *Development of an Optimization Code for the Logistics of Spent Fuel Assembly Loading into Final Disposal Canisters*. PhD thesis, ETH Zurich - Swiss Federal Institute of Technology, mar 2015. URL https://www.research-collection.ethz.ch/handle/20.500.11850/248319.

[2] Dan Gabriel Cacuci. *Handbook of Nuclear Engineering*. Springer US, 1 edition, 2010. ISBN 978-0-387-98150-5. URL https://www.springer.com/gp/book/9780387981307.

[3] T. R. Allen, R. J.M. Konings, and A. T. Motta. Corrosion of Zirconium Alloys. In *Comprehensive Nuclear Materials*, volume 5, pages 49–68. Elsevier Ltd, jan 2012. ISBN 9780080560335. doi: 10.1016/B978-0-08-056033-5.00063-X.

[4] Ki Nam Jang and Kyu Tae Kim. The effect of neutron irradiation on hydride reorientation and mechanical property degradation of zirconium alloy cladding. *Nuclear Engineering and Technology*, 49(7):1472–1482, oct 2017. ISSN 2234358X. doi: 10.1016/j.net.2017.05.006.

[5] A. Casagranda, D. S. Stafford, G. Pastore, R. L. Williamson, B. W. Spencer, and J. D. Hales. UFD Proof-of-Concept Demonstration, INL/EXT-17-42487. Technical report, Idaho National Laboratory, Idaho Falls, ID (United States), jun 2017. URL http://www.osti.gov/servlets/purl/1408525/.

[6] Peter Kaufholz, Maik Stuke, Felix Boldt, and Marc Péridis. Influence of kinetic effects on terminal solid solubility of hydrogen in zirconium alloys. *Journal of Nuclear Materials*, 510:277–281, nov 2018. ISSN 00223115. doi: 10.1016/j.jnucmat.2018.08.011.

[7] Ju Seong Kim, Jong Dae Hong, Yong Sik Yang, and Dong Hak Kook. Rod internal pressure of spent nuclear fuel and its effects on cladding degradation during dry storage. *Journal of Nuclear Materials*, 492:253–259, aug 2017. ISSN 00223115. doi: 10.1016/j.jnucmat.2017.05.047.

[8] A Zéachandirin, M Dallongeville, P Purcell, and A Cory. Description of Fuel Integrity Project methodology principles. *Packaging, Transport, Storage & Security of Radioactive Material*, 22(4):184–191, 2011. ISSN 1746-5095. doi: 10.1179/1746510912y.0000000001.

[9] Thomas L. Sanders, Kevin D. Seager, Yusef R. Rashid, Peter R. Barrett, Anthony P. Malinauskas, Robert E. Einziger, Hans Jordan, Thomas A. Duffey, Stephen H. Sutherland,

and Philip C. Reardon. SAND90-2406, "A Method for Determining the Spent-Fuel Contribution to Transport Cask Containment Requirements.". (November):53–67, 1992. URL https://www.nrc.gov/docs/ML0427/ML042710347.pdf.

[10] C Guerin, T Laporte, C Cappelaere, C Vaille, P Mongabure, A Miquet, and P Bouffioux. CAST3M modelling of a spent fuel assembly bending during a handling accident . Rod failure risk evaluation from the experimental results of spent fuel rod bending test. *Mechanics & Industry*, 305:301–305, 2013. ISSN 22577750. doi: 10.1051/meca/2014031.

[11] V. Ballheimer, F. Wille, and B. Droste. Mechanical safety analysis for high burn-up spent fuel assemblies under accident transport conditions. *Packaging, Transport, Storage & Security of Radioactive Material*, 21(4):212–217, 2010. ISSN 1746-5095. doi: 10.1179/174650910x12913756439836.

[12] International Organization for Standardization. Metallic materials - Bend test, ISO 4738:2016, 2016. URL https://www.iso.org/standard/67980.html.

[13] Scott V. Franklin, F. Mertens, and M. Marder. Portevin–Le Chatelier effect. *Physical Review E*, 62(6):8195–8206, dec 2000. doi: 10.1103/PhysRevE.62.8195. URL https://link.aps.org/doi/10.1103/PhysRevE.62.8195.

[14] A. Wijler and J. Schade van Westrum. Strain rate experiments and the Portevin – Le Chatelier effrct in Au (14 at%Cu). *Scripta Metallurgica*, 5:531–536, 1971.

[15] D Papaioannou, R Nasyrow, and V V Rondinella. Fuel release experiments on irradiated fuel rodlets under transient impact conditions, Report No: JRC-ITU-TPW-2009/01. Tpw, European Commission - Joint Research Centre - Institute for Transuranium Elements, Karlsruhe, 2009.

[16] D. Papaioannou, R. Nasyrow, V.V. Rondinella, W. Goll, H.P. Winkler, R. Liedtke, and D. Hoffmann. Fuel release experiments on irradiated fuel rodlets under transient impact conditions. *Proc. KTG 2009, May 12-14, 2009, Dresden, Germany, INIS Vol.42, INIS Issue.16*, 2009. doi: INISVolume:42,INISIssue:16. URL https://inis.iaea.org/search/search.aspx?orig{_}q=RN:42029473.

[17] V.V. Rondinella, T. Wiss, D. Papaioannou, and R. Nasyrow. Studies on nuclear fuel evolution during storage and testing of used fuel response to impact loadings. *11th International Probabilistic Safety Assessment and Management Conference and the Annual European Safety and Reliability Conference 2012, PSAM11 ESREL 2012*, 4, 2012.

[18] Camera Calibration and 3D Reconstruction — OpenCV 2.4.13.4 documentation. URL https://docs.opencv.org/2.4/modules/calib3d/doc/camera{_}calibration{_}and{_}3d{_}reconstruction.html.

[19] Marcus F. Aguilar, Walter M. McDonald, and Randel L. Dymond. Benchmarking laboratory observation uncertainty for in-pipe storm sewer discharge measurements. *Journal of Hydrology*, 534:73–86, mar 2016. ISSN 00221694. doi: 10.1016/j.jhydrol.2015.12.052.

[20] Hugh W. Coleman and W. Glenn Steele. Engineering application of experimental uncertainty analysis. *AIAA Journal*, 33(10):1888–1896, 1995. ISSN 00011452. doi: 10.2514/3.12742.

[21] Die Bundesversammlung der Schweizerischen Eidgenossenschaft. Nuclear Energy Act of 21 March 2003 (NEA), . URL https://www.admin.ch/opc/en/classified-compilation/20010233/index.html.

[22] Die Bundesversammlung der Schweizerischen Eidgenossenschaft. Nuclear Energy Ordinance of 10 December 2004 (NEO), . URL https://www.admin.ch/opc/en/classified-compilation/20042217/index.html.

[23] Swiss Federal Department of Energy (SFOE). Sectoral plan for deep geological repositories: Conceptual part, 2008.

[24] E. Vlassopoulos, R. Nasyrow, D. Papaioannou, R. Gretter, L. Fongaro, J. Somers, V. V. Rondinella, S. Caruso, P. Grünberg, J. Helfenstein, P. Schwizer, and A. Pautz. Response of irradiated nuclear fuel rods to quasi-static and dynamic loads. *Kerntechnik*, 83(6):507–512, dec 2018. ISSN 0932-3902. doi: 10.3139/124.110948. URL https://www.hanser-elibrary.com/doi/10.3139/124.110948.

[25] E. Vlassopoulos, B. Volmert, and A. Pautz. Logistics optimization code for spent fuel assembly loading into final disposal canisters. *Nuclear Engineering and Design*, 325: 246–255, 2017. doi: 10.1016/j.nucengdes.2017.04.036.

[26] Swiss Federal Nuclear Safety Inspectorate - ENSI. Joint Convention on the Safety of Spent Fuel Management and on the Safety of Radioactive Waste Management. Technical report, ENSI, oct 2017.

[27] Swissnuclear. Kostenstudie 2016 (KS16) - Mantelbericht. Technical report, Tech. rep. Fachgruppe Kernenergie der swisselectric, Olten, 2016. URL https://www.swissnuclear.ch/de/downloads/217.html.

[28] Efstathios Vlassopoulos, Ben Volmert, and Andreas Pautz. Logistics optimization code for spent fuel assembly loading into final disposal canisters. *Nuclear Engineering and Design*, 325:246–255, dec 2017. ISSN 00295493. doi: 10.1016/j.nucengdes.2017.04.036. URL http://linkinghub.elsevier.com/retrieve/pii/S0029549317302200.

[29] IAEA Nuclear Energy Series: Status and Trends in Spent Fuel and Radioactive Waste Management. Technical report, Vienna, 2018.

[30] Efstathios Vlassopoulos, Ramil Nasyrow, Dimitrios Papaioannou, Vincenzo V.V. Rondinella, Stefano Caruso, and Andreas Pautz. Destructive Tests for Determining Mechanical Integrity of Spent Nuclear Fuel Rods. In *ANS IHLRWM 2017 - 16th International High-Level Radioactive Waste Management Conference: Creating a Safe and Secure Energy Future for Generations to Come - Driving Toward Long-Term Storage and Disposal*, pages 726–733, Charlote, NC, apr 2017. American Nuclear Society. ISBN 9780894487422.

[31] UFDC. Review of Used Nuclear Fuel Storage and Transportation Technical Gap Analyses. Technical Report FCRD-USED-2012-000215, PNNL-21596, Pacific Northwest National Laboratory, Prepared for the U.S. Department of Energy Used Fuel Disposition Campaign, 2012. URL https://www.energy.gov/sites/prod/files/GapComparisonRev0.pdf.

[32] Douglas B. Rigby. Review Board Evaluation of the Technical Basis for Extended Dry Storage and Transportation of Used Nuclear Fuel. *United States Nuclear Waste Technical Review Board*, (December):1–10, 2010.

[33] Studsvik. SCIP III – Technical Description, STUDSVIK/N-13/172. Technical report, 2013.

[34] M. C. Billone, T. A. Burtseva, Z. Han, Y. Y. Liu, and (NE). Used Fuel Disposition Campaign - Embrittlement and DBTT of High-Burnup PWR Fuel Cladding Alloys. Technical report, Argonne National Laboratory (ANL), Argonne, IL (United States), oct 2013. URL http://www.osti.gov/servlets/purl/1096165/.

[35] M.C. Billone, T.A. Burtseva, and R.E. Einziger. Ductile-to-brittle transition temperature for high-burnup cladding alloys exposed to simulated drying-storage conditions. *Journal of Nuclear Materials*, 433(1-3):431–448, feb 2013. ISSN 00223115. doi: 10.1016/j.jnucmat.2012.10.002. URL https://linkinghub.elsevier.com/retrieve/pii/S0022311512005181.

[36] M.C. Billone. Spent Fuel and Waste Disposition: Ductility of High-Burnup Fuel ZIRLO™ following Drying and Storage, M2SF-19AN010201011, ANL-19/14. Technical report, Argonne National Laboratory, jun 2019. URL https://publications.anl.gov/anlpubs/2019/04/151845.pdf.

[37] Rose Montgomery, Robert N Morris, Ralph Ilgner, Benjamin Roach, Jy-An Wang, Zachary Burns, James T Dixon, and Stephanie M Curlin. Spent Fuel and Waste Disposition: Sister Rod Destructive Examinations (FY19), M2SF-19OR010201026. Technical report, Oak Ridge National Laboratory, sep 2019. URL https://info.ornl.gov/sites/publications/Files/Pub129852.pdf.

[38] R. S. Daum, S. Majumdar, D. W. Bates, A. T. Motta, D. A. Koss, and M. C. Billone. On the embrittlement of Zircaloy-4 under RIA-relevant conditions. In Zirconium in the Nuclear Industry : Thirteenth International Symposium, 2002. ISSN 00660558.

[39] Stéphane Valance and Johannes Bertsch. Hydrides reorientation investigation of high burn-up PWR fuel cladding. *Journal of Nuclear Materials*, 464:371–381, jun 2015. ISSN 00223115. doi: 10.1016/j.jnucmat.2015.05.003.

[40] P. H. Davies and C. P. Stearns. Fracture toughness testing of Zircaloy-2 pressure tube material with radial hydrides using direct-current potential drop. In *ASTM Special Technical Publication*, pages 379–400. ASTM, 1986. ISBN 0803104723. doi: 10.1520/stp17408s. URL http://www.astm.org/DIGITAL{_}LIBRARY/STP/PAGES/STP17408S.htm.

[41] Jacob Bair, Mohsen Asle Zaeem, and Michael Tonks. A review on hydride precipitation in zirconium alloys, jul 2015. ISSN 00223115.

[42] Ju Seong Kim, Young Jun Kim, Dong Hak Kook, and Yong Soo Kim. A study on hydride reorientation of Zircaloy-4 cladding tube under stress. *Journal of Nuclear Materials*, 456:246–252, jan 2015. ISSN 00223115. doi: 10.1016/j.jnucmat.2014.09.032.

[43] United States Nuclear Regulatory Commission, Spent Fuel Project Office Interim Staff Guidance-11, Revision 3 Issue: Cladding Considerations for the Transportation and Storage of Spent Fuel. Technical report, US-NRC.

[44] US NRC. Identification and Prioritization of the Technical Information Needs Affecting Potential Regulation of Extended Storage and Transportation of Spent Nuclear Fuel. Technical Report May, U.S. Nuclear Regulatory Commission, 2014. URL https://www.nrc.gov/docs/ML1404/ML14043A423.pdf.

[45] P.C. Purcell and M. Dallongeville. Testing of Lwr Fuel Rods to Support Criticality Safety Analysis of Transport Accident Conditions. *Packaging, Transport, Storage & Security of Radioactive Material*, 15(3-4):265–272, 2004. ISSN 1746-5095. doi: 10.1179/174650904775295784.

[46] Maurice Dallongeville, Peter Purcell, Aravinda Zeachandirin, and Anthony Cory. Finite elements analysis of intergrid bending tests on used fuel rods samples. In *16th International Symposium on Packaging and Transportation of Radioactive Materials, PATRAM 2010*, London, 2010. Institute of Nuclear Materials Management (INMM). URL https://www.inmm.org/INMM/media/Archives/PATRAMProceedings/2010/211{_}Paper{_}FiniteElementsAnalysisOfIntergridBendingTests.pdf.

[47] M. Dallongeville, J. Werle, and G. McCreesh. Fuel Integrity Project: Analysis of Results of Tests on Light Water Reactor Fuel Rods. *Packaging, Transport, Storage & Security of Radioactive Material*, 16(2):125–134, jul 2005. ISSN 1746-5095. doi: 10.1179/174650905775295422. URL http://www.tandfonline.com/doi/full/10.1179/174650905775295422.

[48] Maurice Dallongeville, Aravinda ZEACHANDIRIN, and MILET Laurent. Simplified Approach to Study Fuel Rod Rupture Risks By Bending or Euler Buckling, Proceedings of the 9th International Conference on the Radioactive Materials Transport and Storage RAMTRANSPORT 2012 22-24 May, 2012 Kensington, London, United Kingdom, 2012.

[49] J Y R Rashid and a J Machiels. A methodology for the evaluation of fuel rod failures under transportation accidents. *Conference proceedings of the 14th international symposium on the packaging and transportation of radioactive materials, Patram 2004*, (Patram), 2004.

[50] J. Rashid, Dunham R., and M. Rashid. Development of a Metal / Hydride Mixture Model for Zircaloy Cladding With Mixed Hydride Structure. Technical report, EPRI, Palo Alto, CA, 1009694, 2004.

[51] J. Rashid, Dunham R., and M. Rashid. Failure Criteria for Zircaloy Cladding Using a Damage-based Metal / Hydride Mixture Model. Technical report, EPRI, Palo Alto,CA, 1009693, 2004.

[52] V V Rondinella, T Wiss, D Papaioannou, and R Nasyrow. Studies on nuclear fuel evolution during storage and testing of used fuel response to impact loadings. *11th International Probabilistic Safety Assessment and Management Conference and the Annual European Safety and Reliability Conference 2012, PSAM11 ESREL 2012*, 4, 2012.

[53] H. Adkins, K. J Geelhood, B. Koeppel, J. Coleman, J. Bignell, G. Flores, J-A. Wang, S. Sanborn, R. Spears, and N. Klymyshyn. Used Nuclear Fuel Loading and Structural Performance Under Normal Conditions of Transport – Demonstration of Approach and Results on Used Fuel Performance Characterization. Technical report, U.S. Department of Energy, 2013. URL https://www.energy.gov/sites/prod/files/2013/12/f5/UsedNucFuelLoadPerformanceTransDemoAppro.pdf.

[54] Bruce Bevard and Rob Howard. *FY14 Status Report : CIRFT Testing Results on High Burnup UNF, ORNL/TM-2014/310*. Number September. 2014. ISBN 1800553684.

[55] Jy-an Wang, Hong Wang, Hao Jiang, and Bruce Bevard. High burn-up spent nuclear fuel transport reliability investigation. *Nuclear Engineering and Design*, 330(October 2017):497–515, 2018. ISSN 0029-5493. doi: 10.1016/j.nucengdes.2018.02.007. URL https://doi.org/10.1016/j.nucengdes.2018.02.007.

[56] Hao Jiang, Jy An John Wang, and Hong Wang. The impact of interface bonding efficiency on high-burnup spent nuclear fuel dynamic performance. *Nuclear Engineering and Design*, 309:40–52, 2016. ISSN 00295493. doi: 10.1016/j.nucengdes.2016.09.013. URL http://dx.doi.org/10.1016/j.nucengdes.2016.09.013.

[57] Hao Jiang and Jy An John Wang. Spent nuclear fuel system dynamic stability under normal conditions of transportation. *Nuclear Engineering and Design*, 310:1–14, 2016. ISSN 00295493. doi: 10.1016/j.nucengdes.2016.09.033. URL http://dx.doi.org/10.1016/j.nucengdes.2016.09.033.

[58] Hao Jiang, Jun Qu, Roger Y. Lu, and Jy An John Wang. Grid-to-rod flow-induced impact study for PWR fuel in reactor. *Progress in Nuclear Energy*, 91:355–361, 2016. ISSN 01491970. doi: 10.1016/j.pnucene.2016.06.003. URL http://dx.doi.org/10.1016/j.pnucene.2016.06.003.

[59] J. L. Coleman and R. E. Spears. Detailed PWR Fuel Rod and Grid Finite Element Analysis to Provide Equivalent Rod Stiffness and Damping and Equivalent Grid Shell Thickness to PWR Used Nuclear Fuel (UNF) Assembly – 14525, Idaho National Laboratory. In *WM2014 Conference, March 2-6, 2014, Phoenix, Arizona, USA Detailed*, pages 1–12, Phoenix,, 2014.

[60] Scott Sanborn, Brian Koeppel, Nicholas Klymyshyn, Harold Adkins, and Kenneth Geelhood. Assembly Level Modeling and Transportation Damage Prediction of Used Nuclear Fuel (UNF) Cladding – 14569. In *Waste Management Symposia 2014*, Phoenix, Arizona, USA, 2014. URL http://www.wmsym.org/archives/2014/papers/14569.pdf.

[61] Eugen Schrödl, Wenzel Brücher, Wolfgang Koch, and Viktor Ballheimer. Experimentelle Untersuchungen zum Verhalten von Brennstäben mit hohem Abbrand bei mechanischen Unfallbelastungen beim Transport, GRS - A - 3490, 2010.

[62] IAEA. Spent Fuel Performance Final Report of a Coordinated Assessment and Research: Research Project (SPAR-III). (IAEA-TECDOC-1771):2009–2014, 2015.

[63] T. HIROSE, M. OZAWA, H. MIURA, T. BABA, and K. KAMIMURA. Research on integrity of high burnup spent fuel under long term dry storage and transport. In *OECD/NEA International Workshop on Safety of Long Term Interim Storage Facilities*, Munich, Germany, 2013.

[64] T. HIROSE, M. OZAWA, H. MIURA, T. BABA, and K. KAMIMURA. Dynamic load impact tests on high burnup spent fuel rods of BWR and PWR. In *NuMat 2012: the Nuclear Materials conference*, Osaka, Japan, 2012.

[65] Hirofumi MINAMOTO and Masafumi NAKATSUKA. Numerical analysis on the dynamic response of nuclear fuel rods under side drop loading. *Transactions of the JSME (in Japanese)*, 81(824):14–00676–14–00676, 2015. ISSN 2187-9761. doi: 10.1299/transjsme.14-00676.

[66] Hirofumi Minamoto, Takayoshi Yasuda, Masafumi Nakatsuka, and Shozo Kawamura. Buckling behavior of fuel rods under impact loads (Numerical study on the effect of material properties). *Nihon Kikai Gakkai Ronbunshu, A Hen/Transactions of the Japan Society of Mechanical Engineers, Part A*, 77(773):16–26, 2011. ISSN 03875008. doi: 10.1299/kikaia.77.1839.

[67] National Cooperative for the Disposal of Radioactive Waste. The Nagra Research, Development and Demonstration (RD&D) Plan for the Disposal of Radioactive Waste in Switzerland, Technical Report 16-02. Technical report, 2016. URL www.nagra.ch.

[68] Eidgenössisches Nuklearsicherheitsinspektorat. Eidgenössisches Nuklearsicherheitsinspektorat ENSI Stellungnahme zum Entsorgungsprogramm 2016 der Entsorgungspflichtigen. Technical report. URL www.ensi.ch.

[69] ASTM D7264/D7264M-15. Standard Test Method for Flexural Properties of Polymer Matrix Composite Materials. *ASTM International*, 2015. doi: 10.1520/D7264_D7264M-15.

[70] Christos C Chamis. NASA TN D-7572 Analysis of three-point-bend test for materials with unequal tension and compression properties. Technical report, National Aeronautics and Space Administration (NASA), Washington D.C., 1974. URL https://ntrs.nasa.gov/search.jsp?R=19740010415.

[71] M. R. Mitchell, R. E. Link, George D. Quinn, Brian T. Sparenberg, Philip Koshy, Lewis K. Ives, Said Jahanmir, and Dwayne D. Arola. Flexural Strength of Ceramic and Glass Rods. *Journal of Testing and Evaluation*, 37(3):101649, 2009. ISSN 00903973. doi: 10.1520/JTE101649. URL http://www.astm.org/doiLink.cgi?JTE101649.

[72] Roger (Roger P.) Brown. *Handbook of polymer testing : physical methods*. Marcel Dekker, 1999. ISBN 9780824701710. URL https://www.crcpress.com/Handbook-of-Polymer-Testing-Physical-Methods/Brown/p/book/9780824701710.

[73] EC Motion GmbH. STEPPING MOTORS 2-Phase Hybrid Type 1.8° and 0.9° Full Step Angle. Technical report, EC Motion. URL https://www.ec-motion.de/fileadmin/user{_}upload/Katalog/kat{_}26.pdf.

[74] A. Portevin and F. Le Chatelier. Sur un phénomène observé lors de l'essai de traction d'alliages en cours de transformation. *Comptes Rendus de l'Académie des Sciences Paris*, 176:507–510, 1923.

[75] W. Ozgowicz, B. Grzegorczyk, A. Pawelek, A. Piatkowski, and Z. Ranachowski. The Portevin - Le Chatelier effect and acoustic emission of plastic deformation CuZn30 monocrystals. *Archives of Metallurgy and Materials*, 59(1):183–188, 2014. ISSN 17333490. doi: 10.2478/amm-2014-0029.

[76] OriginLab Pro 2019. Origin Help - Algorithms discrete Fourier transform (DFT). URL https://www.originlab.com/doc/Origin-Help/FFT1-Algorithm.

[77] Burster. Technical Product Information Commissioning, Function, Fitting Specification Model 8435. Technical report. URL www.burster.de.

[78] Measurement Specialties Inc. GCD Series - DC Operated Gage Heads. Technical report, 2015. URL www.meas-spec.com.

[79] Technical sheet specification, UNIK 5000 | AKS-Messtechnik. URL https://www.aks-gmbh.de/produkte/neugeraete/baker-hughes-ge/drucksensoren/unik-5000/.

[80] CompactRIO-Systeme - National Instruments. URL https://www.ni.com/de-de/shop/compactrio.html.

[81] What is LabVIEW? - National Instruments. URL https://www.ni.com/en-gb/shop/labview.html.

[82] E J HEARN. CHAPTER 4 - BENDING. In E J B T Mechanics of Materials 1 (Third Edition) HEARN, editor, *Mechanics of Materials 1 (Third Edition)*, chapter Chapter 4, pages 62–91. Butterworth-Heinemann, Oxford, 1997. ISBN 978-0-7506-3265-2. doi: https://doi.org/10.1016/B978-075063265-2/50005-0. URL http://www.sciencedirect.com/science/article/pii/B9780750632652500050.

[83] W.D.Jr. Callister and D.G Rethwisch. *Materials Science and Engineering: An Introduction, 9th Edition | Wiley*. John Wiley & Sons, 9e edition, 2014. ISBN 978-1-118-32457-8. URL https://www.wiley.com/en-us/Materials+Science+and+Engineering{%}3A+An+Introduction{%}2C+10th+Edition-p-9781119405498.

[84] David Roylance. STRESS-STRAIN CURVES. Technical report, Department of Materials Science and Engineering, Massachusetts Institute of Technology, Cambridge, MA, 2001.

[85] V.V. Rondinella, R. Nasyrow, D. Papaioannou, Efstathios Vlassopoulos, F. Cappia, T.A.G. Wiss, and O. Dieste-Blanco. Mechanical Integrity Studies on Spent Nuclear Fuel Rods. In *ANS IHLRWM 2017 - 16th International High-Level Radioactive Waste Management Conference: Creating a Safe and Secure Energy Future for Generations to Come - Driving Toward Long-Term Storage and Disposal*, pages 734–740, Charlotte, NC, apr 2017. American Nuclear Society. ISBN 9780894487422.

[86] Jorge Santolaria, David Guillomía, Carlos Cajal, José A. Albajez, and Juan J. Aguilar. Modelling and calibration technique of laser triangulation sensors for integration in robot arms and articulated arm coordinate measuring machines. *Sensors*, 9(9): 7374–7396, 2009. ISSN 14248220. doi: 10.3390/s90907374.

[87] James L Crowley. Computer Vision: Homogeneous Coordinates and Projective Camera Models. chapter Lectures N, pages 1–17. 2009.

[88] Single Camera Calibration - MATLAB & Simulink. URL https://www.mathworks.com/help/vision/ug/single-camera-calibration.html.

[89] Behrad Koohbor, Addis Kidane, Michael A. Sutton, Xing Zhao, and Silas Mallon. Analysis of dynamic bending test using ultra high speed DIC and the virtual fields method. *International Journal of Impact Engineering*, 000:1–12, 2017. ISSN 0734743X. doi: 10.1016/j.ijimpeng.2016.12.021. URL http://linkinghub.elsevier.com/retrieve/pii/S0734743X16306340.

[90] Inc. Media Cybernetics. Image-Pro Plus Start-Up Guide. Technical report, 1993. URL http://www.mediacy.com.

[91] Hong Wang, Jy An John Wang, Ting Tan, Hao Jiang, Thomas S. Cox, Rob L. Howard, Bruce B. Bevard, and Michelle Flanagan. Development of U-frame bending system for studying the vibration integrity of spent nuclear fuel. *Journal of Nuclear Materials*, 440(1-3):201–213, 2013. ISSN 00223115. doi: 10.1016/j.jnucmat.2013.05.009. URL http://dx.doi.org/10.1016/j.jnucmat.2013.05.009.

[92] Hong Wang and Jy An John Wang. Experimental study on surrogate nuclear fuel rods under reversed cyclic bending. In *ASTM Special Technical Publication*, volume STP 1598, pages 19–36. ASTM International, 2017. ISBN 9780803176393. doi: 10.1520/STP159820160051.

[93] Anton Pshenichnikov, Juri Stuckert, and Mario Walter. Microstructure and mechanical properties of Zircaloy-4 cladding hydrogenated at temperatures typical for loss-of-coolant accident(LOCA) conditions. *Nuclear Engineering and Design*, 283:33–39, 2015. doi: 10.1016/j.nucengdes.2014.06.022.

[94] Anton Pshenichnikov, Juri Stuckert, Mario Walter, and D Litvinov. Hydrides and fracture of pure zirconium and Zircaloy-4 hydrogenated at temperatures typical for loss-of-coolant accident conditions. In *23rd International Conference on Nuclear Engineering ICONE-2015*, page Paper 1724, Chiba, Japan.

[95] Y. R. Rashid, D. J. Sunderland, W. F. Lyon, and K. E. Kubischta. End-of-Life Rod Internal Pressures in Spent Pressurized Water Reactor Fuel. page 58, 2013.

[96] R Nasyrow, D Papaioannou, V V Rondinella, Efstathios Vlassopoulos, Konrad Linnemann, Viktor Ballheimer, Jens Sterthaus, Annette Rolle, Frank Wille, and Stefano Caruso. Bending test device for mechanical integrity studies of spent nuclear fuel rods. In *18th International Symposium on the Packaging and Transportation of Radioactive Materials, PATRAM 2016*, Kobe, sep 2016. Institute of Nuclear Materials Management.

[97] Jong Dae Hong, Euijung Kim, Yong Sik Yang, and Dong Hak Kook. Mechanical Property Degradation of Unirradiated Zircaloy-4 Cladding After Creep Deformation. *Nuclear Technology*, 203(3):282–292, 2018. ISSN 14769360. doi: 10.1080/00295450.2018.1448203. URL https://doi.org/10.1080/00295450.2018.1448203.

[98] K. Yueh, J. Karlsson, J. Stjärnsäter, D. Schrire, G. Ledergerber, C. Munoz-Reja, and L. Hallstadius. Fuel cladding behavior under rapid loading conditions. *Journal of Nuclear Materials*, 469:177–186, 2016. ISSN 00223115. doi: 10.1016/j.jnucmat.2015.11.032.

[99] Marcelo Paredes and Tomasz Wierzbicki. On mechanical response of Zircaloy-4 under a wider range of stress states: From uniaxial tension to uniaxial compression. *International Journal of Solids and Structures*, 206:198–223, dec 2020. ISSN 00207683. doi: 10.1016/j.ijsolstr.2020.09.007.

[100] Walter G. Luscher and Kenneth J. Geelhood. Material Property Correlations: Comparisons between FRAPCON-3.4, FRAPTRAN 1.4, and MATPRO. Technical report, Pacific Northwest National Laboratory (PNNL), Richland, WA (United States), aug 2010. URL http://www.osti.gov/servlets/purl/1030897.

[101] Philippe F. Weck, Eunja Kim, Veena Tikare, and John A. Mitchell. Mechanical properties of zirconium alloys and zirconium hydrides predicted from density functional perturbation theory. *Dalton Transactions*, 44(43):18769–18779, oct 2015. ISSN 14779234. doi: 10.1039/c5dt03403e. URL www.rsc.org/dalton.

[102] Philippe Bossis, Bénédicte Verhaeghe, Sylvie Doriot, Didier Gilbon, Valérie Chabretou, Agnès Dalmais, Jean Paul Mardon, Martine Blat, and Alain Miquet. In PWR comprehensive study of high burn-up corrosion and growth behavior of M5® and recrystallized low-tin zircaloy-4. In *ASTM Special Technical Publication*, volume 1505 STP, pages 430–456. American Society for Testing and Materials, 2009. ISBN 9780803145146. doi: 10.1520/stp48148s.

[103] Peter Ruding. Zr Alloy Corrosion and Hydrogen Pickup. Technical report, ANT International, Mölnlycke, Sweden, 2013.

[104] J. Arborelius, M. Dahlbäck, L. Hallstadius, P. Jourdain, T. Andersson, R. Lisdat, M. Hahn, E. H. Toscano, A. Strasses, G. Sabol, and B. Cox. The effect of duplex cladding outer component tin content on corrosion, hydrogen pick-up, and hydride distribution at very high burnup. *ASTM Special Technical Publication*, (1467):526–546, 2005. ISSN 00660558. doi: 10.1520/stp37523s.

[105] EURAD, European Joint Programme on Radioactive Waste Management, https://www.ejp-eurad.eu/ and https://cordis.europa.eu/project/id/847593.

[106] Jean-Paul Mardon, Daniel Charquet, Jean Senevat, and J-r Charquet. Influence of Composition and Fabrication Process on Out-of-Pile and In-Pile Properties of M5 Alloy "Influence of Composition and Fabrication Process on Out-of-Pile and In-Pile Properties of M5 Alloy," Zirconium in the. Technical report, 2000. URL www.astm.org.

[107] Vincenzo V Rondinella, Dimitrios Papaioannou, and Ramil Nasyrow. Impact test on 67 GWd/tHM LWR spent nuclear fuel rodlet, JRC Technical Report, 2016. URL http://publications.jrc.ec.europa.eu/repository/handle/JRC103277.

[108] W. Gong, P. Trtik, A. W. Colldeweih, L. I. Duarte, M. Grosse, E. Lehmann, and J. Bertsch. Hydrogen diffusion and precipitation in duplex zirconium nuclear fuel cladding quantified by high-resolution neutron imaging. *Journal of Nuclear Materials*, 526:151757, dec 2019. ISSN 00223115. doi: 10.1016/j.jnucmat.2019.151757.

[109] Maurice Dallongeville, Jürgen Werle, and Gerard Mccreesh. Fuel Integrity Project : Analysis of Light Water Reactor Fuel Rods Test Results. In *14th International Symposium on the Packaging and Transportation of Radioactive Materials (PATRAM 2004)*, Berlin, 2004. INMM Institute of Nuclear Materials Management.

[110] Michele Bellotti. *Towards beam modelling for static structural analysis of spent nuclear fuel rods*. Msc thesis, École polytechnique fédérale de Lausanne - EPFL, 2020.

[111] E Vlassopoulos, A Pautz, S Caruso, V Raffuzzi, P Grünberg, J Helfenstein, and P Schwizer. Mechanical Integrity of Spent Nuclear Fuel: From Experimental to Numerical Studies. In *TOPFUEL 2018*, Prague, 2018. ENS. URL https://www.euronuclear.org/events/topfuel/topfuel2018/fullpapers/TopFuel2018-A0129-fullpaper.pdf.

[112] Behrad Koohbor, Addis Kidane, Michael A Sutton, Xing Zhao, and Silas Mallon. Analysis of dynamic bending test using ultra high speed DIC and the virtual fields method. *International Journal of Impact Engineering*, 000:1–12, 2017. ISSN 0734743X. doi: 10.1016/j.ijimpeng.2016.12.021. URL http://linkinghub.elsevier.com/retrieve/pii/S0734743X16306340.

[113] Timothy J. Beberniss and David A. Ehrhardt. High-speed 3D digital image correlation vibration measurement: Recent advancements and noted limitations. *Mechanical Systems and Signal Processing*, 86:35–48, 2017. ISSN 10961216. doi: 10.1016/j.ymssp.2016.04.014. URL http://dx.doi.org/10.1016/j.ymssp.2016.04.014.

[114] Sanghoon Lee and Seyeon Kim. Simplified beam model of high burnup spent fuel rod under lateral load considering pellet-clad interfacial bonding influence. *Nuclear Engineering and Technology*, 51(5):1333–1344, aug 2019. ISSN 2234358X. doi: 10.1016/j.net.2019.03.010. URL https://doi.org/10.1016/j.net.2019.03.010.

[115] Konrad Linnemann, Viktor Ballheimer, Jens Sterthaus, Annette Rolle, Frank Wille, Efstathios Vlassopoulos, and Dimitrios Papaioannou. Numerical simulations of spent fuel segments under transport loads (Code 148361). In *International High-Level Radioactive Waste Management Conference, IHLWM 2019*, pages 430–436, Knoxville, TN, 2019. American Nuclear Society.

[116] Joint Committee for Guides in Metrology. Evaluation of measurement data-Guide to the expression of uncertainty in measurement. Technical report, JCGM 100:2008, 2008. URL www.bipm.org.

[117] G F Pezzuto. Manual of Codes of Practice for the Determination of Uncertainties in Mechanical Tests on Metallic Materials The Determination of Uncertainties in Bend Tests on Metallic Materials Issue 1 (UNCERT COP 09: 2000). Technical report, Standards Measurement & Testing Project No. SMT4-CT97-2165, 2000.

[118] I. Štubna, P. Šín, A. Trník, and L. Vozár. Measuring the flexural strength of ceramics at elevated temperatures-an uncertainty analysis, feb 2014. ISSN 13358871. URL https://content.sciendo.com/view/journals/msr/14/1/article-p35.xml.

[119] A. Gunay, S. Fank, T. Gulmez, and N. M. Durakbasa. Calculation of measurement uncertainty for plastic (ABS) material in flexural testing. *International Journal of Metrology and Quality Engineering*, 4(1):29–33, jun 2013. ISSN 21076839. doi: 10.1051/ijmqe/2012034. URL https://www.metrology-journal.org/articles/ijmqe/abs/2013/01/ijmqe120034/ijmqe120034.html.

[120] HBM. Data sheet: Piezoelectric force measurement chain (CMC/70kN), 2018. URL http://www.hottinger.sk/Prospekty/Sila/cmc/p{_}cmc{_}e.pdf.

[121] Zhengyou Zhang. Flexible Camera Calibration By Viewing a Plane From Unknown Orientations. In *Proceedings of the Seventh IEEE International Conference on Computer Vision*, Kerkyra, sep 1999. IEEE. ISBN 0-7695-0164-8. doi: 10.1109/ICCV.1999.791289. URL http://research.microsoft.com/~zhang.

Appendix A

Flexural stress-strain results of surrogate samples

Figs. A.1 and A.2 provide the fexural stress-strain curves as derived for beam elements with circular and hollow-circular cross-sections, respectively. The analysis was performed on the response of the surrogate samples in three-point bending tests, as described in section 3.3.3.

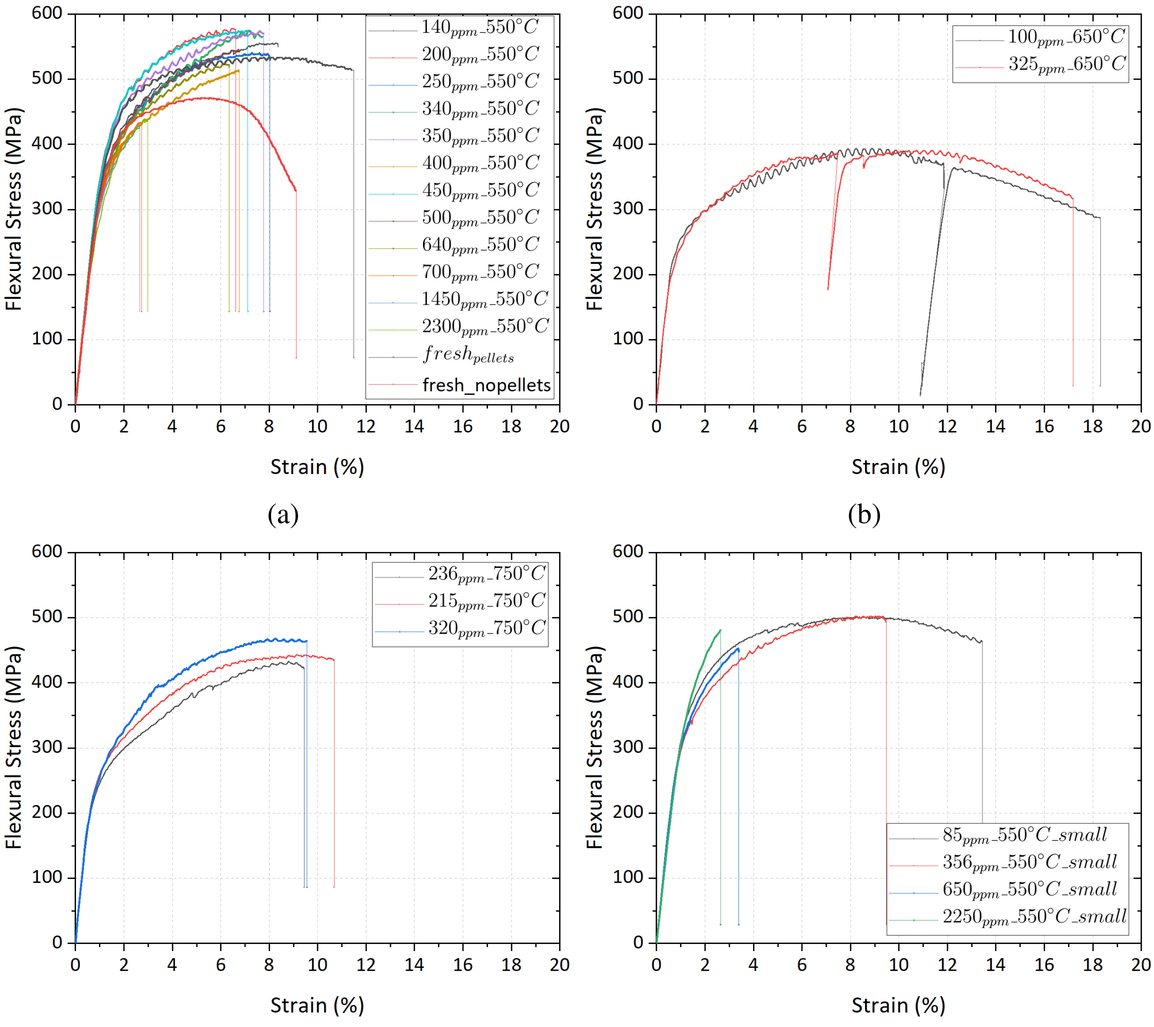

(a) (b)

(c) (d)

Fig. A.1 Flexural stress-strain curves for beam elements with circular cross-section derived from three-point bending tests on surrogate samples including Zry-4 cladding tubes hydrogenated at a) 550°C , b) 650°C, c) 750°C and d) with the use of smaller alumina pellets.

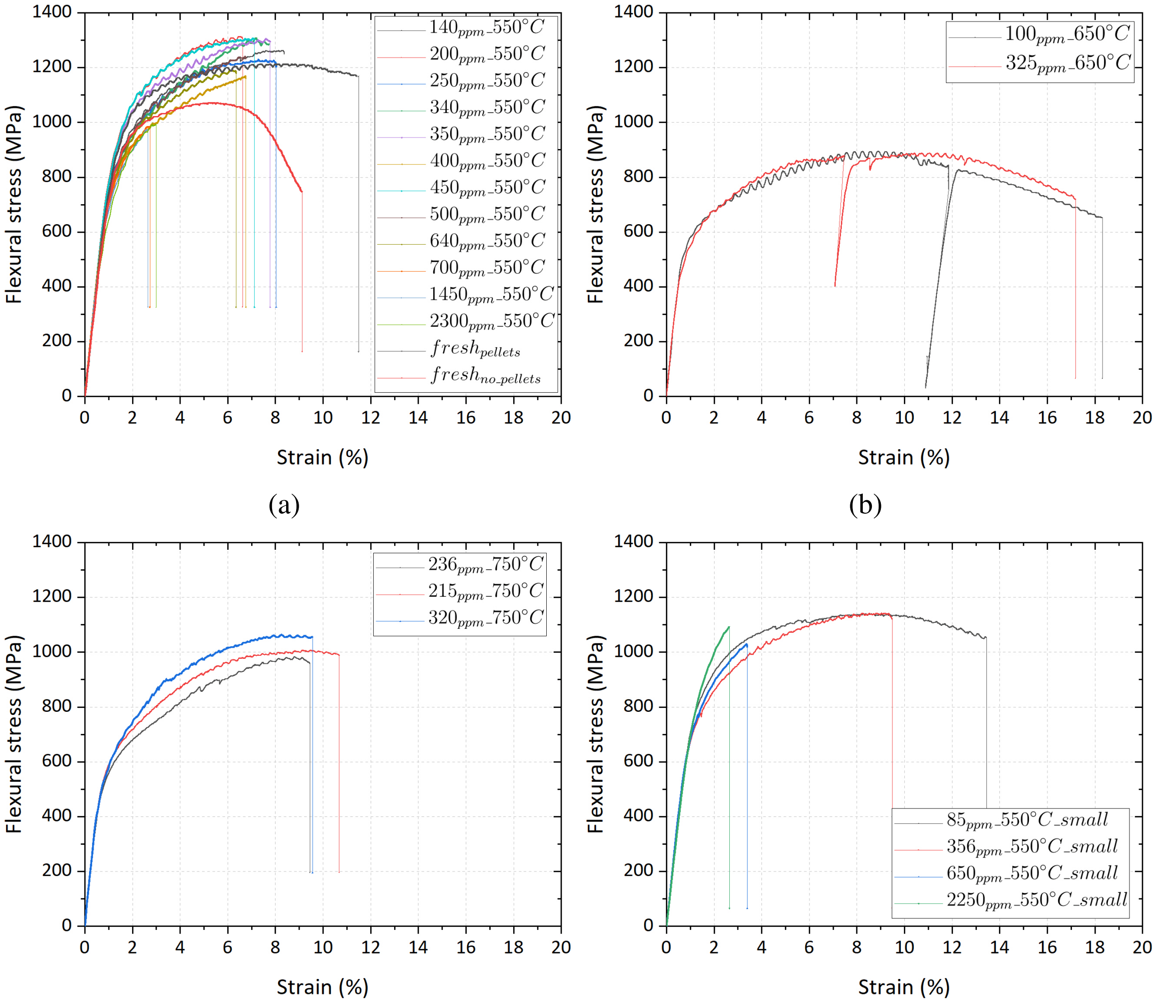

(a) (b)

(c) (d)

Fig. A.2 Flexural stress-strain curves for beam elements with hollow-circular cross-section derived from three-point bending tests on surrogate samples including Zry-4 cladding tubes hydrogenated at a) 550°C , b) 650°C, c) 750°C and d) with the use of smaller alumina pellets.

Appendix B

Uncertainty analysis of flexural properties in three-point bending test

The experimental results in the three-point bending tests consist of the load-displacement curves and with the use of the simple beam theory one could derive the flexural stress, strain and modulus of elasticity for a given beam cross-section (refer to section 2.2.5). In this chapter, the methodology used for the uncertainty analysis of these quantities is presented, using the flexural strength, σ_f, as an example for the uncertainty derivation.

The result of the uncertainty analysis is given as:

$$\sigma_f = \overline{\sigma_f} \pm 2u_c(\sigma_f) \tag{B.1}$$

where the expanded standard uncertainty, u_c is multiplied by a factor of 2 to cover the 95% probability of the true value to lie with this range.

The uncertainty in measurement results is classified in two categories. Sources of uncertainty that can be evaluated by statistical means (i.e. number of observations) are classified as type A; whereas sources of uncertainties that are determined by any other means (certificates, manufacturer information, etc.) are classified as type B [116].

Once each source of uncertainty is estimated, the combined standard uncertainty can be estimated as the square root of the sum of all uncertainties, assuming all sources are fully independent, as:

$$u_c(\sigma_f) = \sqrt{u_A^2(\sigma_f) + u_B^2(\sigma_f)} \tag{B.2}$$

The standard uncertainty of a measured quantity χ_i of type A is given as:

$$u_A(x_i) = \frac{s}{\sqrt{n}} = \sqrt{\frac{\sum_{i=1}^{n}(x_i - \bar{x})^2}{n(n-1)}} \tag{B.3}$$

where s is the standard uncertainty and n is the number of independent measurements.

When no correlation between measured quantities exist, then the standard uncertainty of type A is given as:

$$u_A(\sigma_f) = \sqrt{\sum_{i=1}^{p} A_i^2 u_A^2(x_i)} \tag{B.4}$$

where p is the number of direct measured quantities; i.e. the applied load F, the active length of the sample L, the axis displacement δ and the specimen inner and outer diameter d_i and d_o.

The uncertainties of type B, $u_B(x_i)$, are derived by other means, such as manufacturer's information, expert's estimation, etc. These sources of uncertainty do not submit to statistical treatment. When no crenellation between the measured quantities take place then the standard uncertainty of type Type B is given as:

$$u_B(\sigma_f) = \sqrt{\sum_{i=1}^{m} A_i^2 u_B^2(x_i)} \tag{B.5}$$

where m, is the number of all sources of uncertainties that is divided in two groups. The first group refers to uncertainties arising from quantities that are measured digitally and have a rectangular probability density function, $u_B(x_i) = MAE/\sqrt{3}$, where MAE is the maximum admissible error. The second group refers to uncertainties arising from quantities that are arise from analogue measurements and have a triangular probability density function, $u_B(x_i) = r/\sqrt{12}$, where r is the measurement resolution [117–119].

Values, A_i, in Eqs. B.4 and B.5 are the sensitivity coefficients calculated as partial derivatives of the flexural stress (Eq.2.10) with respect to the measured quantities.

The combined uncertainty of flexural stress is expressed as:

$$\left[u_c(\sigma_f)\right]^2 = \sum \left(\frac{\partial \sigma_f}{\partial x_i}\right)^2 u^2(x_i) \tag{B.6}$$

The flexural stress of a beam with cylindrical cross-section is derived according to Eqs.2.8b, 2.9 and 2.10 as:

$$\sigma_f = \frac{FL}{\pi r_o^3} \tag{B.7}$$

Therefore, the combined uncertainty of the maximum flexural stress can be written as:

$$\begin{aligned}\left[u_c(\sigma_f)\right]^2 &= \left(\frac{\partial\sigma_f}{\partial F}\right)^2 u_F^2(F) + \left(\frac{\partial\sigma_f}{\partial L}\right)^2 u_L^2(L) + \left(\frac{\partial\sigma_f}{\partial r_o}\right)^2 u_{r_o}^2(r_o)\\ &= \left(\frac{1}{\pi}\frac{L}{r_o^3}\right)^2 u_F^2(F) + \left(\frac{1}{\pi}\frac{F}{r_o^3}\right)^2 u_L^2(L) + \left(\frac{-3}{\pi}FLr_o^{-4}\right)^2 u_{r_o}^2(r_o)\end{aligned} \tag{B.8}$$

Table B.1 provides the list of uncertainties in the measuring quantities, as well as the total combined uncertainty for each one of them, calculated with the use of Eq. B.2.

Table B.1 List of sources of uncertainties in all measuring quantities

Measurement quantity	Sources of uncertainty	Type	Distribution	Value	Standard deviation	Standard uncertainty	Units
Load	Repeatability	B	Rectangular	0.15% (FS=5000)		4.33013	N
	Load-cell sensitivity	B	Rectangular	0.05% (FS=5000)		1.44338	N
	Measurement resolution	B	Rectangular	1.403	0.81002	0.65614	N
	Statistical error (data spread)	A	Normal		0.07003	0.00490	N
	total					4.61127	N
Displacement	Repeatability	B	Rectangular	0.0006		0.00035	mm
	Linearity	B		0.05% (FS=50)		0.14434	mm
	Residuals of linear fit	A	Uniform		0.02375	0.00056	mm
	total					0.14434	mm
Outer diameter	Manufacturer info	B	Rectangular	0.05		0.02887	mm
Inner diameter	Manufacturer info	B	Rectangular	0.04		0.02309	mm
Effective length	Construction	B	Rectangular	1		0.57735	mm

Some uncertainties are given directly from the manufacturer specifications and others are derived from measurements. The statistical error on load measurements are calculated by analysing the acquired data when no force is applied. Fig. B.1 shows the load measurements registered when no contact between the sample and the former is established. From the analysis, it is apparent that the data spread follows a normal distribution, as expected for digital measurements. The mean value gives the measurement off-set and from the standard deviation the load measuring uncertainty is estimated (or the measurement precision).

The load measurement resolution is also derived from the analysis of the recorded data and represents the smallest step between two measurements. In other words, the load-cell sensor cannot measure anything smaller than this value.

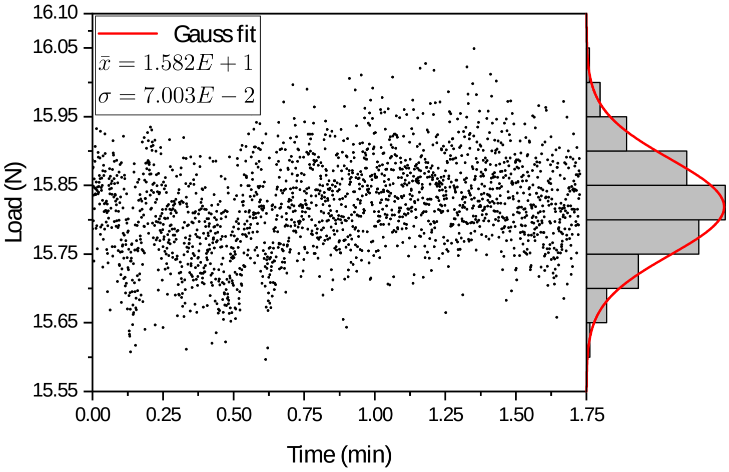

Fig. B.1 Standard deviation of load measurements.

Fig. B.2 gives the measurement precision of the displacement sensor. This is derived by analysing the residuals after a linear fit on the acquired data. In Fig. B.2b the residuals of the linear fit are plotted revealing an important insight on the performance of the three-point bending test setup, as discussed in section 2.2.1. The data oscillate around the mean value with a period of 1 min, which coincides to one full turn of the loading axis (for this specific test). This is another proof that the observed oscillations on the applied load during plastic deformation could originate from a (possibly) uneven axis displacement rate.

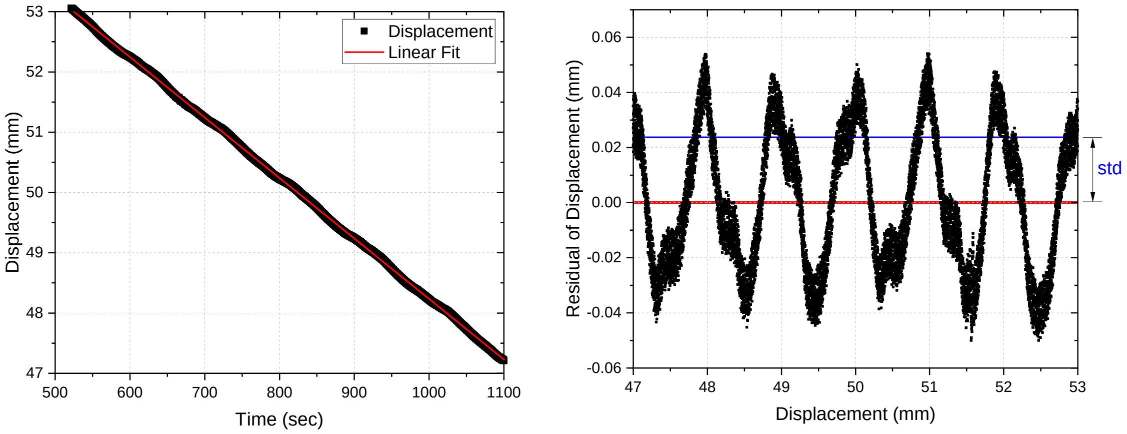

(a) (b)

Fig. B.2 Standard deviation of displacement measurements.

Appendix C

Effect of sample pressurization on its dynamic response

An IA methodology has been successfully developed (refer to section 2.3.4) to quantitatively determine the mechanical response of SNF rodlets under impact loads. This method aims to estimate of the Strain Energy Density (SED) required to fracture the rodlet. Although the validity of this approach has been shown (refer to section 4.4.3), it is not possible to directly derive the associated errors. The current IA method provides no indication regarding the introduced errors with respect to the applied image recording frequency, to the spatial calibration assumption and to the inertia effects introduced by the pressure end-plugs used to pressurize sample and monitor the RIP. To confirm that the IA method employed for the analysis of the impact tests is suitable for its intended use, the process has to be validated. In the following paragraphs, the procedure followed to estimate the uncertainty of this method or (better) to determine with higher confidence the SED is described.

C.1 Impact Mock-up Tower

Consequently, a mock-up device has been constructed replicating the geometrical dimensions of the impact tower installed in the hot-cell and placed in a cold laboratory, as shown in Fig. C.1. The only difference between the two setups lies on the on the load application and specifically at the impactor's diameter. To facilitate the examination of the strain rate dependence on the sample's mechanical response, the same impactor diameter has been used as in the case of the 3-point bending. A 2D drawing illustrating the load application of the new impact device is given in Fig.C.2, where this difference is highlighted. To recall the

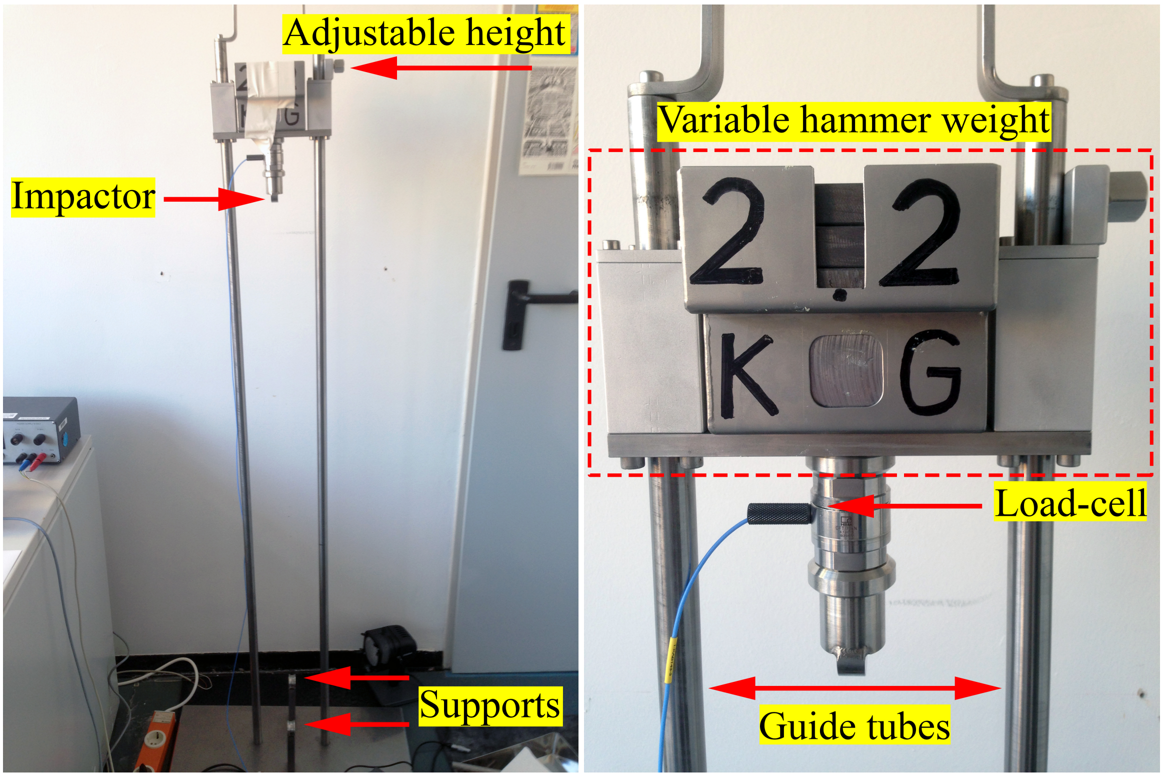

(a) Overview of the impact mock-up tower. (b) Hammer and load-cell attachment.

Fig. C.1 Impact mock-up test rig placed in cold laboratory, replicating the impact tower installed in the hot-cell, with extended acquisition capabilities.

reasoning on the change of the former's dimension between the bending and the impact devices installed in the hot-cell, the reader can refer to section 2.3.3. Despite this difference, it can be assumed that the effective area of load transmission during the tests (or contact area between former and sample) would be approximately the same, since the SNF fractures at relatively short deflection ranges, of less than 2 cm.

This new test-rig is equipped with further features extending the acquisition capabilities during an impact sequence, including:

- a piezoelectric (high-frequency) load cell recording the impact load in a similar way to the bending test-rig;
- a new high-speed camera enabling much higher image recording frequencies compared to the one used in the hot-cell;

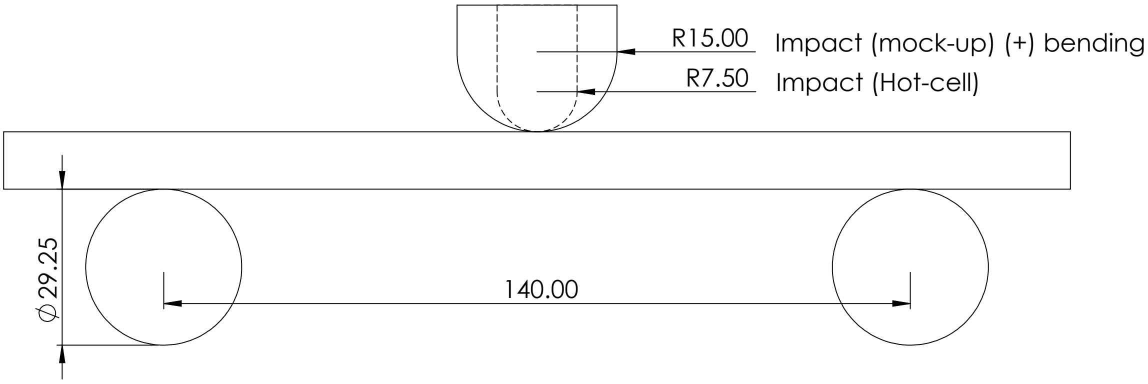

Fig. C.2 2D drawing of the load application at the impact and bending devices.

- a chessboard pattern attached to the impactor facilitating both the estimation of the sample's displacement with higher confidence and camera calibration process with the use of dedicated IA software (e.g. MATLAB toolbox App).

The setup configuration of the new mock-up device is depicted in Fig. C.3. To reproduce the geometrical configuration of the impact tower installed in the hot-cell, the new high-speed camera has been placed at a similar distance and angle with respected to the sample.

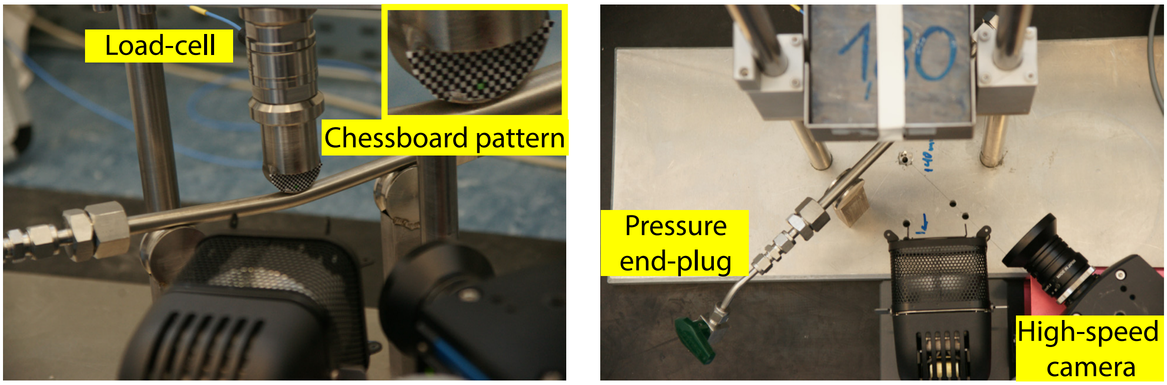

Fig. C.3 Set-up of new acquisition capabilities on the impact mock-up test rig.

A piezoelectric force measurement chain with nominal force of 70 kN (HBM PACEline CMC [120]) is used to measure the applied impact loads; an information which was not possible to acquire based only on the IA methodology. Consequently, on the same principle as in the 3-point bending tests, the load-displacement and stress-strain curves can be derived, allowing the calculation of the SED.

The new high-speed camera can be synchronized to the load-cell acquisition frequency enabling the coupling of the sample's visual response (or displacement via the IA) to the

Table C.1 Test parameters for the IA validation campaign.

Test [#]	Test name	Material	End plugs	Cam. frequency [Hz]
1	10k_a_NOplugs	SST	✗	10000
2	10k_a	SST	✓	10000
3	10k_b	SST	✓	10000
4	20k	SST	✓	20000
5	4k	SST	✓	4000
6	10k_b_NOplugs	SST	✗	10000
7	10k_c	SST	✓	10000

applied load. The influence of the recording frequency to the sample's response signal (and therefore to the SED derivation) will be examined as well, by performing the same test in a wide range of frequencies.

Finally, the chessboard pattern is used as an alternative method to accurately derive the impactors displacement during the impact sequence. This derivation is decoupled from the applied IA methodology and can be used to calibrate/validate its results. Subsequently, it can be used to calibrate the camera based on the pinhole principle, which provides the relationship of a 3D point to its image projection [121].

C.2 Experimental Campaign

To estimate the uncertainty on the characterization of the sample's dynamic response, a set of tests has been performed on SST solid bars. The test parameters are given in Table C.1. In contrast to the quasi-static tests, the added weight of the pressure transducer to the ends of the sample could influence its dynamic response. In other words, the recorded sample's response represents the hybrid sample/end-plug system, rather than the sample itself, which is under investigation. The dimensions and masses of the SST sample parts are given in Fig C.4 and in Table C.2, respectively. The mass of the SST bar stands for only 28% of the total sample weight. In comparison to the irradiates samples, this ratio is considerably lower due to its smaller length and average density. To examine the relative influence of the end-plugs to the sample's response, tests have been performed with and without those attachments.

Typical results from the impact tests are given in Fig. C.5. The graph gives the reaction force (before calibration in units of Volt) recorded at the load-cell during the impact loading. The load increases as soon as the impactor touches the hammer. The shape of the curve

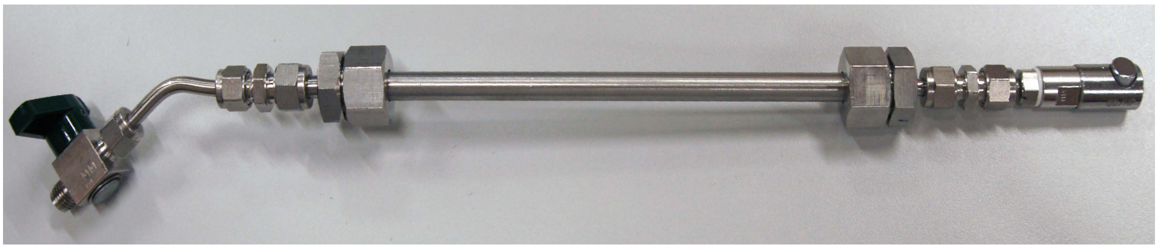

Fig. C.4 SST sample prepared for the IA impact validation campaign with the use of the mock-up impact tower.

Table C.2 Test parameters for the IA validation campaign.

Specimen	Mass [g]	Mass ratio [%]	Axial length [mm]	Diameter [mm]
SST bar	146.9	28%	238.50	10
Right end-plug	170.2	32%	126.35	-
Left end-plug	211.2	40%	155.00	-
Total	528.3	100%	519.85	

resembles the typical load-displacement curves observed in the three-point bending tests. Initially, the load increases linearly up to a certain point, where the sample start to deform plastically. The load drops after the sample has reached its maximum deformation and due to reaction forces the sample moves upwards together with the hammer. In addition, small periodic oscillation can be observed, which represent the damping frequencies of the sample.

Fig. C.6 gives the results from the impact tests on SST with the use of the end-plugs, but in different recording frequencies. The graph gives a direct comparison on the resolution of the registered data. As expected, lower frequencies provide smoother curves, however the information on the damping frequency of the sample is lost. The oscillation became apparent in higher frequencies, when 10 kHz or 20 kHz were used.

The influence of the pressure end-plugs in the resulting data can be observed in Fig. C.7. Fig. C.7a gives the raw data, while Fig. C.7b provides the same results after smoothing. The area under these curves give the energy that has been absorbed from the sample during its deformation under dynamic bending loads. As expected, these results provide the confirmation that the dynamic response of the samples differ when the end-plugs are used, since the effective sample mass and geometry are changed.

To evaluate the difference in the resulting data, the area under the curve from each impact test is calculated and the results are presented in Fig. C.8. The test without the use of the end-plugs showed that approximately 10% less energy is absorbed from the sample during

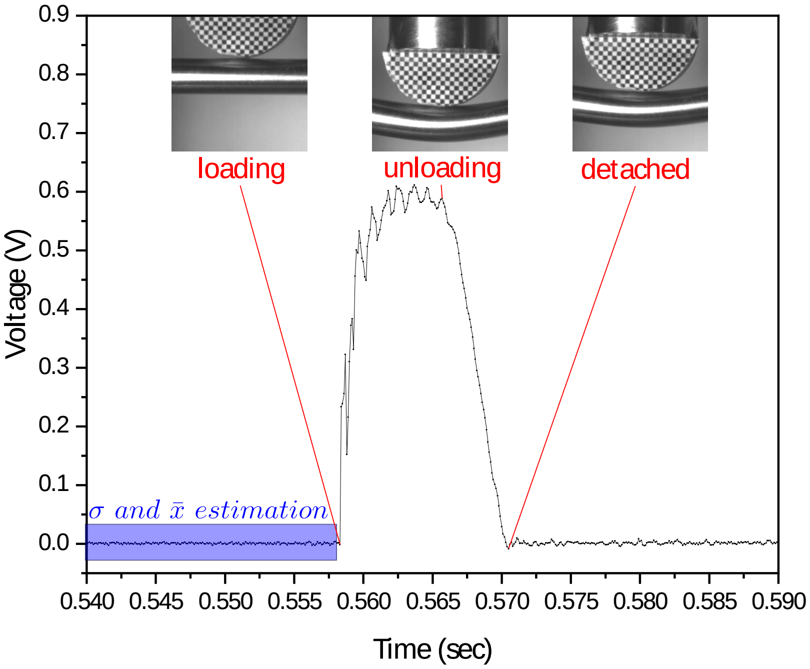

Fig. C.5 Piezoelectric load cell response to impact loads on SST rodlet.

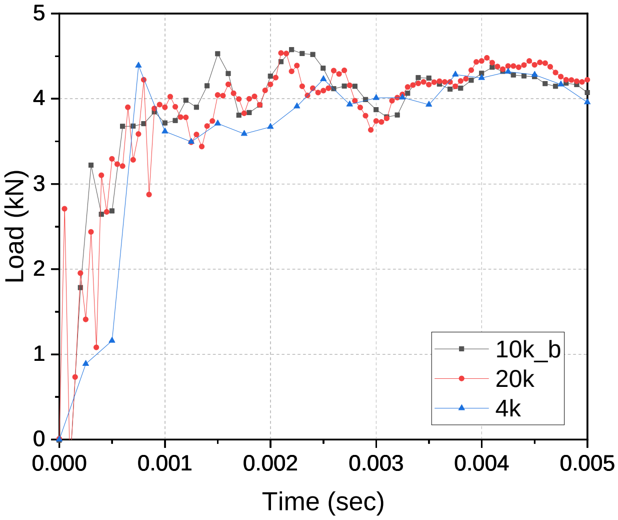

Fig. C.6 Load-cell reaction force in impact loading for different recording frequencies.

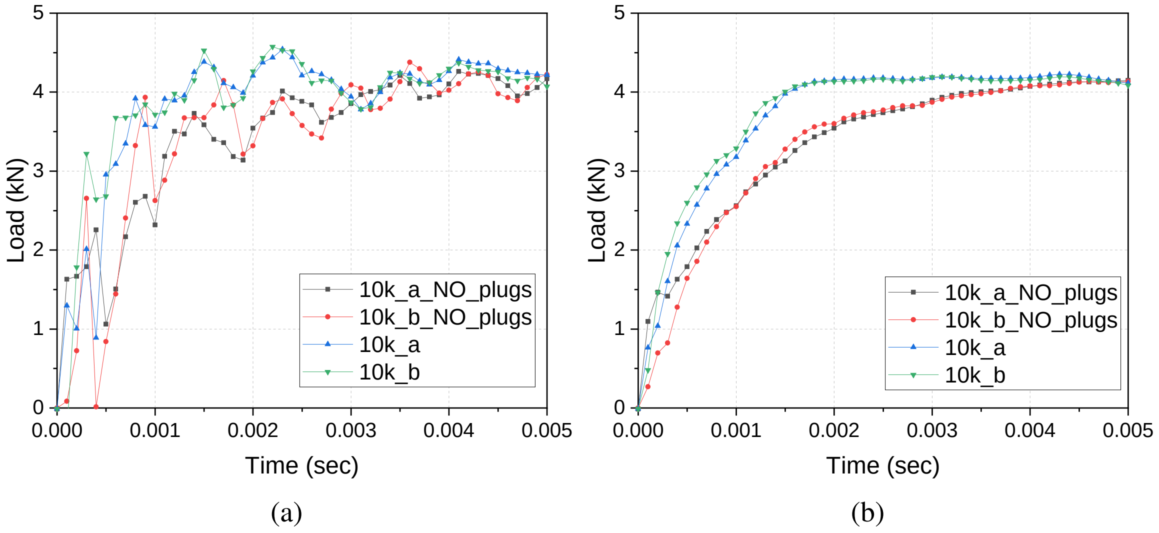

(a) (b)

Fig. C.7 Dynamic response of the SST sample with and without the use of end-plugs; a) raw and b) smoothed data of the recorded loads against time

the impact loading, compared to the samples where the end-plugs were used. These results where derived for 10 kHz recording frequencies. In higher frequencies (20 kHz) the results were similar, however approximately 5% less absorbed energy was calculated when 4 kHz was used.

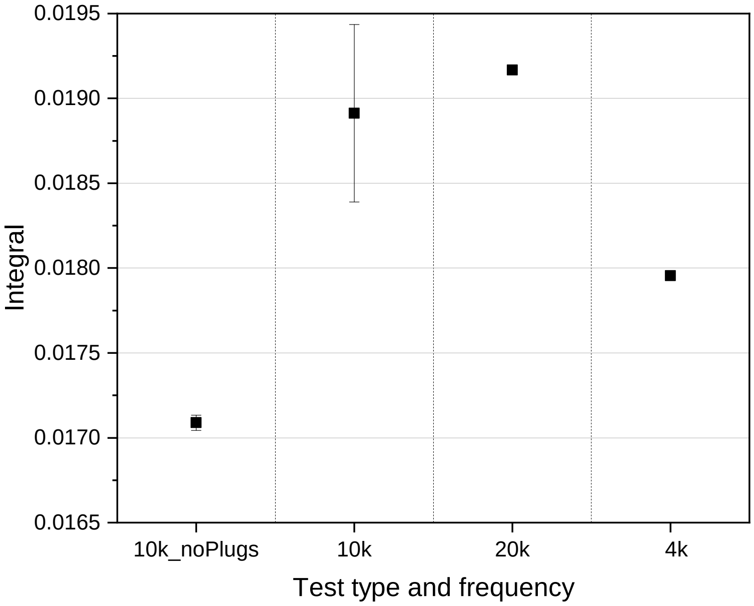

Fig. C.8 table:IAval

As a result, there are two sources of uncertainty in the derivation of the dynamic response of the samples. The first is related to the use of pressure end-plugs, where the geometry and mass of the samples is changed leading to an overestimation of the sample's absorbed energy. The second source of uncertainty is related to the recording frequency used for the data acquisition. It was observed that for frequencies $\geq$ 10 kHz, the resulting data were not changed. In addition, in higher frequencies the characteristic damping frequency of the sample was also revealed.

Appendix D

Hydrogen measurement analysis

This method for the hydrogen determination relies on the analysis of certified reference materials to generate calibration curves to accurately determine the concentration of unknown samples. This section gives the analysis followed to estimate the calibration curves and corresponding uncertainties. Table D.1 gives the certified materials used and number of measurements made for the calibration process.

Table D.1 Overview of measurements performed on certified materials for the calibration process.

Standard H2 content [ppm]		Number of metal pieces			Number of measurements
62		1	2	3	
	# meas.	3	3	3	9
107		1	2	3	
	# meas.	3	3	3	9
192		1	2	3	
	# meas.	2	3	2	7

Each measurement results to single peak of no characteristic shape. Therefore, there is not a standard method to evaluate the peak area nor the background contribution. The analysis for these measurements was made with the use of the OriginLab Pro software and in particular with the ALSS method for the baseline estimation. Table D.2 provides the settings used for the baseline determination for most of the measurements. The signal peaks along with the baseline determination are given in Fig. D.1.

Table D.2 Method and parameters used for the baseline determination of the peak signal with the use of the OriginPro software.

ALSS Baseline settings	
Asymmetric Factor (0-1)	0.001
Threshold	0.0005
Smoothing Factor	8
Number of Iterations	1000

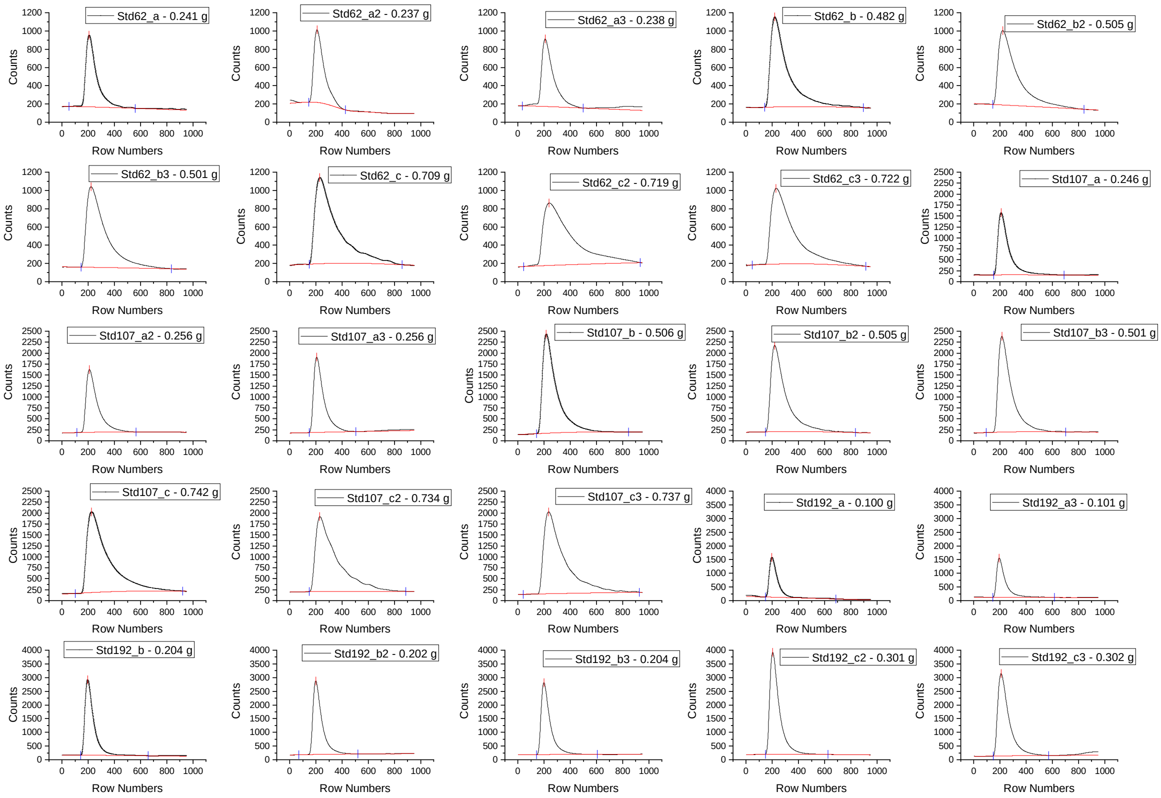

Fig. D.1 ALSS baseline determination for all measurements on certified material with different hydrogen content.

D.1 Calibration methodology

There are 2 possible methods to approximate the calibration curves by:

- considering all measurements of each certified material or;
- estimating hydrogen ranges and considering the calibration curves defined by the closest certified material.

The linear regression model was used to fit the data to the following form:

$$y_i = \beta_0 + \beta_1 \chi_i + \varepsilon_i \tag{D.1}$$

, where χ is the independent variable and y is the depended variable, β_0 are parameters, and ε_i is a random error term with mean $E\{\varepsilon_i\} = 0$ and variance $Var\{\varepsilon_i\} = \sigma^2$. The constant term β_0 was fixed to zero, based on the assumption that no peak will be estimated for “blank” measurements. A verification to that assumption made by performing a “blank” measurement (without using any sample), where no peak was detected.

Figs. D.2 and D.3 provide the calibration curves as estimated based on the first and second method, respectively. The area between the peak and the baseline has been estimated and plotted against the product of hydrogen concentration and sample weight of each measurement.

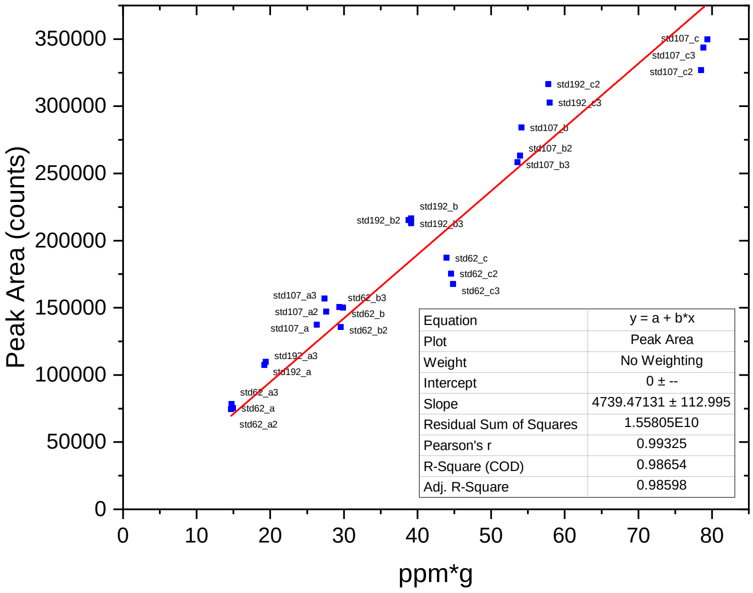

Fig. D.2 Linear regression model used to fit all certified material measurements.

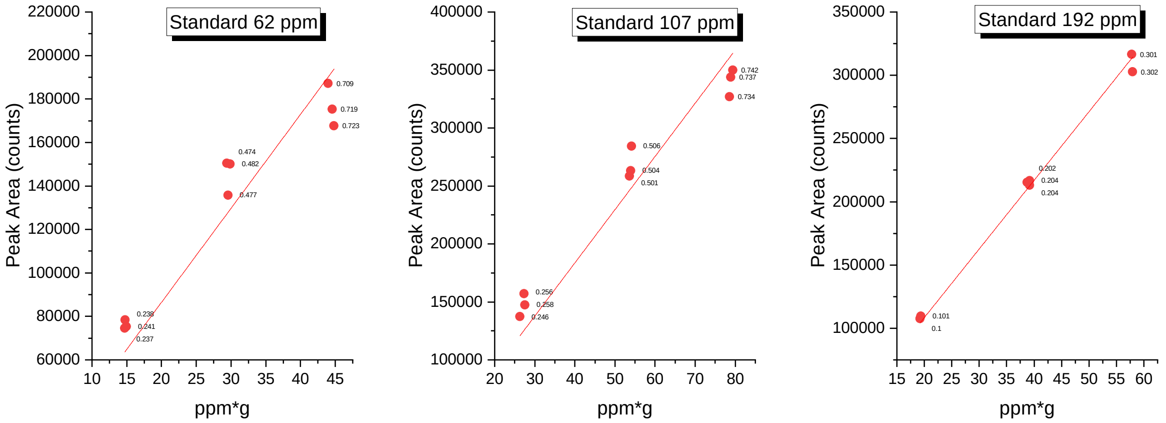

Fig. D.3 Linear regression model used to fit measurements of a) 62 ppm, b) 107 ppm and c) 192 ppm standard samples, respectively.

Table D.3 provides the values of the linear regression models as estimated for the first and second method. In particular, the slope is given along with its standard error and the adjusted R-square values of the models.

Table D.3 Linear regression model parameters as derived for the different methods.

Method	Intercept	Intercept	Slope	Slope	Statistics
#	Value	Standard Error	Value	Standard Error	Adj. R-Square
1. All data	0	–	4741.4	113.4	0.986
2a. Std 62	0	–	4324.2	183.6	0.984
2b. Std 107	0	–	4591.2	145.5	0.991
3b. Std 192	0	–	5423.1	55.5	0.999

D.2 Bias estimation

Although, the uncertainty of each method had been evaluated, the bias must be determined as well. Bias is graphically described in Fig. D.3 and refers to the tendency of a measurement process to over- or under-estimate the value of a population parameter. In our case, bias refers to the relative distance between the true value of the hydrogen concentration of the certified samples and the mean value of the calculated concentrations based on each method used for their determination.

To determine the bias associated with each method, the derived calibration curves are used to analyse the measurements of the certified materials. For the sake of completeness, all

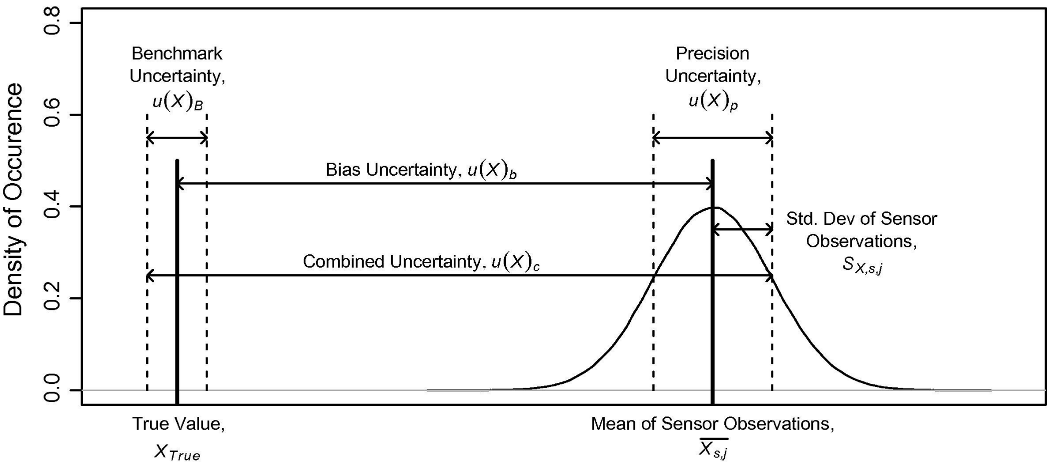
Density of Occurence
0.0
0.2
0.4
0.6
0.8
Benchmark Uncertainty, $u(X)_B$
Precision Uncertainty, $u(X)_p$
Bias Uncertainty, $u(X)_b$
Combined Uncertainty, $u(X)_c$
Std. Dev of Sensor Observations, $s_{X,s,j}$
True Value, X_{True}
Mean of Sensor Observations, $\overline{X_{s,j}}$

Fig. D.4 Uncertainty associated with the observation of a measurand χ, adapted from [19, 20]

4 calibration curves were used to analyse those measurements. Tables D.4, **??** and **??** give the results of each measurement as derived from each method, as well as the mean value and the standard deviation of the derived hydrogen content for every group of certified materials. Color coding was used to highlight the deviation of the calculated values from the true value of the standard samples. Reddish colors depict higher values, while bluish depict lower.

These tables provided two useful outcomes.The first is on the bias uncertainty of each method. This information is summarized in Fig. D.5, showing the precision and the accuracy of the each of the selected methods in different hydrogen ranges. Instantly, we can exclude specific calibration curves in certain ppm ranges; e.g. although the use of the 192-calibration curve (method 3b) predicts accurately and precisely samples in the range of 192 ppm, it is not appropriate to use for lower hydrogen content samples since it has both low accuracy and precision. The second main outcome deals with the optimum sample weight for measuring samples in different ppm ranges. For example, the use of the 62-calibration curve (method 2a) tends to overpredict samples in this ppm range when the sample weight is low, however its accuracy is much higher for samples of higher weight.

D.3 Methodology selection and application

The slope standard error or calibration uncertainty (as referred from now on) has been determined. The bias uncertainty has been derived as well for the different calibration methods and for specific hydrogen content of unknown samples (refer to Table D.7). There are three main points to be considered to finalize the calibration methodology:

Table D.4 Derivation of hydrogen content of the certified standard materials (62 ppm) using different calibration curves.

Measurement (standard 62)	Sample mass	ppm*g	Peak area calculation	Hydrogen concentration			
				Std 62	Std 107	Std 192	All data
std062_a	0.241	14.942	75351	72.3	68.1	57.7	65.9
std062_a2	0.237	14.694	74482	72.7	68.4	58.0	66.3
std062_a3	0.238	14.756	78336	76.1	71.7	60.7	69.4
std062_b	0.482	29.884	150077	72.0	67.8	57.4	65.7
std062_b2	0.477	29.574	135629	65.8	61.9	52.4	60.0
std062_b3	0.474	29.388	150509	73.4	69.2	58.6	67.0
std062_c	0.709	43.958	187167	61.0	57.5	48.7	55.7
std062_c2	0.719	44.578	175342	56.4	53.1	45.0	51.4
std062_c3	0.723	44.826	167708	53.6	50.5	42.8	48.9
			$\bar{\chi}$	**67.0**	**63.1**	**53.5**	**61.1**
			σ	**8.2**	**7.7**	**6.5**	**7.5**

Table D.5 Derivation of hydrogen content of the certified standard materials (107 ppm) using different calibration curves.

Measurement (standard 107)	Sample mass	ppm*g	Peak area calculation	Hydrogen concentration			
				Std 62	Std 107	Std 192	All data
std107_a	0.246	26.322	137390	129.2	121.6	103.0	117.8
std107_a2	0.258	27.606	147158	131.9	124.2	105.2	120.3
std107_a3	0.256	27.392	156921	141.8	133.5	113.0	129.3
std107_b	0.506	54.142	284176	129.9	122.3	103.6	118.5
std107_b2	0.504	53.928	263260	120.8	113.8	96.3	110.2
std107_b3	0.501	53.607	258270	119.2	112.3	95.1	108.7
std107_c	0.742	79.394	349743	109.0	102.7	86.9	99.4
std107_c2	0.734	78.538	326827	103.0	97.0	82.1	93.9
std107_c3	0.737	78.859	343659	107.8	101.6	86.0	98.3
			$\bar{\chi}$	**121.4**	**114.3**	**96.8**	**110.7**
			σ	**12.9**	**12.2**	**10.3**	**11.8**

Table D.6 Derivation of hydrogen content of the certified standard materials (192 ppm) using different calibration curves.

Measurement (standard 192)	Sample mass	ppm*g	Peak area calculation	Hydrogen concentration Std 62	Std 107	Std 192	All data
std192_a	0.1	19.2	107372	248.3	233.9	198.0	226.5
std192_a3	0.101	19.392	109636	251.0	236.4	200.2	228.9
std192_b	0.204	39.168	216519	245.4	231.2	195.7	223.9
std192_b2	0.202	38.784	215151	246.3	232.0	196.4	224.6
std192_b3	0.204	39.168	212929	241.4	227.3	192.5	220.1
std192_c2	0.301	57.792	316408	243.1	229.0	193.8	221.7
std192_c3	0.302	57.984	302541	231.7	218.2	184.7	211.3
			$\bar{\chi}$	**243.9**	**229.7**	**194.5**	**222.4**
			σ	**6.3**	**5.9**	**5.0**	**5.7**

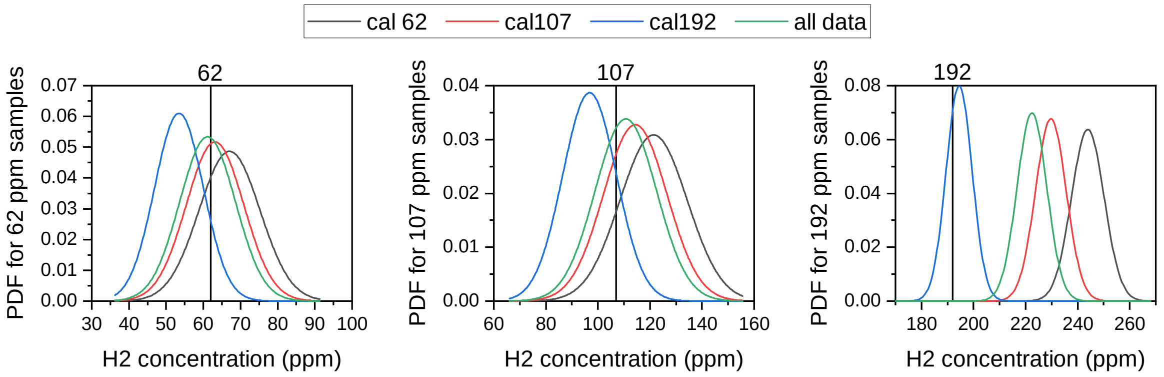

Fig. D.5 Uncertainty associated with the measurement of certified materials of different hydrogen content with the use of different calibration curves.

Table D.7 Bias uncertainty based on different calibration methods for a range of hydrogen content samples.

H2 content [ppm]	Bias Uncertainty 2a. – Cal-62	2b. – Cal-107	2c. – Cal-192	1. – All data
62	5.04	1.14	-8.54	-0.86
107	14.39	7.33	-10.21	3.71
192	51.89	37.71	2.47	30.86

1. Is a single calibration curve (Method 1) appropriate to be applied to every unknown sample?
2. If not, the calibration curves produced from each certified material (Method 2) must be valid within given ppm ranges. How this sub-groups should be produced?
3. How the uncertainty bias should be treated (subtracted or divided from the measurement value)?

Based on Table D.7, the use of the first method for the calibration curve, by considering all standard samples, seems to be appropriate for hydrogen ranges up 107 ppm. Unfortunately, method 1 is not suitable to be applied for higher hydrogen content ranges, therefore its universal use should be excluded.

Method 2 will be used instead; however, the hydrogen range of validity must be defined. Since there is no information from the user manual or manufacturer, the range of validity will be defined as shown in Fig. D.6. For ranges between the hydrogen content of the certified materials, the first half distance will be used to apply the calibration curve of the lower hydrogen content standard, whereas the second half will be used to apply the calibration curve of the higher hydrogen content standard.

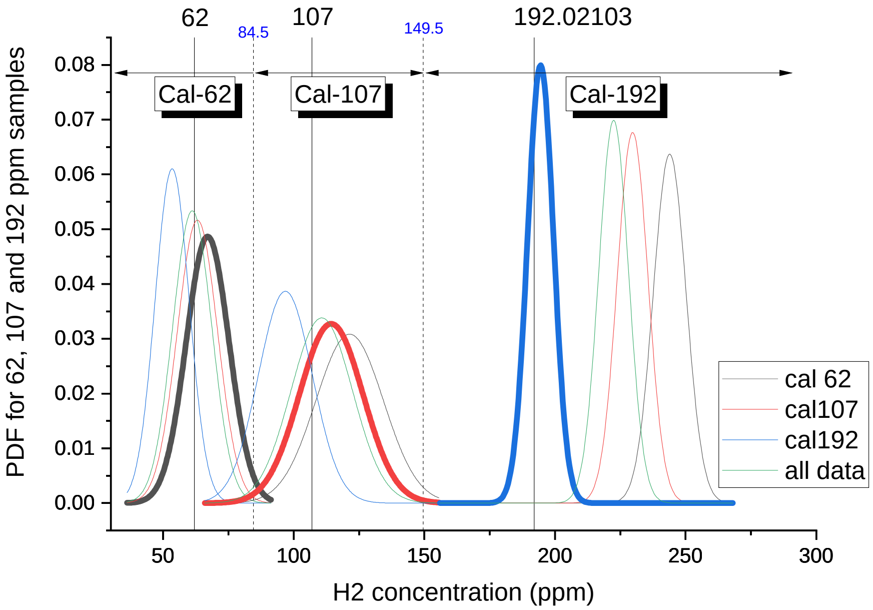

Fig. D.6 Hydrogen range of validity for the application of the three calibration curves.

Table D.8 summarizes the calibration curves and the associated errors. In this stage the fitting parameter is the slope or “α” .

Table D.8 Ranges of applicability of calibration curves given fitting parameters and experimental bias.

Hydrogen range [ppm]	Calibration method	Slope (a)	Exp. bias
0 - 84.5	Cal-62	4324 ± 184	5.04
84.5 - 149.5	Cal-107	4591 ± 146	7.33
149.5 - higher	Cal-192	5423 ± 55	2.47

The hydrogen content will be evaluated from the following equation:

$$y = \frac{P}{\alpha \times m} \tag{D.2}$$

where,

P = peak area as determined with OriginLab with the use of ALSS for the baseline

α= slope selected from Table tab:aplicrang

m = mass (g)

Appendix E

Finite element modeling details

The hardware specifications of the computer system used to run all ANSYS simulations was the following:

- **Processor**: AMD Ryzen Threadripper 1950x, 16cores - 32threads
- **Graphic card**: NVIDIA Quadro FX 3800 @594 MHz (GPU core clock speeds), 1GB dedicated GDDR3 memory @792 MHz (GPU memory clock speeds)
- **RAM**: 8*16GB (128GB in total) DDR4 sticks @2133 MHz
- **Hard disk drive**: Samsung SSD 960 Pro, 1TB, Max sequential read speed 3500MB/s, Max sequential write speed 2100MB/s

The following parameters were used for the construction of the reference 3D static structural FEM.

- **Geometry**
  Cladding = BODY element
  Former and support = Shell element with rigid behavior, 0.1 thick, stainless steel
  Pellets = BODY elements, attached to cladding bottom, non-linear effects OFF
- **Materials**
  - **Pellets - Cast-iron model**
    Young’s modulus: 380 GPa
    Elastic Poisson”s ratio: 0.22
    Compressive yield strength: 3500 MPa

  Compression to tension coefficient: 100
  Plastic modulus: 35 GPa
  Plastic Poisson's ratio: 0.04
  Density: 3.9 gcm^3

  - **Cladding - Voce model**
    Young's modulus: 85 GPa
    Poisson's ratio: 0.35
    Yield strength: 500 MPa
    Linear coefficient R_0: 500 MPa
    Exponential coefficient R_{inf} : 180 MPa
    Exponential saturation coefficient, b: 120
    Density: 6.6 gcm^3

- **Symmetry**
  One fourth, half pellet at symmetry region

- **Contact formulation**

  - **Pellet to cladding contacts**
    Frictional:0.6, Stiffness: 2, update each iteration aggressive, asymmetric behaviour, interface: "adjust to touch", pinball radius: 2mm, trim tolerance: 3mm, type: Programme Controlled

  - **Pellet to pellet contacts**
    Frictional: 0.7, Stiffness: 2 update each iteration aggressive, offset set to 0, pinball: Programme Controlled, trim tolerance: 2mm, type: Programme Controlled

  - **Former to cladding contact**
    Frictional: 0.1, Stiffness: 1, update each iteration, , interface: "adjust to touch", type: Programme Controlled

  - **Support to cladding contact**
    Frictionless, Stiffness: 5, interface: 'adjust to touch', type: Programme Controlled

- **Spring**
  Stiffness: 2N/mm, 10 mm long

- **Mesh**
  Hexa, approx. 4000 nodes, elements: linear order, max. face size: 1.5mm

- **Gravity** OFF

- **Pressure** 4 MPa
- **Solution**
  Weak spring: ON, Stiffness: Programme controlled, Newton-Raphson (Programme controlled)

A final revised version of the 3D static structural FEM was constructed based on the results of the extended sensitivity analysis performed on reference model. The final FEM version was built as the best compromise between the solution quality and the computational time required for the simulation. The modelling approach and parameters used for this final model are provided bellow and the material properties refer to the values used for simulating the irradiated samples.

- **Geometry**
  Cladding = BODY element
  Former and support = Shell element with rigid behavior, 0.1 thick, stainless steel
  Pellets = BODY elements, 10 Pellets touching the clad, non-linear effects OFF
- **Materials**
  - **Pellets - Cast-iron model**
    Young’s modulus: 201 GPa
    Elastic Poisson”s ratio: 0.32
    Compressive yield strength: 2146 MPa
    Compression to tension coefficient: 100
    Plastic modulus: 20 GPa
    Plastic Poisson’s ratio: 0.04
    Density: 10.53 gcm^3
  - **Cladding - Voce model**
    material properties assigned after model optimization against experimental results
- **Symmetry**
  One fourth, half pellet at symmetry region
- **Contact formulation**
  - **Pellet to cladding contacts**
    Frictional: 0.4, Stiffness: 2, update each iteration aggressive, asymmetric behavior, interface: “adjust to touch”, pinball radius: 2mm, trim tolerance: 3mm, formulation: Program Controlled

  - **Pellet to pellet contacts**
    Frictional: 0.5, Stiffness: 2, update each iteration aggressive, interface: “add offset, ramped effects”, offset: 0mm, pinball region: Program Controlled, trim tolerance: 2mm, Formulation: Program Controlled
  - **Former to cladding contact**
    Frictional: 0.1, Stiffness: 1, update each iteration, , interface: “adjust to touch”, formulation: Program Controlled
  - **Support to cladding contact**
    Frictionless, Stiffness: 1, interface: “adjust to touch”, formulation: Program Controlled

- **Spring**
  Stiffness: 1000N/mm, 45 mm long

- **Mesh**
  General settings: element order: linear, element size: 4mm, 6114 nodes, 3897 elements in total, HEX8, QUAD4 and TRI3 element types
  Pellets: method: ‘sweep’, element order: “use global setting”, src/trg selection: “automatic”, free face mesh type: “Quad/Tri”, sweep number of divisions: 8 for pellet no. 1, 5 for pellets no. 2 to no. 5, 3 for pellets no. 6 and 7, 2 for pellets no. 8 to no. 10 (counting from the side of the former towards the other side)
  Cladding: element order: “use global setting”, method: “sweep”, source: inner face of cladding, target: outer face of cladding, free face mesh type: “all quad”, sweep number of divisions: 2
  Former: face sizing with element size 1.5mm
  Support: face sizing with element size 1.3mm

- **Gravity** OFF

- **Pressure** Dependent on the sample burnup of each experiment: A11 – 2.88 MPa, D08 – 4.345 MPa, A07 – 3.205 MPa

- **Solution**
  Weak spring: ON, Stiffness: Program controlled, Newton-Raphson (Program controlled)

Efstathios Vlassopoulos

Sonnmattstrasse 1
CH-5400, Baden
Phone: +41 78 840 2906
stvlasso@hotmail.com

Date of birth: 29 June 1988
Nationality: Greek
Marital status: Single

Education

10.2015 – 2021 **Ph.D. in Nuclear Engineering**
Swiss Federal Institute of Technology Lausanne in Lausanne (EPFL)
PhD thesis: “*Structural performance and mechanical properties investigation of spent nuclear fuel rods under static and dynamic bending loads*”
Advisors: Prof. Andreas Pautz, Dr. Stefano Caruso

09.2013 – 09.2015 **M.Sc. in Nuclear Engineering**
Swiss Federal Institute of Technology Lausanne in Zurich (ETHZ)
M.Sc. thesis: “*Development of an optimization code for the logistics of spent fuel assembly loading into final disposal canisters*”
Advisors: Prof. Andreas Pautz, Dr. Ben Volmert

10.2006 – 07.2013 **Diploma in Mechanical Engineering** (B.Sc. & M.Sc.)
National Technical University of Athens (NTUA)
Diploma Thesis: “*Optimization of the NED-NTUA XRF facility for the analysis of environmental samples*”
Advisors: Prof. Marios Anagnostakis

Professional Experience

03.2019 – Present **Project Manager – Nuclear Engineer**
Nagra, Unit of Inventory and Logistics

- Optimization of SNF disposal strategies in deep-geological repositories
- Radionuclide inventory and decay heat calculations for all Swiss SNF assemblies
- SNF structural integrity investigations

01.2016 – 05.2017 **Visiting Research Scholar**
EC-JRC – Karlsruhe

- Mechanical testing on SNF rods

07.2014 – 10.2014 **Nuclear Engineer Intern**
Nagra, Unit of Radioactive Materials

- Monte Carlo techniques (MCNP-6) on rare event simulation

11.2012 – 07.2013 **Military Service**, Force: Hellenic Army

Language Skills

Greek (native), English (fluent), German (beginner)

Computer Skills

Programming:	Fortran, MATLAB, LabView, LaTeX, Python
Engineering Tools:	ANSYS Mechanical, optiSLang, OriginLab, AutoCAD, SolidWorks, Office Suite
Nuclear codes:	MCNP, Serpent, SCALE, MicroShield, PENELOPE, QXAS-IAEA